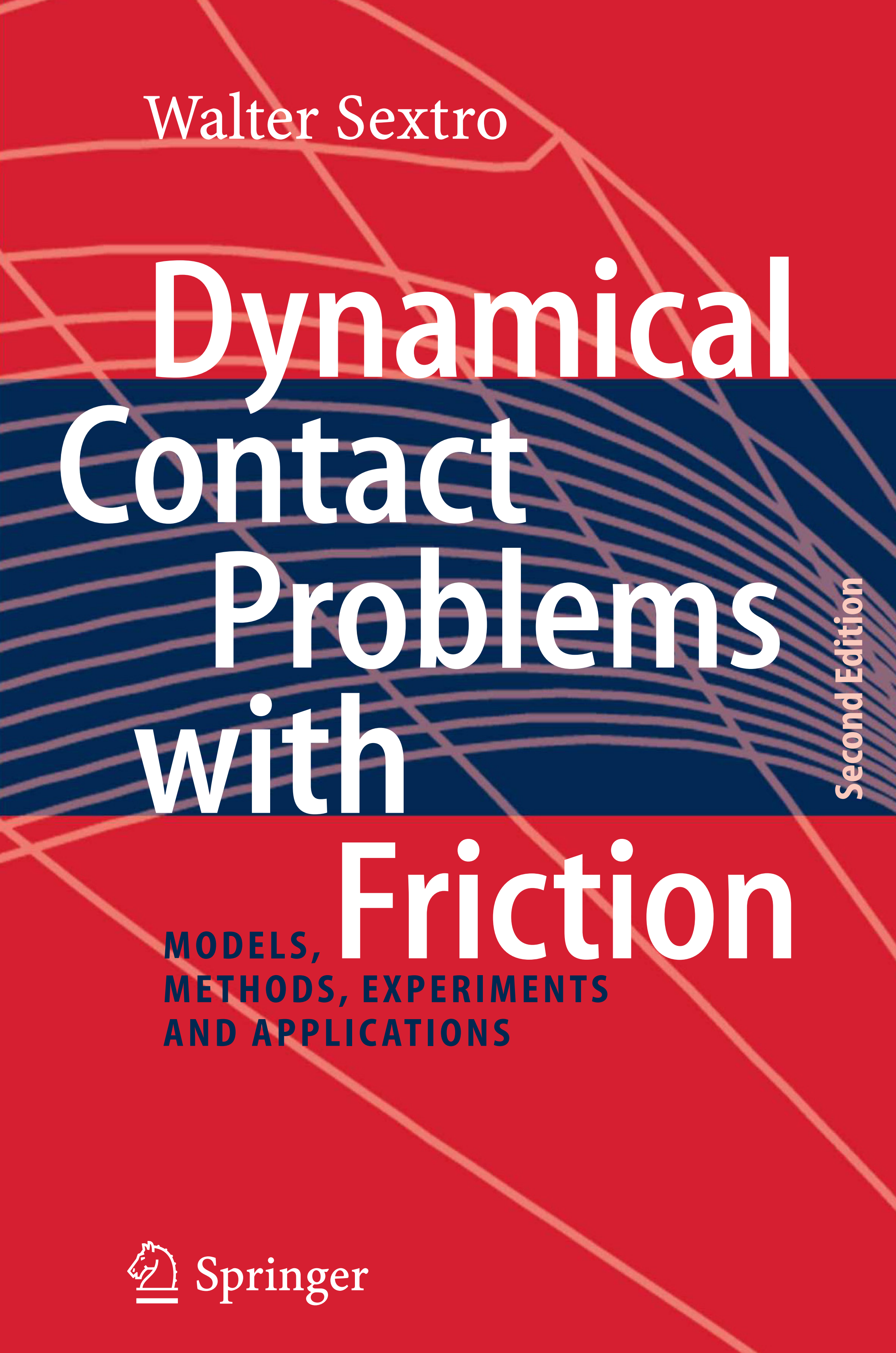

Walter Sextro

Dynamical Contact Problems with Friction

MODELS, METHODS, EXPERIMENTS AND APPLICATIONS

Second Edition

Springer

Dynamical Contact Problems with Friction

Walter Sextro

Dynamical Contact Problems with Friction

MODELS, METHODS, EXPERIMENTS AND APPLICATIONS

With 133 Figures

Springer

Prof. Dr.-Ing. habil. Walter Sextro
Graz University of Technology
Institute of Mechanics
Kopernikusgasse 24/III
A-8010 Graz
Austria
E-mail: sextro@tugraz.at

Originally published as volume 3 of the series Lecture Notes in Applied Mechanics, Springer-Verlag Berlin Heidelberg 2002.
Library of Congress Control Number: 2006940067

ISBN-10 3-540-69535-4 Springer Berlin Heidelberg New York
ISBN-13 978-3-540-69535-6 Springer Berlin Heidelberg New York

Springer is a part of Springer Science+Business Media.

springer.com

Typesetting by the author and SPi
Cover design: Erich Kirchner, Heidelberg

Printed on acid-free paper SPIN 11405887 89/3100/SPi 5 4 3 2 1 0

Preface

Friction contacts are used to transmit forces or to dissipate energy. A better understanding of friction phenomena can result in improvements like the reduction of noise and maintenance costs, increased life time of machines and improved energy efficiency. There exists a rich literature on friction. Depending on the features of the friction contact, different contact models are applied and dependent on the contact model, different solution methods are preferred. The aim of this book is to describe an efficient procedure to model dynamical contact problems with friction. This procedure is applied to different practical problems and verified by experiments.

The dynamics of the elastic bodies in contact are described by a reduced order model through the so called modal description, to speed up calculations. This description is presented in Chap. 2. In Chap. 3 the generalized contact model is developed, which includes the main physical effects like contact elasticity, roughness, friction characteristics etc.. The contact planes are discretized and a point contact model is applied to each area element. The thermomechanics of the contact is investigated, as well as the calculation of wear. The application of the combined procedure of the point contact model and the modal description of the elastic components are illustrated by three different examples. An impact and friction oscillator, see Chap. 4, is investigated in the time domain, while the friction damping of elastic structures with expanded friction contacts is analyzed within the frequency domain, see Chap. 5. The stationary rolling contact is presumed to calculate the wear of wheel-rail-systems, see Chap. 6.

This work arose during my research at the Institute of Mechanics of the University of Hannover in Germany. Part of the work was supported by the “Forschungsvereinigung Verbrennungskraftmaschinen e.V. (FVV, Frankfurt)” and was sponsored by the “Bundesministerium für Wirtschaft” through the “Arbeitsgemeinschaft industrieller Forschungsvereinigungen e.V. (AiF, Köln), (AiF Nr. 10684)”, a federal collaboration of the turbomachinery-industry and the “Deutsche Forschungsgemeinschaft (Projekt Nr. SE 895/3-1)”.

This book is based on the script that leads to my “Habilitation” in *Mechanics*. The “Habilitation” marks the end of the education as lecturer. In this context I would like to thank Prof. Dr.-Ing. habil. K. Popp, Prof. Dr.-Ing. habil. P. Wriggers and Prof. Dr.-Ing. habil. G.-P. Ostermeyer for carefully reading the script and for their support.

Furthermore, I would like to thank all of my colleagues at the Institute of Mechanics for the open discussion of any problems and the successful cooperation. I would especially like to emphasize Prof. Dr.-Ing. habil. K. Popp. During my time at the institute, he always supported me and therefore most of my thanks belong to him.

Hannover, 2002 Walter Sextro

Preface to the Second Edition

Since the last edition of this book the knowledge about friction has increased. Therefore several new results have been added like the wear calculation of a wheel-rail system as well as the efficient calculation of multi-coupled bladed disc assemblies with friction contacts.

This book can be seen as the result of more than ten years research at the Institute of Mechanics (now Institute of Dynamics and Vibration) at the University of Hannover (now Leibnitz University Hannover). Again I have to thank Prof. Dr.-Ing. habil. Karl Popp for the good collaboration and his support. He passed away in April 2005 and therefore I would like to dedicate this book to him.

Furthermore I would like to thank the “Deutsche Forschungsgemeinschaft (DFG)” for the financial support of the project of the “Forschergruppe: Dynamische Kontaktprobleme mit Reibung bei Elastomeren”. Regarding Chapter 3.6 I have to acknowledge Dr.-Ing. Markus Lindner, Dipl.-Ing. Patrick Moldenhauer and Dipl.-Ing. M. Wangenheimof of the Institute of Dynamics and Vibration, Leibnitz University Hannover, for their work done with regard to the friction characteristics of rubber. With regard to the results presented in Chapter 6.10 dealing with the instationary rolling contact I have to thank Dipl.-Ing. Florian Gutzeit.

Furthermore I have to thank Dr. Jaroslaw Szwedowicz, ABB Turbo Systems, Baden, Switzerland, who carried out spin pit tests with regard of bladed disc assemblies with shrouds to validate the developed method as presented in Chapter 5.

The numerical investigations in chapter 5.4 due to the multi-coupling of bladed disc was supported by the “Forschungsvereinigung Verbrennungskraftmaschinen e.V. (FVV, Frankfurt)” and was sponsored by the “Bundesministerium für Wirtschaft (BMWi)” through the “Arbeitsgemeinschaft industrieller Forschungsvereinigungen e.V. (AiF, Köln), (AiF Nr. 12565)”. Here, I have to thank the corresponding working group and the chairman Dr.-Ing. Karl Urlichs, Siemens Power Generation AG, Nürnberg for the good collaboration.

The application of the theory to a system with extended friction contacts was carried out by Dipl.-Ing. Alexander Genzo, Volkswagen, Wolfsburg. I have to thank him for this investigation presented in Chapter 5.5 and Volkswagen for their support.

Furthermore I would like to thank Dipl.-Ing. Ingo Kaiser, German Aerospace Center (DLR), Wesseling for his support in the application of the developed module to calculate the wear of railway wheels as presented in Chapter 6.9.

Last but not least I would like to thank my wife Ursula and my children Marvin and Rocco for their moral support in writing this book.

Graz, 2006 Walter Sextro

Contents

1 Introduction

1.1 Problem Description

Friction is the resistance against sliding and, therefore, friction plays an important role in dynamical engineering systems. In (Moore 1975) the mechanisms of friction are reviewed in a rich literature and the components of dry friction are summarized in (Seireg 1998) as follows:

- *Mechanical interlocking* due to the surface roughness, which leads to a higher static friction coefficient, compared to the sliding friction coefficient and explains the dynamic friction force as the force to lift off the contacts of the upper surface over the contacts of the lower surface.
- If the developed pressure at discrete contacts results in local *welding*. Due to relative motion, the welded surfaces are *sheared*. *Ploughing* of the harder material through the softer material contributes to the friction forces as well.
- *Molecular attraction*, which attributes to frictional forces and to energy dissipation, if atoms are plucked out of the attraction range,
- and for completeness, the *electrostatic forces* between the surfaces.

On the one hand, there exist dynamic systems, where friction has to be minimized, so that wear is reduced and the lifetime as well as the efficiency of a dynamic system is increased. Due to friction and wear the economic loss is estimated by five percent of the gross national product, see (Persson 1994). Hence, reducing friction and wear saves money. On the other hand, friction is used to transmit forces or to reduce vibration amplitudes, see (Popp 1994). A possibility to reduce the vibration of a machine is to use friction contacts to dissipate energy. The reduction of vibration amplitudes results in a reduction of alternating stresses and furthermore in an increase of lifetime and safety. The main part of the dissipated energy is transferred to heat. Dependent on the vibration frequencies the noise development can be reduced as well. From here, there is a need for efficient calculation procedures to optimize the dynamics of systems with friction contacts (Wriggers and Nackenhorst 2006). Before summarizing the main features of an elastic contact with friction, some important machines and machine components are presented, where friction plays an important role.

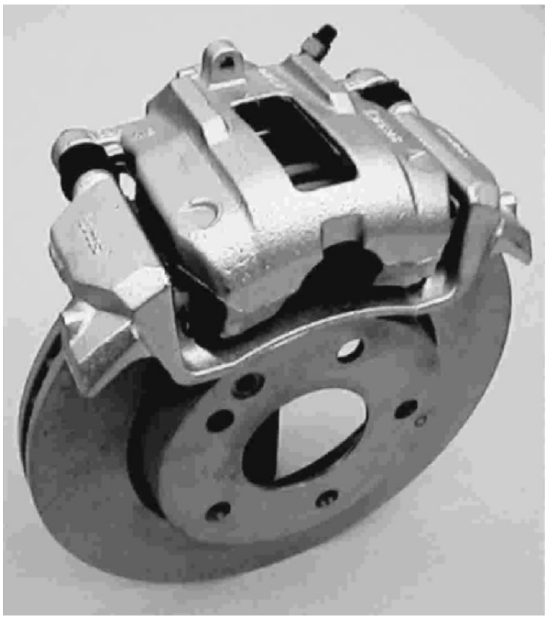

Fig. 1.1-1 Brake system (Lucas, Germany)

Brakes

Brakes are used to transmit forces to reduce the velocity of a vehicle, see **Fig. 1.1-1**. Dependent on the friction characteristic stick-slip vibration and, in extreme, a squealing noise can occur. One reason for the squealing noise is that, if the friction coefficient reaches a certain value, the brake system will become unstable, see also (Ibrahim 1994; Wallaschek et al. 1999; Allgaier et al. 1999). With respect to brakes, the manufacturing industry is not only interested in reducing the squealing noise, but also in reducing the temperature development within brakes. Otherwise, cooling devices would have to be installed. In general, the friction and therefore the dynamical behavior of brakes is very sensitive on the presence of moisture.

Machine Tools

A machine tool with friction is, for example a grinding machine, shown in **Fig. 1.1-2**, where friction plays an important role to develop smooth surfaces. The worn particles have high temperatures since they are red-hot. During grinding, it is common to use cooling fluid to remove worn material from the grinding disc, to reduce the temperature of the workpiece and the possibility of surface-burn and, hence, to increase the surface quality. Dependent on the system parameters machine chattering can occur. In this case, so-called chatter marks on the workpiece are found. Up to now, the occurrence of chatter vibrations as well as surface-burn is not understood in full detail. But there are hints, that chatter vibrations belong to friction-induced vibrations, see (Schütte and Heimann 1998).

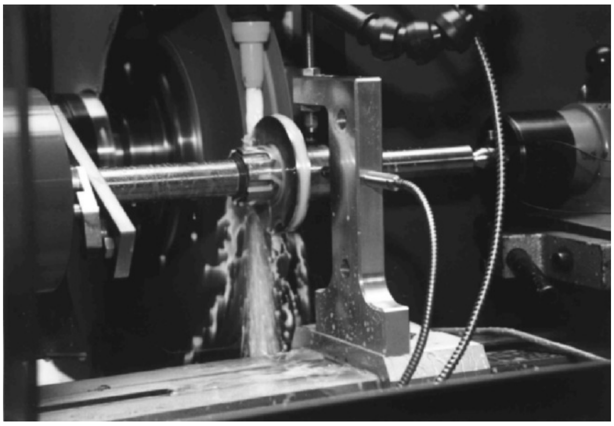

Fig. 1.1-2 Grinding machine

Motors

On the one hand, friction and wear problems between piston and cylinder of a motor are still a dynamic contact problem, see **Fig. 1.1-3**. The oil acts as a lubricant within the contact regions and reduces friction and wear. On the other hand, the calculation of the dynamics of chains is a typical problem of solving a multibody and multicontact system. Since many components are connected to each other in a motor, friction damping could be used to reduce the noise as well as the alternating stresses. Looking at the motor in full detail, there exist a huge potential to increase the lifetime of motor components, if the corresponding calculation methods are available, to optimize the system behavior.

Fig. 1.1-3 Motor (BMW, Germany, http://www.bmw.com/)

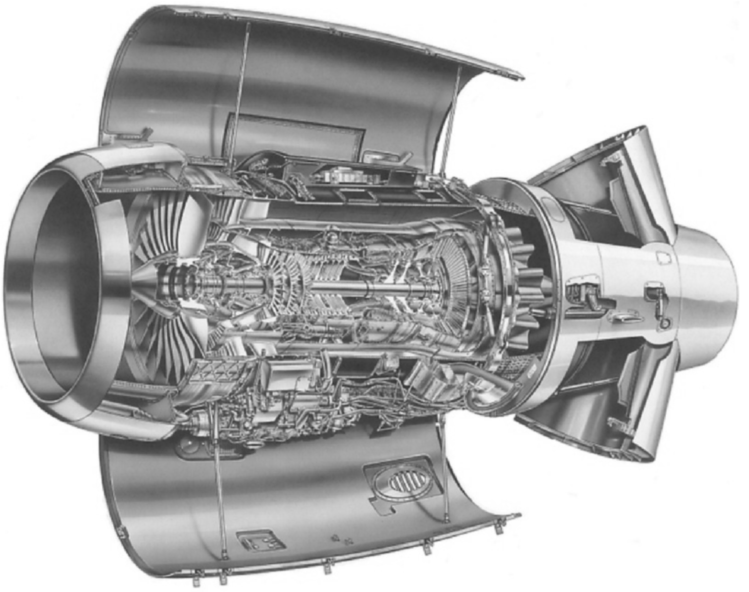

Fig. 1.1-4 Turbine (Rolls Royce, England, http://www.rolls-royce.com/)

Turbines

Turbine blades, see **Fig. 1.1-4**, are excited by fluctuating gas forces. To increase the lifetime of the turbine blades, friction is introduced to dissipate the vibration energy. Additionally, friction contacts are designed between adjacent blades or between the disc and the blades. The relative displacement of the contacting components and dry friction is used to dissipate energy and, hence, to reduce the vibrations amplitudes, noise and alternating stresses. Since a bladed disc assembly is a very large dynamical system, efficient contact models have to be developed for optimizing theses structures.

Bearings

To increase the efficiency of slide and ball bearings, see **Fig. 1.1-5**, the bearing friction has to be lowered and, therefore, lubrication is used. For example, the oil film on the ball bearings reduces friction forces because a part of the normal force is carried by the hydrodynamic forces developed by the oil film. Therefore, the hydrodynamic forces in the contact will decrease the friction and, hence, the wear. Again, for this multibody and multicontact problem with friction, there is a need for fast calculation algorithms to determine, for example, the longtime behavior of ball bearings in connection within the surroundings.

Fig. 1.1-5 Ball bearing (SKF, Germany)

Wheel-Rail Systems

The wheel-rail contact is a typical example for friction used to transmit forces, see **Fig. 1.1-6**. The contact behavior depends on the material properties of the contacting bodies. Also, the macroscopic geometry and the roughness of the surfaces influence the dynamical behavior of the system. The development of heat within the rolling contact influences the tangential contact forces as well. Here, the development of wear can lead to unround wheels, which increases the cost of maintenance and the generation of noise. Since wear is a longtime phenomenon, fast calculation procedures have to be developed to solve this problem.

Fig. 1.1-6 Wheel-rail contact (ISB, University of Hannover, Germany)

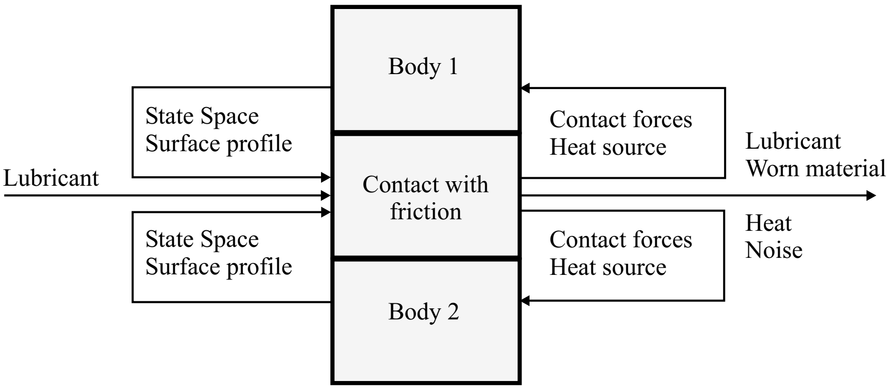

Fig. 1.1-7 Elastic contact with friction

All friction problems described above can be summarized as shown in the flow chart of **Fig. 1.1-7**. Two bodies, which can have different surface profiles and different materials, are in contact with each other. In general, both bodies can vibrate and move spatially, which is described by displacements and velocities of both elastic bodies in the so-called state space. Friction is always correlated with the development of wear and heat. The development of wear influences the surfaces profiles. The modified surfaces have an effect on the normal pressure distribution within the contact and therefore onto the dynamical behavior.

The heat generated and the temperature distribution within the bodies affects the material parameters and thus the contact forces, which can change the dynamics of the whole system. If the temperature is high enough, material transformation like oxidation can occur at the surfaces, which results again in different contact parameters and hence, will influence the contact and friction forces. Besides the contact forces, the worn material can act as a lubricant on both structures, which can reduce the friction forces. The lubricant and the worn material are defined to be the so-called third body. The output of the contact with friction is the worn material, lubricant, heat and noise.

1.2 Review

Friction contacts can be distinguished with respect to the following properties, see (Popp 1994):

- size of the contact area relative to the structure: local or expanded,
- type of normal contact force: static or dynamic,
- condition in normal direction: Hertzian or non-Hertzian,
- motion in tangential direction: micro- or macroslip.

Therefore, within the literature there exist a large number of different friction contact models.

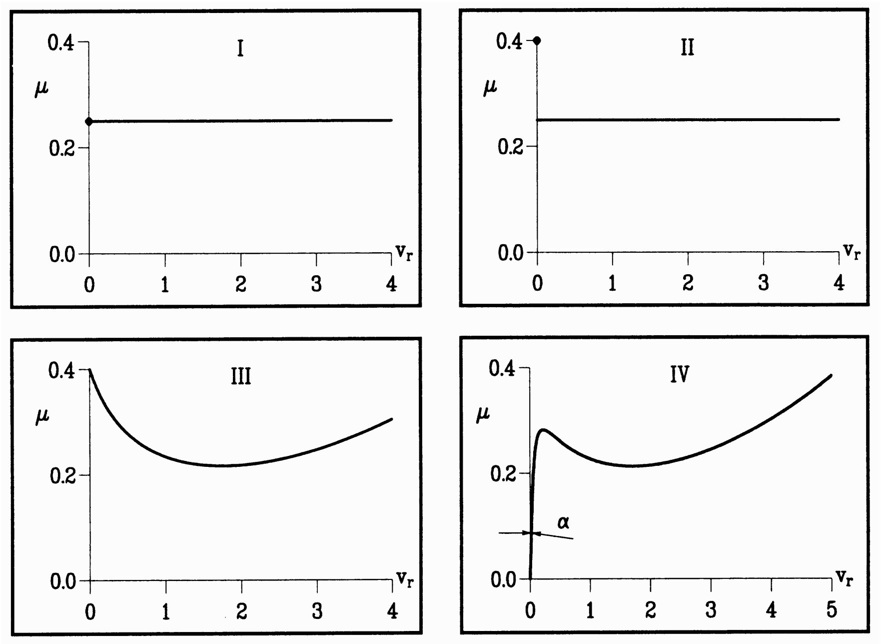

Fig. 1.2-1 Friction coefficient characteristics (Hinrichs 1997a) **I**) Coulomb friction characteristic **II**) Coulomb-Amontons friction characteristic **III**) Identified friction characteristic **IV**) Smoothened friction characteristic

Dependent on the above described properties of the friction contact, different friction contact models and solution methods are used, see for example (Johnson 1989), (Aliabadi 1993, 1995, 1997), (Gaul and Brebbia 1999) and (Gaul and Nitsche 2000). Detailed historical reviews are presented in several publications, see (Hinrichs 1997a), (Feeny et al. 1998) and (Seireg 1998). In the following, we will focus on dynamical contact problems with friction in the fields of:

- Multibody Systems,
- Continuum Mechanics and
- Finite Element Methods.

A *Multibody Systems* is built-up by springs, dampers and rigid bodies, see (Schiehlen 1990; Schwertassek and Wallrapp 1999; Shabana 2005). Within these systems, dynamic contact problems with friction are modeled by using non-smooth functions, see (Hinrichs 1997a), (Pfeiffer and Glocker 1996, 1999), (Wösle 1997), (Oestreich et al. 1996, 1998), (Brogliato 1999) and (Fidlin 2006). An overview on non-smooth systems with friction is given in (Popp 1998). To describe the dynamical behavior in the normal direction with respect to the contact surface, for example Newton's classical non-smooth impact law is used. This contact law combines the velocities before and after the impact in normal direction using a kinematic condition.

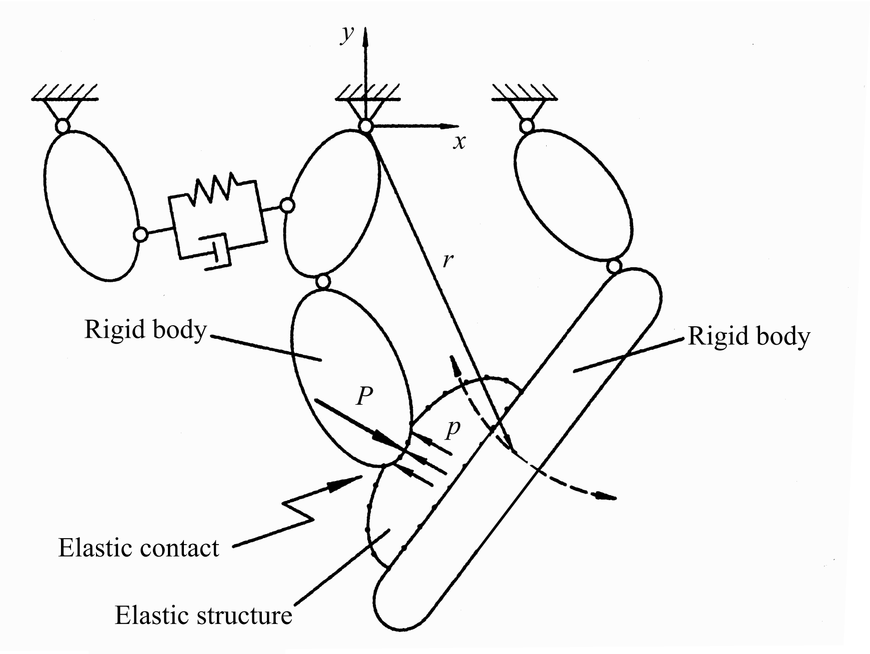

Fig. 1.2-2 Elastic Multibody System (ADAMS User Manual)

To describe the tangential contact problem the well-known, non-smooth friction characteristic developed by Coulomb in 1785 is used very often, see **Fig. 1.2-1 I**. With respect to the kinematics one distinguishes between sticking, which corresponds to zero relative velocity, $v_r=0$, and sliding, $v_r>0$. The friction coefficient μ is assumed independent on the contact area and the friction force acts opposite to the relative velocity. The normal contact and friction forces are applied in a single point. In case of sliding, the friction force is proportional to the normal contact force. Multibody systems including non-smooth friction and impact laws lead to structural variant equations of motion, which means, that the degrees of freedom of the investigated system change with time. Pfeiffer and Glocker (1996) developed a theory, using complementary equations, to handle this kind of problems, where many rigid bodies are involved.

In **Fig. 1.2-1 II**, the non-smooth so-called Coulomb-Amonton friction characteristic is shown, where the friction coefficient due to sticking, is larger than for sliding. In (Hinrichs 1997a) and (Kammerer 1998), the expanded friction contact is reduced to a point contact, where the normal force is assumed to be static.

In (Stelter 1992), the used friction law is nonlinear dependent on the relative velocity and is approximated by spline functions based on identified values of the friction coefficient, see **Fig. 1.2-1 III**. This functional behavior of the friction coefficient with respect to the relative velocity is often called Stribeck-characteristic. Further characteristics and their physical motivation can be found in (Kragelski et al. 1982).

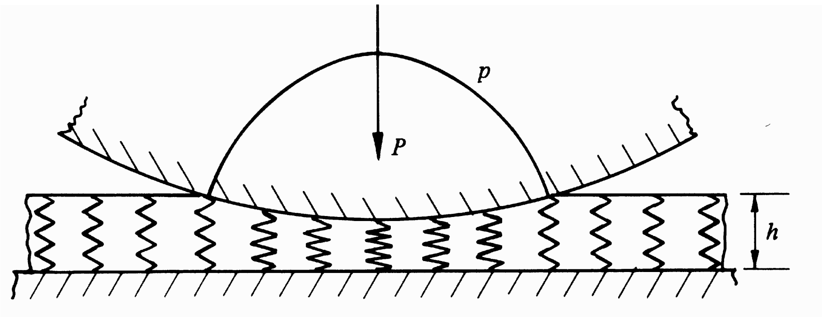

Fig. 1.2-3 Elastic foundation model (Johnson 1989)

By using smoothing function, for example the *arctan*-function, see (Popp et al. 1995), the slope at zero relative velocity has a finite value, see **Fig. 1.2-1 IV**, whereby the friction characteristic is now differentiable. Then, the non-smooth system equations can be transferred to structural invariant ones, which can be solved by standard numerical integration methods or special solvers for stiff differential equation, see for example (SIMULINK 1999).

The assumption of a rigid body corresponds to a simplified model of the real system, which is in general elastic. In extreme, the rigid body assumption and a non-smooth description of the contact can lead to a non-existent solution of the system equations, see (Glocker 1995). The non-existence of a solution is a hint, that the system is not modeled in a sufficient way. This problem can be overcome, if elastic deformations are modeled within the contact regions. In **Fig. 1.2-2**, a so-called *Elastic Multibody System* with one elastic contact is depicted. Applying for example the elastic foundation model developed by Winkler in 1867, see **Fig. 1.2-3**, a more detailed description of the reality is possible, since the contact time is finite. This simple elastic contact layer allows local deformations. Due to a cylindrical rigid body, the normal pressure distribution p is parabolic because of the linear springs of length h, see (Johnson 1989).

Within elastic multibody systems continuous structures can be approximated by so-called superelements, see (Dragos 2000), built-up by rigid bodies, springs and dampers. An alternative method to reduce the number of degrees of freedom of the continuous structures is the modal description, see for example (Hurty 1960, 1965) and (Schwertassek and Wallrapp 1999). Here, the spatial dynamical behavior of the elastic structures can be considered and described by the eigenvectors, eigenfrequencies and modal damping. These modal parameters can be for example identified by an experimental modal analysis, see (Ewins 1986).

The basis for the contact model used in *Continuum Mechanics* is the so-called elastic half-space assumption. In many cases, the contacting bodies are large compared to the contact area. Then, it can be assumed, that the contacting bodies are infinitely large, which corresponds to the elastic half-space assumption.

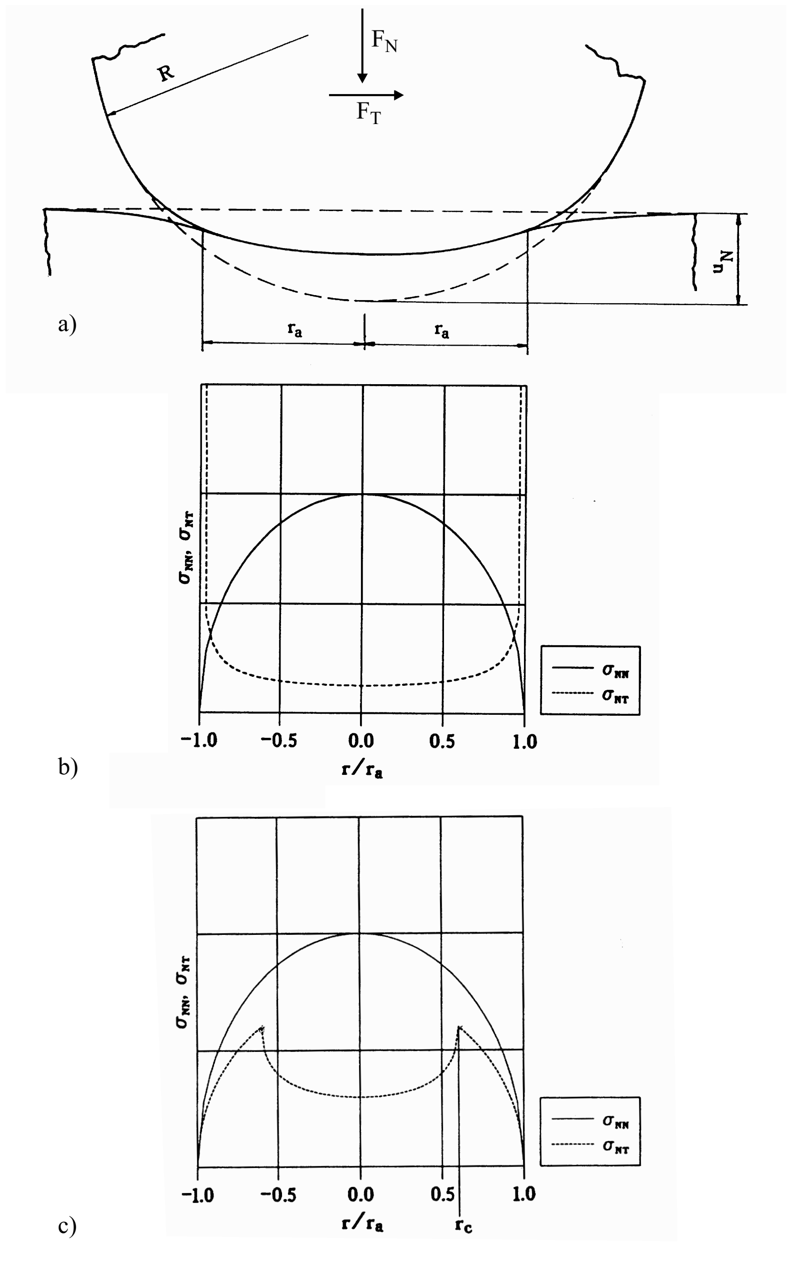

Fig. 1.2-4 **a**) Hertzian normal contact of an elastic ball contacting an elastic half-space **b**) Normal pressure σ_{NN} and tangential traction σ_{NT} due to an infinite friction coefficient **c**) Normal pressure distribution and tangential traction due to a finite friction coefficient

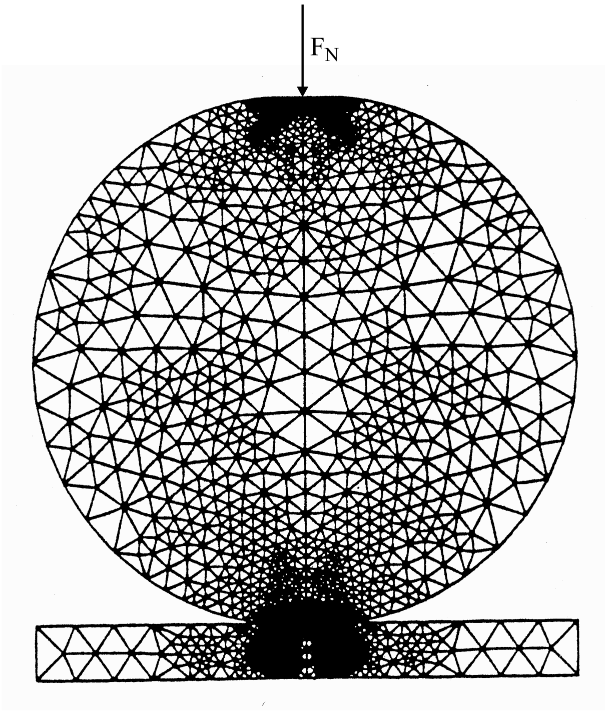

Fig. 1.2-5 Discretized Hertzian normal contact of a cylinder contacting a plate (Wriggers 1995)

Hooke's law is used to describe the elastic material behavior. Applying this linear law to a half-space, Boussinesq calculated the deformations due to a single point normal contact force, see (Johnson 1989) and (Hill et al. 1993). Superposing the deformations due to single point contact forces, the distributed contact forces can be applied to the half-space. Then, the corresponding displacements, strain and stress distributions can be determined. If two parabolic curved structures contact each other, using the half-space assumption for both structures and neglecting friction within the contact interface, this leads to the Hertzian theory, assuming that the outer contact radius r_a is small compared to the ball radius R, see **Fig. 1.2-4a**. The Hertzian theory is well known to solve normal contact problems as well as elastic impact problems based on the quasi-static analysis, see (Oestreich 1998). In Fig. 1.2-4a, the Hertzian normal contact of a ball with the radius R contacting the elastic half-space is shown. The corresponding deflection of both is due to a normal contact load F_N. Here, the normal pressure distribution σ_{NN} is elliptical within the contact region, see **Fig. 1.2-4b**.

In (Cattaneo 1938), (Mindlin 1949) and (Mindlin et al. 1952) the tangential force-displacement relationship is derived for the Hertzian contact. The assumption for the calculation of the force-displacement relationship is again the elastic half-space.

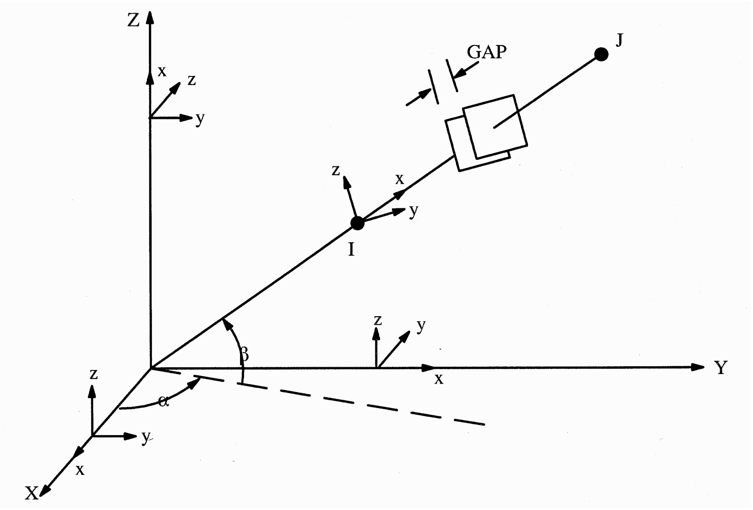

Fig. 1.2-6 FEM contact element (ANSYS User Manual)

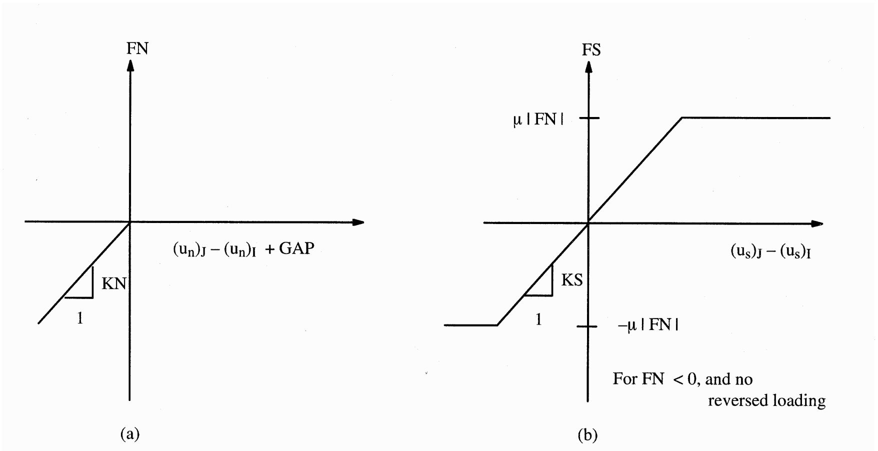

Fig. 1.2-7 Force-displacement relationship (ANSYS User Manual) **a**) in normal direction and **b**) in tangential direction

Assuming an infinite friction coefficient and a constant tangential load, the shear traction within the contact regime is singular at the edges of the contact areas, see Fig. 1.2-4b. Assuming Coulomb friction, the shear traction is limited to the Hertzian normal pressure times the friction coefficient. Within the contact area, sticking occurs up to the radius r_c, while sliding occurs in the outer ring, see **Fig. 1.2-4c**. If stick and slip regions occur within one contact region, this phenomenon is called microslip. Menq et al. (1986a, 1986b) found that microslip does affect the system vibrations, which was verified by experiments.

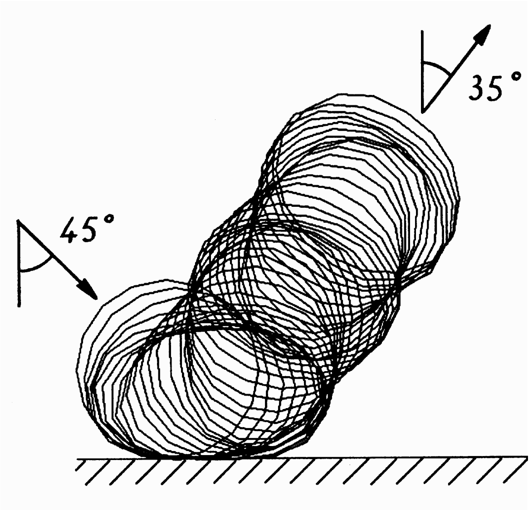

Fig. 1.2-8 Motion of an elastic ring touching a rough ground (Vu Van 1990)

The application of discrete calculation methods, such as the *Finite Element Method* (FEM) is very common, because of the general application to geometric complex structures and for quasi-static contact problems, see example (Wriggers 1995, 1996) and (Graeff-Weinberg and Berger 1996). In **Fig. 1.2-5**, the discretized Hertzian normal contact is modeled. For solving such contact problems the Penalty Method or the Lagrangian Multiplier Method is applied or a combination of both methods, the so-called Argumented Lagrangian Method. The basic idea of these methods is, to change a problem with boundary conditions to a problem without boundary conditions. The description of statics and dynamics of geometric complex structures is possible, including the effects of temperature, centrifugal forces and external forces applied to the elastic components. Also, the dynamic contact problem with dry friction can be modeled. Different contact elements can be used: point to point, point to surface, surface to surface, to solve the contact problem. For spatial dynamical contact problems with friction, three-dimensional point contact models for each discretized contact are applied, see **Fig. 1.2-6** and **Fig. 1.2-7**.

The contact laws including the roughness of the contact surfaces can be modeled by theoretical or empirical derived nonlinear equations, which are dependent on the normal penetration, see (Bhushan 1996; Greenwood 1966–1992; Hess 1991–1995; Kragelski et al. 1982; Vu Van 1990; Willner 1995a; Woo 1980). For example, in **Fig. 1.2-8**, the dynamical motion of a ring dicretized by 16 beam elements using FEM, is shown, see (Vu Van 1990). The Coulomb friction was used to describe the tangential contact forces. The normal contact force is approximated by an empirical identified potential law, which dependents on the normal penetration. After touching the ground, the resulting motion of the ring corresponds approximately to the first bending mode. The angle changes from 45° to 35° because dry friction reduces the velocity parallel to the ground.

In (Greenwood and Williamson 1966) and (Willner 1995a), contact models including the effect of rough surfaces are derived assuming a Gaussian distribution for the heights of the asperities and the Hertzian theory for each contact. These approaches need the value of the mean curvature of the asperities to be able to calculate the contact forces and are very sensitive with respect to the resolution of the profile measurement. In (Zavarise et al. 1992–1995; Willner 1995b), penalty approaches for the contact behavior of rough surfaces based on FEM are realized.

The developed heat source within the contact will increase the temperature distribution of the contacting bodies. For geometrically complex structures, the FEM can be used to calculate the thermo-mechanic contact behavior, see for example (Du et al. 1997) and (Willner 1999). This is important, because the temperature can change the corresponding material parameters and, hence, the deformations and stresses of the contacting bodies change, which in extreme can lead to thermoelastic instabilities, see (Johnson 1989; Willner 1999).

Investigating the spatial nonlinear forced vibrations of elastic structures with friction contacts leads to an enormous increase in computation time using FEM, which is caused by the number of degrees of freedom, the possibility of separation of the contacts, the strong non-linearity of dry friction and the transient solution procedure to calculate the stationary vibrations. To reduce the degrees of freedom of the elastic bodies, for example Bohlen (1987) used the modal description. The modal condensation turns out to be an efficient tool to overcome numerical problems.

1.3 Aim of this Work

The aim of this work is to develop an alternative method to investigate dynamical contact problems with friction applicable to elastic bodies. Since continuous bodies have an infinite number of degrees of freedom, the modal description is used to reduce the number of degrees of freedom and, hence, the system complexity. Thus, the dynamics of the elastic components is described by modal parameter using the eigenfrequencies, eigenvectors and modal damping. The minimum number of modes corresponds to the number of rigid body modes.

The contact forces are dependent on many parameters, such as contact stiffnesses, friction characteristic, surface profiles, material parameters, temperature distribution, relative motion and normal pressure distribution. These parameters can change within the contact area and due to the in general spatial motion of the contacting bodies, it is impossible to derive a general contact force law. The only possibility to overcome this problem is to discretize the contact areas, since in general the relative motion and the contact parameters are not constantly distributed within the contact surface. This leads to a point contact model, which has to include all main physical effects as described above, which are important when simulating dynamical contact problems with friction. A multi-scaling technique is used to develop the point contact model. After the dynamical description of an elastic body, this point contact model will be developed first.

The nonlinear contact forces for rough surfaces have to be verified by experiments for the normal and tangential direction with respect to the contact area. The characteristic of the friction coefficient with respect to the relative velocity and the normal force has to be modeled in a sufficient way. For the investigation of the temperature distribution, the energy balance will give an answer on the developed heat source, while the mass balance will give an insight on the wear behavior of the contacting bodies. The temperature distribution in the contact area influences the force-displacement relationship and has to be modeled and investigated. The question, how wear and the temperature distribution influence the system parameters will be investigated. Due to the dissipation of energy, the hysteresis behavior has to be investigated with respect to the normal and tangential direction. The possibility of separation of the contact has to be included and furthermore stick-slip phenomena have to be investigated. Limits with respect to the application of the point contact model have to be discussed.

The point contact model will be applied to real contact problems. Experimental investigations will be used to verify the assumptions made. The general application of the point contact model is documented by three examples:

- impact and friction oscillators,
- friction damping and
- rolling contact.

All investigated problems will include the application of the generalized point contact model, the solution methods and the comparison of measurements with the calculations as well as parameter studies. For the impact and friction oscillator a single point contact model is used while for the friction damping and rolling contact a further multi-scaling technique is developed.

In the first set of examples, a simple impact oscillator with an elastic contact is used to check the overall modeling with respect to the elastic normal contact. Then, a self-excited friction oscillator is investigated with respect to the tangential vibrations.

Friction damping can be used to reduce the vibration amplitudes. This will be demonstrated by friction damping of turbine blades with respect to non-Hertzian contact conditions. One part of the investigations is the modeling of microslip effects and the influence onto the system behavior. Efficient solution methods for calculating the spatial forced response of elastic structures, including microslip effects are not available up to now, and are being developed. A bladed disc assembly coupled by means of non-Hertzian contacts is optimized with respect to the spatial vibration of the blades, which is optimized with regard to minimal alternating stresses.

In the case of rolling contact, the general friction contact model will be applied to Hertzian contact conditions. Due to this dynamical contact problem, fast calculation methods are developed to calculate the normal and tangential contact problem, the temperature as well as the wear distribution.

2 Dynamical Descriptions of Elastic Bodies

2.1 Kinematics of Elastic Bodies

For the kinematical description of an elastic body two coordinate systems are introduced, see **Fig. 2.1-1**. On the one hand, the inertia *I*-coordinate system is fixed in space and on the other hand, the *R*-coordinate system is fixed to the elastic body at the point *R*. In the limiting case these two coordinate systems can be used to describe the rigid body dynamics. Here, the elastic deformations are introduced additionally to describe the kinematics of an elastic body. Both coordinate systems are related by

$${}_I\vec{\boldsymbol{e}} = {}^{IR}\boldsymbol{A}\,{}_R\vec{\boldsymbol{e}} \tag{2.1-1}$$

with the orthogonal transformation matrix ${}^{IR}\boldsymbol{A}$ with the properties

$${}^{RI}\boldsymbol{A}\,{}^{IR}\boldsymbol{A} = \boldsymbol{E} \tag{2.1-2}$$

and

$${}^{IR}\boldsymbol{A}^T = {}^{RI}\boldsymbol{A}\,. \tag{2.1-3}$$

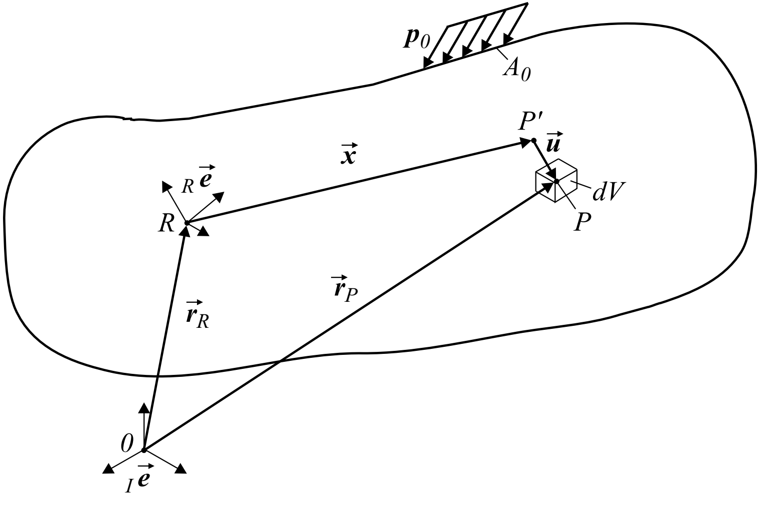

Fig. 2.1-1 Bases and vectors for the description of a deformed body

The vector $\vec{x}$ defines the observed point P' of the undeformed body and the vector $\vec{u}$ the displacement due to the deformation with respect to the R-coordinate system. The coordinates of the point P of the center of a mass element with the volume dV is described by

$$ {}_{R}\boldsymbol{r}_{P} = {}_{R}\boldsymbol{r}_{R} + {}_{R}\boldsymbol{x} + {}_{R}\boldsymbol{u} \,, \tag{2.1-4}$$

where ${}_{R}\boldsymbol{r}_{R}$ describes the distance between the origins of the I- and R-coordinate system in R-coordinates. The index in the left lower corner of a vector defines the used coordinate system. At the left upper corner, the coordinate system is cited, where the differentiation with respect to time is carried out. Noting that the distance ${}_{R}\boldsymbol{x}$ is constant with respect to time the velocity of the point P with respect to the R-coordinate system is given by

$$ {}^{R}_{R}\boldsymbol{v}_{P} = {}^{R}_{R}\dot{\boldsymbol{r}}_{R} + {}^{R}\dot{\boldsymbol{u}} \tag{2.1-5}$$

and the acceleration is given by

$$ {}^{R}_{R}\boldsymbol{a}_{P} = {}^{R}_{R}\ddot{\boldsymbol{r}}_{R} + {}^{R}\ddot{\boldsymbol{u}} \,. \tag{2.1-6}$$

In the following, the absolute velocity of the point P with respect to the R-coordinate system is derived. The absolute displacement of the point P with respect to the I-coordinate system is given by

$$ {}_{I}\boldsymbol{r}_{P} = {}^{IR}\boldsymbol{A}\,{}_{R}\boldsymbol{r}_{P} \,. \tag{2.1-7}$$

With respect to the I-coordinate system the absolute velocity is given by differentiation of Eq.(2.1-7) using the product rule

$$ {}^{I}_{I}\boldsymbol{v}_{P} = \frac{{}^{I}d\boldsymbol{r}_{P}}{dt} = {}^{IR}\dot{\boldsymbol{A}}\,{}_{R}\boldsymbol{r}_{P} + {}^{IR}\boldsymbol{A}\,{}^{R}_{R}\dot{\boldsymbol{r}}_{P} \,. \tag{2.1-8}$$

Back transformation of the absolute velocity in Eq.(2.1-8) in the R-coordinate system gives

$$ {}^{I}_{R}\boldsymbol{v}_{P} = {}^{RI}\boldsymbol{A}\,{}^{I}_{I}\boldsymbol{v}_{P} \,. \tag{2.1-9}$$

Inserting Eq.(2.1-8) in Eq.(2.1-9) and using Eq.(2.1-2) gives the velocity of the point P with respect to the R-coordinate system

$$ {}^{I}_{R}\boldsymbol{v}_{P} = {}^{R}_{R}\dot{\boldsymbol{r}}_{P} + {}^{RI}\boldsymbol{A}\,{}^{IR}\dot{\boldsymbol{A}}\,{}_{R}\boldsymbol{r}_{P} \tag{2.1-10}$$

or

$$ {}^{I}_{R}\boldsymbol{v}_{P} = {}^{R}_{R}\boldsymbol{v}_{P} + {}^{IR}\tilde{\boldsymbol{\omega}}\,{}_{R}\boldsymbol{r}_{P} \tag{2.1-11}$$

with the tilde matrix of the angular velocity

$$ {}^{IR}\tilde{\boldsymbol{\omega}} := {}^{IR}\boldsymbol{A}^{T}\,{}^{IR}\dot{\boldsymbol{A}} \,. \tag{2.1-12}$$

Then, corresponding to the calculation of the velocity, the absolute acceleration of the point P can be derived by Eq.(2.1-11) and is given by

$$ {}^{I}_{R}\boldsymbol{a}_{P} = {}^{R}_{R}\dot{\boldsymbol{v}}_{P} + {}^{IR}\dot{\tilde{\boldsymbol{\omega}}}\,{}_{R}\boldsymbol{r}_{P} + {}^{IR}\tilde{\boldsymbol{\omega}}\,{}^{R}_{R}\dot{\boldsymbol{r}}_{P} + {}^{IR}\tilde{\boldsymbol{\omega}}\left({}^{R}_{R}\boldsymbol{v}_{P} + {}^{IR}\tilde{\boldsymbol{\omega}}\,{}_{R}\boldsymbol{r}_{P}\right) \tag{2.1-13}$$

or

$$ {}^{I}_{R}\boldsymbol{a}_{P} = {}^{R}_{R}\boldsymbol{a}_{P} + 2\,{}^{IR}\tilde{\boldsymbol{\omega}}\,{}^{R}_{R}\boldsymbol{v}_{P} + \left({}^{IR}\dot{\tilde{\boldsymbol{\omega}}} + {}^{IR}\tilde{\boldsymbol{\omega}}\,{}^{IR}\tilde{\boldsymbol{\omega}}\right){}_{R}\boldsymbol{r}_{P} \,. \tag{2.1-14}$$

An alternative description of the absolute velocity of the point P is given by inserting Eq.(2.1-4) and Eq.(2.1-5) in Eq.(2.1-11). This leads to

$$ {}^{I}_{R}\boldsymbol{v}_{P} = {}^{I}_{R}\boldsymbol{v}_{R} + {}^{IR}\tilde{\boldsymbol{\omega}}(\boldsymbol{x} + \boldsymbol{u}) + {}^{R}\dot{\boldsymbol{u}} \tag{2.1-15}$$

with the absolute velocity of the point *R*

$$ {}_R^I\boldsymbol{v}_R = {}_R^R\boldsymbol{v}_R + {}^{IR}\tilde{\boldsymbol{\omega}}_R \boldsymbol{r}_R \,. \tag{2.1-16}$$

The absolute acceleration of the point *P* is given by inserting Eq.(2.1-4), Eq.(2.1-5) and Eq.(2.1-6) in Eq.(2.1-14), which gives

$$ {}_R^I\boldsymbol{a}_P = {}_R^I\boldsymbol{a}_R + ({}^{IR}\dot{\tilde{\boldsymbol{\omega}}} + {}^{IR}\tilde{\boldsymbol{\omega}}\,{}^{IR}\tilde{\boldsymbol{\omega}})(\boldsymbol{x}+\boldsymbol{u}) + 2\,{}^{IR}\tilde{\boldsymbol{\omega}}\,{}^R\dot{\boldsymbol{u}} + {}^R\ddot{\boldsymbol{u}} \,. \tag{2.1-17}$$

with the absolute acceleration of the point *R*

$$ {}_R^I\boldsymbol{a}_R = {}_R^R\boldsymbol{a}_R + 2\,{}^{IR}\tilde{\boldsymbol{\omega}}\,{}_R^R\boldsymbol{v}_R + ({}^{IR}\dot{\tilde{\boldsymbol{\omega}}} + {}^{IR}\tilde{\boldsymbol{\omega}}\,{}^{IR}\tilde{\boldsymbol{\omega}})_R \boldsymbol{r}_R \,. \tag{2.1-18}$$

With the relation

$$ \tilde{\boldsymbol{a}}\boldsymbol{b} = -\tilde{\boldsymbol{b}}\boldsymbol{a} \tag{2.1-19}$$

Eq.(2.1-15) can be rearranged by

$$ {}_R^I\boldsymbol{v}_P = {}_R^I\boldsymbol{v}_R - (\tilde{\boldsymbol{x}} + \tilde{\boldsymbol{u}})\,{}^{IR}\boldsymbol{\omega} + {}^R\dot{\boldsymbol{u}} \tag{2.1-20}$$

and Eq.(2.1-17) by

$$ {}_R^I\boldsymbol{a}_P = {}_R^I\boldsymbol{a}_R - (\tilde{\boldsymbol{x}} + \tilde{\boldsymbol{u}})\,{}^{IR}\dot{\boldsymbol{\omega}} + {}^R\ddot{\boldsymbol{u}} + 2\,{}^{IR}\tilde{\boldsymbol{\omega}}\,{}^R\dot{\boldsymbol{u}} + {}^{IR}\tilde{\boldsymbol{\omega}}\,{}^{IR}\tilde{\boldsymbol{\omega}}(\boldsymbol{x}+\boldsymbol{u}) \,, \tag{2.1-21}$$

which is used in the next chapter.

2.2 Governing Equations for Linear Elasticity

In a first step, the equations of motion with respect to a volume element *dV* in the current configuration are developed with respect to cartesian coordinates. Consider a volume element with the side lengths *dx*, *dy* and *dz*, see **Fig. 2.2-1**. The stresses shown are only those acting in the *x*-direction. Note, that on one plane the stress σ_{xx} is acting while on the opposite side it has changed by the rate of change of σ_{xx} with respect to the coordinate *x*, times the distance *dx*. The partial derivative is used, as σ_{xx} may vary with respect to the coordinates *y* and *z* as well. The body force in *x*-direction is denoted by b_x to describe for example gravity forces. Applying Newton's law to the x-direction leads to

$$\begin{aligned} dm\,{}^I a_x &= dm\; b_x + \\ &\left(\frac{\partial \sigma_{xx}}{\partial x} dx\right) dy\; dz + \left(\frac{\partial \sigma_{yx}}{\partial y} dy\right) dx\; dz + \left(\frac{\partial \sigma_{zx}}{\partial z} dz\right) dx\; dy \end{aligned} \tag{2.2-1}$$

with the absolute acceleration ${}^I a_x$ of the center *P* of the mass element in the *x*-direction as defined in Eq.(2.1-21). The mass of the volume element in the current configuration is given by

$$ dm = \rho\; dV = \rho\; dx\; dy\; dz \tag{2.2-2}$$

with the density ρ. Dividing Eq.(2.2-1) by the element volume gives

$$ \frac{\partial \sigma_{xx}}{\partial x} + \frac{\partial \sigma_{yx}}{\partial y} + \frac{\partial \sigma_{zx}}{\partial z} + \rho b_x = \rho\,{}^I a_x \tag{2.2-3}$$

and similar in the *y*-direction

$$ \frac{\partial \sigma_{xy}}{\partial x} + \frac{\partial \sigma_{yy}}{\partial y} + \frac{\partial \sigma_{zy}}{\partial z} + \rho b_y = \rho\,{}^I a_y \tag{2.2-4}$$

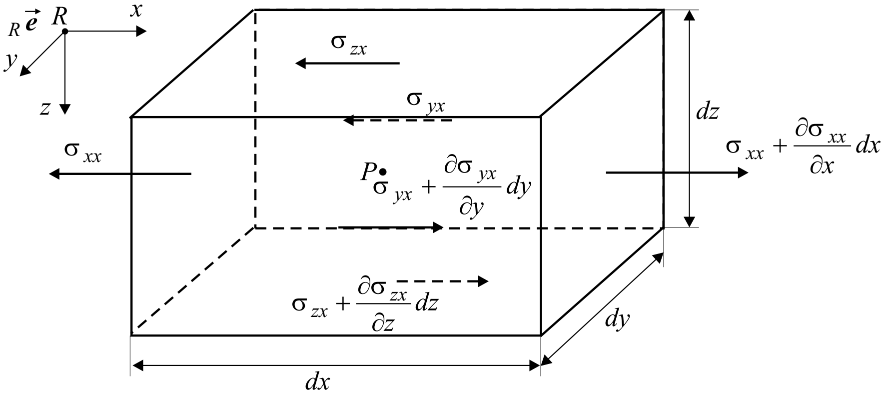

Fig. 2.2-1 Stress distribution in *x*-direction

and in *z*-direction

$$\frac{\partial \sigma_{xz}}{\partial x} + \frac{\partial \sigma_{yz}}{\partial y} + \frac{\partial \sigma_{zz}}{\partial z} + \rho b_z = \rho \, {}^I a_z \, . \tag{2.2-5}$$

Summarizing Eq.(2.2-3), Eq.(2.2-4) and Eq.(2.2-5) gives the equation of motion

$$div \, \boldsymbol{\Sigma} + \rho \boldsymbol{b} = \rho \, {}^I \boldsymbol{a} \, , \tag{2.2-6}$$

where $\boldsymbol{\Sigma}$ denotes the Cauchy stress tensor,

$$\boldsymbol{\Sigma} = \begin{bmatrix} \sigma_{xx} & \sigma_{xy} & \sigma_{xz} \\ \sigma_{yx} & \sigma_{yy} & \sigma_{yz} \\ \sigma_{zx} & \sigma_{zy} & \sigma_{zz} \end{bmatrix} , \tag{2.2-7}$$

$\rho \boldsymbol{b}$ the volume or body force vector and ${}^I\boldsymbol{a}$ the absolute acceleration of the center *P* with

$$\boldsymbol{b} = \begin{bmatrix} b_x \; b_y \; b_z \end{bmatrix}^T , \quad {}^I\boldsymbol{a} = {}^I \begin{bmatrix} a_x \; a_y \; a_z \end{bmatrix}^T , \tag{2.2-8}$$

respectively. The Boltzmann axiom or the principle of angular momentum with respect to the point *P* leads to

$$\sigma_{xy} = \sigma_{yx} , \quad \sigma_{yz} = \sigma_{zy} , \quad \sigma_{xz} = \sigma_{zx} \, . \tag{2.2-9}$$

Hence, the Cauchy stress tensor is symmetric with

$$\boldsymbol{\Sigma} = \boldsymbol{\Sigma}^T . \tag{2.2-10}$$

The mass of the initial configuration is given by

$$dm = \rho_0 \, dV_0 \, . \tag{2.2-11}$$

From the mass balance, the mass is constant for the current and initial configuration with

$$dm = \rho \, dV = \rho_0 \, dV_0 \, . \tag{2.2-12}$$

For small deformations of the volume element of the current configuration with respect to the reference configuration, it is assumed that the element volume is approximately constant

$$dV \approx dV_0 \tag{2.2-13}$$

and hence from Eq.(2.2-12) the density is assumed to be approximately constant with time

$$\rho \approx \rho_0 \,. \tag{2.2-14}$$

Then, the linear equation of motion of the current configuration are described by parameters of the initial configuration by

$$div\,\boldsymbol{\Sigma} + \rho_0 \boldsymbol{b} = \rho_0 {}^{I}\boldsymbol{a} \,. \tag{2.2-15}$$

For small strains the stresses are modeled by Hooke's law, see (Schwertassek and Wallrapp 1999), which considers a linear relation between stresses and strains for homogeneous and isotropic material behavior. The Hooke's law can be summarized by

$$\boldsymbol{\sigma} = \boldsymbol{H\varepsilon} \tag{2.2-16}$$

with the stress vector

$$\boldsymbol{\sigma} = \left[\sigma_{xx}\ \sigma_{yy}\ \sigma_{zz}\ \sigma_{xy}\ \sigma_{yz}\ \sigma_{xz}\right]^T , \tag{2.2-17}$$

the matrix of elasticity

$$\boldsymbol{H} = \frac{E}{(1+\nu)(1-2\nu)} \begin{bmatrix} 1-\nu & \nu & \nu & 0 & 0 & 0 \\ & 1-\nu & \nu & 0 & 0 & 0 \\ & & 1-\nu & 0 & 0 & 0 \\ & & & \frac{1-2\nu}{2} & 0 & 0 \\ & symmetric & & & \frac{1-2\nu}{2} & 0 \\ & & & & & \frac{1-2\nu}{2} \end{bmatrix} \tag{2.2-18}$$

and the strain vector

$$\boldsymbol{\varepsilon} = \left[\varepsilon_{xx}\ \varepsilon_{yy}\ \varepsilon_{zz}\ 2\varepsilon_{xy}\ 2\varepsilon_{yz}\ 2\varepsilon_{xz}\right]^T \tag{2.2-19}$$

with

$$\varepsilon_{xy} = \varepsilon_{yx},\quad \varepsilon_{yz} = \varepsilon_{zy},\quad \varepsilon_{xz} = \varepsilon_{zx} \,. \tag{2.2-20}$$

The linear strain-displacement relationship is given by

$$\boldsymbol{\varepsilon} = \boldsymbol{Bu} \tag{2.2-21}$$

with the operator-matrix

$$\boldsymbol{B} = \begin{bmatrix} \frac{\partial}{\partial x} & 0 & 0 \\ 0 & \frac{\partial}{\partial y} & 0 \\ 0 & 0 & \frac{\partial}{\partial z} \\ \frac{\partial}{\partial y} & \frac{\partial}{\partial x} & 0 \\ 0 & \frac{\partial}{\partial z} & \frac{\partial}{\partial y} \\ \frac{\partial}{\partial z} & 0 & \frac{\partial}{\partial x} \end{bmatrix} \tag{2.2-22}$$

and the relative displacement vector

$$\boldsymbol{u} = \begin{bmatrix} u_x & u_y & u_z \end{bmatrix}^T. \tag{2.2-23}$$

In (Schwertassek and Wallrapp 1999) the theory of nonlinear elasticity is explained in full detail. For small deformations, these constitutive equations reduce to Hooke's classical law again. If non-linear constitutive laws have to be used to describe the structure, then for further information see (Ogden 1984).

2.3 Equation of Motion of an Elastic Body

The equations of motion of an elastic body can be derived using the principle of d'Alembert, Jourdain or Hamilton. Here the principle of Jourdain is used to develop the basic equation, see also (Schwertassek and Wallrapp 1999). Note that all variables are described with respect to the R-coordinate system. With Eq.(2.2-10) the external distributed pressure which has to be equal to the surface stresses is given by the Cauchy theorem

$$\boldsymbol{p}_0 = \boldsymbol{\Sigma n}_0\,, \tag{2.3-1}$$

where $\boldsymbol{n}_0$ denotes the normal vector of the surface A_0, see Fig. 2.1-1. The virtual power of the applied forces are given by the forces acting on one volume element multiplied by the virtual velocity and integrated with respect to the body volume,

$$\int_{V_0} \delta^I\dot{\boldsymbol{r}}^T(\rho_0 \boldsymbol{b} + div\boldsymbol{\Sigma} - \rho_0{}^I\ddot{\boldsymbol{r}})dV_0 + \int_{A_0} \delta^I\dot{\boldsymbol{r}}^T(\boldsymbol{p}_0 - \boldsymbol{\Sigma n}_0)dA_0 = 0\,. \tag{2.3-2}$$

Since the terms within the brackets are identical to zero, as derived in chapter 2.2, the integral are identical to zero. In the following Eq.(2.3-2) is rearranged to derive the equation of motion of the elastic body. Using the product rule, the following relation holds,

$$\int_{V_0} \delta^I\dot{\boldsymbol{r}}^T div\boldsymbol{\Sigma}\; dV_0 = \int_{V_0}\sum_{\alpha} \frac{\partial(\delta^I\dot{\boldsymbol{r}}^T\boldsymbol{\Sigma}_\alpha)}{\partial\alpha}\, dV_0 - \int_{V_0}\sum_{\alpha}\left(\frac{\partial\delta^I\dot{\boldsymbol{r}}}{\partial\alpha}\right)^T \boldsymbol{\Sigma}_\alpha dV_0\,, \tag{2.3-3}$$

with

$$\alpha = x, y, z.$$

Using the divergence theorem the second integral in Eq.(2.3-3) can be described by

$$\int_{V_0}\sum_{\alpha} \frac{\partial(\delta^I\dot{\boldsymbol{r}}^T\boldsymbol{\Sigma}_\alpha)}{\partial\alpha} dV_0 = \int_{V_0} div(\delta^I\dot{\boldsymbol{r}}^T\boldsymbol{\Sigma})dV_0 = \int_{A_0} \delta^I\dot{\boldsymbol{r}}^T\boldsymbol{\Sigma n}_0 dA_0\,. \tag{2.3-4}$$

From Eq.(2.1-20) it follows, that the virtual velocity of the point P is given by

$$\delta^I\dot{\boldsymbol{r}} = \delta^I\dot{\boldsymbol{r}}_R - \tilde{\boldsymbol{x}}\delta\boldsymbol{\omega} + \delta^I\dot{\boldsymbol{u}} = \delta^I\dot{\boldsymbol{r}}_R - (\tilde{\boldsymbol{x}} + \tilde{\boldsymbol{u}})\delta\boldsymbol{\omega} + \delta^R\dot{\boldsymbol{u}}\,. \tag{2.3-5}$$

Differentiating with regard to the coordinate α and shifting the linear operator δ in front of the brackets gives

$$\left(\frac{\partial \delta^I \dot{\boldsymbol{r}}}{\partial \alpha}\right) = \left(\frac{\partial \delta^I \dot{\boldsymbol{u}}}{\partial \alpha}\right) = \delta \left(\frac{\partial^I \dot{\boldsymbol{u}}}{\partial \alpha}\right). \tag{2.3-6}$$

Note that this differentiation is done with respect to the coordinate system, which is shifted corresponding to the virtual displacement. After some mathematical operations using the definition of the strain and stress vector in Eq.(2.2-17) and Eq.(2.2-19), the third integral of Eq.(2.3-3) leads to

$$\int_{V_0} \sum_{\alpha} \left(\frac{\partial \delta^I \dot{\boldsymbol{r}}}{\partial \alpha}\right)^T \boldsymbol{\Sigma}_\alpha dV_0 = \int_{V_0} \delta \dot{\boldsymbol{\varepsilon}}^T \boldsymbol{\sigma} \, dV_0 \, . \tag{2.3-7}$$

Inserting Eq.(2.3-4) and Eq.(2.3-7) in Eq.(2.3-3) gives

$$\int_{V_0} \delta^I \dot{\boldsymbol{r}}^T div \boldsymbol{\Sigma} \, dV_0 = \int_{A_0} \delta^I \dot{\boldsymbol{r}}^T \boldsymbol{\Sigma} \boldsymbol{n}_0 dA_0 - \int_{V_0} \delta \dot{\boldsymbol{\varepsilon}}^T \boldsymbol{\sigma} \, dV_0 \tag{2.3-8}$$

and finally inserting Eq.(2.3-8) in Eq.(2.3-2) leads to

$$\int_{V_0} \left(\delta^I \dot{\boldsymbol{r}}^T \rho_0 (\boldsymbol{b} - {}^I \ddot{\boldsymbol{r}}) - \delta \dot{\boldsymbol{\varepsilon}}^T \boldsymbol{\sigma}\right) dV_0 + \int_{A_0} \delta^I \dot{\boldsymbol{r}}^T \boldsymbol{p}_0 dA_0 = 0 \, . \tag{2.3-9}$$

The elastic displacements can be described by the Ritz-Ansatz

$$\boldsymbol{u}(\boldsymbol{x},t) = \boldsymbol{N}(\boldsymbol{x}) \, \boldsymbol{z}(t) \, , \tag{2.3-10}$$

where the matrix $\boldsymbol{N}(\boldsymbol{x})$ includes the global Ansatzfunctions defined in the R-coordinates, which have to be linear independent, differentiable and must satisfy the geometric boundary conditions, see (Schiehlen 1986). They are dependent on the coordinates $\boldsymbol{x}$, while the functions $\boldsymbol{z}(t)$ are time dependent. Note, with respect to the Finite Element Method local Ansatzfunctions are used to describe the deformations. Then the vector $\boldsymbol{z}(t)$ defines the vector of nodal displacements. Inserting Eq.(2.3-10) in Eq.(2.2-21) gives the strain

$$\boldsymbol{\varepsilon} = \boldsymbol{B}_N \boldsymbol{z} \tag{2.3-11}$$

with

$$\boldsymbol{B}_N = \boldsymbol{B}\boldsymbol{N} \, . \tag{2.3-12}$$

Then the variation of the strain rate is given by

$$\delta \dot{\boldsymbol{\varepsilon}} = \boldsymbol{B}_N \delta \dot{\boldsymbol{z}} \, . \tag{2.3-13}$$

Inserting Eq.(2.2-16), Eq.(2.3-5), Eq.(2.3-10), Eq.(2.3-11) and Eq.(2.3-13) in Eq.(2.3-9) and noting that the velocity of the reference point R, the angular velocity and the coordinates $\boldsymbol{z}(t)$ are only dependent on the time, see Eq.(2.3-10), Eq.(2.3-9) result in

$$\begin{aligned}
&\delta^I\dot{\boldsymbol{r}}_R^T\left(\int_{V_0}\rho_0(\boldsymbol{b}-{}^I\ddot{\boldsymbol{r}})dV_0+\int_{A_0}\boldsymbol{p}_0\,dA_0\right)+\\
&\delta\boldsymbol{\omega}^T\left(\int_{V_0}(\tilde{\boldsymbol{x}}+\tilde{\boldsymbol{u}})\rho_0(\boldsymbol{b}-{}^I\ddot{\boldsymbol{r}})dV_0+\int_{A_0}(\tilde{\boldsymbol{x}}+\tilde{\boldsymbol{u}})\boldsymbol{p}_0\,dA_0\right)+\qquad(2.3\text{-}14)\\
&\delta\dot{\boldsymbol{z}}^T\left(\int_{V_0}\boldsymbol{N}^T\rho_0(\boldsymbol{b}-{}^I\ddot{\boldsymbol{r}})dV_0-\int_{V_0}\boldsymbol{B}_N^T\boldsymbol{H}\boldsymbol{B}_N\,dV_0\,\boldsymbol{z}+\int_{A_0}\boldsymbol{N}^T\boldsymbol{p}_0\,dA_0\right)=0.
\end{aligned}$$

Since the virtual velocities are arbitrary, the terms within the brackets have to be zero. Then, the equations of motion are given by

$$\int_{V_0}\rho_0{}^I\ddot{\boldsymbol{r}}\,dV_0=\underbrace{\int_{V_0}\rho_0\boldsymbol{b}\,dV_0}_{\boldsymbol{f}_{ab}}+\underbrace{\int_{A_0}\boldsymbol{p}_0\,dA_0}_{\boldsymbol{f}_{ap}}\,,\qquad(2.3\text{-}15)$$

$$\int_{V_0}(\tilde{\boldsymbol{x}}+\tilde{\boldsymbol{u}})\rho_0{}^I\ddot{\boldsymbol{r}}\,dV_0=\underbrace{\int_{V_0}(\tilde{\boldsymbol{x}}+\tilde{\boldsymbol{u}})\rho_0\boldsymbol{b}\,dV_0}_{\boldsymbol{f}_{\omega b}}+\underbrace{\int_{A_0}(\tilde{\boldsymbol{x}}+\tilde{\boldsymbol{u}})\boldsymbol{p}_0\,dA_0}_{\boldsymbol{f}_{\omega p}}\qquad(2.3\text{-}16)$$

and

$$\int_{V_0}\boldsymbol{N}^T\rho_0{}^I\ddot{\boldsymbol{r}}\,dV_0+\underbrace{\int_{V_0}\boldsymbol{B}_N^T\boldsymbol{H}\boldsymbol{B}_N\,dV_0}_{\boldsymbol{K}_N}\,\boldsymbol{z}=\underbrace{\int_{V_0}\boldsymbol{N}^T\rho_0\boldsymbol{b}\,dV_0}_{\boldsymbol{f}_{zb}}+\underbrace{\int_{A_0}\boldsymbol{N}^T\boldsymbol{p}_0\,dA_0}_{\boldsymbol{f}_{zp}}\,.$$

$$(2.3\text{-}17)$$

The first integral in Eq.(2.3-15) up to Eq.(2.3-17) can be rewritten by inserting the absolute acceleration derived in Eq.(2.1-21) by

$$\begin{aligned}
&\int_{V_0}\rho_0{}^I\ddot{\boldsymbol{r}}\,dV_0=\int_{V_0}\rho_0\,dV_0{}^I\boldsymbol{a}_R-\int_{V_0}\rho_0(\tilde{\boldsymbol{x}}+\tilde{\boldsymbol{u}})\,dV_0\dot{\boldsymbol{\omega}}+\int_{V_0}\rho_0\boldsymbol{N}\,dV_0\,\ddot{\boldsymbol{z}}+\\
&\underbrace{\int_{V_0}\rho_0 2\tilde{\boldsymbol{\omega}}\boldsymbol{N}\,dV_0\,\dot{\boldsymbol{z}}+\int_{V_0}\rho_0\tilde{\boldsymbol{\omega}}\tilde{\boldsymbol{\omega}}\boldsymbol{N}\,dV_0\,\boldsymbol{z}+\int_{V_0}\rho_0\tilde{\boldsymbol{\omega}}\tilde{\boldsymbol{\omega}}\boldsymbol{x}\,dV_0,}_{\boldsymbol{f}_{ac}}
\end{aligned}$$

$$(2.3\text{-}18)$$

$$\begin{aligned}&\int_{V_0}(\tilde{\boldsymbol{x}}+\tilde{\boldsymbol{u}})\rho_0\,{}^I\ddot{\boldsymbol{r}}\,dV_0 = \int_{V_0}(\tilde{\boldsymbol{x}}+\tilde{\boldsymbol{u}})\rho_0\,dV_0\,{}^I\boldsymbol{a}_R - \\ &\int_{V_0}(\tilde{\boldsymbol{x}}+\tilde{\boldsymbol{u}})\rho_0(\tilde{\boldsymbol{x}}+\tilde{\boldsymbol{u}})\,dV_0\dot{\boldsymbol{\omega}} + \int_{V_0}(\tilde{\boldsymbol{x}}+\tilde{\boldsymbol{u}})\rho_0\boldsymbol{N}\,dV_0\,\ddot{\boldsymbol{z}} + \\ &\underbrace{\int_{V_0}(\tilde{\boldsymbol{x}}+\tilde{\boldsymbol{u}})\rho_0 2\tilde{\boldsymbol{\omega}}\boldsymbol{N}\,dV_0\,\dot{\boldsymbol{z}} + \int_{V_0}(\tilde{\boldsymbol{x}}+\tilde{\boldsymbol{u}})\rho_0\tilde{\boldsymbol{\omega}}\tilde{\boldsymbol{\omega}}\boldsymbol{N}\,dV_0\,\boldsymbol{z} + \int_{V_0}(\tilde{\boldsymbol{x}}+\tilde{\boldsymbol{u}})\rho_0\tilde{\boldsymbol{\omega}}\tilde{\boldsymbol{\omega}}\boldsymbol{x}\,dV_0}_{\boldsymbol{f}_{\omega c}}\end{aligned}$$

and (2.3-19)

$$\begin{aligned}&\int_{V_0}\boldsymbol{N}^T\rho_0\,{}^I\ddot{\boldsymbol{r}}\,dV_0 = \int_{V_0}\boldsymbol{N}^T\rho_0\,dV_0\,{}^I\boldsymbol{a}_R - \int_{V_0}\boldsymbol{N}^T\rho_0(\tilde{\boldsymbol{x}}+\tilde{\boldsymbol{u}})\,dV_0\dot{\boldsymbol{\omega}} + \int_{V_0}\boldsymbol{N}^T\rho_0\boldsymbol{N}\,dV_0\,\ddot{\boldsymbol{z}} + \\ &\underbrace{\int_{V_0}\boldsymbol{N}^T\rho_0 2\tilde{\boldsymbol{\omega}}\boldsymbol{N}\,dV_0\,\dot{\boldsymbol{z}} + \int_{V_0}\boldsymbol{N}^T\rho_0\tilde{\boldsymbol{\omega}}\tilde{\boldsymbol{\omega}}\boldsymbol{N}\,dV_0\,\boldsymbol{z} + \int_{V_0}\boldsymbol{N}^T\rho_0\tilde{\boldsymbol{\omega}}\tilde{\boldsymbol{\omega}}\boldsymbol{x}\,dV_0.}_{\boldsymbol{f}_{zc}}\end{aligned}$$

(2.3-20)

Summarizing Eq.(2.3-15) up to Eq.(2.3-17) and using Eq.(2.3-18) up to Eq.(2.3-20) gives the equation of motion for the *elastic body*

$$\boldsymbol{M}(\boldsymbol{w})\ddot{\boldsymbol{w}}+\boldsymbol{K}\boldsymbol{w}+\boldsymbol{f}_c(\boldsymbol{w},\dot{\boldsymbol{w}}) = \boldsymbol{f}_b+\boldsymbol{f}_p \qquad (2.3\text{-}21)$$

with the generalized acceleration vector

$$\ddot{\boldsymbol{w}} = \begin{bmatrix}{}^I\ddot{\boldsymbol{r}}_R & \dot{\boldsymbol{\omega}} & \ddot{\boldsymbol{z}}\end{bmatrix}^T \qquad (2.3\text{-}22)$$

the symmetric mass matrix

$$\boldsymbol{M} = \int_{V_0}\rho_0\begin{bmatrix}\boldsymbol{E} & -(\tilde{\boldsymbol{x}}+\tilde{\boldsymbol{u}}) & \boldsymbol{N} \\ -(\tilde{\boldsymbol{x}}+\tilde{\boldsymbol{u}})^T & (\tilde{\boldsymbol{x}}+\tilde{\boldsymbol{u}})(\tilde{\boldsymbol{x}}+\tilde{\boldsymbol{u}}) & (\tilde{\boldsymbol{x}}+\tilde{\boldsymbol{u}})\boldsymbol{N} \\ \boldsymbol{N}^T & \boldsymbol{N}^T(\tilde{\boldsymbol{x}}+\tilde{\boldsymbol{u}})^T & \boldsymbol{N}^T\boldsymbol{N}\end{bmatrix}dV_0 \qquad (2.3\text{-}23)$$

and the symmetric stiffness matrix

$$\boldsymbol{K} = \begin{bmatrix}\boldsymbol{0} & \boldsymbol{0} & \boldsymbol{0} \\ \boldsymbol{0} & \boldsymbol{0} & \boldsymbol{0} \\ \boldsymbol{0} & \boldsymbol{0} & \boldsymbol{K}_N\end{bmatrix}, \qquad (2.3\text{-}24)$$

the vector of the gyroscopic and centrifugal forces $\boldsymbol{f}_c$, the body forces $\boldsymbol{f}_b$ and the external forces $\boldsymbol{f}_p$

$$\boldsymbol{f}_c = \begin{bmatrix}\boldsymbol{f}_{ac} \\ \boldsymbol{f}_{\omega c} \\ \boldsymbol{f}_{zc}\end{bmatrix}, \quad \boldsymbol{f}_b = \begin{bmatrix}\boldsymbol{f}_{ab} \\ \boldsymbol{f}_{\omega b} \\ \boldsymbol{f}_{zb}\end{bmatrix}, \quad \boldsymbol{f}_p = \begin{bmatrix}\boldsymbol{f}_{ap} \\ \boldsymbol{f}_{\omega p} \\ \boldsymbol{f}_{zp}\end{bmatrix}, \qquad (2.3\text{-}25)$$

respectively. The stiffness matrix $\boldsymbol{K}$ is symmetric as well since the matrix of elasticity $\boldsymbol{H}$ defined in Eq.(2.2-18) is symmetric.

All the components of the systems described in the introduction, where the material behavior follows Hooke's law, can be described dynamically by these equations of motion. With respect to several applications, where small rotations are involved, the dynamics of the elastic body can be described by linear equations of motion. If terms of second and higher order are neglected, this leads to the linear equations of motion

$$\boldsymbol{M}\ddot{\boldsymbol{w}} + \boldsymbol{K}\boldsymbol{w} = \boldsymbol{f}_b + \boldsymbol{f}_p \tag{2.3-26}$$

with the symmetric mass matrix

$$\boldsymbol{M} = \int_{V_0} \rho_0 \begin{bmatrix} \boldsymbol{E} & -\tilde{\boldsymbol{x}} & \boldsymbol{N} \\ -\tilde{\boldsymbol{x}}^T & \tilde{\boldsymbol{x}}\tilde{\boldsymbol{x}} & \tilde{\boldsymbol{x}}\boldsymbol{N} \\ \boldsymbol{N}^T & \boldsymbol{N}^T\tilde{\boldsymbol{x}}^T & \boldsymbol{N}^T\boldsymbol{N} \end{bmatrix} dV_0 \, . \tag{2.3-27}$$

For the investigation of a rotating brake disc or turbine blade, the absolute velocity of the reference point R is often assumed to be zero and the angular velocity of the rotating frame to be constant. Then the dynamics of the *rotating elastic structure* is given by

$$\boldsymbol{M}\ddot{\boldsymbol{z}} + \boldsymbol{G}\dot{\boldsymbol{z}} + \boldsymbol{K}\boldsymbol{z} = \boldsymbol{f}_{zb} + \boldsymbol{f}_{zp} - \boldsymbol{f}_{zc0} \tag{2.3-28}$$

with

$$\begin{aligned} \boldsymbol{M} &= \int_{V_0} \boldsymbol{N}^T \rho_0 \boldsymbol{N} \, dV_0, \quad \boldsymbol{G} = \int_{V_0} \boldsymbol{N}^T \rho_0 2\tilde{\boldsymbol{\omega}}_0 \boldsymbol{N} \, dV_0, \\ \boldsymbol{K} &= \boldsymbol{K}_N + \int_{V_0} \boldsymbol{N}^T \rho_0 \tilde{\boldsymbol{\omega}}_0 \tilde{\boldsymbol{\omega}}_0 \boldsymbol{N} \, dV_0, \quad \boldsymbol{f}_{zc0} = \int_{V_0} \boldsymbol{N}^T \rho_0 \tilde{\boldsymbol{\omega}}_0 \tilde{\boldsymbol{\omega}}_0 \boldsymbol{x} \, dV_0. \end{aligned} \tag{2.3-29}$$

Within multibody systems like the chains in motors, elastic deformations are often neglected. This assumption leads to the equations of motion of a *rigid body*

$$m\,{}^I\boldsymbol{a}_R + m(\dot{\tilde{\boldsymbol{\omega}}} + \tilde{\boldsymbol{\omega}}\tilde{\boldsymbol{\omega}})\boldsymbol{r}_{RC} = \boldsymbol{f}_{ab} + \boldsymbol{f}_{ap} \, , \tag{2.3-30}$$

$$m\tilde{\boldsymbol{r}}_{RC}\,{}^I\boldsymbol{a}_R + \boldsymbol{J}^{(R)}\dot{\boldsymbol{\omega}} + \tilde{\boldsymbol{\omega}}\boldsymbol{J}^{(R)}\boldsymbol{\omega} = \boldsymbol{f}_{\omega b} + \boldsymbol{f}_{\omega p} \, , \tag{2.3-31}$$

where the mass is defined by

$$m := \int_{V_0} \rho_0 dV_0 \, , \tag{2.3-32}$$

the position of the center of mass is given by

$$\boldsymbol{r}_{RC} := \frac{1}{m} \int_{V_0} \boldsymbol{x} \rho_0 dV_0 \tag{2.3-33}$$

and the inertia with respect to the reference point R is defined by

$$\boldsymbol{J}^{(R)} := \int_{V_0} \tilde{\boldsymbol{x}}^T \tilde{\boldsymbol{x}} \rho_0 dV_0 \, . \tag{2.3-34}$$

2.4 Modal Description of Elastic Bodies

In general, continuous elastic bodies have an infinite number of degrees of freedom. A first step to reduce the dynamical problem is to discretize the continuous body and, hence, to reduce the degrees of freedom to a finite number. Using standard Finite Element Methods, see for example (Bathe 1990; Reddy 1993; Gaul 2005), the discretization of geometric complex bodies is very comfortable. Based on the Eq.(2.3-10) a Ritz-Ansatz with local Ansatz-functions in connection with the displacements of the nodes is used to describe the deformations. The dynamical problem can be reduced furthermore, if the modal description of the elastic body is applied. Here, the basis for the modal description of an elastic body is the linearized equations of motion neglecting gyroscopic effects. Regarding the linearized equations of motion of an elastic body given by Eq.(2.3-28) viscous damping is assumed, where the damping forces are linear dependent on the velocities. Then the dynamics of the linear viscous-elastic body is approximated by the following equation of motion with n_F degrees of freedom,

$$\boldsymbol{M}\ddot{\boldsymbol{w}} + (\boldsymbol{D} + \boldsymbol{G})\dot{\boldsymbol{w}} + \boldsymbol{K}\boldsymbol{w} = \boldsymbol{f}_{ex}(t), \qquad (2.4\text{-}1)$$

see (Magnus and Popp 1997) and (Müller and Schiehlen 1977), where $\boldsymbol{M}$ denotes the symmetric mass matrix, $\boldsymbol{D}$ the damping matrix, $\boldsymbol{K}$ the symmetric stiffness matrix, $\boldsymbol{w}$ the generalized displacement vector relative to the position of equilibrium and $\boldsymbol{f}_{ex}$ the generalized time dependent external force vector. From Eq.(2.3-24), Eq.(2.3-27) and Eq.(2.3-29) the mass and stiffness matrix are symmetric and, hence,

$$\boldsymbol{M} = \boldsymbol{M}^T, \quad \boldsymbol{K} = \boldsymbol{K}^T, \quad \boldsymbol{G} = -\boldsymbol{G}^T. \qquad (2.4\text{-}2)$$

The damping matrix is approximated by the Rayleigh assumption, where the damping matrix is the linear combination of the mass and stiffness matrix,

$$\boldsymbol{D} = \alpha\, \boldsymbol{M} + \beta\, \boldsymbol{K}. \qquad (2.4\text{-}3)$$

Because of Eq.(2.4-2), the damping matrix is symmetric as well,

$$\boldsymbol{D} = \boldsymbol{D}^T. \qquad (2.4\text{-}4)$$

For the solution of the homogeneous differential equation of Eq.(2.4-1), one can choose the Ansatz

$$\boldsymbol{w} = \hat{\boldsymbol{w}} e^{\lambda t}. \qquad (2.4\text{-}5)$$

Inserting this function in the homogenous differential equation of Eq.(2.4-1) leads to the eigenvalue problem

$$\left(\lambda^2 \boldsymbol{M} + \lambda[\boldsymbol{D} + \boldsymbol{G}] + \boldsymbol{K}\right)\hat{\boldsymbol{w}} = \boldsymbol{0}. \qquad (2.4\text{-}6)$$

In general, this leads to complex eigenvectors and eigenvalues. If the damping and the gyroscopic effects are neglected, the harmonic Ansatz

$$\boldsymbol{w} = \boldsymbol{w}_0\, e^{i\omega_0 t} \qquad (2.4\text{-}7)$$

leads to the eigenvalue problem

$$\left(-\omega_0^2 \boldsymbol{M} + \boldsymbol{K}\right)\boldsymbol{w}_0 = \boldsymbol{0}. \qquad (2.4\text{-}8)$$

The eigenvalues in this case are reel as well as the eigenvectors, which can be summarized within the so-called modal matrix

$$\boldsymbol{T} = \left[\boldsymbol{w}_{01} \quad \boldsymbol{w}_{02} \quad \dots \quad \boldsymbol{w}_{0m}\right]. \tag{2.4-9}$$

With an increasing number of modes, the dynamical description of the linear elastic body can be improved, using the modal transformation

$$\boldsymbol{w} = \boldsymbol{Tq}, \tag{2.4-10}$$

where $\boldsymbol{q}$ denotes the vector of modal coordinates. The dimension of this vector is equal to the number m of eigenvectors used to describe the displacements of the elastic body. Note that gyroscopic effects would lead to complex eigenvectors, while damping effects would lead to complex eigenvalues. Multiplying Eq.(2.4-1) with the transposed modal matrix from the left side and using Eq.(2.4-10) leads to

$$\boldsymbol{T}^T\boldsymbol{MT}\ddot{\boldsymbol{q}} + \boldsymbol{T}^T\boldsymbol{DT}\dot{\boldsymbol{q}} + \boldsymbol{T}^T\boldsymbol{KTq} = \boldsymbol{T}^T\boldsymbol{f}_{ex}. \tag{2.4-11}$$

If the eigenvectors in Eq.(2.4-9) are mass normalized, which is defined by

$$\boldsymbol{T}^T\boldsymbol{MT} = \boldsymbol{E}, \tag{2.4-12}$$

this leads to

$$\boldsymbol{T}^T\boldsymbol{DT} = \boldsymbol{diag}(2\omega_{0j}D_j), \tag{2.4-13}$$

with the modal damping coefficient D_j and

$$\boldsymbol{T}^T\boldsymbol{KT} = \boldsymbol{diag}(\omega_{0j}^2), \quad j = 1(1)m, \tag{2.4-14}$$

with the angular eigenfrequency ω_{0j} of the j^{th} mode. Note, that the modal matrix $\boldsymbol{T}$ can include rigid body modes of the elastic body. The corresponding angular eigenfrequencies of those modes are zero. Inserting Eq.(2.4-12) up to Eq.(2.4-14) in Eq.(2.4-11) gives the resulting system equation

$$\boldsymbol{diag}(\ddot{q}_j + 2\omega_{0j}D_j\dot{q}_j + \omega_{0j}^2 q_j) = \boldsymbol{T}^T\boldsymbol{f}_{ex}, \tag{2.4-15}$$

where the vibration modes are uncoupled. If the external forces are known, Eq.(2.4-15) can be solved by numerical integration. With respect to each normalized eigenvector, the corresponding normalized strain and stress vectors can be calculated and can be used to analyze the strain state of the elastic body with

$$\boldsymbol{\varepsilon} = \boldsymbol{T}_{\varepsilon}\boldsymbol{q} \tag{2.4-16}$$

and the stress state with

$$\boldsymbol{\sigma} = \boldsymbol{T}_{\sigma}\boldsymbol{q}. \tag{2.4-17}$$

In (Schwertassek and Wallrapp 1999), an approximation of the deformations of an elastic body is given by using the eigenmodes and static modes. Both sets of modes have to fulfill the geometric boundary conditions. An alternative and efficient method is described in (Hurty, 1960 and 1965), where main coordinates are introduced. Main coordinates are defined by the occurrence of external forces. The advantage of this method is the exact description of the dynamics of the main coordinates.

The accuracy of the modal description increases with an increasing number of modes. How many modes have to be used to model the dynamical behavior sufficiently is problem dependent. In general, the number m of the used modes is relatively small compared to the number of degrees of freedom of the finite element model. This will reduce the computation time dramatically.

The modal description of a linear elastic body is exact, if an infinite number of eigenvectors is used to describe the dynamics. The advantage of the modal description is the dramatic reduction of the number of degrees of freedom only if the influence of higher modes can be neglected. For a linear system, the investigated frequency spectrum defines the number of eigenmodes. In general, this does not hold for nonlinear systems. A first estimation with respect to the minimum number of modes gives the comparison of the modal stiffness at zero excitation frequency with the static stiffness, see (Stelter 1990).

Note, if the angular velocity is constant, see Eq.(2.3-28), the centrifugal forces can be included in the modal analysis, with the so called pre-stress function within finite element programs. In this case, the results of the quasi-static analysis are the basis for the modal analysis. The influence of the gyroscopic forces is often neglected within the modal analysis of commercial finite element programs. Nevertheless, they can be calculated, see (Nackenhorst 2000).

3 Contact Model

In this Chapter, the components of the point contact model are described and the corresponding equations are derived. This includes the contact stiffnesses, the surface roughness and the friction characteristic. Then, the three-dimensional point contact model is investigated within the time domain. Finally, temperature effects coupled with microslip and the development of wear are investigated using the point contact model.

3.1 Contact Stiffnesses and Microscopic Contact

The elasticity of the contacting bodies influences the dynamic behavior of the whole system. There exist several possibilities to get the normal contact force-displacement relationship and the tangential contact stiffness:

- With an experimental setup to identify both, as it is done for example in (Treyde 1995; Sextro 1998).
- With a statical investigation of geometric complex contact designs using the Finite Element Method, see (Wriggers 1995).
- With the assumption of a Hertzian normal contact, the normal contact force-displacement relationship is described in (Hertz 1882; Hill 1993) and the tangential contact stiffness for elliptical contact areas and for arbitrary axis-symmetric surfaces is derived in (Deresiewicz 1957; Jäger 1995), respectively.
- With the assumption of equal-distanced, independent normal and tangential springs, the so-called Winkler foundation, elastic foundation, wire-brush model or thin elastic contact, see (Winkler 1867; Bentall and Johnson 1968; Johnson 1989; Jäger 1999).

The basic assumption is that the contact elements are only coupled by the contact kinematics. This is a big advantage with respect to the numerical investigations of dynamic systems with friction contacts. However, this reduced model leads of course to a lower accuracy.

To overcome this problem, the information of the normal and tangential contact stiffnesses derived from measurements, Finite Element Method or from calculation based on the half-space assumption, as described above, can be used and therefore can improve the calculations.

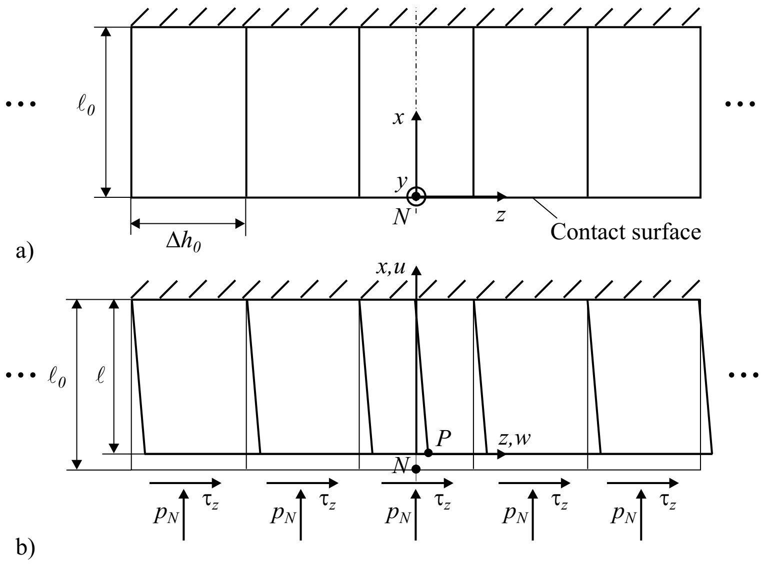

Fig. 3.1-1 **a**) Undeformed smooth contact surface **b**) deformed surface

In **Fig. 3.1-1a**, a plane elastic foundation or a so-called thin elastic contact is shown. The contact has to be discretized due to the in general spatial motion and the non-linearity of the contact behavior. The contact plane is discretized using rectangular area elements with the width Δh_0 and the depth Δb_0. The nominal contact area of one area element is given by

$$\Delta A_0 = \Delta b_0 \Delta h_0 . \tag{3.1-1}$$

The length ℓ_0 describes the length of the undeformed elastic foundation. For the derivation of the contact stiffnesses, a constant distribution of the normal pressure p_N and the shear stresses τ_y and τ_z in the y- and z-direction is assumed over the contact surface. Then, each contact element will behave in the same manner. The elastic foundation deflects due to the constant normal contact pressure p_N and the constant shear stress τ_z, see **Fig. 3.1-1b**, where the relative displacement of the surface is defined by the coordinates of the point P relative to N. The classical constitutive law of Hooke is used neglecting the influence of the temperature, see Chapter 2.2. Due to the assumed constant loading in normal and tangential direction, the deformed contact surface remains planar. The stresses at the position $x=0$ are given by

$$\sigma_{xx} = -p_N , \quad \sigma_{xy} = -\tau_y , \quad \sigma_{xz} = -\tau_z . \tag{3.1-2}$$

The slope of the contact surface is zero,

$$\frac{\partial u}{\partial y} = 0, \quad \frac{\partial u}{\partial z} = 0 . \tag{3.1-3}$$

From here it follows, that the shear stress is given by

$$\sigma_{xz} = G\frac{\partial w}{\partial x}. \tag{3.1-4}$$

Furthermore, because of the constant loading the displacements in the *y*- and *z*-direction are constant, hence

$$\frac{\partial v}{\partial z} = 0, \quad \frac{\partial w}{\partial y} = 0 \tag{3.1-5}$$

and from Hooke's law it follows

$$\sigma_{yz} = 0. \tag{3.1-6}$$

With the length ℓ of the deformed foundation the boundary conditions are

$$\begin{aligned} &u(x=0) = u_P, \quad u(x=\ell) = 0, \\ &v(x=0) = v_P, \quad v(x=\ell) = 0, \\ &w(x=0) = w_P, \quad w(x=\ell) = 0, \end{aligned} \tag{3.1-7}$$

where the point *P* lies in the center of one contact area element. Three sets of boundary conditions (denoted by $i=1,2,3$) will be investigated in the following. In a first step, it is assumed, that the normal stresses in the *y*- and *z*-direction are zero

$$\sigma_{yy} = \sigma_{zz} = 0, \quad (i=1) \tag{3.1-8}$$

and hence

$$\sigma_{xx} = E\varepsilon_{xx}. \tag{3.1-9}$$

Then the force-displacement relationships for a single elastic element of the contact interface can be calculated

$$p_N = \frac{E}{\ell}u_P, \quad \tau_y = \frac{G}{\ell}v_P, \quad \tau_z = \frac{G}{\ell}w_P. \tag{3.1-10}$$

For one contact area element, the stresses are assumed to be constant as well, hence,

$$p_N = \frac{\Delta F_N}{\Delta A_0}, \quad \tau_y = \frac{\Delta F_{Ty}}{\Delta A_0}, \quad \tau_z = \frac{\Delta F_{Tz}}{\Delta A_0}. \tag{3.1-11}$$

Inserting Eq.(3.1-11) in Eq.(3.1-10) gives the force-displacement relationships

$$\Delta F_N = \frac{E\Delta A_0}{\ell}u_P, \quad \Delta F_{Ty} = \frac{G\Delta A_0}{\ell}v_P, \quad \Delta F_{Tz} = \frac{G\Delta A_0}{\ell}w_P. \tag{3.1-12}$$

The length ℓ of the deformed elastic foundation is given by

$$\ell = \ell_0 - u_P, \tag{3.1-13}$$

see Fig. 3.1-1b. Differentiating the forces defined by Eq.(3.1-12) with respect to the corresponding displacement and assuming the displacement of the point *P* in the *x*-direction is small,

$$\frac{u_P}{\ell_0} << 1, \tag{3.1-14}$$

leads to the nominal normal contact stiffness

$$\Delta c_{N0} = \frac{E\Delta A_0}{\ell_0} \tag{3.1-15}$$

and the nominal tangential contact stiffness

$$\Delta c_{R0} = \frac{G \Delta A_0}{\ell_0} . \tag{3.1-16}$$

Using the length ℓ_0 of the undeformed contact element instead of the length ℓ of the deformed element gives the relative error ε_{rel} with respect to the normal and tangential forces defined in Eq.(3.1-12)

$$\varepsilon_{rel} = \frac{\frac{1}{\ell_0} - \frac{1}{\ell}}{\frac{1}{\ell}} 100\% = -\frac{u_P}{\ell_0} 100\% . \tag{3.1-17}$$

If this relative error is small, say 2% up to 4%, this effect can be neglected. Further investigations will follow in Chapter 3.4, where the hyperbolic contact is modeled.

The tangential contact stiffness defined in Eq.(3.1-16) can be derived from the theory of thin contacts described in (Bental and Johnson 1968) as well. Due to the investigated boundary conditions, the tangential contact behavior is isotropic. That means, both tangential contact stiffnesses in the *y*- and *z*-direction are identical.

Different boundary conditions lead to different results for the contact stiffnesses. This will be discussed in the following. Assuming instead of Eq.(3.1-8) an hydrostatic stress field, see (Jäger 1999) with

$$\sigma_{yy} = \sigma_{zz} = -p_N , \quad (i = 2) \tag{3.1-18}$$

leads to the normal stresses

$$\sigma_{xx} = \sigma_{yy} = \sigma_{zz} = \frac{E}{(1-2\nu)} \varepsilon_{xx} \tag{3.1-19}$$

and the normal contact stiffness

$$\Delta c_{N0} = \frac{E \Delta A_0}{\ell_0 (1-2\nu)} . \tag{3.1-20}$$

Another possibility is to assume zero strains in the *y*- and *z*-direction

$$\varepsilon_{yy} = \varepsilon_{zz} = 0, \quad (i = 3) . \tag{3.1-21}$$

This boundary condition leads to the following normal stresses

$$\sigma_{xx} = \frac{E(1-\nu)}{(1-2\nu)(1+\nu)} \varepsilon_{xx} \tag{3.1-22}$$

and

$$\sigma_{yy} = \sigma_{zz} = -\frac{\nu}{1-\nu} p_N . \tag{3.1-23}$$

Then, the normal contact stiffness is given by

$$\Delta c_{N0} = \frac{E \Delta A_0}{\ell_0 (1-2\nu)} \frac{(1-\nu)}{(1+\nu)} . \tag{3.1-24}$$

This normal contact stiffness can be derived from the theory of thin contacts described in (Bental and Johnson 1968) as well. Summarizing the results gives the contact stresses

$$p_N = \frac{\Delta c_{N0}}{\Delta A_0} u_P, \quad \tau_y = \frac{\Delta c_{R0}}{\Delta A_0} v_P, \quad \tau_z = \frac{\Delta c_{R0}}{\Delta A_0} w_P \,, \tag{3.1-25}$$

where the contact stiffnesses can vary dependent on the boundary conditions ($i=1,2,3$).

The limit of the above theory is given by yielding of the material. For mathematical simplicity, the equivalent stress due to the Tresca criterion is used and is given by

$$\sigma_{Tresca} = \max\left\{ |\sigma_1 - \sigma_2|, |\sigma_2 - \sigma_3|, |\sigma_3 - \sigma_1| \right\} = 2\tau_S = Y, \tag{3.1-26}$$

where $\sigma_{1,2,3}$ are the principal stresses, τ_S and Y denote the values of the yield stress of the material in simple shear and simple tension or compression respectively. In the following, only the shear stress in the z-direction is regarded. Summarizing the different stresses due to the three different investigated boundary conditions, $i=1,2,3$, as defined in Eq.(3.1-8), Eq.(3.1-18) and Eq.(3.1-23) gives

$$\begin{aligned} &\sigma_{xx} = -p_N, \quad \sigma_{yy} = \sigma_{zz} = -s_i \, p_N \,, \\ &\sigma_{xz} = -\tau_z, \quad \sigma_{yx} = \sigma_{yz} = 0 \,, \end{aligned} \tag{3.1-27}$$

where the parameter s_i depends on the used boundary condition with

$$s_1 = 0, \quad s_2 = 1, \quad s_3 = \frac{\nu}{1-\nu} \,. \tag{3.1-28}$$

From Eq.(3.1-27) it can be derived, that the three principle stresses are given by

$$\begin{aligned} \sigma_1 &= \left(-\frac{1+s_i}{2} p_N + \sqrt{\tau_z^2 + \frac{(1-s_i)^2}{4} p_N^2} \right) \\ \sigma_2 &= \sigma_{yy} = -s_i p_N \\ \sigma_3 &= \left(-\frac{1+s_i}{2} p_N - \sqrt{\tau_z^2 + \frac{(1-s_i)^2}{4} p_N^2} \right) \end{aligned} \,. \tag{3.1-29}$$

Then, the maximum equivalent stress by Tresca is given by

$$\sigma_{Tresca} = |\sigma_3 - \sigma_1| = \sqrt{4\tau_z^2 + (1-s_i)^2 p_N^2} \,. \tag{3.1-30}$$

Hence, the contact behavior is elastic, if

$$\sqrt{\tau_z^2 + \frac{(1-s_i)^2}{4} p_N^2} < \tau_S \,. \tag{3.1-31}$$

If Eq.(3.1-31) does not hold, perfect plasticity is defined by

$$\sqrt{\tau_{z,max}^2 + \frac{(1-s_i)^2}{4} p_N^2} = \tau_S \,. \tag{3.1-32}$$

with the yield stress τ_S, which is dependent on the temperature. The limiting maximum shear strength $\tau_{z,\max}$ is given by solving Eq.(3.1-31) for the shear stress

$$\tau_{z,max} = \mu_{max} p_N = \sqrt{\tau_S^2 - \frac{(1-s_i)^2}{4} p_N^2} \,, \tag{3.1-33}$$

assuming that

$$\tau_S^2 \geq \frac{(1-s_i)^2}{4} p_N^2 \,. \tag{3.1-34}$$

If Eq.(3.1-34) does not hold, then in the limit the normal pressure is given by

$$p_{N,max} = \frac{2\tau_S}{(1-s_i)} \,. \tag{3.1-35}$$

whereby the maximum shear stress is zero,

$$\tau_{z,max} = 0 \,. \tag{3.1-36}$$

In case of the hydrostatic pressure distribution $s_2=1$ the maximum allowable pressure defined by Eq.(3.1-35) is infinite, which means, in this case yielding does not occur.

3.2 Limits of Application of the Contact Model

The point contact model will be used to model the quasi-static contact behavior, while the modal description is used to describe the dynamics of the contacting bodies. Hence, the excitation frequency must be very small compared to the eigenfrequencies of the elastic contact in the normal and tangential direction. For small deformations, the eigenfrequencies due to the vibration in the normal direction are calculated first. The elastic contact described in Fig. 3.1-1 includes inertia. A mass element of the elastic contact is shown in Fig. 2.2-1 with

$$dm = \rho_0 dV_0 \tag{3.2-1}$$

and the volume

$$dV_0 = dA_0 dx \,. \tag{3.2-2}$$

The normal stress in the x-direction is dependent on the applied three boundary conditions ($i=1,2,3$) as discussed in Chapter 3.1. With Eq.(3.1-9), Eq.(3.1-19) and Eq.(3.1-22) the result can be summarized with

$$\sigma_{xx} = \widetilde{E}_i \varepsilon_{xx} \,, \tag{3.2-3}$$

and

$$\begin{aligned} \widetilde{E}_1 &= E, \\ \widetilde{E}_2 &= \frac{E}{(1-2\nu)}, \\ \widetilde{E}_3 &= \frac{E(1-\nu)}{(1-2\nu)(1+\nu)}. \end{aligned} \tag{3.2-4}$$

Applying Newton's law with respect to the x-direction leads to

$$d\sigma_{xx} dA_0 = dm\, \ddot{u}(x,t) \,. \tag{3.2-5}$$

Inserting Eq.(3.2-1) and Eq.(3.2-3) gives the partial differential equation

$$\widetilde{E}_i u''(x,t) = \rho_0 \ddot{u}(x,t) \,. \tag{3.2-6}$$

This equation describes waves in the contact. The solution for standing waves is given by

$$u(x,t) = \tilde{u}(x)\sin(\omega t + \phi) \tag{3.2-7}$$

with

$$\tilde{u}(x) = a_1 \sin(a_3 x) + a_2 \cos(a_3 x)\,. \tag{3.2-8}$$

Inserting Eq.(3.2-7) leads to the linear differential equation

$$\tilde{u}''(x) + \omega^2 \frac{\rho_0}{\tilde{E}_i}\tilde{u}(x) = 0\,. \tag{3.2-9}$$

Neglecting the contact surface loads, the boundary conditions at the surface ($x=0$) and at the built-in end ($x=\ell_0$) are given by

$$\sigma_{xx}(x=0,t) = 0, \quad u(x=\ell_0,t) = 0\,, \tag{3.2-10}$$

respectively, or with Eq.(3.2-3) and Eq.(3.2-7)

$$\tilde{u}'(x=0) = 0, \quad \tilde{u}(x=\ell_0) = 0\,. \tag{3.2-11}$$

Applying these boundary conditions to Eq.(3.2-8) lead to the solution

$$a_1 = 0 \tag{3.2-12}$$

and

$$a_3 = \frac{\pi}{2\ell_0}(2k-1), \quad k = 1,2,3,\dots\,. \tag{3.2-13}$$

Inserting Eq.(3.2-8) with Eq.(3.2-12) and Eq.(3.2-13) in the Eq.(3.2-9) gives the angular eigenfrequencies for the normal vibration modes

$$\omega_{Nk} = (2k-1)\frac{\pi}{2\ell_0}\sqrt{\frac{\tilde{E}_i}{\rho_0}}\,. \tag{3.2-14}$$

The eigenfunctions defined in Eq.(3.2-8) can be mass normalized corresponding to the procedure described in Chapter 2.4 with

$$\int_0^{\ell_0} \rho_0 \Delta A_0 \tilde{u}_k^2(x)\,dx = 1\,. \tag{3.2-15}$$

Integrating Eq.(3.2-15) with respect to the coordinate x and solving for the mass normalized amplitude gives

$$a_2 = \sqrt{\frac{2}{\Delta A_0 \ell_0 \rho_0}}\,. \tag{3.2-16}$$

Hence, the resulting mass-normalized eigenfunctions are given by

$$\tilde{u}_k(x) = \sqrt{\frac{2}{\Delta A_0 \ell_0 \rho_0}}\cos\left(\frac{\pi}{2\ell_0}(2k-1)x\right), \quad k = 1,2,3,\dots\,. \tag{3.2-17}$$

For zero angular excitation frequency, the normal modal stiffness is given by

$$c_M = \frac{1}{\sum_{k=1}^{m} \frac{\tilde{u}_k^2(0)}{\omega_{Nk}^2}}\,, \tag{3.2-18}$$

see (Stelter 1990). The static stiffness reads

$$\Delta c_{N0} = \frac{\widetilde{E}_i \Delta A_0}{\ell_0}\,, \tag{3.2-19}$$

where the displacement are linear with respect to the coordinate x. Inserting Eq.(3.2-17) and Eq.(3.2-14) leads to

$$c_M^* = \frac{c_M}{\Delta c_{N0}} = \frac{\pi^2}{8\sum_{k=1}^{m} \frac{1}{(2k-1)^2}}\,. \tag{3.2-20}$$

An infinite number of modes give the exact value of the stiffness at zero excitation frequency. The limiting value of the normalized modal stiffness is one,

$$\lim_{m \to \infty} c_M^* = 1\,. \tag{3.2-21}$$

In **Fig. 3.2-1** the relative error with respect to the exact stiffness given by Eq.(3.2-19) is plotted versus the number of modes. Using five modes leads to a relative error of less than 5%, while using twenty modes leads to a relative error less than 1%. This figure can be used to estimate the minimum number of modes to simulate the dynamical behavior.

Since the relative error is relatively large for a very small number of modes, in case of a quasi-static system behavior it is more practical to use the static stiffness for modeling the deformations. Hence, the modal description is not very useful to describe the quasi-static contact behavior but is very useful for modeling the dynamics of the elastic bodies as discussed in Chapter 2.4.

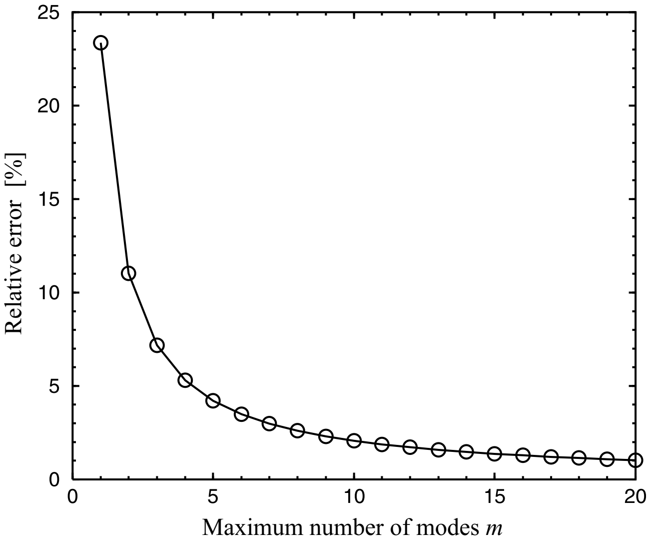

Fig. 3.2-1 Modal stiffness at zero excitation frequency

For the tangential vibrations, the procedure is similar to the one described above. Applying Newton's law, see Fig. 2.2-1, with respect to the *z*-direction gives in analogy to Eq.(3.2-5)

$$d\sigma_{xz} dA_0 = dm\,\ddot{w}(x,t)\,. \tag{3.2-22}$$

With Eq.(3.1-4) and Eq.(3.2-1) this leads to

$$G w''(x,t) = \rho_0 \ddot{w}(x,t)\,. \tag{3.2-23}$$

Neglecting the surface load, the boundary conditions are given by

$$\sigma_{xz}(x = 0,t) = 0, \quad w(x = \ell_0,t) = 0\,. \tag{3.2-24}$$

Similar to the procedure described above the angular eigenfrequencies for the tangential vibration modes are given by

$$\omega_{Tk} = (2k-1)\frac{\pi}{2\ell_0}\sqrt{\frac{G}{\rho_0}}, \quad k = 1,2,3,\ldots\,. \tag{3.2-25}$$

The analysis with respect to the modal stiffness as described above can be used for the tangential direction in the same way, because both investigations are based on the same structure of differential equations, compare Eq.(3.2-23) with Eq.(3.2-6). With respect to the limits of the application of the point contact model the first eigenfrequencies are needed and given by $k=1$ for the tangential vibrations. Using Eq.(3.1-16) gives the first angular eigenfrequency of the elastic contact

$$\omega_{T1} = \sqrt{\frac{\Delta c_{R0}}{\Delta m_{D0}}} \tag{3.2-26}$$

with Eq.(3.1-16) for the tangential contact stiffness, the reduced mass

$$\Delta m_{D0} = \gamma \Delta m_{R0}, \quad \gamma = \frac{4}{\pi^2} \tag{3.2-27}$$

and the resultant mass of one contact element

$$\Delta m_{R0} = \rho_0 \Delta A_0 \ell_0\,. \tag{3.2-28}$$

Corresponding to the normal direction the first angular eigenfrequency is given by

$$\omega_{N1} = \sqrt{\frac{\Delta c_{N0}}{\Delta m_{D0}}} \tag{3.2-29}$$

with

$$\Delta c_{N0} = \frac{\tilde{E}_i \Delta A_0}{\ell_0}\,. \tag{3.2-30}$$

The point contact model will be used to model the quasi-static contact behavior. Hence, the excitation frequency must be very small compared to the eigenfrequencies of the elastic contact in the normal and tangential direction, hence, the following equation must hold, when applying the point contact model

$$\omega_0 << \min\left\{\sqrt{\frac{\Delta c_{N0}}{\Delta m_{D0}}}, \sqrt{\frac{\Delta c_{R0}}{\Delta m_{D0}}}\right\}. \tag{3.2-31}$$

Note, that the eigenfrequencies of the elastic contact are not dependent on the contact area. This equation must hold for rough contact surfaces as well.

3.3 Mesoscopic Contact Laws for Rough Surfaces

The surface roughness has an effect on the normal force-displacement relationship, which can not be neglected. In (Greenwood and Williamson 1966; Greenwood 1984; Johnson 1989; Zavarise et al. 1992-1995; Willner 1995; Wriggers 1996; Willner 2000), contact models including the effect of rough surfaces are derived using the distribution for the height of the asperities and the Hertzian theory for each contact. Based on an exponential distribution, for example, Greenwood derived an exponential relationship for the normal force-displacement relationship with

$$\frac{F_N}{F_{NS}} = e^{\left(\frac{u_N - u_{N0}}{\sigma_S}\right)}, \tag{3.3-1}$$

where F_N denotes the compressive contact force, σ_S denotes the standard deviation of the cumulative height distribution and the parameter F_{NS} is defined by the mean summit curvature of the asperities, material parameters and the standard deviation of the cumulative height distribution, see (Johnson 1989). In **Fig. 3.3-1** this relationship is shown assuming a standard deviation of

$$\sigma_S = \frac{1}{4} u_{NS} \quad \text{and} \quad u_{N0} = u_{NS}\,. \tag{3.3-2}$$

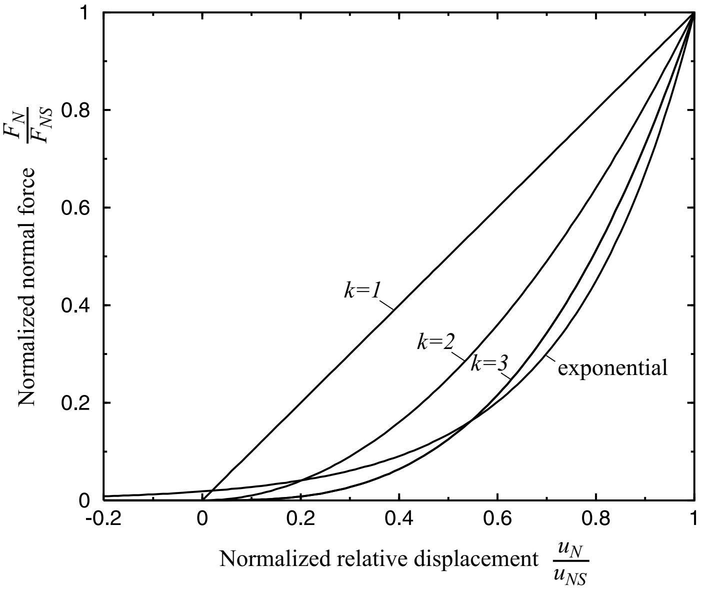

Fig. 3.3-1 Normal force-displacements relationship for rough surfaces

The disadvantage using this description of the normal contact force is that separation of the contact is not defined. Furthermore, these approaches need the information about the mean summit curvature of the asperities to be able to calculate the contact forces. It is quite difficult to obtain a good estimation for this value, since the topography or at least a surface profile measurement has to be analyzed with respect to the curvatures of the asperities. Furthermore, the resolution or sampling of the surface roughness measurement does influence the results very strong, see (Willner 2000).

In (Kragelski 1982; Wriggers 1996) a potential law approximates the normal force displacement relationship

$$\frac{F_N}{F_{NS}} = \left(\frac{u_N - u_{N0}}{u_{NS}} \right)^k , \tag{3.3-3}$$

based on experimental investigations. In principle measured values of the exponent vary in the range of $2.0 \le k \le 3.3$, see (Kikuchi and Oden 1988). In Fig. 3.3-1 these normal force-displacement relationships with $k=1$, 2 and 3 are compared with the exponential description. The exponential contact law is very close to the cubic potential law within the investigated range. Note, the cubic functional behavior has also been identified by experiments, see (Kragelski 1982; Kikuchi and Oden 1988), and is often used within the FEM to model rough surfaces, see (Wriggers 1995). The classical penalty approach is applied, where the compressive contact forces are linear dependent on the penetration, when the exponent k is equal to one. With respect to Eq.(3.3-3) the contact parameters are unknown. In the following an alternative contact model is developed, which avoids the discussed difficulties with respect to the usage of Eq.(3.3-1) and Eq.(3.3-3).

The surface profiles depend on the manufacturing procedure, whether the surface is polished, grinded or has changed due to wear. For example, in **Fig. 3.3-2** the measured profile of a grinded surface is shown. One possibility to describe an equivalent surface is to use the so-called cumulative height distribution of the contact surface with respect to the height of the asperities, see also (Greenwood and Williamson 1966). The cumulative height distribution, shown in **Fig. 3.3-3**, corresponds to the measured surface profile, shown in Fig. 3.3-2.

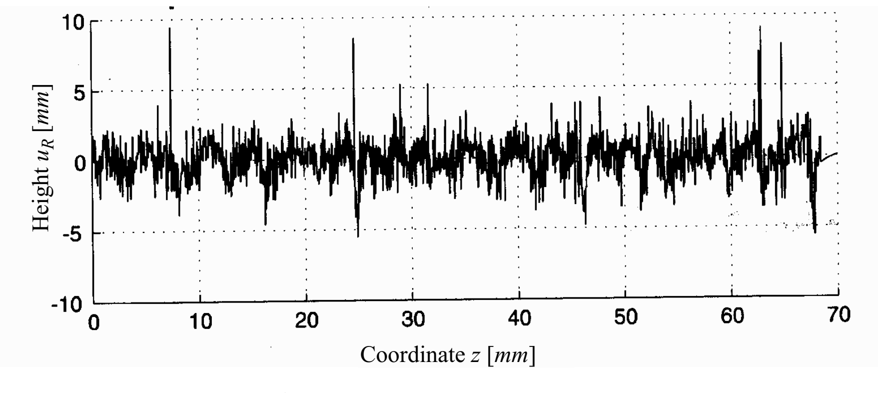

Fig. 3.3-2 Measured surface profile

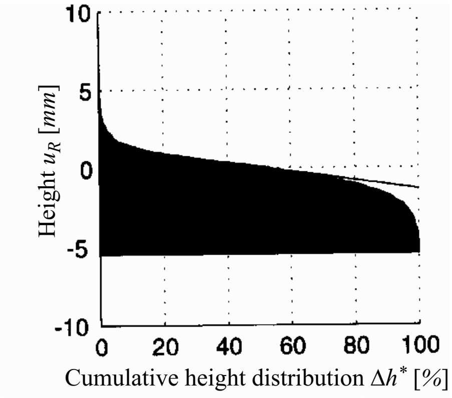

Fig. 3.3-3 Measured cumulative height distribution

Since the measured surface profile is relatively long and no filtering has been applied, the cumulative height distribution includes in general the waviness, see (Warnecke and Dutschke 1984). The measured cumulative height distribution can be approximated by analytical functions and these will be used to develop the contact laws.

The cumulative height distribution, shown in Fig. 3.3-3, can be approximated for example by the following function

$$\Delta h^* = 0 \quad for \quad x^* < 0,$$

$$\Delta h^*(x^*) = 3x^{*2} - 2x^{*3} \quad for \quad 0 \le x^* \le 1,$$

and

$$\Delta h^* = 1 \quad for \quad x^* > 1, \tag{3.3-4}$$

with

$$\Delta h^* = \frac{\Delta h}{\Delta h_0}, \quad x^* = \frac{x}{R_0}, \tag{3.3-5}$$

see **Fig. 3.3-4**. The parameter R_0 can be identified from a surface measurement using for example the least square method or can be approximated by characteristic values of the surface like the peak to valley height R_{max} or the average surface roughness R_Z. With respect to the measured cumulative height distribution, shown above, the peak to valley height R_{max} of the surface is approximately equal to the average surface roughness R_Z, because, here the waviness of the surface is very small. The approximated cumulative height distribution is zero for $x^*=0$ and one (corresponds to 100%) for $x \ge R_Z$. Differentiating Eq.(3.3-4) with respect to the coordinate x^* gives the corresponding normalized probability density function Δp^*,

$$\Delta p^* = 0 \quad for \quad x^* < 0 \quad and \quad x^* > 1$$

and

$$\Delta p^*(x^*) = 6x^*(1 - x^*) \quad for \quad 0 \le x^* \le 1, \tag{3.3-6}$$

see **Fig. 3.3-5**.

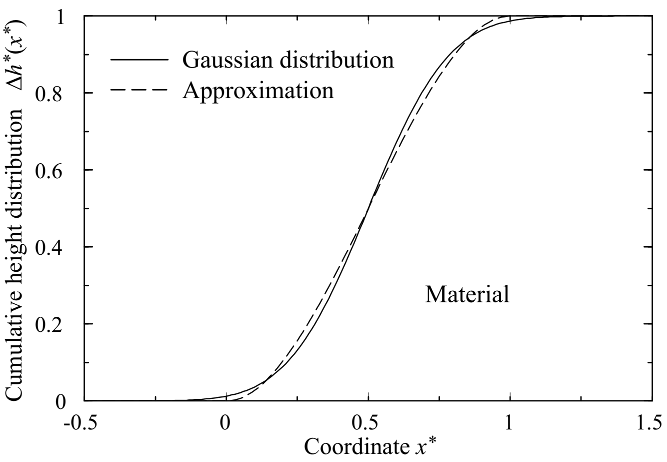

Fig. 3.3-4 Cumulative height distribution

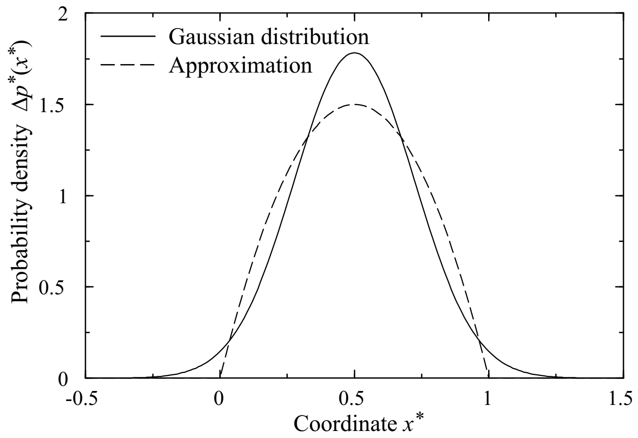

Fig. 3.3-5 Probability density function

Alternatively, the Gaussian distribution can be used to approximate the measured surface data. The difference between the Gaussian distribution and the approximation is relatively small, see Fig. 3.3-4 and Fig. 3.3-5. The mean value and the standard deviation of the Gaussian distribution and the approximation are the same with

$$x_m^* = 0.5, \quad \sigma_x^* = \frac{1}{\sqrt{20}}, \tag{3.3-7}$$

respectively.

Using the Gaussian distribution the possibility to distinguish between separating, piecewise contact and full contact is not given, because in any case, there will be piecewise contact, which does not correspond to the reality. Therefore, from a practical point of view, the approximation given in Eq.(3.3-4) is used in the following.

The contact behavior of two elastic and rough structures can be approximated by a system, where a smooth rigid wall contacts a rough elastic surface, by adjusting the corresponding parameters, see (Johnson 1989). If two elastic surfaces *1* and *2* contact each other, the overall normal and tangential contact stiffnesses are given by

$$\frac{1}{\Delta c_{N0}} = \frac{1}{\Delta c_{N01}} + \frac{1}{\Delta c_{N02}} \tag{3.3-8}$$

and

$$\frac{1}{\Delta c_{R0}} = \frac{1}{\Delta c_{R01}} + \frac{1}{\Delta c_{R02}}\,, \tag{3.3-9}$$

respectively. If two different rough surfaces *1* and *2* are contacting, an equivalent cumulative height distribution can be approximated using the rules of probability by

$$u_R(z) = \sqrt{u_{R1}^2(z) + u_{R2}^2(z)}\,. \tag{3.3-10}$$

If identical functional descriptions of the cumulative height distributions for both surfaces is assumed with

$$\frac{u_{R1}(z^*)}{R_{Z1}} = \frac{u_{R2}(z^*)}{R_{Z2}} = \frac{u_R(z^*)}{R_Z}\,, \tag{3.3-11}$$

and inserting Eq.(3.3-11) in Eq.(3.3-10) gives the equivalent average surface roughness, see (Johnson 1989),

$$R_Z = \sqrt{R_{Z1}^2 + R_{Z2}^2}\,, \tag{3.3-12}$$

to reduce the problem to a smooth rigid surface contacting a rough elastic surface, see **Fig. 3.3-6**.

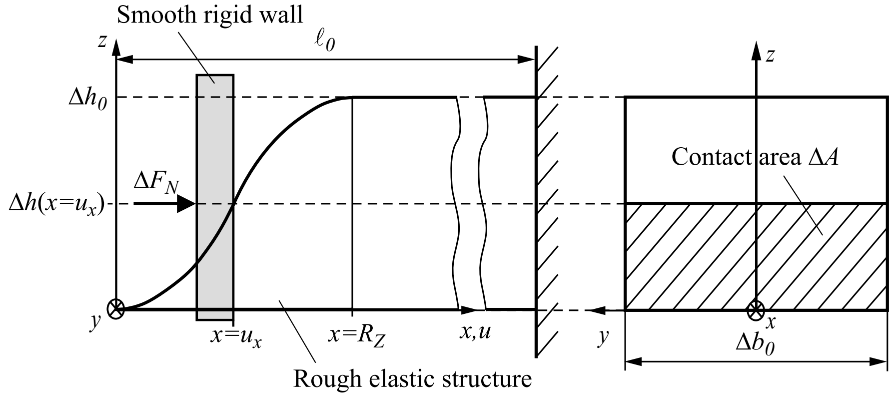

Fig. 3.3-6 Contact model for rough surfaces

The approximation of the cumulative height distribution is placed on top of one elastic element of the elastic foundation. The normal force ΔF_N is applied to the rigid wall. In the depicted case, contact between the rigid wall and the elastic surface exist up to the position $z=\Delta h(x=u_x)$, based on the assumption, that the asperities do act independently on each other, as assumed by Greenwood and Williamson (1966).

With respect to the region where separation takes place, $\Delta h(x=u_x)<z<\Delta h_0$, the lubricant can act onto the wall and the elastic surface and can reduce the normal load applied to the elastic contact. In the following, all physical effects due to the lubricant are neglected. For further information on lubrication, see for example (Bowden and Tabor 1956; Jacobsen 1991; Leudema 1996; Seireg 1996).

The contact area, see Fig. 3.3-6, is given by

$$\Delta A = \Delta h(x = u_x)\Delta b_0 \tag{3.3-13}$$

or in dimensionless form

$$\Delta A^* = \frac{\Delta A}{\Delta A_0} = \Delta h^*(x^* = u_x^*) \quad with \quad \Delta A_0 = \Delta b_0 \Delta h_0 . \tag{3.3-14}$$

Now, one is able to calculate the equivalent normal pressure distribution due to the rough elastic surface from Eq.(3.1-25) with

$$p_N = \frac{\Delta c_{N0}}{\Delta A_0}\left(u_x - u_{Rx}(z)\right), \tag{3.3-15}$$

where u_{Rx} describes the shape of the undeformed equivalent rough contact surface, which has to be calculated iteratively from Eq.(3.3-4). The normalized equivalent pressure distribution is given by

$$p_N^* = u_x^* - u_{Rx}^*(z^*) \tag{3.3-16}$$

with the dimensionless parameters

$$u_x^* = \frac{u_x}{R_Z}, \quad z^* = \frac{z}{\Delta h_0}, \quad p_N^* = \frac{p_N \Delta A_0}{R_Z \Delta c_{N0}} . \tag{3.3-17}$$

In **Fig. 3.3-7** the normalized equivalent pressure distribution for different normal displacements is presented. For example, a normal displacement of $u_x^*=0.5$ leads to a contact area of *50%* of the nominal area. The maximum normal pressure is given from Eq.(3.3-15) at the position $z^*=0$ with

$$p_{N,\max}^* = u_x^* . \tag{3.3-18}$$

The normal contact force for one contact element is given by integration of the normal pressure distribution with respect to the coordinate z

$$\Delta F_N = \Delta b_0 \int_0^{\Delta h(x=u_x)} p_N(z)\; dz . \tag{3.3-19}$$

Inserting Eq.(3.3-15), the relationship

$$\int_0^{\Delta h(x=u_x)} \left(u_x - u_{Rx}(z)\right) dz \quad = \quad \int_{-\infty}^{x=u_x} \Delta h(x)\; dx \tag{3.3-20}$$

and Eq.(3.3-14) give the dimensionless normal contact force

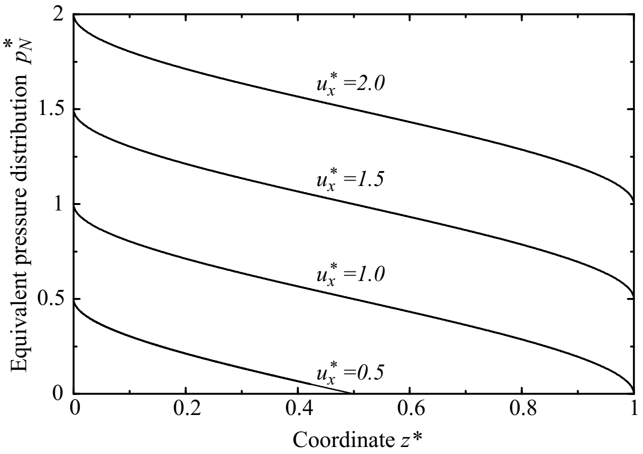

Fig. 3.3-7 Equivalent normal pressure distribution

$$\Delta F_N^* = \int_{-\infty}^{x^*=u_x^*} \Delta h^*(x^*)\,dx^* = \int_{-\infty}^{x^*=u_x^*} \Delta A^*(x^*)\,dx^* \tag{3.3-21}$$

with dimensionless parameters

$$\Delta F_N^* = \frac{\Delta F_N}{\Delta c_{N0} R_Z}, \quad \Delta h^* = \frac{\Delta h}{\Delta h_0}, \quad x^* = \frac{x}{R_Z} \tag{3.3-22}$$

and

$$u_x^* = \frac{u_x}{R_Z}. \tag{3.3-23}$$

Hence, the normal force is proportional to the overlapping volume. Inserting Eq.(3.3-4) in Eq.(3.3-21) gives

$$\begin{aligned} &\Delta F_N^* = 0 \quad for \quad u_x^* < 0, \\ &\Delta F_N^* = u_x^{*3} - \tfrac{1}{2} u_x^{*4} \quad for \quad 0 \le u_x^* \le 1, \\ &\Delta F_N^* = u_x^* - \tfrac{1}{2} \quad for \quad u_x^* > 1. \end{aligned} \tag{3.3-24}$$

In **Fig. 3.3-8**, the nonlinear behavior of the dimensionless normal contact force with respect to the relative normal displacement is shown. For a relative normal displacement of $u_x^*>1$ the behavior is linear, because the complete contact area carries the load and for $u_x^*<0$ separation takes place.

The constitutive contact law described in Eq.(3.3-21) can be used to calculate the normal-force-displacement relationship for any rough contact surface. For example it is possible to recalculate this relationship if wear leads to a change of the cumulative height distribution. Due to different cumulative height distribution the normal force-displacement relationship will change. In the following some basic cumulative height distributions are investigated and applied to the general calculation of the normal contact force described in Eq.(3.3-21).

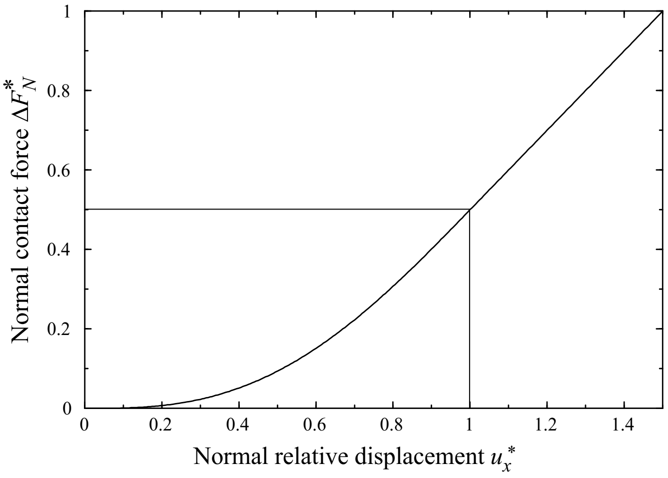

Fig. 3.3-8 Normal force-displacement relationship

For very small relative normal displacements, $u_x^* << 1$, the cumulative height distribution defined in Eq.(3.3-4) can be approximated by

$$\Delta A^*(x^*) = 3x^{*2} .$$

Then Eq.(3.3-24) used to calculate the normal contact force reduces to

$$\Delta F_N^* = u_x^{*3} \qquad (3.3\text{-}25)$$

or with Eq.(3.3-22) and Eq.(3.3-23)

$$\frac{\Delta F_N}{\Delta c_{N0} R_Z} = \left(\frac{u_x}{R_Z} \right)^3 . \qquad (3.3\text{-}26)$$

Comparing Eq.(3.3-26) with Eq.(3.3-3) leads to an exponent of $k=3$ as described in the introduction. Furthermore, the parameter of the contact law can be identified to

$$F_{NS} = \Delta c_{N0} R_Z \qquad (3.3\text{-}27)$$

and

$$u_{NS} = R_Z , \quad u_N = u_x , \quad u_{N0} = 0 . \qquad (3.3\text{-}28)$$

Hence, the physical interpretation of the empirical contact laws is given. Assuming a cumulative height distribution, which is linearly dependent on the x-coordinate with

$$\Delta A(x^*) = x^* , \quad 0 \le x^* \le 1 \qquad (3.3\text{-}29)$$

results in a parabolic function for the normalized normal contact force using Eq.(3.3-21)

$$\Delta F_N^* = \frac{1}{2} u_x^{*2} , \quad 0 \le u_x^* \le 1 \qquad (3.3\text{-}30)$$

or

$$\frac{2\Delta F_N}{\Delta c_{N0}R_Z}=\left(\frac{u_x}{R_Z}\right)^2, \qquad (3.3\text{-}31)$$

see Fig. 3.3-1 with $k=2$. If the roughness is set to be zero, which corresponds to

$$\Delta A^*(x^*)=1, \qquad (3.3\text{-}32)$$

the penalty approach is modeled by

$$\Delta F_N=\Delta c_{N0}u_x, \qquad (3.3\text{-}33)$$

see Fig. 3.3-1 with $k=1$. If the cumulative height distribution is given by the exponential function

$$\Delta A^*(x^*)=e^{4\left(x^*-1\right)} \qquad (3.3\text{-}34)$$

the normal force can be calculated with

$$\Delta F_N^*=\tfrac{1}{4}e^{4\left(u_x^*-1\right)} \qquad (3.3\text{-}35)$$

or

$$\frac{4\Delta F_N}{\Delta c_{N0}R_Z}=e^{4\left(\frac{u_x-R_Z}{R_Z}\right)}, \qquad (3.3\text{-}36)$$

see Fig. 3.3-1. Combining Eq.(3.3-34) and Eq.(3.3-35), here the contact normal force is proportional to the contact area and is given by

$$\Delta F_N^*=\frac{1}{4}\Delta A^*(u_x^*), \qquad (3.3\text{-}37)$$

see also (Johnson 1989). Hence, with the described contact model all relevant contact laws can be derived.

The tangential contact force in the z-direction is calculated by integrating the shear stress distribution with

$$\Delta F_T=\Delta b_0\int\limits_0^{\Delta h(x=u_x)}\tau_{Tz}\quad dz. \qquad (3.3\text{-}38)$$

Inserting the corresponding shear stress of Eq.(3.1-25) and integrating gives

$$\Delta F_T=\frac{\Delta c_{R0}}{\Delta A_0}\Delta b_0\Delta h\left(x=u_x\right)w_P=\Delta c_{R0}\Delta A^*(u_x^*)w_P. \qquad (3.3\text{-}39)$$

Differentiating Eq.(3.3-39) with respect to the displacement w_P gives the tangential contact stiffness

$$\Delta c_R^*=\Delta A^*(x^*=u_x^*)=\Delta h^*(x^*=u_x^*) \qquad (3.3\text{-}40)$$

with Eq.(3.3-14) and

$$\Delta c_R^*=\frac{\Delta c_R}{\Delta c_{R0}}. \qquad (3.3\text{-}41)$$

Hence, the tangential contact stiffness for one area element is proportional to the contact area, but is nonlinearly dependent on the relative normal displacement. Hence, the tangential stiffness dependent is nonlinear dependent on the normal contact force as shown in **Fig. 3.3-9**. Due to the developed contact model, the contact stiffnesses of a rough surface are identical in the y- and z-direction and, hence, the modeled contact behavior is isotropic. The limiting value of the dimensionless contact stiffness of one is reached, if the contact area is identical to the nominal contact area.

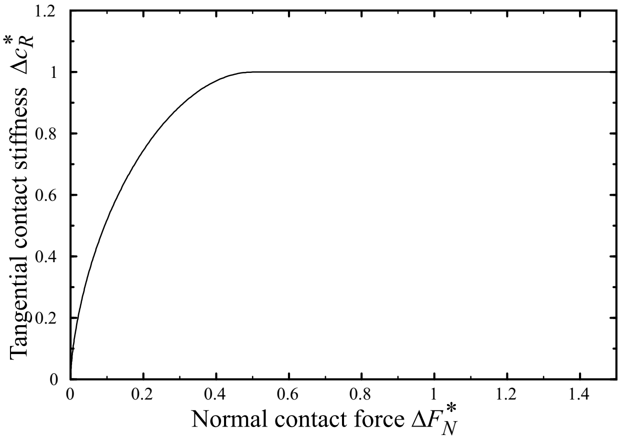

Fig. 3.3-9 Tangential contact stiffnesses

3.4 Hyperbolic Contact Laws for Rough Surfaces

The above-described analysis holds only, if the relative normal displacements are small. If the normal deformations are relative large, then the length of one deformed strip has to be used for the calculation of the contact forces as described in Chapter 3.1, see Eq.(3.1-12). The deformed length of a contact element is given by

$$\ell = \ell_0 - u_x \, , \qquad (3.4\text{-}1)$$

see Fig. 3.1-1. If the average roughness is identical to zero, the normal force-displacement relationship is given by

$$\Delta F_N = \frac{\Delta c_{N0} u_x}{1 - \dfrac{u_x}{\ell_0}} \qquad (3.4\text{-}2)$$

using Eq.(3.1-15). The deformed length can be normalized

$$\ell^* = 1 - R_Z^* u_x^* \qquad (3.4\text{-}3)$$

with

$$\ell^* = \frac{\ell}{\ell_0}, \quad R_Z^* = \frac{R_Z}{\ell_0}, \quad u_x^* = \frac{u_x}{R_Z} \, . \qquad (3.4\text{-}4)$$

As described in Chapter 3.3 the recalculation of the normal contact force for large deformations including the effect of roughness gives the constitutive law

$$\Delta F_{NL}^{*} = \frac{\Delta F_N^{*}(u_x^{*})}{\ell^{*}} = \frac{\Delta F_N^{*}(u_x^{*})}{1 - R_Z^{*} u_x^{*}} \qquad (3.4\text{-}5)$$

using of Eq.(3.3-24).

In **Fig. 3.4-1**, the influence of the normalized roughness R_Z^{*} onto the normal contact force-displacement relationship is depicted. For $R_Z^{*} << 1$, the normal force-displacement relationship is identical to the relationship shown in Fig. 3.3-8. In the limit, the nominal length ℓ_0 is identical to the roughness R_Z, which corresponds to $R_Z^{*}=1$. Then, the normal contact force is identical to infinite, if the relative displacement u_x is equal to the value of R_Z or $u_x^{*}=1$. This normal force-displacement relationship would have been used, if an infinite number of modes is used to describe the elasticity of the contacting bodies completely.

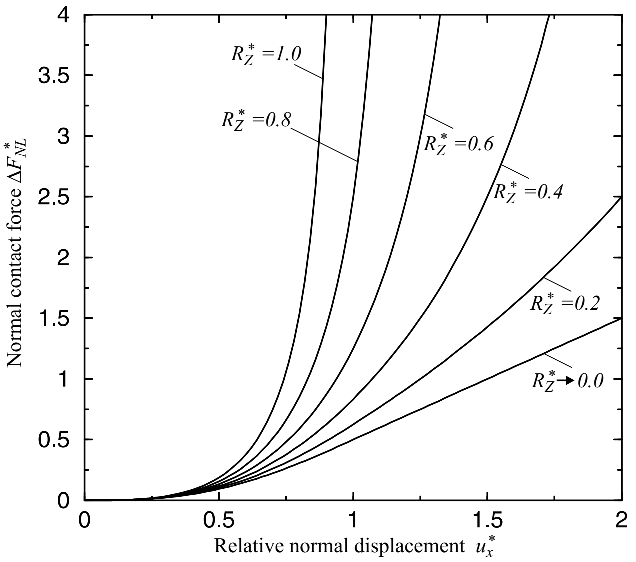

Fig. 3.4-1 Normal force-displacement relationship for large displacements

The recalculation of the tangential contact stiffness for large deformations gives the constitutive law

$$\Delta c_{RL}^{*} = \frac{\Delta c_R^{*}(u_x^{*})}{\ell^{*}} = \frac{\Delta c_R^{*}(u_x^{*})}{1 - R_Z^{*} u_x^{*}} \qquad (3.4\text{-}6)$$

with Eq.(3.3-40). In **Fig. 3.4-2**, **t**he corresponding tangential stiffness for large deformations versus the normal contact force is shown. If the normalized roughness is increased, then the tangential contact stiffness increases as well. If the deformation are relative large, the developed constitutive contact laws in Eq.(3.4-5) and Eq.(3.4-6) can be applied. The physical validation of these contact laws is verified in the next Chapter, where it is assumed that the deformations are relative small and that the roughness compared to the undeformed length is very small.

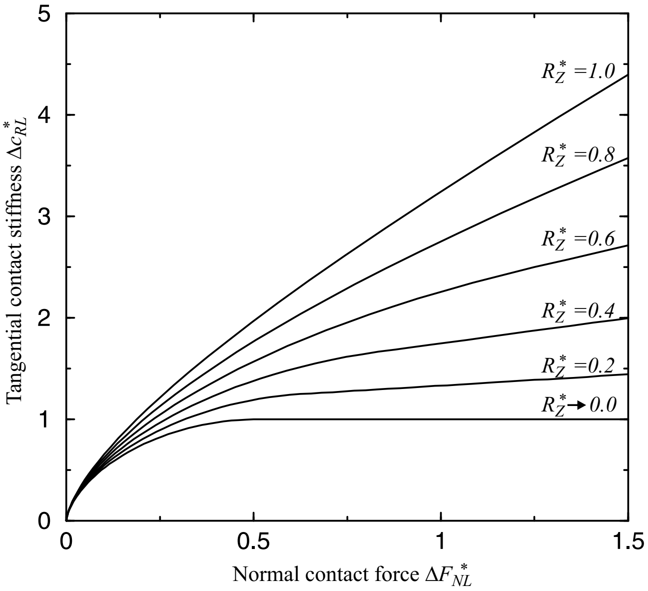

Fig. 3.4-2 Tangential contact stiffnesses for large displacements

3.5 Experimental Validation of the Contact Laws

In (Treyde 1995), two beams contacting each other at the tip are used to identify the normal force-displacement relationship and the tangential contact stiffness. The corresponding experimental setup is shown in **Fig. 3.5-1**, where an electromagnetic shaker has been used to excite the first and second vibration mode to identify the bending and the tangential contact stiffnesses, respectively. The normal force-displacement relationship was identified by applying a static normal load using weights and measuring the relative normal displacement with a laser vibrometer, which is not shown in the figure.

Fig. 3.5-2 shows the comparison of measured, see (Treyde 1995), and calculated normal contact forces versus the normal displacements using the cumulative height distribution defined by Eq.(3.3-4). Due to the experimental setup the following data for the normal contact stiffness and the average surface roughness are used $c_{N0}=240.0\ 10^6$ [N/m] and $R_Z=12.0$ [μm].

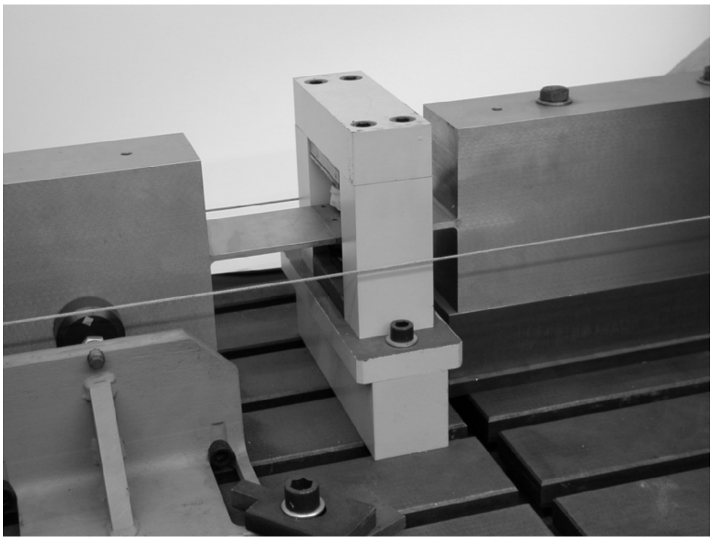

Fig. 3.5-1 Experimental setup with two beams

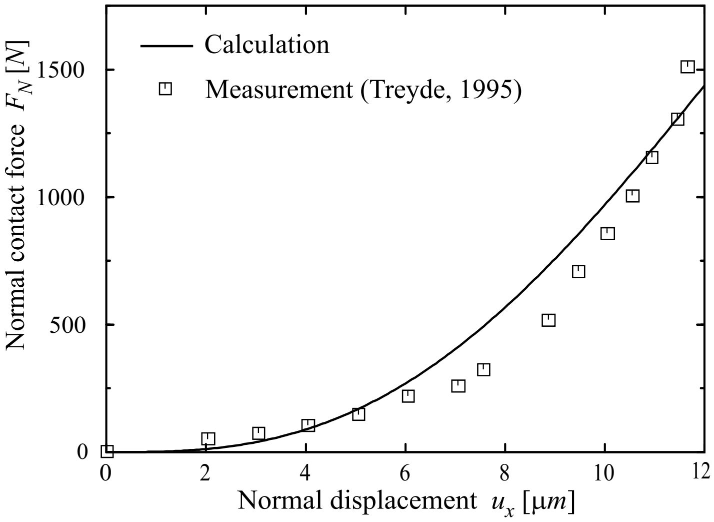

Fig. 3.5-2 Comparison of measurement and calculation due to the normal force-displacement relationship

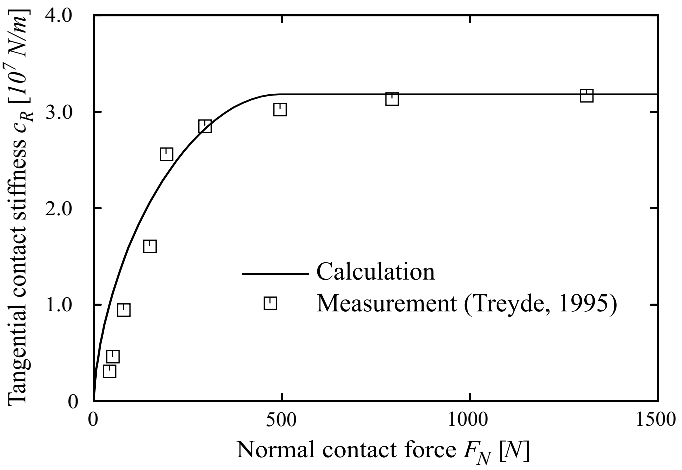

Fig. 3.5-3 Comparison of measurement and calculation due to the tangential contact stiffness

In **Fig. 3.5-3**, the calculated tangential stiffness is compared with identified values, see (Treyde 1995). The contact parameters used for the calculation are $c_{N0}=82.5\ 10^6$ [N/m], $R_Z=12.0$ [μm] and $c_{R0}=31.7\ 10^6$ [N/m]. One reason for the differences between the measurements and the calculations is due to the used theoretical cumulative height distribution, which reflects the reality only approximately. Nevertheless, both comparisons between measurement and calculation show a relative good agreement.

3.6 Friction Characteristics

The friction coefficient can depend on system parameters like the relative velocity and the normal force; this is called the friction characteristic. Different friction characteristics used in the literature are summarized in (Kragelski et al. 1982; Stelter 1990; Hinrichs 1997a), see also Fig. 1.2-1.

In (Hinrichs 1997a), a test stand for the identification of friction characteristics is used, see **Fig. 3.6-1**. For the identification of the friction characteristic, the work piece is pressed onto the disc by dead weights, which are not shown in the Figure. The friction and normal forces are measured directly by a three-component force transducer. The displacement and the velocity are measured by a laser vibrometer. The friction force and the normal contact force can be measured simultaneously very close to the contact area. From here, it is possible to calculate the friction coefficient for different constant relative velocities and normal loads. A more detailed explanation of the test stand is given in Chapter 4 and in (Popp et al. 1996).

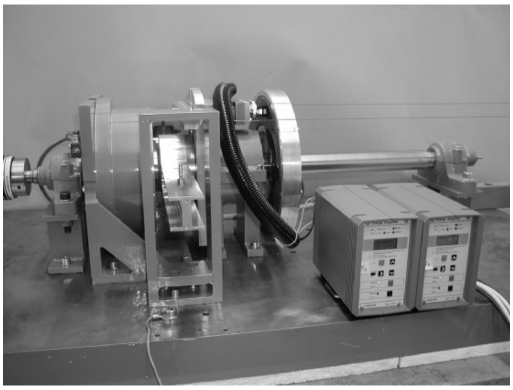

Fig. 3.6-1 Experimental setup

In (Lindner et al. 2004), (Moldenhauer et al. 2005) and (Sextro et al. 2006) a friction model for rubber is developed, where the calculated friction coefficients are compared by the identified friction coefficients. Within the theory, hysteretic and adhesive contact forces are modeled including the influence of temperature. The hysteretic friction of rubber originates from internal material damping caused by the deformation during sliding across the rough surface. The temperature influences the dynamic properties of the material significantly as it is formulated in the well-known WLF-equation (Williams et al. 1955). A modified theory of Achenbach is used to model adhesion friction, see (Achenbach et al. 2001 and 2003), which are based on molecular binding forces. **Fig. 3.6-2** depicts the measured friction coefficient, the hysteresis and adhesion simulation and the corresponding superposition. The measurements show an explicit maximum at a relative velocity of about v = 200 mm/s. In a higher velocity range the friction coefficient falls due to the hysteretic friction. Up to a velocity of 20 mm/s the friction coefficient decreases which can result from adhesion friction. The comparison of the simulations with the experiments is very good. These results from local rubber friction investigations can be used as an input for larger systems like tread blocks as a part of tyres.

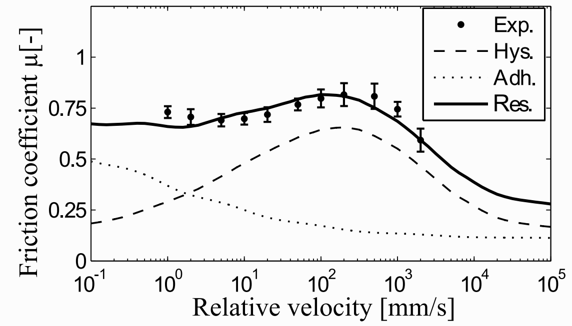

Fig. 3.6-2 Friction characteristic rubber-grinding paper

It appears that the friction coefficient is not stationary and depends on time even for stationary experimental conditions. This physical effect is explained in (Hinrichs 1997a) by the brush model, where for a constant relative velocity two asperities lose contact and both will find new contacts and then will lose contact again and so on. Using the Gaussian distribution the mean value and the standard deviation of the friction coefficient are calculated from measured normal and tangential contact forces. These values are shown in **Fig. 3.6-3** for the contact: steel-brass. It was observed that the identified friction coefficient has a negative slope with respect to the relative velocity v_r. In the following, the phenomenon of a decreasing characteristic with respect to the relative velocity will be analyzed from a theoretical point of view.

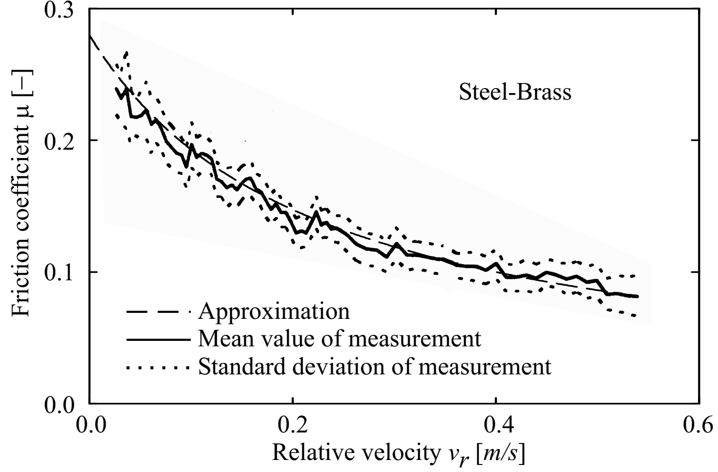

Fig. 3.6-3 Friction coefficient versus relative velocity

In case of the hydrostatic pressure distribution ($i=2$), see Chapter 3.1, assuming Coulomb friction, constant pressure distribution and solving Eq.(3.1-31) with Eq.(3.1-28) for the friction coefficient gives

$$\mu = \frac{\tau_S}{p_N}, \tag{3.6-1}$$

see also (Holland and Rick 1997). Assuming a linear temperature dependency of the shear strength of steel with

$$\tau_S(\Delta T) = \tau_{S0}\left(1 - \frac{\Delta T}{\Delta T_E}\right), \quad \frac{\Delta T}{\Delta T_E} < 1, \tag{3.6-2}$$

where ΔT denotes the temperature relative to the room temperature, ΔT_E defines the slope of the temperature dependency and τ_{S0} the shear strength at room temperature. Inserting Eq.(3.6-2) in Eq.(3.6-1), then the friction coefficient is given by

$$\mu(\Delta T) = \mu_0\left(1 - \frac{\Delta T}{\Delta T_E}\right) \tag{3.6-3}$$

with

$$\mu_0 = \mu(\Delta T = 0) = \frac{\tau_{S0}}{p_N}. \tag{3.6-4}$$

In the following, the effect of temperature within the contact region and its influence onto the friction coefficient characteristic is investigated. In general, the heat transfer equation has to be used to calculate the temperature distribution. Here, the average temperature within the contact area is approximated to be proportional to the distributed heat source, see (Johnson 1989),

$$\Delta T = T_m - T_0 = k_T q_H\,, \tag{3.6-5}$$

with the heat source q_H per unit area. To derive the distributed heat source, it is necessary to investigate the energy balance for a stationary process assuming a constant relative velocity. In this case, the deformation energy does not influence the energy balance.

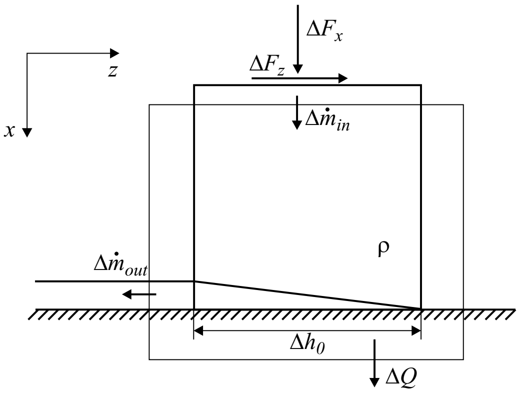

Fig. 3.6-4 Energy balance for one mass element

The work done to a mass element sliding on a smooth rigid plane, see **Fig. 3.6-4**, which moves with the constant velocity v_z, is equal to heat

$$\Delta W_x + \Delta W_z = \Delta Q \tag{3.6-6}$$

with the work done of both external forces

$$\Delta W_x = \Delta F_x u_x, \quad \Delta W_z = \Delta F_z u_z \tag{3.6-7}$$

and the heat ΔQ. All other energy sources are neglected and likewise the influence of the worn material is neglected. Equilibrium for the mass element and assuming Coulomb friction yields

$$\Delta F_x = \Delta F_N = const., \quad \Delta F_z = \mu \Delta F_N = const. \tag{3.6-8}$$

For a stationary process, the velocities are assumed constant,

$$\dot{u}_x = v_x = const., \quad \dot{u}_z = v_z = v_r = const. \tag{3.6-9}$$

with the relative velocity v_r. Using Eq.(3.6-7), Eq.(3.6-8) and Eq.(3.6-9) and differentiating Eq.(3.6-6) with respect to time gives

$$\Delta \dot{Q} = \Delta F_N v_x + \mu \Delta F_N |v_r|\,. \tag{3.6-10}$$

The heat source is identical to the distributed heat flow, hence,

$$q_H = \frac{\Delta\dot{Q}}{\Delta A_0} = \mu p_N |v_r| + p_{N0} v_x \tag{3.6-11}$$

with the normal pressure

$$p_N = \frac{\Delta F_N}{\Delta A_0}, \quad \Delta A_0 = \Delta b_0 \Delta h_0 . \tag{3.6-12}$$

Assuming that the velocity in the x-direction is relatively small

$$\frac{v_x}{\mu v_r} << 1 , \tag{3.6-13}$$

which corresponds to a small wear rate. Then, the average heat source can be approximated by the distributed frictional power

$$q_H \approx \frac{\Delta P_R}{\Delta A_0} = \mu p_N |v_r| . \tag{3.6-14}$$

Inserting Eq.(3.6-14) in Eq.(3.6-5) and Eq.(3.6-5) in Eq.(3.6-3) and solving for the friction coefficient gives

$$\mu(v_r) = \frac{\mu_0}{1 + p_v |v_r|} , \tag{3.6-15}$$

with the normalized pressure parameter

$$p_v = \frac{k_T \mu_0 p_N}{\Delta T_E} . \tag{3.6-16}$$

Fig. 3.6-3 shows additionally the comparison of Eq.(3.6-15) with a friction coefficient at zero relative velocity of $\mu_0=0.28$, the parameter $1/p_v=0.22\ m/s$ and assuming the hydrostatic pressure distribution with $s_i=s_2=1$. This comparison shows a good agreement. From Eq.(3.6-15) the dependency of the friction coefficient with respect to the load, kinematics, material and geometry parameters of the contact bodies are described. If the contact is complex with regard to these parameters, a common method is to identify the friction coefficient within a stationary process by an experimental setup with respect to the normal load and the relative velocity, see again (Hinrichs 1997a).

The influence of a viscous fluid can be approximated by Newtons law for laminar flow. The shear stress is given by

$$\tau_F = \eta \frac{dv}{dx} \tag{3.6-17}$$

with the viscosity η, which is dependent on temperature. Applying this rule to the developed contact model gives

$$\frac{dv}{dx} \approx \frac{v_r}{x - u_x} \tag{3.6-18}$$

with the relative velocity v_r, which is assumed to be constant. The additional shear force due to the fluid is given by

$$\Delta F_F = \Delta b_0 \int_{\Delta h(x=u_x)}^{\Delta h_0} \tau_F \, dz \,. \tag{3.6-19}$$

The tangential force due to friction is given by

$$\Delta F_R = \Delta b_0 \int_0^{\Delta h(x=u_x)} \mu(T) p_N(z) \, dz \,. \tag{3.6-20}$$

Again, it is assumed that the friction coefficient decreases linear with the temperature independently from the normal pressure, see Eq.(3.6-3). Using the Eq.(3.3-6), Eq.(3.3-24), Eq.(3.6-5) and Eq.(3.6-14) the equivalent friction coefficient can be calculated by

$$f^* = \frac{\Delta F_R + \Delta F_F}{\mu_0 \Delta F_N} =$$

$$\frac{1}{\Delta F_N^*(u_x^*)} \int_0^{u_x^*} \frac{(u_x^* - x^*) p(x^*)}{1 + v_r^*(u_x^* - x^*)} dx^* + \frac{\eta^* v_r^*}{\Delta F_N^*(u_x^*)} \int_{u_x^*}^{1} \frac{p(x^*)}{(x^* - u_x^*)} dx^* \tag{3.6-21}$$

with

$$v_r^* = \frac{\mu_0 k_T R_Z \Delta c_{N0}}{\Delta T_E \Delta A_0} v_r \,, \quad \eta^* = \frac{\Delta A_0^2 \Delta T_E}{k_T \mu_0^2 \Delta c_{N0}^2 R_Z^3} \eta \tag{3.6-22}$$

In **Fig. 3.6-5**, the equivalent friction coefficient is shown versus the relative velocity varying the normal displacement which corresponds to a normal force. If the rough surface is compressed ($u^*=1$) no tangential forces due to the fluid act onto the body. In this case, the equivalent friction characteristic decreases with respect to the relative velocity. Reducing the normal displacement, the friction coefficient increases with increasing velocity.

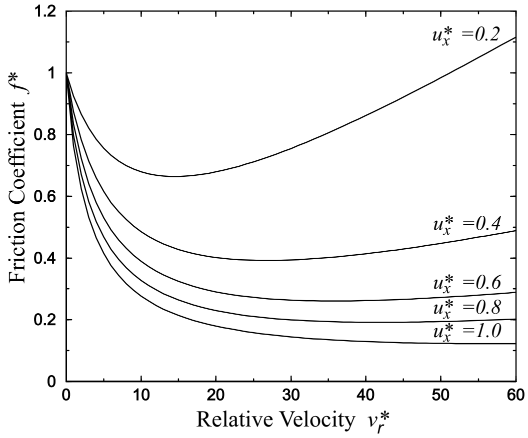

Fig. 3.6-5 Equivalent friction coefficient

3.7 Three-dimensional Point Contact Element

Within this Chapter, the results of the previous investigations are summarized to a single point contact element. One contact element is shown in **Fig. 3.7-1**. The contact element can be reduced to a simplified point contact model shown in **Fig. 3.7-2**, where **a)** shows the normal and **b)** the tangential point contact model. The elasticity of the point contact is modeled by springs with the tangential stiffness Δc_R the normal stiffness Δc_N. The point P is the position of the point mass Δm_D. Dry friction occurs at the point P with the friction coefficient $\mu(v_r)$, which is dependent on the relative velocity $v_r = v_P$. The normal contact force ΔF_N acts perpendicular to the y,z-contact plane. The friction force ΔF_R acts opposite to the velocity of the point P. For a given motion of the point M in the y,z-contact plane and the displacement of the point N in x-direction, the corresponding motion of the point P and the friction forces can be calculated. Here, the equivalent pressure distribution is approximated by an average contact pressure, which means microslip effects are not included in this investigation. In the following, the equation of motion of the point mass will be derived and the point contact element will be investigated by parameter studies.

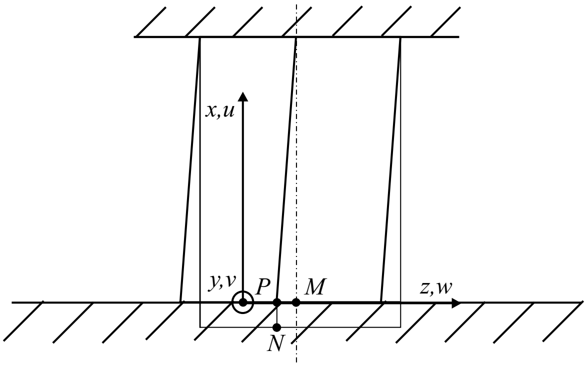

Fig. 3.7-1 Contact element

The displacements of the points M, N and P are:

$$\begin{aligned} \boldsymbol{r}_M &= \left[x_M, y_M, z_M\right]^T, \\ \boldsymbol{r}_N &= \left[x_N, y_N, z_N\right]^T, \\ \boldsymbol{r}_P &= \left[x_P, y_P, z_P\right]^T \end{aligned} \tag{3.7-1}$$

with

$$x_M = x_P, \quad y_N = y_P, \quad z_N = z_P \,. \tag{3.7-2}$$

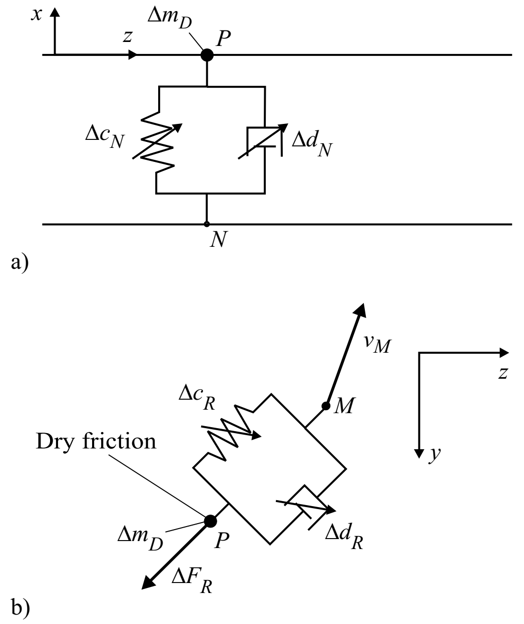

Fig. 3.7-2 Point contact model **a**) normal and **b**) tangential contact model

The displacements x_N, y_M and z_M are assumed to be given depending on the time. The three coordinates of the point P and the corresponding velocities are calculated by Newton's law. The equation of motion is given by

$$\Delta m_D \ddot{\boldsymbol{r}}_P = \Delta \boldsymbol{F}_C + \Delta \boldsymbol{F}_S + \Delta \boldsymbol{F}_D , \tag{3.7-3}$$

where Δm_D denotes the reduced point mass, $\Delta \boldsymbol{F}_C$ the contact force, $\Delta \boldsymbol{F}_S$ the spring force and $\Delta \boldsymbol{F}_{SD}$ additionally damping forces.

Using Eq.(3.3-14) for calculating the contact area, the resultant mass Δm_R involved is given by

$$\Delta m_R (u_x) = \Delta A(u_x) \rho_0 \ell_0 , \tag{3.7-4}$$

where ρ_0 denotes the density and ℓ_0 the depth of the undeformed elastic foundation. Inserting Eq.(3.3-14) in Eq.(3.7-4) gives

$$\Delta m_R (u_x) = h^* \rho_0 \Delta A_0 \ell_0 \tag{3.7-5}$$

with the abbreviation

$$h^* = \Delta h^* (u_x^*) . \tag{3.7-6}$$

The reduced point mass Δm_D is assumed to be proportional to the resultant mass by

$$\Delta m_D = \gamma \Delta m_R \tag{3.7-7}$$

with the proportionality factor γ as defined in Eq.(3.2-27). Inserting Eq.(3.7-5) in Eq.(3.7-7) gives

$$\Delta m_D = \gamma \Delta m_{R0} h^* \tag{3.7-8}$$

with

$$\Delta m_{R0} = \rho_0 \Delta A_0 \ell_0 \,. \tag{3.7-9}$$

The approximation of the reduced point mass holds only if the excitation angular frequency ω_0 of the system is relatively low, compared to the eigenfrequencies of the contact for the normal and tangential direction

$$\omega_0 << \min\left\{\sqrt{\frac{\Delta c_{N0}}{\Delta m_{D0}}}, \sqrt{\frac{\Delta c_{R0}}{\Delta m_{D0}}}\right\}, \tag{3.7-10}$$

see Chapter 3.2. In Eq.(3.7-3) the contact force $\Delta \boldsymbol{F}_C$ is defined by

$$\Delta \boldsymbol{F}_C = \left[\Delta F_N, \quad \Delta F_{Ry}, \quad \Delta F_{Rz}\right]^T \tag{3.7-11}$$

with the normal contact force ΔF_N and the friction forces ΔF_{Ry} and ΔF_{Rz} in the y- and z-direction, respectively. Assuming dry friction, the friction forces are given by

$$\Delta F_{Ry} = -\mu(v_P)\Delta F_N \frac{\dot{y}_P}{v_P}, \tag{3.7-12}$$

$$\Delta F_{Rz} = -\mu(v_P)\Delta F_N \frac{\dot{z}_P}{v_P} \tag{3.7-13}$$

with the relative velocity

$$v_P = \sqrt{\dot{y}_P^2 + \dot{z}_P^2} \,. \tag{3.7-14}$$

Due to the anisotropic rolling contact, the tangential contact stiffnesses in the y- and z-direction have to be introduced. Using the following abbreviation

$$f^* = \Delta F_N^*(u_x^*), \tag{3.7-15}$$

the spring force is given by

$$\boldsymbol{F}_S = \left[-\Delta c_{N0} R_Z f^*, \quad \Delta c_{R0y} h^* u_y, \quad \Delta c_{R0z} h^* u_z\right]^T, \tag{3.7-16}$$

see Eq.(3.3-24) and Eq.(3.3-40), assuming non-isotropic contact behavior in y- and z-direction with respect to the nominal tangential contact stiffnesses. The relative displacements in the normal and tangential directions are given by

$$\boldsymbol{u}_S = \left[u_x, \quad u_y, \quad u_z\right]^T = \left[x_P - x_N, \quad y_M - y_P, \quad z_M - z_P\right]^T. \tag{3.7-17}$$

The internal damping force is approximated by

$$\boldsymbol{F}_D = \beta\, \dot{\boldsymbol{F}}_S = \beta\, h^* \left[-\Delta c_{N0} \dot{u}_x, \quad \Delta c_{R0y} \dot{u}_y, \quad \Delta c_{R0z} \dot{u}_z\right]^T, \tag{3.7-18}$$

where second and higher order terms have been neglected, see also (Hunt and Crossley 1975). Inserting Eq.(3.7-11), Eq.(3.7-16) and Eq.(3.7-18) in Eq.(3.7-3) leads to the nonlinear coupled differential equations of motion:

$$\begin{aligned} \Delta m_{D0} h^{*} \ddot{x}_P &= \Delta F_{Fx} + \Delta F_N \\ \Delta m_{D0} h^{*} \ddot{y}_P &= \Delta F_{Fy} - \mu(v_P) \Delta F_N \frac{\dot{y}_P}{v_P} \\ \Delta m_{D0} h^{*} \ddot{z}_P &= \Delta F_{Fz} - \mu(v_P) \Delta F_N \frac{\dot{z}_P}{v_P} \end{aligned} \tag{3.7-19}$$

with the viscous elastic force in normal direction

$$\Delta F_{Fx} = -\Delta c_{N0} R_Z f^{*} - \beta \Delta c_{N0} h^{*} \dot{u}_x \tag{3.7-20}$$

and the viscous elastic tangential forces

$$\Delta F_{Fy} = \Delta c_{R0y} h^{*} u_y + \beta \Delta c_{R0y} h^{*} \dot{u}_y \tag{3.7-21}$$

and

$$\Delta F_{Fz} = \Delta c_{R0z} h^{*} u_z + \beta \Delta c_{R0z} h^{*} \dot{u}_z \,. \tag{3.7-22}$$

If the point mass gets in contact with a rigid surface, the position of the point *P* in normal direction is given and the normal force is larger than zero

$$x_P = 0, \quad F_N > 0. \tag{3.7-23}$$

Then, from Eq.(3.7-19) the normal force can be calculated with

$$\Delta F_N = -\Delta F_{Fx} \,. \tag{3.7-24}$$

If separation takes place, the equation of motion is fulfilled, since $f^{*}=h^{*}=0$ and therefore the normal contact force vanishes, hence

$$x_P > 0, \quad \Delta F_N = 0. \tag{3.7-25}$$

Combining Eq.(3.7-23) and Eq.(3.7-25) leads to the so-called complementary equation

$$\Delta F_N x_P = 0, \tag{3.7-26}$$

see (Pfeiffer and Glocker 1996). In case of separation the equation of motion is fulfilled in any case, since $f^{*}=h^{*}=0$. Therefore, in this case it is assumed that the velocity of the point *P* is identical to the point *M* and, hence, the accelerations of both points are identical

$$\ddot{\boldsymbol{r}}_P = \ddot{\boldsymbol{r}}_M \,. \tag{3.7-27}$$

In case of contact, the equation of motion can be transformed to

$$\begin{aligned} \Delta m^{*}_{D0} h^{*} y''^{*}_P &= \Delta F^{*}_{Fy} - \mu^{*}(v^{*}_P) \Delta F^{*}_N \frac{y'^{*}_P}{v^{*}_P}, \\ \Delta m^{*}_{D0} h^{*} z''^{*}_P &= \Delta F^{*}_{Fz} - \mu^{*}(v^{*}_P) \Delta F^{*}_N \frac{z'^{*}_P}{v^{*}_P} \end{aligned} \tag{3.7-28}$$

with the dimensionless time

$$t^{*} = \omega_0 t \,, \tag{3.7-29}$$

the dimensionless normal contact force

$$\Delta F^{*}_N = \begin{cases} 0 & for \quad f^{*} + \beta^{*} h^{*} u'^{*}_x < 0 \\ f^{*} + \beta^{*} h^{*} u'^{*}_x & for \quad f^{*} + \beta^{*} h^{*} u'^{*}_x \geq 0 \end{cases} \tag{3.7-30}$$

to ensure positive normal contact forces and the dimensionless tangential forces

$$\Delta F_{Fy}^{*} = \Delta c_{R0y}^{*} h^{*} u_y^{*} + \beta^{*} \Delta c_{R0y}^{*} h^{*} u_y'^{*} \tag{3.7-31}$$

and

$$\Delta F_{Fz}^{*} = \Delta c_{R0z}^{*} h^{*} u_z^{*} + \beta^{*} \Delta c_{R0z}^{*} h^{*} u_z'^{*} , \tag{3.7-32}$$

the differentiation with regard to the dimensionless time

$$y' = \frac{dy}{dt^{*}} = \frac{dy}{\omega_0 dt} = \frac{1}{\omega_0} \dot{y}, \quad z' = \frac{1}{\omega_0} \dot{z} , \tag{3.7-33}$$

the normalized displacement

$$y_P^{*} = \frac{y_P}{R_Z}, \quad z_P^{*} = \frac{z_P}{R_Z} \tag{3.7-34}$$

and the following normalized parameter

$$\Delta m_{D0}^{*} = \frac{\Delta m_{D0} \omega_0^2}{\mu_0 \Delta c_{N0}} , \tag{3.7-35}$$

$$\Delta F_{Fy,z}^{*} = \frac{\Delta F_{Fy,z}}{\mu_0 \Delta c_{N0} R_Z}, \quad \Delta F_N^{*} = \frac{\Delta F_N}{\Delta c_{N0} R_Z} , \tag{3.7-36}$$

$$\Delta F_{Ry,z}^{*} = \frac{\Delta F_{Ry,z}}{\mu_0 \Delta c_{N0} R_Z} , \tag{3.7-37}$$

$$\mu^{*} = \frac{\mu}{\mu_0} , \tag{3.7-38}$$

$$v_P^{*} = \frac{v_P}{\omega_0 R_Z} , \tag{3.7-39}$$

$$\Delta c_{R0y,z}^{*} = \frac{\Delta c_{R0y,z}}{\mu_0 \Delta c_{N0}} \tag{3.7-40}$$

and

$$\beta^{*} = \omega_0 \beta . \tag{3.7-41}$$

The formulation of a non-smooth multi-contact problem leads to a combinatorial problem, which has to be solved to determine the status of each single contact, whether it separates, sticks or slides, see (Glocker 1995; Pfeiffer and Glocker 1996). In case of a multi-contact problem, an alternative method is to smooth the friction law by an *arctan*-function for example. Including the normal contact elasticity with Eq.(3.7-30), the system equations are invariant, that means that the number of degrees of freedom do not change with time. From a numerical point of view, this is an advantage and is used in the following. The friction characteristic defined in Eq.(3.6-15) can be normalized with

$$\mu^{*} = \frac{1}{1 + p_v^{*} \,|\, v_P^{*} \,|} s^{*}(v_P^{*}) , \tag{3.7-42}$$

where the following smoothing function is used

$$s^*(v_P^*) = \frac{2}{\pi}\arctan(k_S^* v_P^*)\,. \qquad (3.7\text{-}43)$$

The parameter k_S define the slope at zero relative velocity. The dimensionless parameter used are given by

$$k_S^* = k_S\omega_0 R_Z, \quad p_v^* = p_v\omega_0 R_Z\,. \qquad (3.7\text{-}44)$$

Due to the definition of a smoothing function exact sticking of the point *P* will not occur. However, the velocities are relatively small, so that the case of sticking is only approximated. Nevertheless, in the following sticking means the velocity of the point *P* is very small.

With respect to limits of this point contact model, it was shown in Chapter 3.2 that the lowest eigenfrequency of the contact occurs in the tangential direction. Using the dimensionless parameter defined in Eq.(3.7-35) and Eq.(3.7-40), Eq.(3.7-10) can be written in dimensionless form with

$$\Delta m_{D0}^* << \Delta c_{R0y,z}^*\,, \qquad (3.7\text{-}45)$$

which must hold true, if applying this point contact model. For a better understanding of the three-dimensional point contact model, different motions of the point *M* will be investigated. Within the following parameter studies, the parameters are given by: $c_{R0y}^*=c_{R0z}^*=1.0$, $F_N^*=1.0$, $\Delta m_{D0}^*=10^{-3}$ and $\beta^*=0.2$, if not defined else. In a first step the slope parameter k_S has to be adjusted. To find a reasonable value, a parameter study is carried out with a constant velocity v_{0y} of the point *M* in the *y*-direction. Then the displacement of the point *M* is given by

$$y_M = v_{0y}t \qquad (3.7\text{-}46)$$

or in dimensionless notation

$$y_M^* = v_{0y}^* t^* \qquad (3.7\text{-}47)$$

with

$$v_{0y}^* = \frac{v_{0y}}{\omega_0 R_Z}\,. \qquad (3.7\text{-}48)$$

Because of a decreasing friction characteristic with $p_v^*=100.0$, see Eq.(3.7-42), stick-slip motion occur. In **Fig. 3.7-3** the phase plots of the corresponding limit cycle are investigated varying the slope of the smoothing function for a velocity of $v_{0y}^*=1.0$. The results are relatively sensitive to the slope parameter. Hence, there is a need for high values of the slope, which leads to a stiff set of differential equations. The increase of computation time can be reduced, if special solver are used, which are designed for those cases, see (SIMULINK 1999) and make use of the numerical and if known of the analytical Jacobian to speed up the solution procedure. These solvers in combination with a variable step size lead to reasonable computation times. Within the following parameter studies, the normalized slope is set to be $k_S=10^6$, which lead to a relatively small error, see Fig. 3.7-3.

In **Fig. 3.7-4a** corresponding to the above investigation presented in Fig. 3.7-3, the displacement of the point *M*, which moves with the velocity v_{0y}, and the displacement of the point *P* are shown. The point *P* is sticking where the displacement y_P is constant with respect to time and else sliding. The slip time compared to the stick time is relatively small. The stick-slip motion can be seen by observing the velocity of the point P, see **Fig. 3.7-4b**. The point P sticks if the velocity v_{Py} is zero. The difference of the friction force F_{Ry}, see **Fig. 3.7-4c**, and spring force F_{Fy}, see **Fig. 3.7-4d**, belongs to the inertia forces. Within the stick region, the spring force increases linearly with time due to the constant velocity v_{0y} and is approximately equal to the friction force because the inertia forces are relatively small. If the reduced mass tends to zero, than the spring force will be identical to the friction force in the stick and slip region.

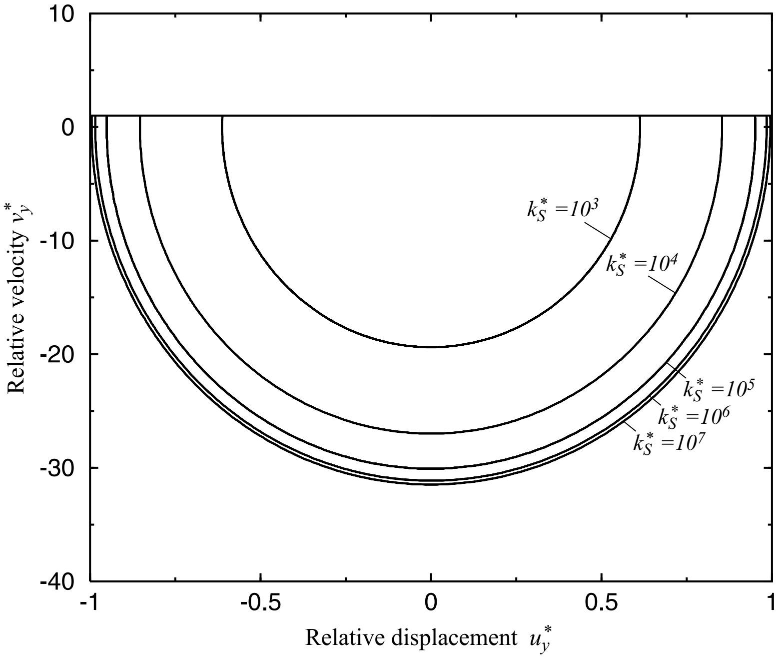

Fig. 3.7-3 Phase plots for different slope parameters

The energy dissipation for one period can be investigated assuming harmonic relative displacements. Knowing the normal displacement of the point N, the normal force can be calculated by Eq.(3.7-30). In **Fig. 3.7-5**, the normalized normal contact force is calculated versus the normalized relative normal displacement with

$$u_x^* = 0.3 + 0.3 \sin t^*, \quad y_M^* = 0.0, \quad z_M^* = 0.0\,,$$

varying the damping factor β^*. The area of the hysteresis corresponds to the dissipated energy per period with respect to the rough elastic contact. For $\beta^*=0$ the same functional behavior appears as shown in Fig. 3.3-8.

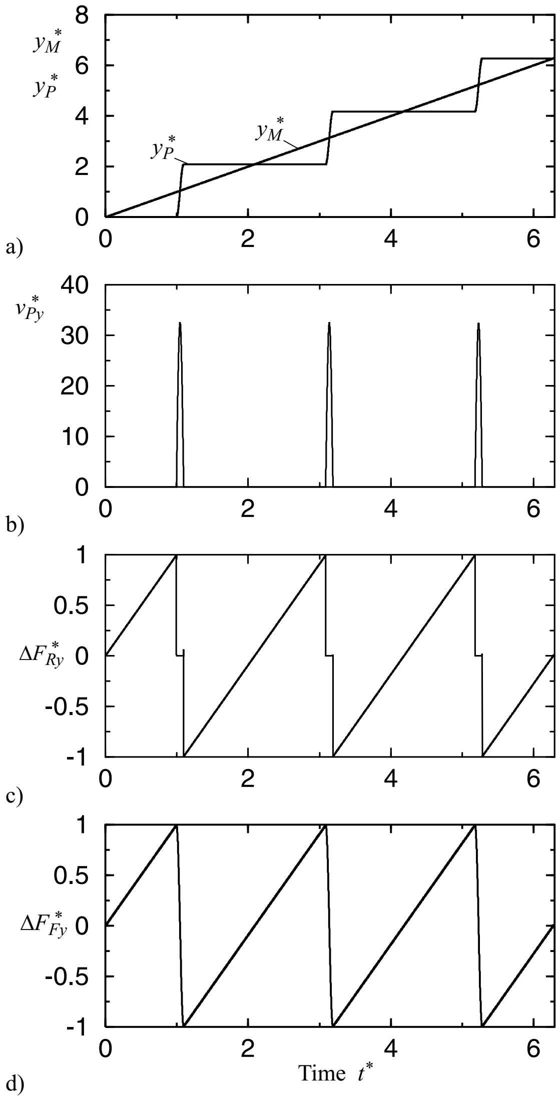

Fig. 3.7-4 Time histories of the **a**) displacements **b**) velocity **c**) friction force **d**) and spring force in the y-direction

For the investigation on the tangential contact model, in the following Coulomb friction is assumed with $p_v^*=0.0$, see Eq.(3.7-42). Applying the relative harmonic displacements in the y- and z-direction with

$$u_x^* = 1.5, \quad y_M^* = 1.0\cos t^*, \quad z_M^* = 2.0\sin t^*,$$

the corresponding tangential forces can be calculated with respect to the relative displacement in y- and z-directions and are shown in **Fig. 3.7-6**. Here, the dissipated energy is the sum of both hysteresis areas. The tangential force is limited by the Coulomb friction. This investigated example corresponds to the effect of friction damping, where friction contacts are used to dissipate energy. For further information on this topic, see Chapter 5.

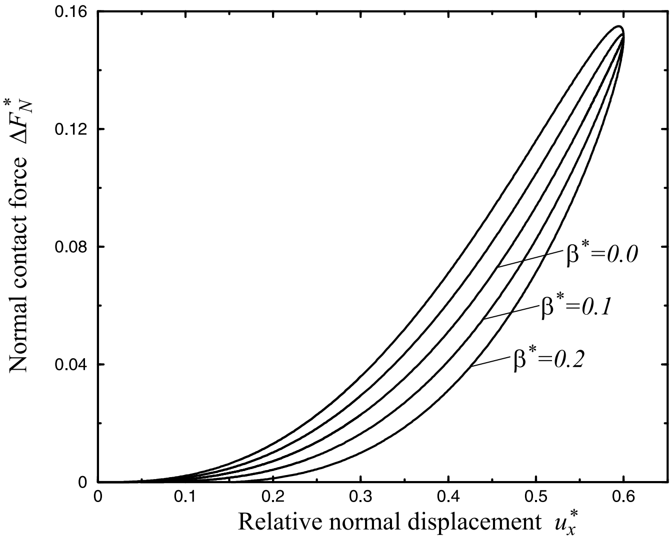

Fig. 3.7-5 Hysteresis behavior in the normal direction for different damping factors

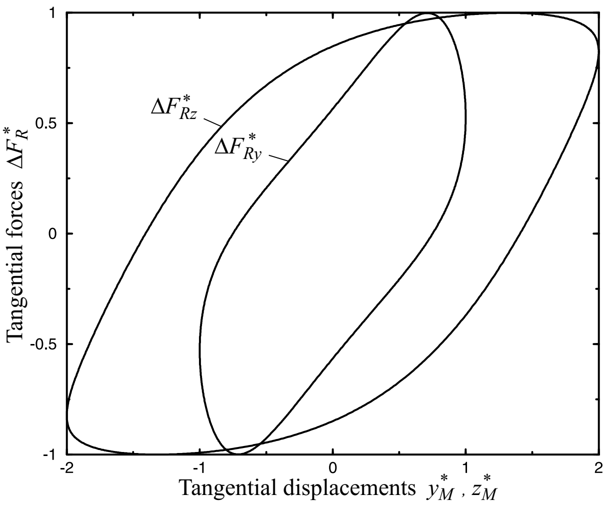

Fig. 3.7-6 Hysteresis behavior in tangential direction

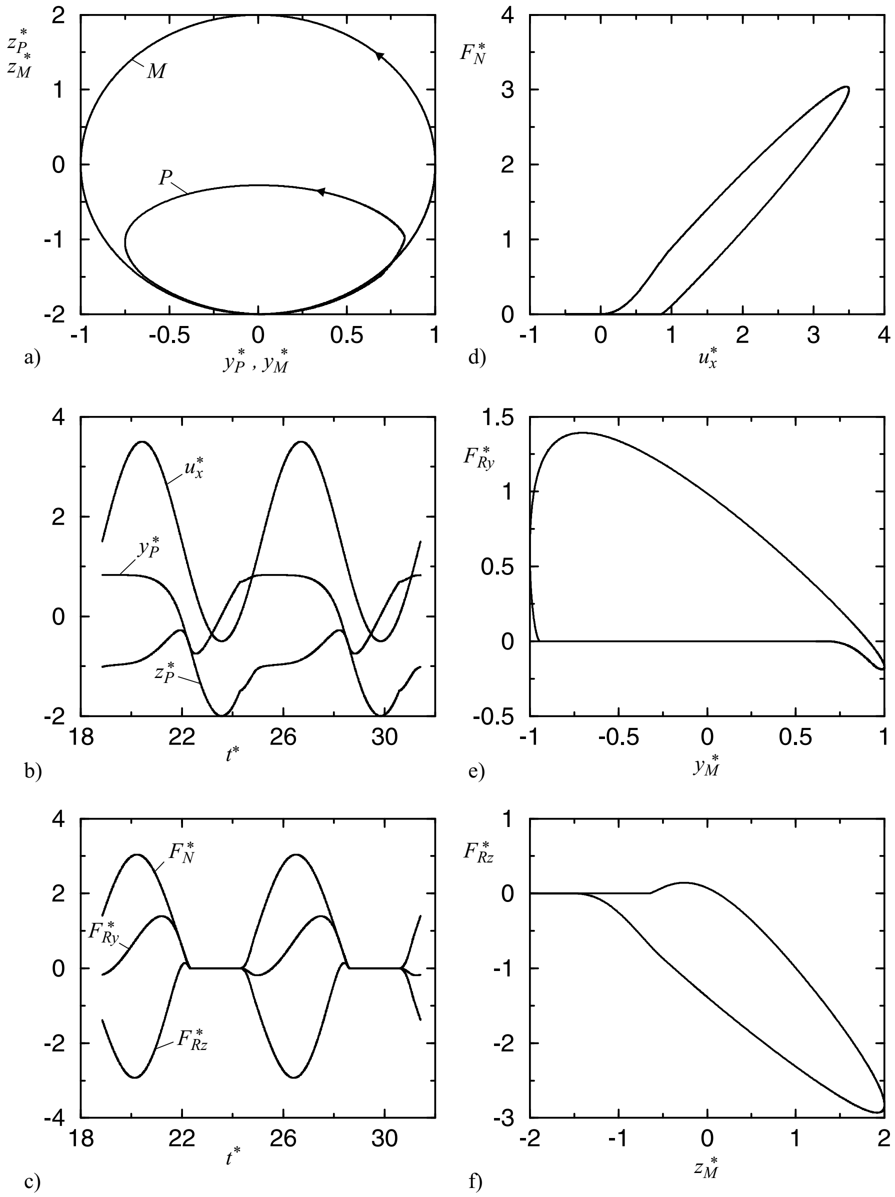

Fig. 3.7-7 Three-dimensional point contact behavior **a**) Orbits of the points *M* and *P* **b**) Relative normal displacement and the displacement of the point *P* in *y*- and *z*-direction versus time **c**) Contact forces versus time **d**) Normal contact force versus relative normal displacement **e**) Tangential contact force versus displacement of the point *M* in *y*-direction **f**) Tangential contact force versus displacement of the point *M* in *z*-direction

In general, due to three-dimensional motion three contact forces are calculated, where stick, slip and separation of the contact point *P* can occur. In **Fig. 3.7-7**, the results for the displacements in the normal direction and the tangential displacement with

$$u_x^* = 1.5 + 2.0\sin t^*, \quad y_M^* = 1.0\cos t^*, \quad z_M^* = 2.0\sin t^*,$$

are shown. In **Fig. 3.7-7a**, the orbits of the point *P* and *M* are shown within the contact plane. If the normal contact force is identical to zero, separation takes place. As defined above, the velocity and acceleration of the point *P* are identical to those of the point *M*. In **Fig. 3.7-7b**, the input value of the relative normal displacement u_x^* is shown and the calculated coordinates of the point *P* with respect to the dimensionless time t^*. The three-dimensional behavior is investigated including separation, where the normal and tangential contact forces are identical to zero, see **Fig. 3.7-7c**. The hysteresis behavior because of the three-dimensional motion is investigated in the **Figs. 3.7-7d–f**. In Fig. 3.7-7 d, the normal contact force versus relative normal displacement is shown, while Fig. 3.7-7e and f show the friction forces versus displacement of the point *M* in *y*- and *z*-direction, respectively. Again, the dissipated energy is given by the summation of the areas described in Fig. 3.7-7d, e and f.

Now, the three-dimensional point contact model is developed and can be calculated by standard numerical methods. The analysis of the motion leads to stick, slip or separation. Microslip effects cannot be modeled, because with respect to the three-dimensional point contact model the three contact forces are applied in a single point. To simulate microslip effects within one contact area several point contact elements have to be used. If the contact element area is discretized again and several point contact model are used to describe the local contact behavior, the non-constant pressure distribution, as presented in Fig. 3.3-7 can be included, which leads to so-called microslip effects. These microslip effects are investigated in the next chapter.

3.8 Microslip Effects due to Rough Surfaces

If within one contact area, some contact points stick while others slide, then this phenomenon is called microslip. Here, for rough surfaces the effect of microslip occurs, because of the non-constant pressure distribution for one area element. In **Fig. 3.8-1**, the nominal contact area $\Delta A_0 = \Delta h_0 \Delta b_0$ is divided into regions, where separation, sliding and sticking can take place. The displacement u_x denotes the position of the rigid wall, see also Fig. 3.3-6. Each contact region is defined by the normal and shear stress

$$\begin{array}{lll} \text{Separation:} & \sigma_{xx} = 0, & \sigma_{xz} = 0 \\ \text{Sliding:} & \sigma_{xx} = -p_N(z), & \sigma_{xz} = \mu p_N(z) \\ \text{Sticking:} & \sigma_{xx} = -p_N(z), & \sigma_{xz} = \tau_z, \end{array}$$

with the tangential traction τ_z.

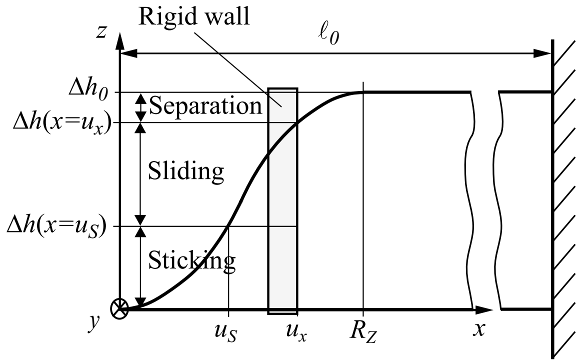

Fig. 3.8-1 Contact model

If the deformations are elastically, than the traction within the stick region is given by

$$\tau_z = \frac{\Delta c_{R0z} w_P}{\Delta A_0} \,. \tag{3.8-1}$$

In the following the hydrostatic pressure distribution is assumed, see Eq.(3.1-32). If yielding occurs, than the traction is limited by the shear strength

$$\tau_z = \tau_S \,. \tag{3.8-2}$$

The minimum value of the Eq.(3.8-1) and Eq.(3.8-2) defines the traction within the stick region

$$\tau_z = \min\left\{ \frac{\Delta c_{R0z}}{\Delta A_0} w_P , \tau_S \right\} \tag{3.8-3}$$

and furthermore defines whether the deformations are elastically or plastically. As discussed in Chapter 3.6 the shear strength τ_S is assumed linearly dependent on the temperature with

$$\tau_S = \tau_{S0}\left(1 - \frac{\Delta T}{\Delta T_E} \right). \tag{3.8-4}$$

Then, the dimensionless shear traction within the stick region is given by Eq.(3.8-3)

$$\tau_z^* = \min\left\{ \Delta c_{R0z}^* w_P^* , \tau_{S0}^* (1 - \Delta T^*) \right\}. \tag{3.8-5}$$

with

$$\tau_{S0}^* = \frac{\tau_{S0} \Delta A_0}{\mu_0 \Delta c_{N0} a_0}, \quad \Delta c_{R0z}^* = \frac{\Delta c_{R0z}}{\mu_0 \Delta c_{N0}} \tag{3.8-6}$$

and

$$w_P^* = \frac{w_P}{a_0}, \quad \Delta T^* = \frac{\Delta T}{\Delta T_E} \,, \tag{3.8-7}$$

using the unit length a_0. Assuming a constant velocity v_P of the rigid wall relative to the elastic contact in the z-direction, the tangential displacement is determined by

$$w_P = v_P t \tag{3.8-8}$$

or in dimensionless form

$$w_P^* = t^* \tag{3.8-9}$$

with

$$w_P^* = \frac{w_P}{a_0}, \quad t^* = \frac{v_P t}{a_0}. \tag{3.8-10}$$

From Eq.(3.8-5) the maximum elastic deformation is given by

$$w_{P\max}^* = \frac{\tau_{S0}^*}{\Delta c_{R0z}^*}(1 - \Delta T^*). \tag{3.8-11}$$

The boundary condition between the stick and the slip region is defined by the tangential traction at the position $x=u_S$, see Fig. 3.8-1, with

$$\tau_z = \mu(\Delta T) p_{NS}, \tag{3.8-12}$$

where the friction coefficient is assumed to be linearly dependent on the temperature, see Eq.(3.6-3). From Eq.(3.1-25) the local normal pressure at the boundary is given by

$$p_{NS} = \frac{\Delta F_{NS}}{\Delta A_0} = \frac{\Delta c_{N0}}{\Delta A_0}\left(u_x - u_S\right). \tag{3.8-13}$$

Inserting Eq.(3.8-13) in Eq.(3.8-12) and solving for the normal displacement u_S gives

$$u_S^* = u_x^* - \frac{\tau_z^*}{\mu^*(\Delta T^*)}, \quad for \quad 0 \le u_S^* \le u_x^* \tag{3.8-14}$$

with the dimensionless friction coefficient

$$\mu^*(\Delta T^*) = 1 - \Delta T^* \quad for \quad \Delta T^* \le 1 \tag{3.8-15}$$

and the dimensionless parameters

$$u_S^* = \frac{u_S}{a_0}, \quad \mu^* = \frac{\mu}{\mu_0}. \tag{3.8-16}$$

The average temperature with respect to the contact area is assumed to be proportional to the average heat source, see also Eq.(3.6-5),

$$\Delta T = k_T q_H \tag{3.8-17}$$

and can be written in dimensionless form

$$\Delta T^* = k_T^* q_H^* \tag{3.8-18}$$

with

$$k_T^* = \frac{k_T \mu_0 \Delta c_{N0} a_0 v_P}{\Delta T_E \Delta A_0}, \quad q_H^* = q_H \frac{\Delta A_0}{\mu_0 \Delta c_{N0} a_0 v_P}. \tag{3.8-19}$$

The heat source q_H is calculated by the distributed frictional power related to the contact area, see also Eq.(3.6-14), while the heat source due to plastic deformations is neglected, hence

$$q_H = \frac{\mu(\Delta T)\Delta F_{NH} v_P}{\Delta A} \tag{3.8-20}$$

with the contact area ΔA and the resultant normal force due to the sliding contact region

$$\Delta F_{NH} = \Delta F_N(u_x) - \Delta F_N(u_S) - \Delta h(u_S)\Delta b_0 p_{NS} \tag{3.8-21}$$

or in dimensionless form

$$q_H^* = \frac{\mu^*(\Delta T^*)\Delta F_{NH}^*}{\Delta h^*(u_x^*)} \tag{3.8-22}$$

with

$$\Delta F_{NH}^* = \Delta F_N^*(u_x^*) - \Delta F_N^*(u_S^*) - \Delta h^*(u_S^*)\,(u_x^* - u_S^*)\,, \tag{3.8-23}$$

using the normal pressure defined in Eq.(3.8-13).

The resultant tangential force is calculated by the integration of the tangential traction with respect to the contact area

$$\Delta F_T = \Delta b_0 \int\limits_0^{\Delta h(x=u_x)} \tau_{Tz}\, dz\,, \tag{3.8-24}$$

which gives

$$\begin{aligned}\Delta F_T &= \tau_z \Delta h(u_S)\Delta b_0 + \\ &\quad \mu(\Delta T)\big(F_N(u_x) - F_N(u_S) - p_{NS}\Delta h(u_S)\Delta b_0\big).\end{aligned} \tag{3.8-25}$$

Inserting Eq.(3.8-12) gives the dimensionless tangential contact force

$$\Delta F_T^* = \mu^*(\Delta T^*)\big(\Delta F_N^*(u_x^*) - \Delta F_N^*(u_S^*)\big) \tag{3.8-26}$$

with

$$\Delta F_N^* = \frac{\Delta F_N}{\Delta c_{N0} a_0}, \quad \Delta F_T^* = \frac{\Delta F_T}{\mu_0 \Delta c_{N0} a_0}\,. \tag{3.8-27}$$

This theory holds for monotonous increasing tangential displacements in one direction, see also (Jäger 1996, 1998). The normal force displacement relationship is given by Eq.(3.3-24) using the normalized roughness

$$R_Z^* = \frac{R_Z}{a_0}\,. \tag{3.8-28}$$

In **Fig. 3.8-2a**, the tangential contact force is shown varying both, the normalized tangential displacement w_P^* and the relative normal displacement u_x^* with the dimensionless parameters:

$$\Delta c_{R0z}^* = 1, \quad R_Z^* = 1, \quad k_T^* = 0, \quad \tau_{S0}^* = 2, \quad u_x^* = 0\ (0.15)\ 1.5\,.$$

With increasing normal displacement, the maximum possible tangential force, which can be transmitted increases as well. In comparison to a single point contact, see Fig. 1.2-7b, the microslip effect leads to a smooth increase of the tangential force.

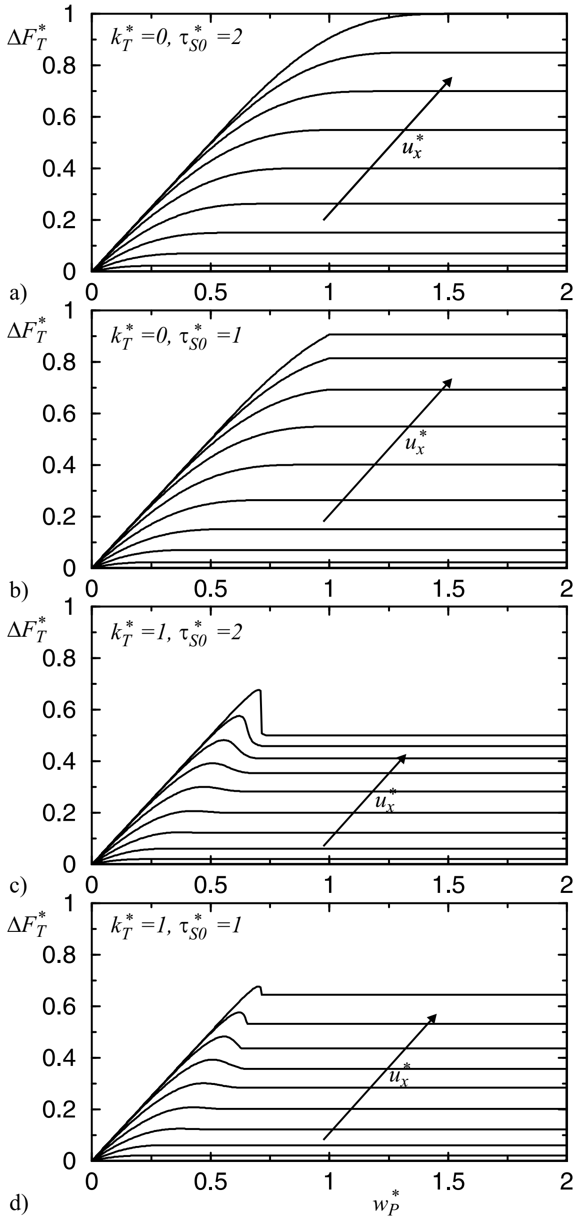

Fig. 3.8-2 Tangential force versus tangential displacement varying the normal displacement for different parameters **a**) Influence of microslip **b**) Influence of the shear strength **c**) Influence of the decreasing friction factor with respect to the temperature **d**) Influence of both the decreasing friction factor and the shear strength

In **Fig. 3.8-2b** the influence of the maximum shear strength onto the tangential contact force is shown with the following parameters

$$\Delta c^*_{R0z} = 1,\quad R^*_Z = 1,\quad k^*_T = 0,\quad \tau^*_{S0} = 1,\quad u^*_x = 0\,(0.15)\,1.5\,.$$

The maximum tangential force is limited by the shear strength.

In **Fig. 3.8-2c**, the influence of the temperature, see Eq.(3.8-15), onto the tangential contact force is shown for the following parameters

$$\Delta c^*_{R0z} = 1,\quad R^*_Z = 1,\quad k^*_T = 1,\quad \tau^*_{S0} = 2,\quad u^*_x = 0\,(0.15)\,1.5\,.$$

The decreasing character of the friction factor appears as well with respect to the tangential force.

In **Fig. 3.8-2d** the influence of both the linear decreasing friction factor with respect to the temperature and the maximum shear strength onto the tangential contact force is shown with the following parameters

$$\Delta c^*_{R0z} = 1,\quad R^*_Z = 1,\quad k^*_T = 1,\quad \tau^*_{S0} = 1,\quad u^*_x = 0\,(0.15)\,1.5\,.$$

In the following, a comparison is done between calculations and the measurements carried out by Musiol (1994). Starting from equilibrium with constant velocity, the normal and tangential forces onto a work peace have been measured with time. The normal and the tangential force are used to define an equivalent friction coefficient by

$$f = \frac{F_T}{F_N} = \mu_0 \frac{F^*_T}{F^*_N}\,. \tag{3.8-29}$$

In **Fig. 3.8-3**, the results of five hundred measurements of the equivalent friction coefficient versus time are shown. It appears that the results cannot be reproduced, because wear does change the contact surfaces and therefore the contact parameters. Nevertheless, these experiments converge to a limiting case, where the contact parameters are approximately constant with time. However, in the beginning of all experiments all contact parameter do change with time. It appears that the average roughness is the main parameter for this effect. Assuming that the shape of the cumulative high distribution is approximately constant with time, the physical behavior can be modeled. All parameter have been fit to the experimental results and have been estimated by

$$\Delta c^*_{R0z} = 0.00019,\quad F^*_N = 2.0,\quad k^*_T = 0.7,\quad \tau^*_{S0} = 1.9,\quad R^*_Z = 1.5...14.65$$

and using the friction coefficient of $\mu_0 = 0.75$. The contact partners are identical to those used in real brake systems. The difference to the procedure described above is, here the normal contact force is set to be constant in analogy to experiments described in (Musiol 1994). The normal displacement is solved iteratively from Eq.(3.3-24). The comparison of the measurements and the calculations is relatively good, compare **Fig. 3.8-4** with Fig. 3.8-3. Additionally the decreasing characteristic due to a decreasing equivalent friction factor is recalculated relatively well. If the average roughness is very small, from the above theory it follows, that for the transition from stick to slip coincides with a jump in the tangential contact force, which was measured by Musiol (1994) as well. One reason for the differences between measurement and calculations belong to the change of the cumulative height distribution due to wear, because wear influences the contact area, contact stiffnesses and normal pressure distribution. Therefore, in the next Chapter the change of the cumulative height distribution due to wear is investigated.

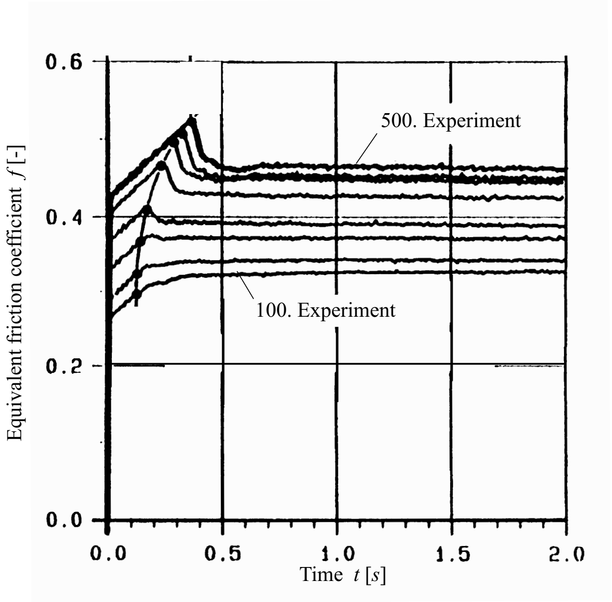

Fig. 3.8-3 Measurement of the equivalent friction coefficient (Musiol 1994)

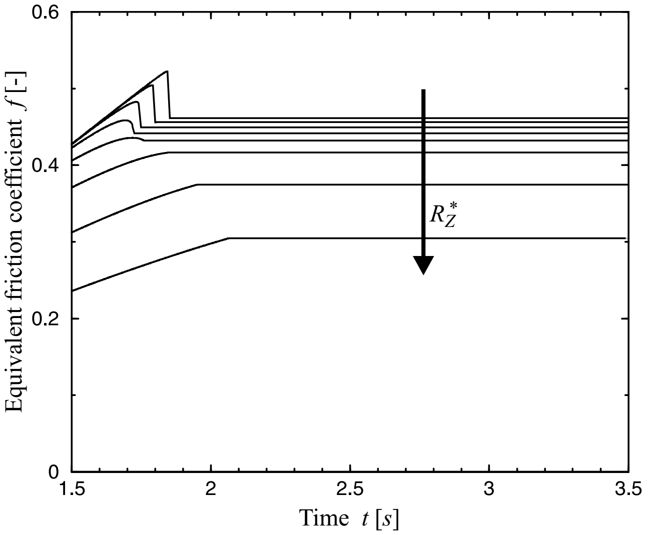

Fig. 3.8-4 Calculated equivalent friction coefficient varying the normalized roughness

3.9 Wear of Rough Surfaces

As observed in the Chapter before, wear changes the surface profile. Furthermore, wear can influence the dynamical behavior of the system i.e. brake systems, see (Ostermeyer 2003, Ostermeyer and Müller 2006). In **Fig. 3.9-1a** a surface profile of the grinded surface of the disc used in the experimental setup, see Fig. 3.6-1, and the corresponding cumulative height distribution are shown. After one run-over the peaks are cut off, see **Fig. 3.9-1b**, and the corresponding cumulative height distributions shows the reduced maximum value of the asperities height, which is decreased from *29.45* [μm] to *17.44* [μm]. After several run-over the cumulative height, distribution converged to a limiting cumulative height distribution shown in **Fig. 3.9-1c** with a maximum value of *9.10* [μm]. One can observe, that the curvatures of the summits do increase, while the roughness decreases with time.

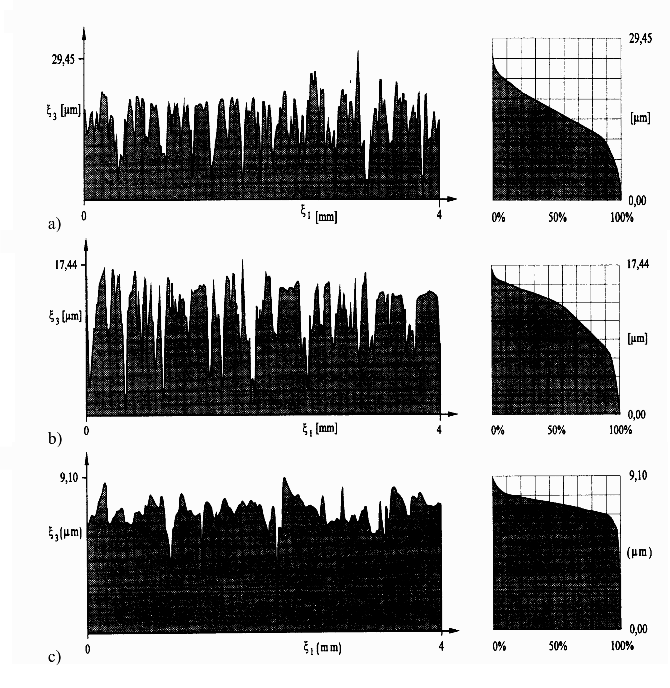

Fig. 3.9-1 Surface profile measurements and cumulative height distribution **a**) starting surface profile **b**) after one run-over **c**) limiting case (Hinrichs 1997a)

In the following, a calculation procedure is presented to calculate the wear effects as described above. Before calculating the wear of the cumulative height distribution, some basic equations are derived for a contact element shown in Fig. 3.6-3. The result of the mass balance is given by

$$\Delta \dot{m}_{in} = \Delta \dot{m}_{out} \tag{3.9-1}$$

with

$$\Delta\dot{m}_{in} = \Delta\dot{W}\rho_0\,, \qquad (3.9\text{-}2)$$

where ρ_0 denotes the density and ΔW the unknown wear volume. To be able to calculate the wear volume, several wear hypotheses have been developed. For example, the wear of convex problems can be described by the hypothesis of Archard (1953). This has been modified by Fleischer (1973), who assumed, that the volume wear rate is proportional to the frictional power

$$\Delta\dot{W} = I_W \Delta P_R \qquad (3.9\text{-}3)$$

with the proportionality factor I_W and the frictional power

$$\Delta P_R = \mu \Delta F_N v_r\,. \qquad (3.9\text{-}4)$$

The proportionality factor I_W has to be identified by experiments, see (Krause and Poll 1986) and is dependent on the frictional power per contact area. The wear rate is defined by the velocity in normal direction

$$v_x = \frac{\Delta\dot{W}}{\Delta A_0}\,, \qquad (3.9\text{-}5)$$

See Fig.3.6-3. Inserting Eq.(3.9-3) and Eq.(3.9-4) and using Eq.(3.6-14) gives

$$v_x = I_W q_H\,. \qquad (3.9\text{-}6)$$

Then the wear rate in x-direction can be determined. Now, for investigating the change of the cumulative height distribution the wear rate is approximated by discrete values

$$v_x \approx \frac{\Delta x_W}{\Delta t}\,, \qquad (3.9\text{-}7)$$

where Δx_W denotes the wear depth for one contact element per time step Δt. With respect to the experiments described above the relative velocity v_r and the friction coefficient $\mu = \mu_0$ are assumed to be constant. If the pressure distribution is known, then the wear can be calculated with respect to time. From Eq.(3.9-6) and Eq.(3.9-7) it follows that the depth of the worn material is given by

$$\Delta x_W = I_W \mu_0 p_N(z) v_r \Delta t \qquad (3.9\text{-}8)$$

or using dimensionless notation

$$\Delta x_W^* = p_N^*(z^*)\Delta t^* \qquad (3.9\text{-}9)$$

with

$$x_W^* = \frac{\Delta x_W}{R_Z}, \quad p_N^* = \frac{p_N \Delta A_0}{\Delta c_{N0} R_Z}, \quad \Delta t^* = \frac{\Delta t I_W \mu_0 v_r \Delta c_{N0}}{\Delta A_0}\,. \qquad (3.9\text{-}10)$$

Here, the worn material is directly proportional to the pressure distribution and the time. The general calculation of the normalized equivalent pressure distribution is given by Eq.(3.3-15). Because of the non-constant pressure distribution, the material is not worn constantly with respect to the contact area. Starting with the cumulative height distribution defined in Eq.(3.3-4) and the relative normal displacement $u_x^* = 0.5$ at the time t_0^*, which corresponds to a normal force of $F_N^* = 0.09375$ using Eq.(3.3-24). In the following, this value of the normal force is held to be constant, while the relative normal displacement u_x^* is adjusted. The time difference is set to be $\Delta t^* = 100.0$.

In **Fig. 3.9-2** and in **Fig. 3.9-3** the change of the cumulative height distribution and the change of the equivalent pressure distribution is presented, respectively, for different time steps. As observed in the experimental results of the surface profile measurements cited in Fig. 3.9-1, the surface profiles are getting smoother with time and the average roughness decreases. Due to the effect that the surface is getting smoother, the contact area increases and the maximum pressure at $z^*=0$ decreases with time.

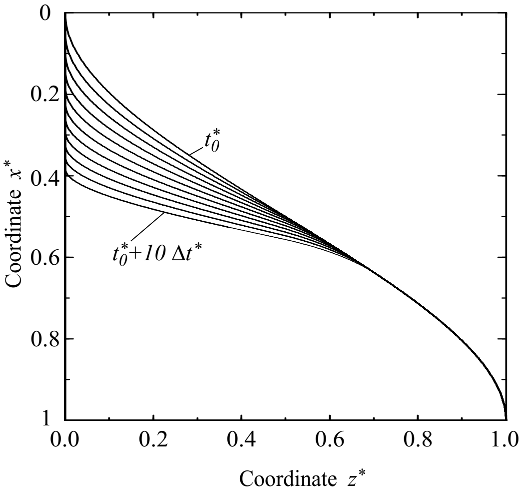

Fig. 3.9-2 Change of the cumulative height due to wear

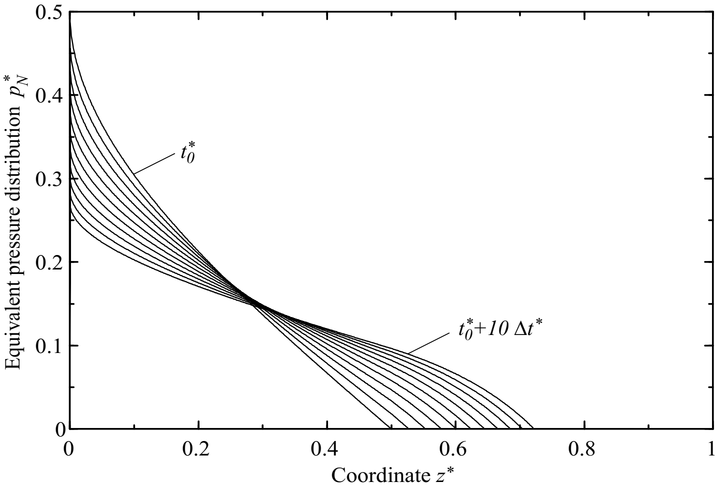

Fig. 3.9-3 Change of the normal equivalent pressure distribution due to wear

Hence, systems with friction are always time dependent since the contact area and the pressure distribution are time dependent. Looking at the long time behavior of dynamical systems with friction, wear analysis has to be included, because this will change the dynamical behavior. Nevertheless, in many cases, this time dependency is very slow compared to the dynamics and can be neglected considering the short time dynamics.

Summarizing Chapter 3.8, where the influence of temperature onto the friction characteristic has been investigated and the present Chapter results in the flow chart shown in **Fig. 3.9-4**. One output parameter of the point contact model is the frictional power. From here, the temperature and the wear can be determined. The loop can be closed from calculating the wear of the contact surface to the measured cumulative height distribution as described in the present Chapter. The contact stiffness for smooth surfaces is combined with the surface profile measurement using the cumulative height distribution. This information is used to describe the normal force-displacement-relationship and the nonlinear tangential contact stiffness due to roughness within the point contact model. The contact stiffness for smooth surfaces can be determined by the finite element method and modal analysis as described in Chapter 3.1. In general, the static system has to be analyzed before using the finite element method and the static contact pressure, nominal contact area, the contact stiffnesses have to be determined. Then the point contact model can be used in combination with the modal description of the elastic bodies to describe the dynamic behavior of the system. This procedure will be applied to different systems as described in Chapter 4, 5 and 6.

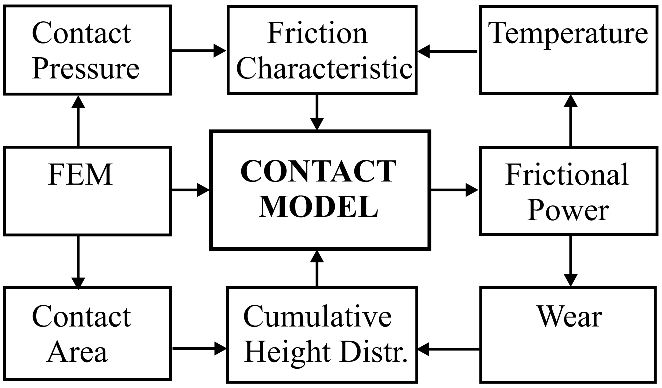

Fig. 3.9-4 Flow chart of the solution procedure

4 Oscillators with Elastic Contact and Friction

To verify the developed point contact model with friction, a comparison of measurements and calculations with respect to the normal and tangential contact behavior is carried out. The experimental setup, shown in Fig. 3.6-1, is used for the investigations in the normal and tangential directions, see also (Hinrichs et al. 1997b, 1998). On the one hand, an oscillator with an elastic normal contact and on the other hand a self-excited oscillator with friction is analyzed. The theoretical foundation for both investigated systems is derived in a more general sense within the next Chapter. Due to the strong non-linearity of the normal and tangential contact, the systems are analyzed in the time domain.

4.1 System Description

In **Fig. 4.1-1**, the investigated system model with n possible contact points at the surface of an elastic body is depicted. The body is assumed linear elastic, as described in Chapter 2. The surface of the elastic body, where contact can occur, is discretized and for each possible contact node, the contact and friction laws have to be formulated. The ground is moving with the constant velocity V. The normal force F_{Nj} and the tangential force F_{Rj} act at the node j.

The vibration amplitudes of the elastic body, the external forces and the contact forces are described in the initial I-coordinate-system. With respect to the elastic body, the excitation point B is introduced, where two external loads and one external moment are applied. A constant force F_{N0} like the gravity force is applied at the node C parallel to the ${}_Iy$-axis. The surface at the node j is defined by the height y_{Rj}. As derived in Chapter 2.4, the dynamics are given by the equation of motion

$$\boldsymbol{diag}(\ddot{q}_i + 2\omega_{0i}D_i\dot{q}_i + \omega_{0i}^2 q_i) = \boldsymbol{T}^T \boldsymbol{f}_{ex} = \boldsymbol{R}\ . \tag{4.1-1}$$

The transformation into the state space requires the definition of the state vector,

$$\boldsymbol{y} = \begin{bmatrix} q_1 & \dot{q}_1 & q_2 & \dot{q}_2 & \cdots & q_m & \dot{q}_m \end{bmatrix}^T , \tag{4.1-2}$$

with the number m of modes. Hence, differential equation of second order defined in Eq.(4.1-1) can be transferred to a set of differential equation of first order

$$\begin{aligned} \dot{y}_{2i-1} &= y_{2i}, \\ \dot{y}_{2i} &= -2\omega_{0i}D_i y_{2i} + \omega_{0i}^2 y_{2i-1} + R_i . \end{aligned} \tag{4.1-3}$$

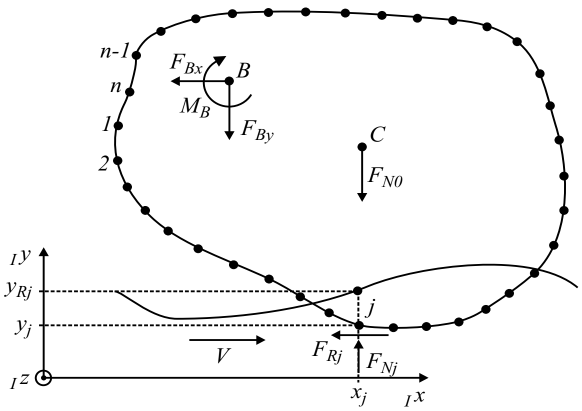

Fig. 4.1-1 Elastic body with friction contacts

Here, the external force vector of the elastic body is defined by

$$\boldsymbol{f}_{ex} = \left[\boldsymbol{F}_B^T \quad \boldsymbol{F}_C^T \quad \boldsymbol{F}_1^T \quad \boldsymbol{F}_2^T \quad \ldots \quad \boldsymbol{F}_j^T \quad \ldots \quad \boldsymbol{F}_n^T\right]^T \tag{4.1-4}$$

with the generalized forces

$$\boldsymbol{F}_B = \left[-F_{Bx} \quad -F_{By} \quad -M_B\right]^T, \tag{4.1-5}$$

$$\boldsymbol{F}_C = \left[0 \quad -F_{N0} \quad 0\right]^T \tag{4.1-6}$$

and the generalized contact forces at the node *j*

$$\boldsymbol{F}_j = \left[-F_{Rj} \quad F_{Nj} \quad 0\right]^T. \tag{4.1-7}$$

The points *B* and *0* are connected by springs in the *x*- and *y*-direction, which are not shown in Fig. 4.1-1. Furthermore, absolute viscous damping with respect to the point *B* is assumed. Then, the external forces of the elastic body are given by

$$F_{Bx} = c_x(x_B - u_{0x}) + b_x\dot{x}_B\,, \tag{4.1-8}$$

$$F_{By} = c_y(y_B - u_{0y}) + b_y\dot{y}_B \tag{4.1-9}$$

and $M_B=0$, where the point *0* is harmonically excited with

$$u_{0x}(t) = x_0\sin(\omega_E t) \tag{4.1-10}$$

and

$$u_{0y}(t) = y_0\sin(\omega_E t)\,. \tag{4.1-11}$$

Using the modal description of the linear elastic body, the generalized displacement vector of the elastic body is given by

$$\boldsymbol{w} = \boldsymbol{Tq} \tag{4.1-12}$$

with

$$\boldsymbol{w} = \left[x_B \quad y_B \quad \varphi_B \quad x_C \quad y_C \quad \varphi_C \quad x_1 \quad y_1 \quad \varphi_1 \quad \ldots\right]^T \tag{4.1-13}$$

and the generalized velocity vector

$$\boldsymbol{v} = \boldsymbol{T\dot{q}} \tag{4.1-14}$$

with

$$\boldsymbol{v} = \left[\dot{x}_B \quad \dot{y}_B \quad \dot{\varphi}_B \quad \dot{x}_C \quad \dot{y}_C \quad \dot{\varphi}_C \quad \dot{x}_1 \quad \dot{y}_1 \quad \dot{\varphi}_1 \quad \ldots\right]^T. \tag{4.1-15}$$

The normal contact force with respect to the node j is given by Eq.(3.2-24)

$$F_{Nj} = c_{N0j} R_{Zj} f^*(u^*_{Nj}) + \beta_j c_{N0j} h^*(u^*_{Nj}) v_{Nj} \geq 0 \, . \tag{4.1-16}$$

The relative normal penetration is given by

$$u_{Nj} = y_{Rj} - y_j \, , \tag{4.1-17}$$

where y_{Rj} denotes the macroscopic displacement of the moving ground like the waviness. Then, the corresponding velocity in the ${}_I y$-direction normal to the ground velocity V is given by

$$v_{Nj} = \dot{u}_{Nj} = \dot{y}_{Rj} - \dot{y}_j \, . \tag{4.1-18}$$

The relative tangential displacement and velocity of each contact element is given by

$$u_{rj} = x_j - Vt \tag{4.1-19}$$

and

$$v_{rj} = \dot{u}_{rj} = \dot{x}_j - V, \tag{4.1-20}$$

respectively.

To reduce the degrees of freedom of the investigated system and, hence, to reduce the computation time, the tangential contact elasticity is modeled as a part of the elastic body. The contact stiffness due to the contact model, described in Chap. 3.3 is then assumed to be infinite.

Assuming dry friction the friction force at the node j is given by

$$F_{Rj} = \mu(v_{rj}) F_{Nj} \; s(v_{rj}) \tag{4.1-21}$$

with the friction coefficient μ, which is assumed to be nonlinearly dependent on the relative velocity v_{rj} with

$$\mu(v_{rj}) = (\mu_0 - \mu_\infty) e^{-\lambda_e |v_{rj}|} + \mu_\infty \, , \tag{4.1-22}$$

with a decreasing characteristic for $\lambda_e > 0$ and the smoothing function

$$s(v_{rj}) = \frac{2}{\pi} \arctan(k_S v_{rj}) \, , \tag{4.1-23}$$

with the slope parameter k_S, which defines the slope at zero relative velocity $v_{rj}=0$. For large slope parameters k_S, the non-smooth system dynamics can be approximated. A disadvantage due to large values of this slope parameter is the occurrence of stiff differential equations. But there exist numerical integration methods with variable step size, which calculate the numerical or, if available, use the analytical Jacobian matrix of the investigated system, see for example (NAG 1986) and (SIMULINK 1999). Both improvements speed up the solution procedure and solve the system equations for relatively large values of the slope parameter in a reasonable time and an acceptable accuracy. Due to the investigations with respect to the relative error, see Chapter 3.7 and Fig. 3.7-3, the slope parameter is set to be $k_S = 10^6$ [s/m] in the following.

4.2 Oscillator with Elastic Contact

The experimental setup is shown in Fig. 3.6-1, where a pendulum supported by springs represents the linear oscillator. The rotational degree of freedom of the pendulum and its degree of freedom normal to the plane of rotation have been realized by air bearings providing small damping. A magnetic excitation force realizes the harmonic excitation, see (Popp et al. 1996). For the experimental investigation of the impact oscillator, the pendulum hits a stop. A more detailed description of the test stand is given in (Hinrichs et al. 1997b). The reduced system parameters of the oscillator shown in Figure 4.2-1 are given by: $m=0.092$ [*kg*], $c_y=99.085$ [*N/m*], $b_y=0.02046$ [*Ns/m*], $y_0=0.00047$ [*m*], $y_R=0.0$. The contact law is defined by Eq.(4.1-16), where the following contact parameter have been used: $c_{N0}=0.3\ 10^6$ [*N/m*], $R_Z=5.2$ [*μm*], $\beta c_{N0}=6.0$ [*Ns/m*]. Additionally, the modal parameters of the first bending mode of the pendulum, see Figure 3.6-1, have been estimated by the simple beam theory.

The model investigated is shown in **Fig. 4.2-1**, which is excited by a harmonic displacement of the point *0*. The contact parameters and relative displacements and velocities are assumed to be constant within the contact region. Then, the system response to the harmonic excitation is independent on the number *n* of contact elements and, hence, the number of contact points can be reduced to one. Here, the error with respect to the discretization of the contact area is identical to zero.

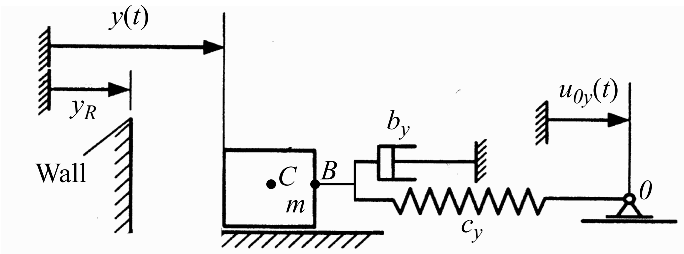

Fig. 4.2-1 Oscillator with elastic contact

In **Fig. 4.2-2**, the comparison of the measurements and calculation of phase diagrams for different excitation angular frequencies ω_E are shown. If the displacement y is less than $y_R=0.0$, the elastic body contacts the wall, see **Fig. 4.2-2a** and **b**. The influence of the higher modes is quite high just after the elastic contact, when separation takes place.

The comparison is good as well for period two oscillations, compare **Fig. 4.2-2c** with **d**, and for higher periodic oscillations, compare **Fig. 4.2-2e** and **f** as well as for chaotic motions, compare **Fig. 4.2-2g** with **h**. Overall, modeling the elasticity of the contact and the higher modes of the elastic body is an extension and an improvement compared to a non-smooth description of the contact law combined with the rigid body formulation, see (Hinrichs et al. 1998).

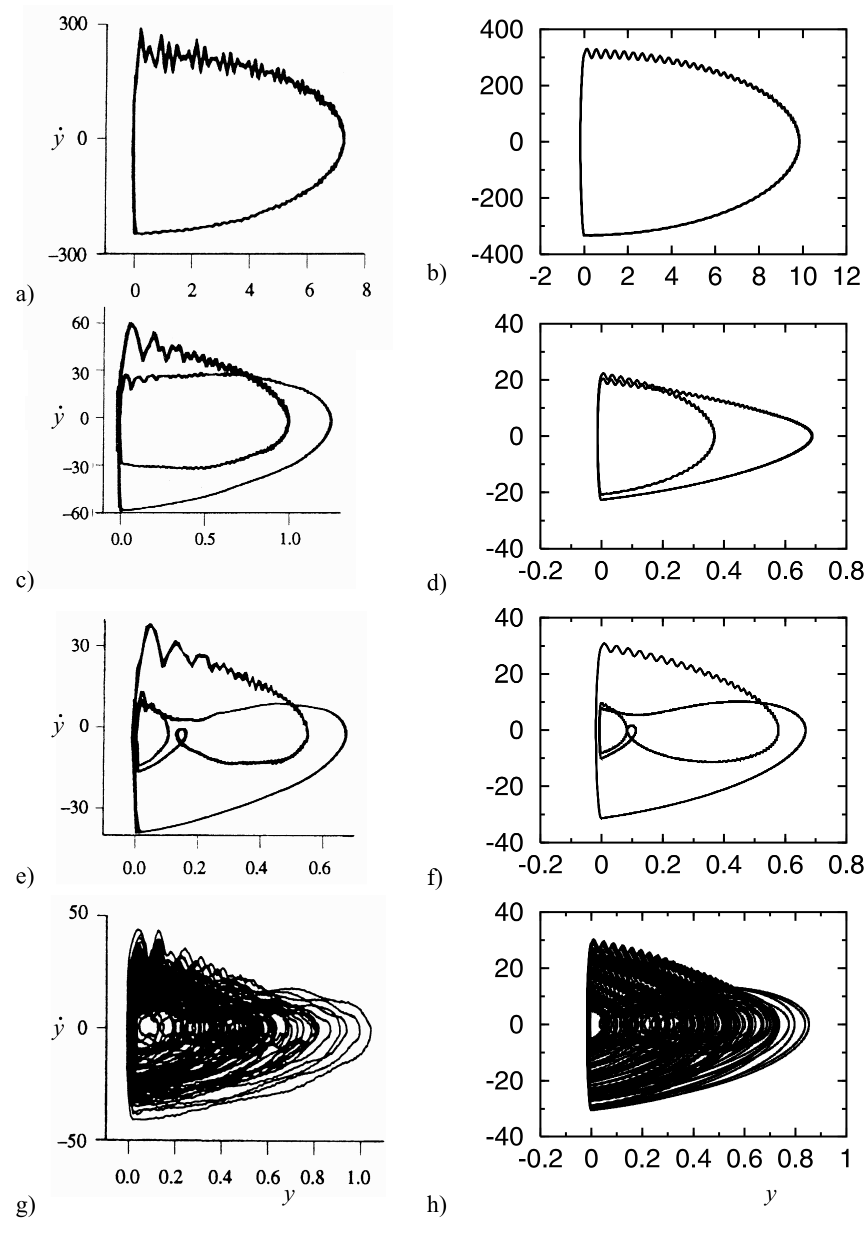

Fig. 4.2-2 Phase diagrams of measurements (Hinrichs 1997b) and calculations for different excitation angular frequencies ω_E **a**) measurement and **b**) calculation for $\omega_E=64.32$ [*rad/s*] **c**) measurement and **d**) calculation for $\omega_E=30.84$ [*rad/s*] **e**) measurement and **f**) calculation for $\omega_E=37.41$ [*rad/s*] **g**) measurement and **h**) calculation for $\omega_E=23.63$ [*rad/s*]

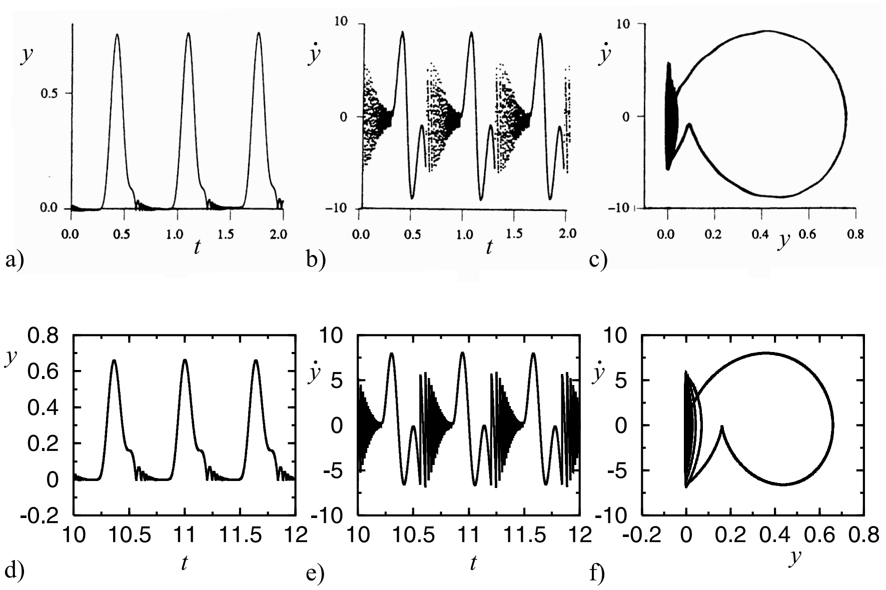

Fig. 4.2-3 Comparison of measurements (Hinrichs 1997b) and calculations for the excitation angular frequencies $\omega_E=9.845\,[rad/s]$ **a**) measurement of displacement and **b**) velocity **c**) measured phase plot **d**) calculation of displacement and **e**) velocity **f**) calculated phase plot

In **Fig. 4.2-3**, a phenomenon is studied which is called chatter. The rebouncing of the oscillator leads to sticking at the stop for an infinite number of elastic contacts. Furthermore, the calculated displacements, velocities and phase plots are compared with the corresponding measurements. In this extreme example, the agreement of measurements and calculations is also very good.

4.3 Friction Oscillator

The experimental setup is shown in Fig. 3.6-1 again and is modified with respect to the friction contact. The pendulum is pressed onto the disc driven with constant speed. The real rotational system is reduced to the friction oscillator shown in **Fig. 4.3-1**, where a belt instead of a disc moves with the velocity *V*. The system is excited by a harmonic displacement of the point *0*. The normal contact force F_{N0} is assumed to be constant.

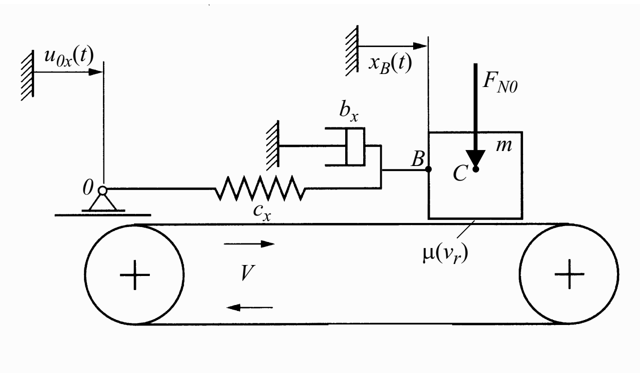

Fig. 4.3-1 Friction oscillator

To verify the tangential contact model, the measurements presented in (Hinrichs et al. 1998), see **Fig. 4.3-2a**, and the following experimental data are used: $V=0.001$ [m/s], $\omega_E=13.8$ [rad/s], $F_{N0}=14.0$ [N], $x_0=0.0005$ [m], $m=5.632$ [kg], $c_x=5610.0$ [N/m], $b_x=0.768$ [Ns/m]. The material contact partners are steel and polyurethane modeled with the following contact parameters: $\mu_0=0.8$, $\mu_\infty=0.55$, $\lambda_e=1000.0$ [s/m], $c_{N0}=10.0\ 10^6$ [N/m], $R_Z=10.0$ [μm], $\beta c_{N0}=40.0$ [Ns/m]. The error with respect to the discretization is again zero, because only translations of the mass are involved. For a given normal contact force, the static normal displacement has to be calculated iteratively, because the normal force is nonlinearly dependent on the relative normal displacement by Eq.(4.1-16). This iteration can be omitted, if the first rigid body mode in the normal direction is included within the model of the elastic body. The rigid body mode of the mass in the tangential direction results in a one-periodic solution shown in **Fig. 4.3-2b**. Including the elasticity of the higher mode leads to an improvement of the calculations, see **Fig. 4.3-2c**, which shows oscillations with higher frequency after the transition from slip to stick. The modal parameters for this higher mode have been approximated by the data given in (Hinrichs 1997a). However, the calculations do not show the measured high-periodic oscillations. Hinrichs (1997a) explained this phenomenon with a stochastic varying friction coefficient.

A further reason for this physical effect can be the surface profile. Besides the roughness, the waviness of the contact surface can influence the dynamical behavior. Assuming that the waviness of the ground is dominated by a single sine wave, the displacement in the y-direction at the node j is given by

$$y_{Rj} = y_A \sin\left(2\pi \frac{u_{rj}}{\lambda}\right), \tag{4.3-1}$$

with the wave amplitude y_A, the wave length λ and the relative displacement u_{rj} given by Eq.(4.1-19). The wave amplitude of $y_A=200.0$ [μm] and the wave length of $\lambda=2.5$ [mm] results in a higher-periodic solution shown in **Fig. 4.3-2d**, which shows a good qualitative and quantitative agreement with the measurement, shown in Fig. 4.3-2a. A further improvement of the calculation could be to use the wave spectrum of the surface and to expand Eq.(4.3-1) in a Fourier series.

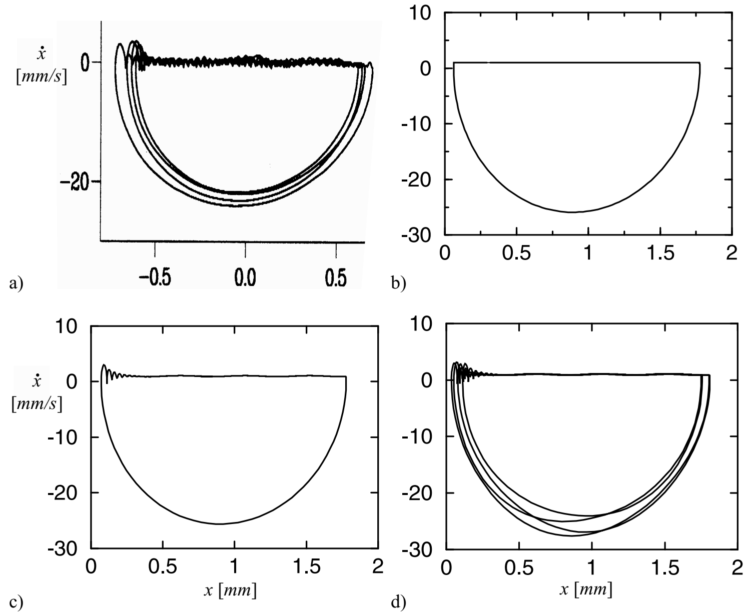

Fig. 4.3-2 Phase diagrams **a**) measurement (Hinrichs 1997a) **b**) calculation using two modes **c**) three modes **d**) three modes plus modeling waviness

The analysis of systems with dry friction shows a rich dynamic behavior from equilibrium to chaos. Bifurcation scenarios like period doubling sequences are described for example in (Feeny and Moon 1994; Oestreich et al. 1996; Popp et al. 1995a, 1995b, 1996, 2005, Hoffmann 2006).

4.4 Bifurcations in Dynamical Systems with Friction

In (Stelter and Sextro 1991) the bifurcation theory described in (Seydel 1983) has been applied to a two degree of freedom system using a smooth friction characteristic. Period doublings and Hopf-bifurcations as well as turning points have been determined. Both, unstable branches and stable coexisting solutions have been calculated. Several jumping effects, which are typical for nonlinear systems, have been found. The mathematical modelling of dry friction forces leads to nonlinear equations of motion. Beside of periodic solutions, more complicated motions are possible. When these motions are generated by deterministic equations, deterministic chaos may occur. The routes to chaos may be via period doublings, torus-bifurcations or intermittency, see (Kreuzer 1987) and (Troger 1991). One aim of the investigations is to calculate the bifurcations, where the solution changes dramatically. The classification of the bifurcations is possible by the Floquet theory, see (Seydel 1988a) and Iooss (1980). Furthermore, the typical bifurcation scenarios are most important for the understanding of self-sustained oscillations. In order to show the basic phenomena of dynamic systems with dry friction, a simple model of a two mass spring system has been taken in account leading to the following set of equation of motion, see (Stelter 1990) and (Stelter and Sextro 1991)

$$\begin{aligned} x_1' &= x_2 \\ x_2' &= \left[-(1+\kappa)x_1 - 2D(1+\delta)x_2 + x_3 + 2Dx_4 + B\rho\{\mu(x_2=0) - \mu(v_{r1})\}\right] \\ x_3' &= x_4 \\ x_4' &= x_1 + 2Dx_2 - x_3 - 2Dx_4 + B\{\mu(x_4=0) - \mu(v_{r2})\} \end{aligned} \tag{4.4-1}$$

Eq.(4.4-1) represents a two-masses-spring-damper system, which is excited by friction forces exerted by a running band. Self-excitation due to dry friction is only possible when the friction force has a decreasing characteristic, see (Magnus 1976). The parameter dependencies of the solution can be calculated with program package BIFPACK. Furthermore, the bifurcation behaviour can be investigated with the use of the Floquet theory, see (Seydel 1988a), (Hagedorn 1984) and (Iooss 1980). With the Floquet theory a unique classification of the global bifurcations is possible. For generalization the following abbreviations have been introduced: the mass ratio

$$\gamma := m_1 / m_2\,, \tag{4.4-2}$$

the damping ratio

$$\delta := d_1 / d_2\,, \tag{4.4-3}$$

the stiffness ratio

$$\kappa := c_1 / c_2\,, \tag{4.4-4}$$

the normal force ratio

$$\rho := F_{N1} / F_{N2} \tag{4.4-5}$$

and the load parameter

$$B := F_{N2} / c_2\,. \tag{4.4-6}$$

The dimensionless damping is given by

$$D := d_2 / 2\sqrt{c_2 m_2}\,. \tag{4.4-7}$$

The chosen parameter values are

$$\omega_2 = 1.0s^{-1}, \gamma = 2.5, \delta = 1.0, \kappa = 2.0 \text{ and } \rho = 1.0\,.$$

The nonlinear structure of equation (4.4-1) becomes obvious by the vector notation

$$\boldsymbol{x}' = \boldsymbol{A}\boldsymbol{x} + \boldsymbol{r}(\boldsymbol{x}) \tag{4.4-8}$$

where **A** is the linear system matrix and **r** is the vector of the nonlinear friction forces. For the use of the program package BIFPACK developed by Seydel (1988b), the function of friction force has to be continuously differentiable. Thus, for the numerical simulations the following model for the friction characteristic was used

$$
\begin{aligned}
&F_{Ri} = -F_{Ni}\mu(v_{ri}) \\
&\mu(v_{ri}) = a_1\big(1 + a_2\exp(-b|v_{ri}|\big)\arctan(b_2 v_{ri}) \\
&i = 1,2
\end{aligned}
\qquad (4.4\text{-}9)
$$

with the constants

$$a_1 = 0.14,\ a_2 = 1.14,\ b_1 = 2.0s/m,\ b_2 = 100.0s/m\,,$$

where γ denotes the friction coefficient, which depends on the relative velocity v_r, and F_N denotes the normal force. The relative velocities is given by

$$v_{ri} = \omega_2 x'_{2i} - v_0\,. \qquad (4.4\text{-}10)$$

To be able to characterize the solution nearby the equilibrium the Jacobian $\boldsymbol{J}$ has to be calculated by differentiation of Eq.(4.4-8) with regard to $\boldsymbol{x}$.

$$\boldsymbol{J}(\boldsymbol{x}) = \boldsymbol{A} + \frac{\partial \boldsymbol{r}(\boldsymbol{x})}{\partial \boldsymbol{x}} \qquad (4.4\text{-}11)$$

The amplitude x_3 has been used to show the bifurcation behaviour. The important parameters of the system are the load parameter B, the band velocity v_0 and the damping D. Within the bifurcation diagrams, Hopf-bifurcations, turning points and period doubling occur, while stationary bifurcations do not appear. To determine the Hopf-bifurcations, one has to calculate the eigenvalues of the Jacobian. They occur when a complex pair crosses the imaginary axis. The equilibrium $\boldsymbol{x=0}$ is stable, when all eigenvalues are within the left side of the complex plane.

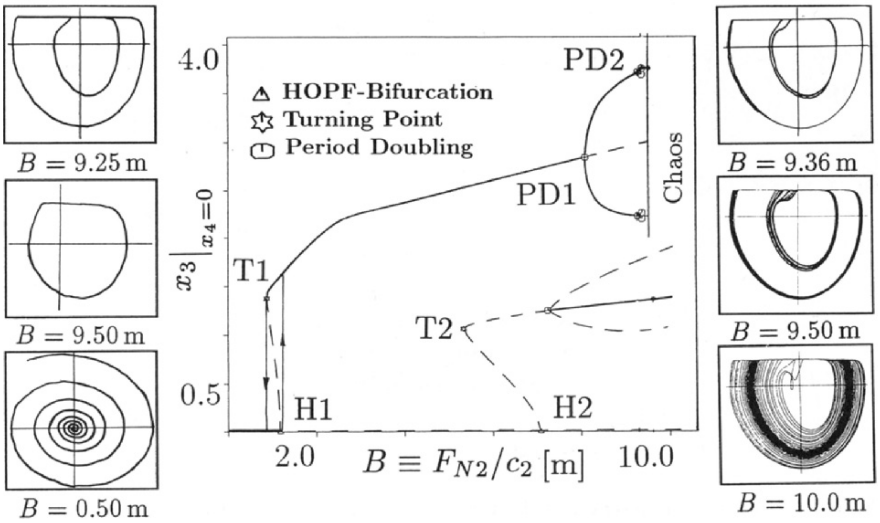

Fig. 4.4-1 Bifurcation diagram of the load parameter with phase plane plots

In the bifurcation diagram of the load parameter, see **Fig. 4.4-1** a sub-critical Hopf-bifurcation (H1) arises at a parameter value of B=1.12 m, while a special Hopf-bifurcation (H2) occurs at B=7.09 m. Starting from the equilibrium the amplitude is jumping from the sub-critical Hopf-bifurcation (H1) to the stable periodic branch. On the other hand, coming from the periodic branch, the amplitude is jumping from the turning point (T1) to the equilibrium. This jumping phenomenon is typical for systems with dry friction. The unstable branch between the turning point and the sub-critical Hopf-bifurcation can be understood as a borderline between the stable attractors. Here, a stable periodic attractor and a stable equilibrium coexist within a parameter range of 0.88 m<B<1.12 m. Following the periodic attractors several period doublings occur, which end in a chaotic motion. The calculated period doublings are at the load parameters of 8.09 m, 9.26 m, and 9.36 m. Beside the bifurcation scenario via period doubling a coexisting periodic solution starts at a load parameter of B=7.25 m.

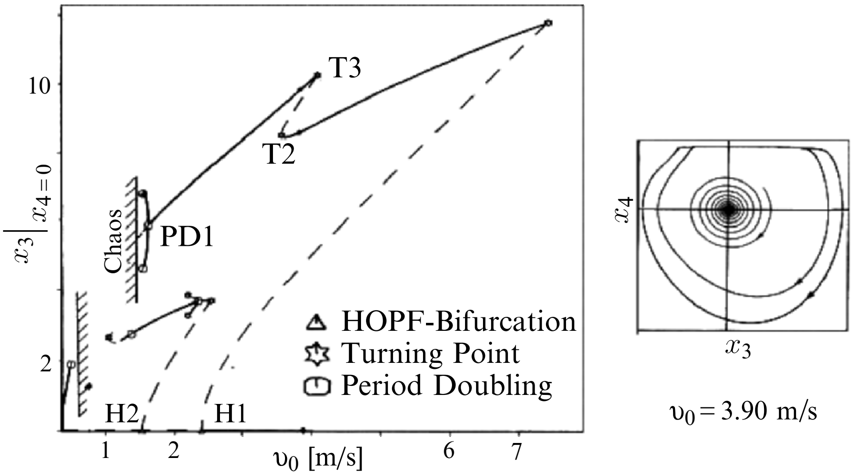

Fig. 4.4-2 Bifurcation diagram of the band velocity

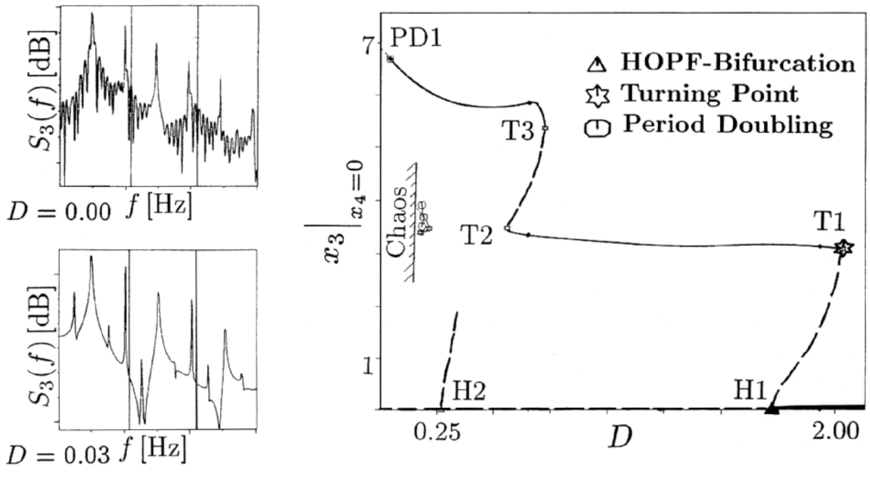

Fig. 4.4-3 Bifurcation diagram of the damping coefficient

Furthermore the bifurcation diagrams of the band velocity, see **Fig. 4.4-2**, and the damping ratio *D*, see **Fig. 4.4-3**, and have been obtained by means of the program package BIFPACK. They also show turning points, Hopf-bifurcations and period doublings. The routes to chaos are also via period doublings. Coexisting solutions, which are limited by sub-critical period doublings and turning points, could be determined. In Fig. 4.4-2, three stable attractors coexist within the parameter range of 3.57 m/s < v_0 < 4.09 m/s.

5 Friction Damping of Elastic Multibody Systems

Contact interfaces with friction can be used as damping device to reduce the alternating stresses of elastic structures. Besides the increase of lifetime, the generation of noise can be reduced as well. A further advantage can be that because of the reduced stresses, the construction can be designed lighter and, hence, this saves energy. Up to now, there exist a rich literature applying different solution methods to friction damping of elastic structures, see for example (Goodman and Braun 1962; Gaul 1983; Wißbrock 1985; Klamt 1990; Brendel 1990; Blohm 1992; Gaul et al. 1994; Braun 1996; Sextro 1999a, 1999b; Petrov 2004). Bohlen (1987) used the modal description to reduce the dynamical problem of a continuous structure to calculate the forced vibration of a system with friction contacts. A detailed overview of literature due to this topic is presented in (Popp 1994; Gaul and Nitsche 2000, Popp et al. 2003). The calculation and the optimization of the spatial dynamics of real elastic structures including expanded friction contacts is still a numerical problem. The scope of this Chapter is to present a calculation method to be able to analyze the spatial dynamic response of realistic systems. This method will be verified by experiments and applied to bladed disc assemblies in Turbomachinery.

5.1 Forced Vibrations of Elastic Structures

A typical example of elastic structures with friction contacts is a bladed disc assembly with shrouds. To calculate the dynamic response due to the forced excitation of the blades with friction contacts, Treyde (1995) used the modal description for the elastic components and the theory of Cattaneo (1938), Mindlin (1949) and Mindlin et al. (1951) to describe the contact between adjacent shrouds, see **Fig. 5.1-1**, and the Harmonic Balance Method to linearize the contact model. In Fig. 5.1-1, two different common designs are shown. For the investigations of the blade vibrations, coordinate systems have to be introduced. The top view of the shroud construction and the used coordinate systems are depicted in **Fig. 5.1-2**. The blade vibrations are described in the *A*-coordinate-system, which is fixed to the root of each blade. The index *N* denotes the number of blades. The *y*- and *z*-axis of each *S*-coordinate-system is parallel to the contact interface of the shroud. The transformation from the *A*- to the *S*-coordinate-system is defined by the shroud angle β. The *R*-coordinate-systems are situated in the contact interfaces and have the same orientation as the *S*-coordinate-systems.

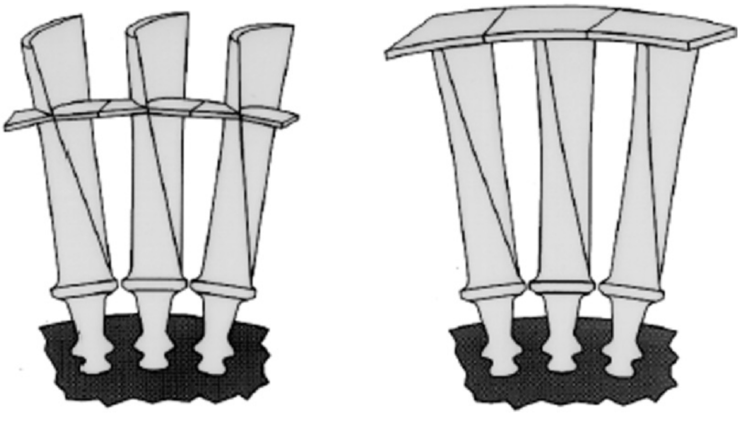

Fig. 5.1-1 Two examples of shrouded blades with friction contacts

The shape of the contact interfaces of shrouds is rectangular in most cases, see **Fig. 5.1-3**, with the width b_0 and the height h_0. The origin *O* of the *R*-coordinate-system is placed in the center of the contact interface. The point *OR* denotes the center of the right contact surface of the i^{th} blade, while the point *OL* denotes the center of the left contact surface of the $(i+1)^{th}$ blade.

In praxis, the amplitudes of the excitation forces of the system are approximated in a common way, using the stationary gas force and introducing the stimulus, which describes the percentage of the dynamical force amplitudes relative to the stationary gas force. Furthermore, it is assumed, that the excitation forces are monofrequent. In this Chapter, it is assumed that the contact behavior is linear. Then, the system response is monofrequent as well. Because of simplicity, the complex notation is used to describe the monofrequent forces and displacements. Hence, the excitation forces are given by

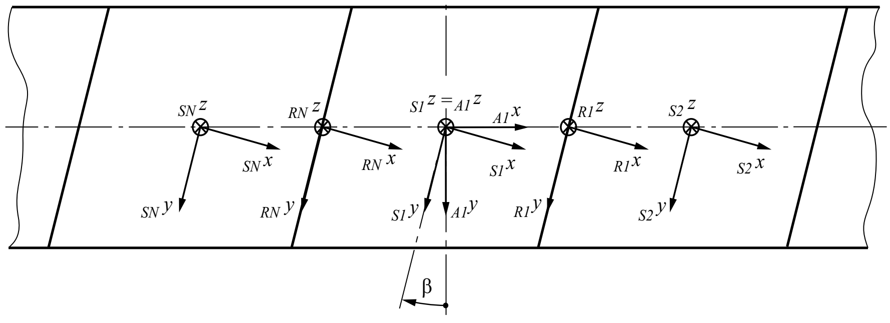

Fig. 5.1-2 Top view and coordinate systems

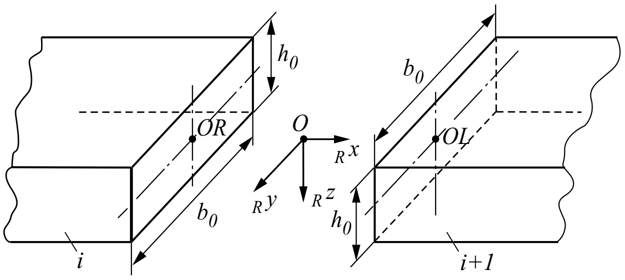

Fig. 5.1-3 Geometry of a contact interface

$$\boldsymbol{f}_E(t) = \hat{\boldsymbol{f}}_E e^{i\Omega t}, \tag{5.1-1}$$

the modal coordinates by

$$\boldsymbol{q}(t) = \hat{\boldsymbol{q}} e^{i\Omega t} \tag{5.1-2}$$

and the physical displacements by

$$\boldsymbol{w}(t) = \hat{\boldsymbol{w}} e^{i\Omega t}. \tag{5.1-3}$$

In a first step, one elastic structure contacting a rigid wall is modeled. This is done, because the extension to a system shown in Fig. 5.1-3, where two elastic structures contact each other is relatively easy. Assuming one elastic structure with one contact interface and inserting Eq.(5.1-1) and Eq.(5.1-2) in Eq.(2.4-15), the equation of motion becomes

$$\hat{\boldsymbol{S}}\,\hat{\boldsymbol{q}} = \boldsymbol{T}_E^T \hat{\boldsymbol{f}}_E + \boldsymbol{T}_O^T \; {}^{RA}\boldsymbol{A}^T \hat{\boldsymbol{f}}_O\,, \tag{5.1-4}$$

with the system matrix for one elastic structure

$$\hat{\boldsymbol{S}} = \boldsymbol{diag}\,(\omega_{0j}^2 - \Omega^2 + \mathrm{i}2\omega_{0j}\Omega \mathrm{D}_\mathrm{j})\,, \tag{5.1-5}$$

the index j for the j^{th} mode, the excitation angular frequency Ω, the vector of the modal coordinates $\boldsymbol{q}$, the modal matrix $\boldsymbol{T}$, the generalized excitation force vector $\boldsymbol{f}_E$ defined in the A-coordinate system, the transformation matrix ${}^{AR}\boldsymbol{A}$, the modal parameters as described in Chapter 2.4 and the generalized contact force vector $\boldsymbol{f}_O$ with respect to the point O in R-coordinates

$$\hat{\boldsymbol{f}}_O = \begin{bmatrix} \hat{F}_x & \hat{F}_y & \hat{F}_z & \hat{M}_x & \hat{M}_y & \hat{M}_z \end{bmatrix}_O^T. \tag{5.1-6}$$

It is assumed, that the generalized contact forces are related to a contact stiffness matrix and the relative motion of both interfaces to each other, which includes six degrees of freedom, can be described by three relative translations and three relative rotations, u_{jO} and φ_{jO} respectively with $j=x,y,z,$ assuming $|\varphi_{jO}| \ll 1$. This can be summarized by

$$\hat{\boldsymbol{f}}_O = \hat{\boldsymbol{K}}_O \hat{\boldsymbol{u}}_O \tag{5.1-7}$$

with

$$\hat{\boldsymbol{u}}_O = \hat{\boldsymbol{u}}_{OL} - \hat{\boldsymbol{u}}_{OR} = \begin{bmatrix} \hat{u}_x & \hat{u}_y & \hat{u}_z & \hat{\varphi}_x & \hat{\varphi}_y & \hat{\varphi}_z \end{bmatrix}_O^T. \tag{5.1-8}$$

Assuming that the $(i+1)$-structure does not vibrate, the generalized relative displacement vector in R-coordinates can be determined by

$$\hat{\boldsymbol{u}}_O = -{}^{RA}\boldsymbol{A}\,\boldsymbol{T}_O\,\hat{\boldsymbol{q}}\,, \tag{5.1-9}$$

Inserting Eq.(5.1-7) and Eq.(5.1-8) in Eq.(5.1-4) gives

$$\hat{\boldsymbol{A}}\,\hat{\boldsymbol{q}} = \boldsymbol{T}_E^T\,\hat{\boldsymbol{f}}_{\mathrm{E}}\,. \tag{5.1-10}$$

with

$$\hat{\boldsymbol{A}} = \hat{\boldsymbol{S}} + \boldsymbol{T}_O^T\;{}^{RA}\boldsymbol{A}^T\,\hat{\boldsymbol{K}}_O\,{}^{RA}\boldsymbol{A}\,\boldsymbol{T}_O\,.$$

Solving this set of linear equations with regard to the modal coordinates, finally, the complex amplitudes of any node can be determined by

$$\hat{\boldsymbol{w}} = \boldsymbol{T}\hat{\boldsymbol{q}}. \tag{5.1-11}$$

Modeling elastic structures with friction contacts leads to the same type of equation as shown in Eq.(5.1-10), where the matrices and vectors have to be adjusted corresponding to the investigated system. For example, the system equation of two elastic structures contacting each other, see Fig. 5.1-3, the corresponding components of Eq.(5.1-10) are given by

$$\begin{gathered}
\hat{\boldsymbol{S}} = \begin{bmatrix} \hat{\boldsymbol{S}}_1 & \boldsymbol{0} \\ \boldsymbol{0} & \hat{\boldsymbol{S}}_2 \end{bmatrix}, \\
\boldsymbol{T}_E^T = \begin{bmatrix} \boldsymbol{T}_{E1}^T & \boldsymbol{0} \\ \boldsymbol{0} & \boldsymbol{T}_{E2}^T \end{bmatrix}, \\
\hat{\boldsymbol{q}} = \begin{bmatrix} \hat{\boldsymbol{q}}_1^T & \hat{\boldsymbol{q}}_2^T \end{bmatrix}^T, \\
\hat{\boldsymbol{f}}_E = \begin{bmatrix} \hat{\boldsymbol{f}}_{E1}^T & \hat{\boldsymbol{f}}_{E2}^T \end{bmatrix}^T, \\
\boldsymbol{T}_O = \begin{bmatrix} -\boldsymbol{T}_{OR1} & \boldsymbol{T}_{OL2} \end{bmatrix}.
\end{gathered} \tag{5.1-12}$$

A system with N elastic structures, where structure i contacts structure $i+1$ is defined by

$$\begin{gathered}
\hat{\boldsymbol{S}} = \boldsymbol{diag}(\hat{\boldsymbol{S}}_i), \quad \hat{\boldsymbol{K}}_O = \boldsymbol{diag}(\hat{\boldsymbol{K}}_{Oi}), \\
{}^{RA}\boldsymbol{A} = \boldsymbol{diag}({}^{RA}\boldsymbol{A}_i), \quad \boldsymbol{T}_E^T = \boldsymbol{diag}(\boldsymbol{T}_{Ei}^T), \\
\hat{\boldsymbol{q}} = \begin{bmatrix} \hat{\boldsymbol{q}}_1^T & \hat{\boldsymbol{q}}_2^T & \cdots & \hat{\boldsymbol{q}}_N^T \end{bmatrix}^T, \quad \hat{\boldsymbol{f}}_E = \begin{bmatrix} \hat{\boldsymbol{f}}_{E1}^T & \hat{\boldsymbol{f}}_{E2}^T & \cdots & \hat{\boldsymbol{f}}_{EN}^T \end{bmatrix}^T, \\
\boldsymbol{T}_O = \begin{bmatrix} -\boldsymbol{T}_{OR1} & \boldsymbol{T}_{OL2} & \cdots & \boldsymbol{0} \\ \boldsymbol{0} & -\boldsymbol{T}_{OR2} & \cdots & \boldsymbol{0} \\ \vdots & \vdots & \ddots & \boldsymbol{T}_{OLN} \\ \boldsymbol{T}_{OL1} & \boldsymbol{0} & \boldsymbol{0} & -\boldsymbol{T}_{ORN} \end{bmatrix}.
\end{gathered} \tag{5.1-13}$$

If this system is cut off at the contact $i=N$, the corresponding contact stiffness matrix is set to be a zero matrix. Then a system with chain type is modeled, which is used with respect to the comparison of measurements and calculations in Chapter 5.3. If a cyclic system is investigated, cyclic boundary conditions can be used to reduce the system equations and therefore the computation time dramatically. In Chapter 5.5, this system reduction is used to simulate and to optimize the dynamics of a bladed disc assembly with shrouds.

Due to the nonlinear behavior of friction contacts the contact stiffness matrix, see Eq.(5.1-7), will be nonlinearly dependent on the generalized relative displacement with respect to the points *OL* and *OR*. This nonlinear contact behavior will be derived using the point contact model from Chapter 3.7 in the following.

5.2 Macroscopic Contact Model

Solving an elastic multibody and multicontact problem with friction leads in general to an enormous calculation time using for example standard FEMs. In the case of monofrequent excitation of the linear elastic structure with friction contacts, the Harmonic Balance Method (HBM), see (Magnus and Popp 1997), is used to linearize the nonlinear contact forces and, hence, to reduce the numerical problem, see (Sextro et al. 1998a). To apply this method to the contact forces, harmonic normal and tangential relative displacements have to be assumed.

Because of the nonlinear contact forces due to friction and the spatial motion, the contact planes have to be discretized, see **Fig. 5.2-1**. The developed point contact model described in Chapter 3.7 is used to calculate the normal and tangential forces for each contact area element. The width and the height of one nominal area element are defined by

$$\Delta b_0 = \frac{b_0}{n_y}, \quad \Delta h_0 = \frac{h_0}{n_z}, \tag{5.2-1}$$

respectively, where n_y and n_z denote the number of area elements in the *y*- and *z*-direction.

The displacement with respect to the point *M* can be approximated by the displacement of the center point *OR*, assuming, that elastic deformations between the points *OR* and *M* can be neglected. Then the relative displacement vector with respect to the point *M* is given by

$$\boldsymbol{u}_M = \boldsymbol{G}_{OM} \boldsymbol{u}_O \tag{5.2-2}$$

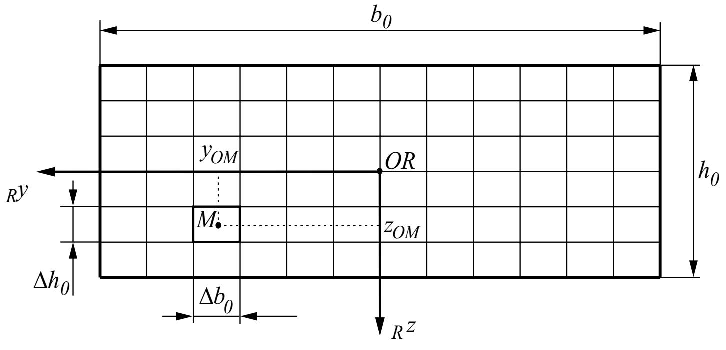

Fig. 5.2-1 Discretized nominal contact area

with

$$\boldsymbol{u}_M = \begin{bmatrix} u_x \; u_y \; u_z \end{bmatrix}_M^T , \qquad (5.2\text{-}3)$$

the transformation matrix

$$\boldsymbol{G}_{OM} = \begin{bmatrix} 1 & 0 & 0 & 0 & z_{OM} & -y_{OM} \\ 0 & 1 & 0 & -z_{OM} & 0 & 0 \\ 0 & 0 & 1 & y_{OM} & 0 & 0 \end{bmatrix} \qquad (5.2\text{-}4)$$

and Eq.(5.1-8).

Before analyzing the dynamic contact model, the equilibrium position of both contact surfaces relative to each other has to be determined. For calculating the equilibrium position, friction is neglected, because if the system is excited monofrequent, the average values of the friction forces are zero. Then, for calculating the equilibrium position the tangential forces and the torsional moment with respect to the *x*-axis are identical to zero, see Fig. 5.2-1. The normal force for each contact element can be calculated using Eq.(3.3-24). The resultant normal force and the moments with respect to the *y*- and *z*-axis are determined by

$$\begin{bmatrix} F_N^* \\ M_y^{*(O)} \\ M_z^{*(O)} \end{bmatrix} = \sum_{i=1}^{n_y n_z} \begin{bmatrix} 1 \\ z^* \\ -y^* \end{bmatrix} \Delta F_N^*(u_x^*) \qquad (5.2\text{-}5)$$

with the dimensionless parameter

$$F_N^* = \frac{F_N}{c_{N0} R_Z}, \quad M_y^{*(O)} = \frac{M_y^{(O)}}{c_{N0} R_Z h_0}, \quad M_z^{*(O)} = \frac{M_z^{(O)}}{c_{N0} R_Z b_0},$$
$$z^* = \frac{z}{h_0}, \quad y^* = \frac{y}{b_0}, \quad \Delta F_N^* = \frac{\Delta F_N}{\Delta c_{N0} R_Z}. \qquad (5.2\text{-}6)$$

If instead of the generalized displacement of the reference point *O*, the generalized forces are known, then Eq.(5.2-5) has to be solved iteratively, for example by the Newton method. Assuming the kinematics of the center points are given, the dimensionless relative normal displacement follows from Eq.(5.2-2) by

$$u_x^* = u_{0x}^* + z^* \varphi_{0y}^* - y^* \varphi_{0z}^* \qquad (5.2\text{-}7)$$

with the normalized generalized displacements

$$u_{0x}^* = \frac{u_{0x}}{R_Z}, \quad \varphi_{0y}^* = \varphi_{0y} \frac{h_0}{R_Z}, \quad \varphi_{0z}^* = \varphi_{0z} \frac{b_0}{R_Z}. \qquad (5.2\text{-}8)$$

In **Fig. 5.2-2** the normalized normal force and the moment with respect to the *y*-axis is calculated varying the relative angle with respect to the *y*-axis for different number n_y of discrete contact elements. The relative error between the results of $n_y=8$ and $n_y=1024$ is relative small, that means, in this case a small number of contact elements results in a good numerical approximation. The presented results are independent on the number of elements in the *z*-direction. If only translations are involved, than the error due to the discretization is identical to zero. Further investigations with respect to the tangential contact problem can be found in (Sextro 1997).

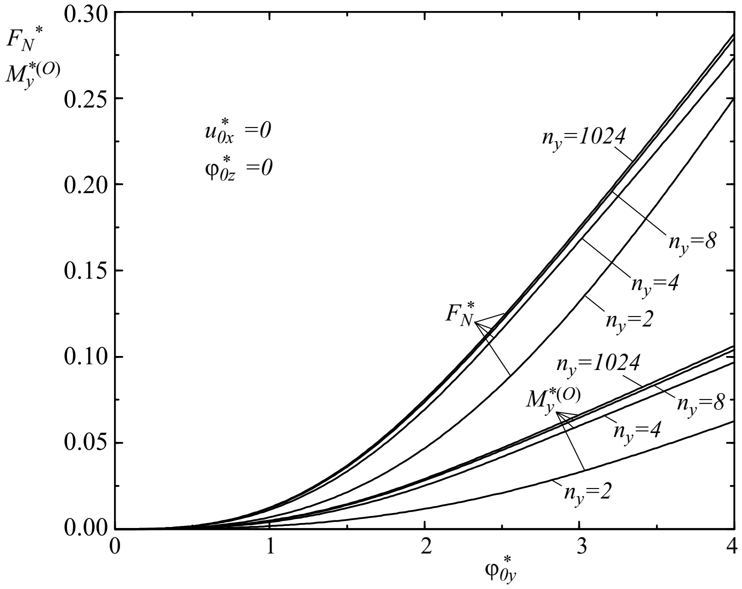

Fig. 5.2-2 Influence of the discretization onto the normal force and moment varying the relative angle with respect to the *y*-axis

The displacements of the center points *OL* and *OR* are calculated using the modal description of both elastic structures described in Chapter 5.1. For monofrequent motions of the points *OL* and *OR*, the kinematics of the relative displacement vector $\boldsymbol{u}_M$ of the point *M* results in an ellipse in space. Starting with the normal contact problem, the harmonic normal displacement can be described by

$$u_x^* = u_G^* + u_A^* \cos t^* , \tag{5.2-9}$$

with the dimensionless time

$$t^* = \omega_0 t , \tag{5.2-10}$$

where u_G denotes the equilibrium position and u_A the amplitude. Now, the harmonic linearized complex normal stiffness

$$\Delta\hat{K}_\xi^* = \Delta c_\xi^* + i\Delta b_\xi^* \tag{5.2-11}$$

is defined by the real stiffness coefficient

$$\Delta c_\xi^* = \frac{1}{\pi u_A^*} \int_0^{2\pi} \Delta F_N^*(t^*) \cos t^* \, dt^* \tag{5.2-12}$$

and the imaginary stiffness coefficient

$$\Delta b_\xi^* = -\frac{1}{\pi u_A^*} \int_0^{2\pi} \Delta F_N^*(t^*) \sin t^* \, dt^* \tag{5.2-13}$$

with the dimensionless parameters

$$\Delta c_\xi^* = \frac{\Delta c_\xi}{\Delta c_{N0}}, \quad \Delta b_\xi^* = \frac{\Delta b_\xi}{\Delta c_{N0}}, \tag{5.2-14}$$

where ξ corresponds to the x-axis, see Fig. 5.1-3. Here, the normal force is given by Eq.(3.7-30) neglecting damping ($\beta=0$). Note, that the linearized stiffness coefficients are nonlinear dependent on the equilibrium position u_G and the vibration amplitude u_A.

To be able to apply the harmonic balance method to the tangential problem, it is assumed, that the vibration amplitudes in the normal direction are relative small, $u_A^* \ll 1$, and hence that the normal force is approximately constant. Then, for monofrequent motions, the kinematics of the point M result in an ellipse in the contact plane, see **Fig. 5.2-3**. The principle η,ζ-axes of the ellipse as well as the orientation can be calculated by the relative displacements, see (Sextro 1999b), and hence the motion can be described more easily in the main E-coordinate system of the ellipse, which corresponds to the ξ,η,ζ-coordinate-system described in Fig. 5.2-3. The half-axes of the ellipse can be calculated by transforming the relative displacements into the main E-coordinate system of the ellipse. Then, the transformation matrix from the R-coordinate system into the E-coordinate system of the ellipse within the contact interface is given by

$$^{ER}\boldsymbol{A} = \begin{bmatrix} 1 & 0 & 0 \\ 0 & \cos\delta & \sin\delta \\ 0 & -\sin\delta & \cos\delta \end{bmatrix} \tag{5.2-15}$$

with the transformation angle δ given by, see (Sextro 1997a, 1999b)

$$\delta = \frac{1}{2}\arctan\left(2\frac{\hat{u}_y^r \hat{u}_z^r + \hat{u}_y^i \hat{u}_z^i}{\left|\hat{u}_y\right|^2 + \left|\hat{u}_z\right|^2} \right). \tag{5.2-16}$$

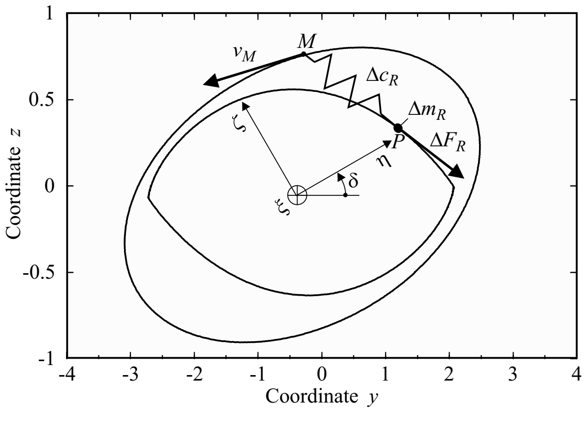

Fig. 5.2-3 Tangential point contact model

For the tangential contact problem, it is assumed, that the normal forces are approximately constant. Then due to the three-dimensional contact model described in Chapter 3.7, the tangential contact problem reduces to a two-dimensional point contact model based on dry friction, constant tangential stiffnesses and elliptical trajectories to calculate the tangential forces, see Fig. 5.2-3. Furthermore, Coulomb friction is assumed and the tangential contact stiffnesses are assumed to be isotropic. Then with the abbreviation of the reduced mass

$$\Delta m_R = \Delta m_{R0} h^* \tag{5.2-17}$$

and the constant tangential stiffness

$$\Delta c_R = \Delta c_{R0\eta} h^* = \Delta c_{R0\zeta} h^* \tag{5.2-18}$$

the coupled equation of motion are given by

$$\begin{aligned} \Delta m_D^* \eta_P''^* &= F_{F\eta}^* - \mu^*(v_P^*) \frac{\eta_P'^*}{v_P^*}, \\ \Delta m_D^* \varsigma_P''^* &= F_{F\zeta}^* - \mu^*(v_P^*) \frac{\zeta_P'^*}{v_P^*} \end{aligned} \tag{5.2-19}$$

with the new dimensionless parameters

$$\begin{aligned} \Delta m_D^* &= \frac{\Delta m_D \omega_0^2}{\Delta c_R}, \quad F_{F\eta,\zeta}^* = \frac{F_{F\eta,\zeta}}{\mu_0 \Delta F_N}, \\ \eta_P^* &= \frac{\Delta c_R \eta_P}{\mu_0 \Delta F_N}, \quad \zeta_P^* = \frac{\Delta c_R \varsigma_P}{\mu_0 \Delta F_N}. \end{aligned} \tag{5.2-20}$$

The damping coefficient $\beta^*=0$ is set to be zero. Then the normalized spring force is given by

$$\begin{aligned} F_{F\eta}^* &= u_\eta^* = \eta_M^* - \eta_P^*, \\ F_{F\zeta}^* &= u_\zeta^* = \zeta_M^* - \zeta_P^*. \end{aligned} \tag{5.2-21}$$

Due the requirements defined in Chapter 3.3, the normalized mass has to be small

$$\Delta m_D^* << 1, \tag{5.2-22}$$

say 10^{-3}. Now, assuming an elliptical motion of the point M with the half-axes η_A and ζ_A,

$$\begin{aligned} \eta_M^* &= \eta_A^* \cos\tau, \\ \zeta_M^* &= \zeta_A^* \sin\tau, \end{aligned} \tag{5.2-23}$$

and applying the HBM to the spring forces ΔF_F, these forces can be approximated by complex stiffnesses, which are nonlinearly dependent on the half-axes of the ellipse. Knowing the tangential stiffness and the average normal force, the harmonic linearized complex tangential stiffnesses for elliptical trajectories

$$\begin{aligned} \Delta\hat{K}_\eta^* &= \Delta c_\eta^* + i\Delta b_\eta^*, \\ \Delta\hat{K}_\varsigma^* &= \Delta c_\varsigma^* + i\Delta b_\varsigma^* \end{aligned} \tag{5.2-24}$$

can be calculated by

$$\Delta c_{\eta}^{*} = \frac{1}{\pi \eta_{A}^{*}} \int_{0}^{2\pi} F_{F\eta}^{*}(\tau) \cos\tau \, d\tau \,, \tag{5.2-25}$$

$$\Delta b_{\eta}^{*} = -\frac{1}{\pi \eta_{A}^{*}} \int_{0}^{2\pi} F_{F\eta}^{*}(\tau) \sin\tau \, d\tau \,, \tag{5.2-26}$$

$$\Delta c_{\varsigma}^{*} = \frac{1}{\pi \zeta_{A}^{*}} \int_{0}^{2\pi} F_{F\varsigma}^{*}(\tau) \sin\tau \, d\tau \,, \tag{5.2-27}$$

$$\Delta b_{\varsigma}^{*} = \frac{1}{\pi \zeta_{A}^{*}} \int_{0}^{2\pi} F_{F\varsigma}^{*}(\tau) \cos\tau \, d\tau \,, \tag{5.2-28}$$

see also (Sextro et al. 1998b). This simplified point contact model is used to calculate the tangential forces for each contact area element. If the mass is set to be zero, then the equation of motion has to be differentiated to be able to solve the differential equation with standard numerical integration methods. This procedure is presented in (Sextro and Popp 1996, 1999c).

Transforming the contact forces with respect to the point *M* back into the *R*-coordinate-system leads to

$$\Delta\hat{\boldsymbol{f}}_{M} = {}^{ER}\boldsymbol{A}^{T} \, \Delta\hat{\boldsymbol{K}}_{M} \, {}^{ER}\boldsymbol{A} \, \hat{\boldsymbol{u}}_{M} \,, \tag{5.2-29}$$

with the complex stiffness matrix for the point contact

$$\Delta\hat{\boldsymbol{K}}_{M} = \begin{bmatrix} \Delta\hat{K}_{\xi}(u_G, u_A) & 0 & 0 \\ 0 & \Delta\hat{K}_{\eta}(\eta_A, \varsigma_A) & 0 \\ 0 & 0 & \Delta\hat{K}_{\varsigma}(\eta_A, \varsigma_A) \end{bmatrix}, \tag{5.2-30}$$

where each diagonal component is nonlinearly dependent on the amplitudes. The numerical integration can be done beforehand for a range of amplitudes and the linearized stiffnesses can be stored in data files. Then, the values of the complex stiffnesses can be found by linear interpolation, which saves enormous computation time.

Now, the resulting forces as well as the resulting moments with respect to the center point *O* can be determined by summation with respect to all area elements

$$\hat{\boldsymbol{f}}_{O} = \sum_{i=1}^{n_y n_z} \boldsymbol{G}_{OM}^{T} \Delta\hat{\boldsymbol{f}}_{M} \,. \tag{5.2-31}$$

Inserting Eq.(5.2-2) and Eq.(5.2-29) in Eq.(5.2-31) and comparing with Eq.(5.1-7) gives the stiffness matrix for one contact interface

$$\hat{\boldsymbol{K}}_{O} = \sum_{i=1}^{n_y n_z} \boldsymbol{G}_{OM}^{T} \, {}^{ER}\boldsymbol{A}^{T} \, \Delta\hat{\boldsymbol{K}}_{M} \, {}^{ER}\boldsymbol{A} \, \boldsymbol{G}_{OM} \,. \tag{5.2-32}$$

The stiffness matrix is symmetric and nonlinear dependent on the generalized relative displacements with respect to the point *O*.

To include the influence of the non-constant pressure distribution for one area element as discussed in Chapter 3.3 and 3.8, the developed Eq.(5.2-32) can be used to determine the corresponding contact stiffnesses for a point contact, where the influence of the rough surface is included. Assuming translation only, where the amplitudes of the displacements are held constant and setting the transformation angle δ to be zero, Eq.(5.2-32) leads to

$$\Delta\hat{\boldsymbol{K}}_{M,new} = \sum_{i=1}^{i_{\max}} \Delta\hat{\boldsymbol{K}}_M(p_{Ni}, \Delta A_{0i}, \Delta c_{R0i}, \Delta c_{N0i}, \mu_i)\,, \tag{5.2-33}$$

where the point contact stiffnesses are dependent on the local contact parameters like the normal pressure p_{Ni}, the contact area ΔA_{0i}, the normal and tangential contact stiffnesses Δc_{N0i} and Δc_{R0i} and the friction coefficient μ_i. This makes it possible to include microslip effects for example due to a non-constant equivalent pressure distribution because of roughness as derived in Chapter 3.3. Modeling the contact shown in Fig. 5.1-3, the discrete contact parameters can be calculated by

$$\Delta c_{N0} = \frac{c_{N0}}{n_y n_z}, \quad \Delta c_{R0} = \frac{c_{R0}}{n_y n_z}, \quad \Delta F_N = \frac{F_N}{n_y n_z}, \tag{5.2-34}$$

with the global normal stiffness c_{N0}, the global tangential stiffness c_{R0} and the average normal contact force F_N. Note, that the friction coefficient μ, the average surface roughness R_Z and the shape of the cumulative height distribution of the contact surfaces are assumed to be constant for all area elements.

If the inverse of the stiffness matrix needs to be calculated, see (Sextro 1997a), the complex stiffness matrix from Eq.(5.2-32) for one contact interface can be reduced to a diagonal form. The following calculation procedure reduces the calculation time of the inverse matrix dramatically. Knowing the relative displacement with respect to the point O and the corresponding resulting forces and moments, the diagonal stiffness matrix is given by

$$\hat{\boldsymbol{K}}_O = \boldsymbol{diag}\left(\hat{K}_x, \hat{K}_y, \hat{K}_z, \hat{K}_{\varphi x}, \hat{K}_{\varphi y}, \hat{K}_{\varphi z}\right)_O \tag{5.2-35}$$

with

$$\hat{K}_j = \frac{\hat{F}_j}{\hat{u}_j}, \quad \hat{K}_{\varphi j} = \frac{\hat{M}_j^{(O)}}{\hat{\varphi}_j}, \quad j = x, y, z. \tag{5.2-36}$$

The dimensionless complex stiffnesses and displacements are defined by

$$\hat{K}_x^* = \frac{\hat{K}_x}{c_{N0}}, \quad \hat{u}_x^* = \frac{\hat{u}_x}{R_Z}, \tag{5.2-37}$$

$$\hat{K}_{y,z}^* = \frac{\hat{K}_{y,z}}{c_{R0}}, \quad \hat{u}_{y,z}^* = \frac{c_{R0}\hat{u}_{y,z}}{\mu F_N}, \tag{5.2-38}$$

$$\hat{K}_{\varphi x}^* = \frac{\hat{K}_{\varphi x}}{c_{R0} b_0^2}, \quad \hat{\varphi}_x^* = \frac{c_{R0} b_0}{\mu F_N}\hat{\varphi}_x, \tag{5.2-39}$$

$$\hat{K}_{\varphi y}^* = \frac{\hat{K}_{\varphi y}}{c_{N0} h_0^2}, \quad \hat{\varphi}_y^* = \frac{h_0}{R_Z}\hat{\varphi}_y \tag{5.2-40}$$

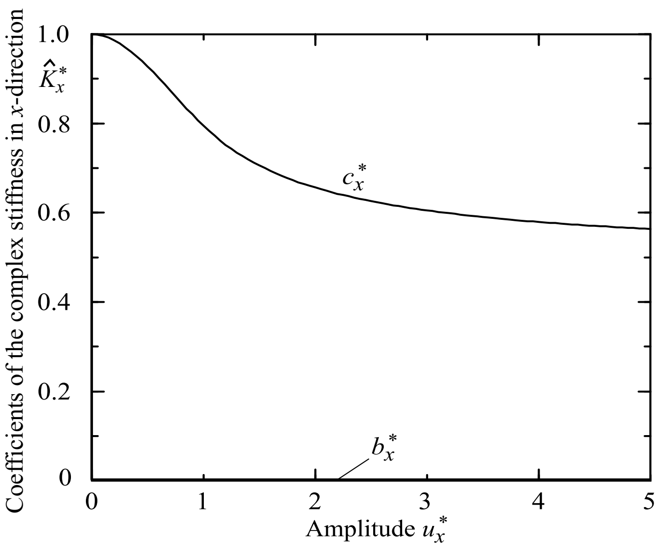

Fig. 5.2-4 Stiffness and damping versus relative amplitude in the x-direction

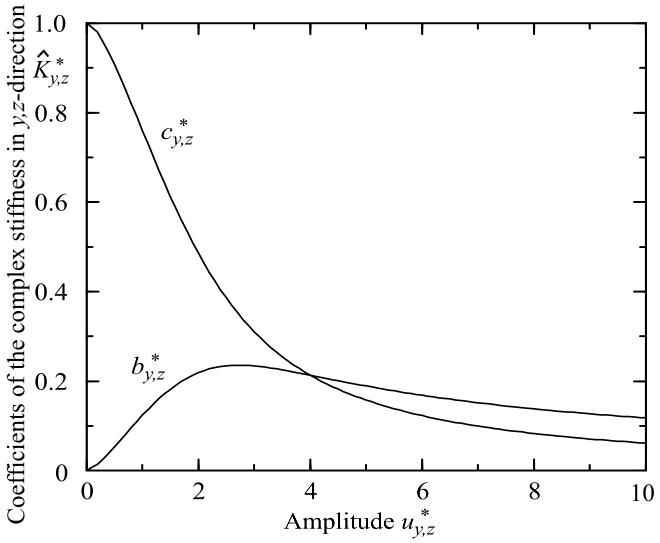

Fig. 5.2-5 Stiffness and damping versus relative amplitude in the y,z-direction

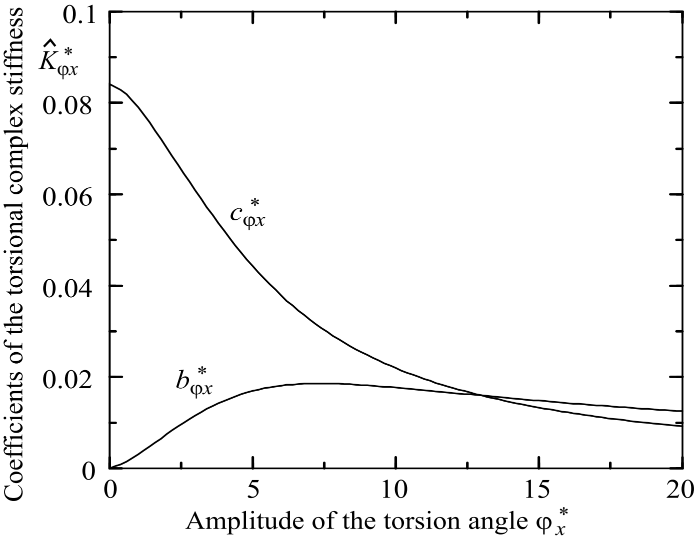

Fig. 5.2-6 Torsional stiffness and damping versus torsion angle

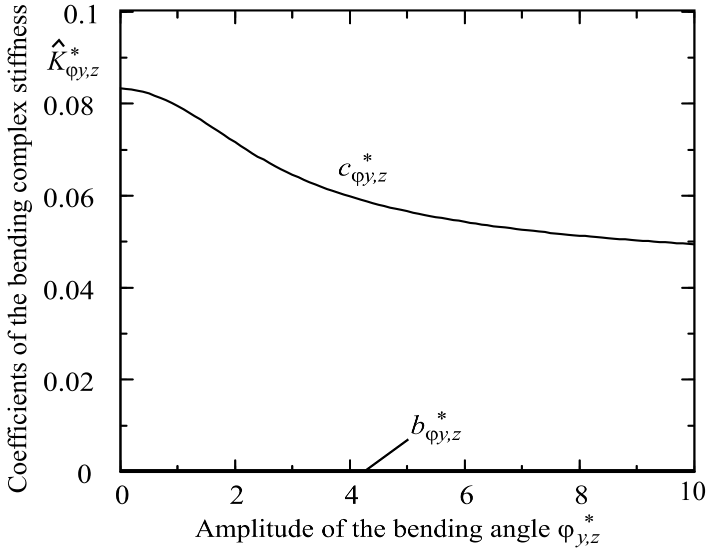

Fig. 5.2-7 Bending stiffness and damping versus bending angle with respect to the *y*,*z*-axis

and

$$\hat{K}^*_{\varphi z} = \frac{\hat{K}_{\varphi z}}{c_{N0} b_0^2}, \quad \hat{\varphi}^*_z = \frac{b_0}{R_Z} \hat{\varphi}_z. \tag{5.2-41}$$

In **Fig. 5.2-4 to 5.2-7** the dimensionless stiffness (real part) and damping (imaginary part) for translation and rotation are shown for an equilibrium position $u_G^*=1$. In each Figure, one generalized displacement is varied, while all other displacements are set to zero. On the one hand, in normal direction with respect to the contact area, viscous forces have not been modeled and therefore the corresponding damping coefficients are identical to zero, see Fig. 5.2-4 and Fig. 5.2-7. On the other hand the surface roughness has been modeled, which leads to microslip effects, which can be seen in the region where the vibration amplitudes are small and the corresponding damping coefficients are not identical to zero, see Fig. 5.2-5 and Fig. 5.2-6.

In general, this description of the friction contact includes the coupling between six degrees of freedom of the non-Hertzian contact. Inserting Eq.(5.2-32) or Eq.(5.2-35) in Eq.(5.1-10) these nonlinear system equations are solved iteratively by the damped Newton method and are analyzed in the frequency domain as done in the next Chapter.

5.3 Experimental Validation of the Contact Model

In the following the calculation model will be verified again by using the experimental setup, shown in **Fig. 5.3-1 and 5.3-2** with three elastic bodies is used, see also (Sextro 1999b). The average normal contact force F_N is simulated by gravity forces. There exist two possibilities of arrangement of the blade. The first arrangement is constructed close to typical constructions in steam turbines, whereas the second arrangement to aircraft gas turbines. The top view of the shroud construction of the first arrangement is shown in **Fig. 5.3-3**. The blade has a rectangular cross section and is excited with $F_E=1.0$ [N] eccentrically to cause spatial vibrations of the blade and the contact surfaces. The excitation of the blade and the accelerometer for measurements of the frequency response function (FRF) are mounted at the same height of the blade.

The geometry of each contact interface is defined by the width $b_0=72$ [mm] and the height $h_0=5$ [mm] and the average roughness is approximately $R_Z=7.5$ [μm] identified by two profile measurements. The friction coefficient was estimated: $\mu=0.2$. With the Young's modulus of $E=2.1\ 10^{11}$ [N/m^2], the nominal contact area $A_0=b_0h_0$ and the approximated depth with $\ell_0=90$ [mm], the nominal normal stiffness is given by Eq.(3.1-15) with $c_{N0}=840.0\ 10^6$ [N/m]. An upper value for the tangential contact stiffness can be found from Eq.(3.1-16) with $c_{R0}=320.0\ 10^6$ [N/m] with the shear modulus of $G=8.1\ 10^{10}$ [N/m^2], because here the shroud is elastically supported by the blade in the *z*-direction. The corresponding tangential contact stiffness was estimated by $c_{R0}=80.0\ 10^6$ [N/m]. The contact area is discretized by $n_y=72$ and $n_z=5$. During the calculations, these parameters are constant. The excitation frequency has to be small compared to the first eigenfrequencies of the contact model, see Chapter 3.7. Here, the maximum excitation frequency is $f_{E,max}=700.0$ [Hz] and the lowest eigenfrequency defined in Eq.(3.2-25) is given by $f_{T,k=1}=8910.0$ [Hz] with respect to the tangential vibration with the density of $\rho_0=7850$ [kg/m^3]. Hence, the maximum excitation frequency is relatively small compared to the lowest eigenfrequency of the contact model.

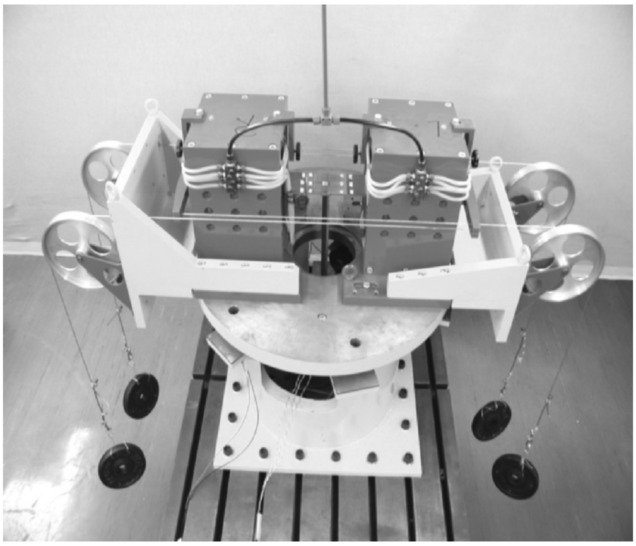

Fig. 5.3-1 Experimental setup

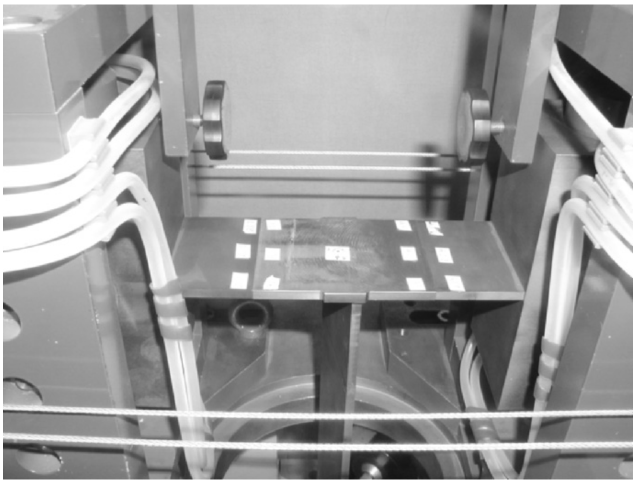

Fig. 5.3-2 Experimental setup with two contact interfaces

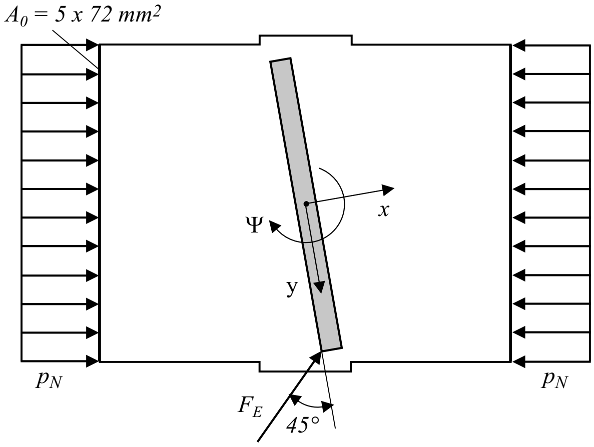

Fig. 5.3-3 Top view of the shrouded blade with respect to the first arrangement

The dynamical behavior of the uncoupled blade is described by the first $m=20$ modes calculated by the FEM, where the first bending eigenfrequency of the blade is $f_1=14.1$ [*Hz*]. In **Fig. 5.3-4**, the first two torsional modes are shown where the color code denotes the resultant mass-normalized deflection u_{max} of each node. The eigenfrequency of the first torsional mode is *159.55* [*Hz*] and the second is *540.61* [*Hz*]. Both modes play an important role in modeling the torsional vibration of the coupled structure through the friction contacts. For the finite element discretization, volume elements with eight nodes are used, where the rotational mass-normalized eigenvectors are calculated additionally within the modal analysis. Furthermore, corresponding to the mass-normalized eigenvector, the mass-normalized strain and stress vector for each mode are determined as well and are used for the stress analysis based on the modal description, see Chapter 5.5.

In **Fig. 5.3-5 and 5.3-6**, the frequency response function (FRF) in the x-direction and the torsional vibration in the Ψ-direction with respect to the center of the rectangular cross section of the blade are shown, respectively. Coupled torsional and bending vibrations occur. The first two resonance frequencies at *120* [*Hz*] and *320* [*Hz*] belong to bending and the third resonance frequency at *470* [*Hz*] belongs to torsional vibrations of the blade. The measurements of the bending and torsional vibrations show a good agreement with the corresponding calculations over a wide range of excitation frequencies.

For selected values of the normal contact force F_N, the corresponding FRFs are shown in **Fig. 5.3-7** in the frequency range from *100* to *125* [*Hz*] at the first resonance frequency, to be able to compare the measurements and the calculations in more detail. With decreasing normal contact force, the resonance frequency decreases as well, because full contact is not reached and the nonlinear contact stiffnesses decrease. Both, the maximum amplitudes and the resonance frequencies show a very good agreement, since the first eigenfrequency of the uncoupled blade is *14.1* [*Hz*].

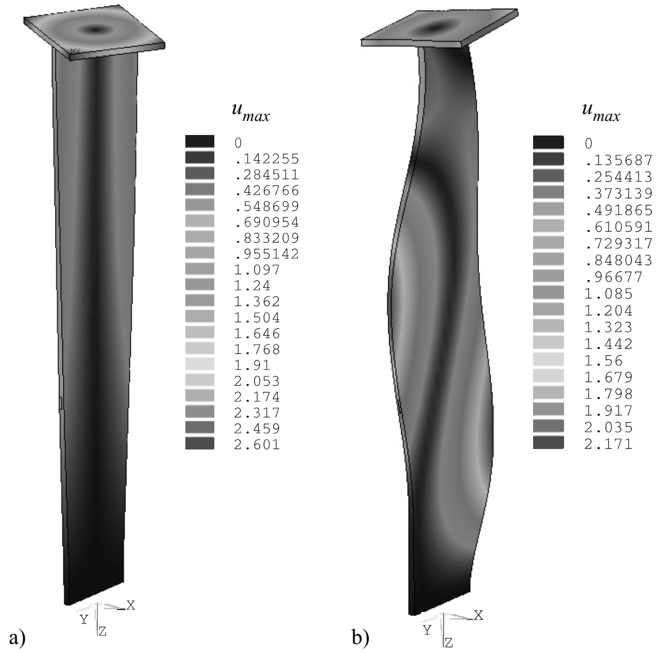

Fig. 5.3-4 The first two torsional modes of the uncoupled blade **a**) first and **b**) second torsional mode

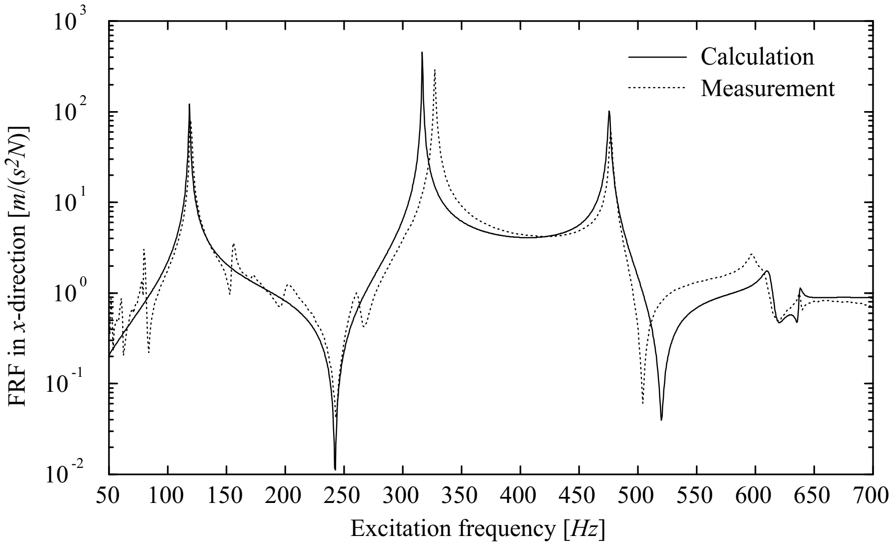

Fig. 5.3-5 Bending vibration for $F_N=780$ $[N]$

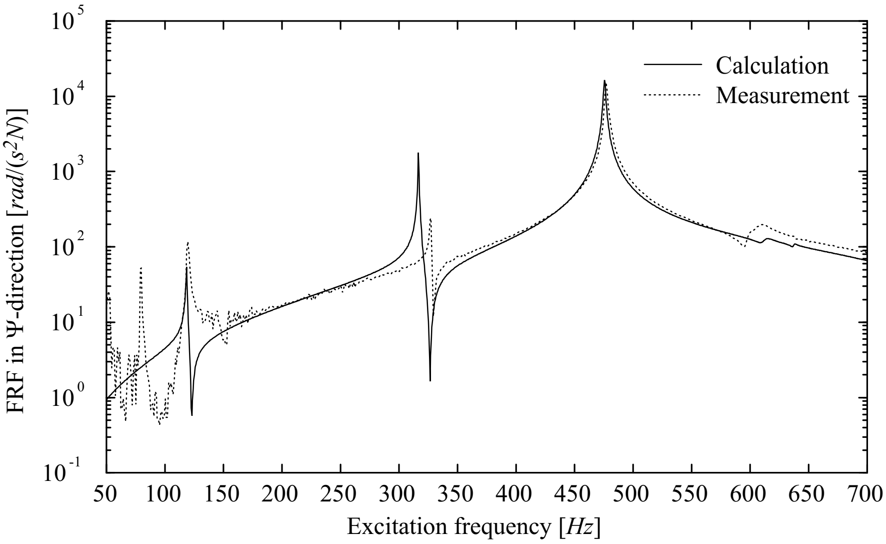

Fig. 5.3-6 Torsional vibration for $F_N=780$ [*N*]

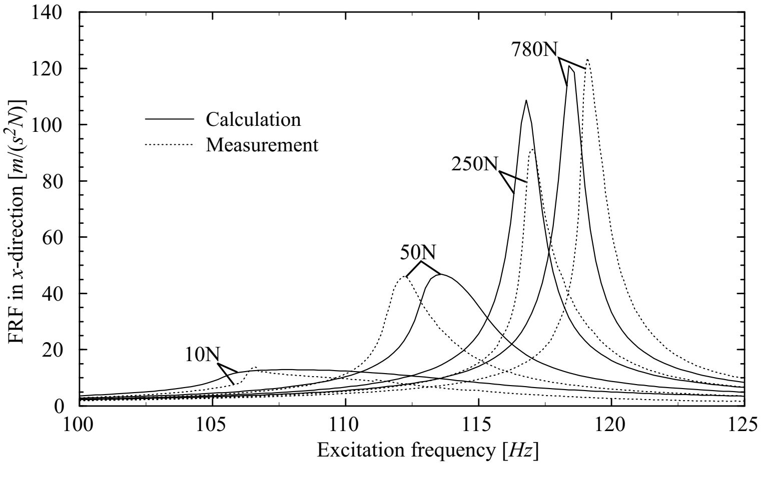

Fig. 5.3-7 Bending vibration for selected values of F_N

Corresponding to the above-described experimental and theoretical investigations, a different design, shown in **Fig. 5.3-8** close to an aircraft gas turbine design, is analyzed. The geometry of each contact interface is defined by $b_0=20$ [*mm*], $h_0=5$ [*mm*] and $R_Z=7.5$ [μm]. The contact area is discretized by $n_y=20$ and $n_z=5$. The friction coefficient is approximated by $\mu=0.4$. The normal and tangential contact stiffnesses are estimated by $c_{N0}=7.6\ 10^9$ [*N/m*] and $c_{R0}=2.9\ 10^9$ [*N/m*] respectively. It appears that the qualitative behavior is very close to the behavior with respect to the first arrangement, see **Fig. 5.3-9 up to Fig. 5.3-11**. The basic differences with respect to the investigations described above are on the one hand the smaller contact area of $A_0=5x20$ [mm^2] and on the other hand the different vibration direction within the contact. Again, the agreement between measurements and calculations is good.

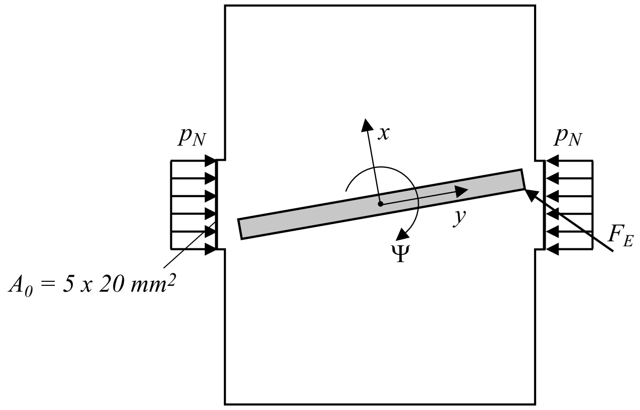

Fig. 5.3-8 Top view of the shrouded blade of the second arrangement

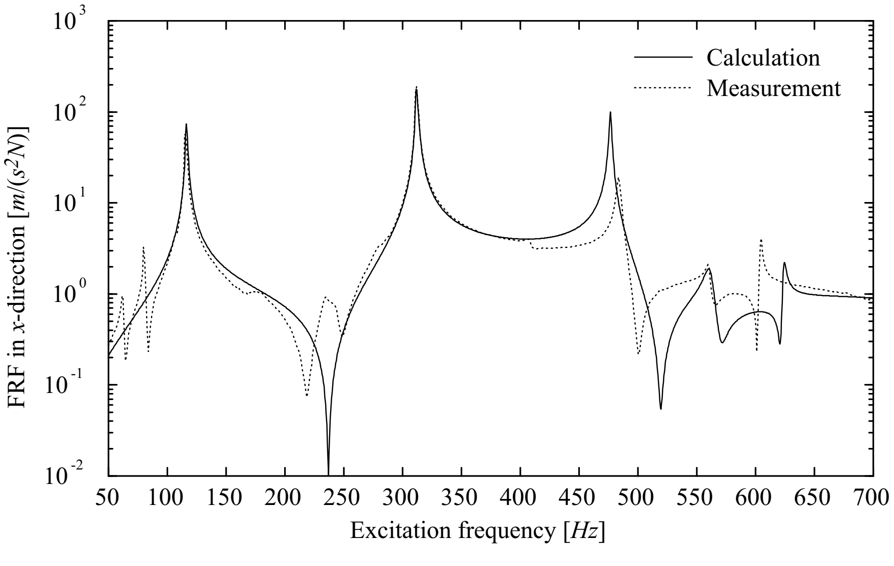

Fig. 5.3-9 Bending vibration for $F_N=780$ [N]

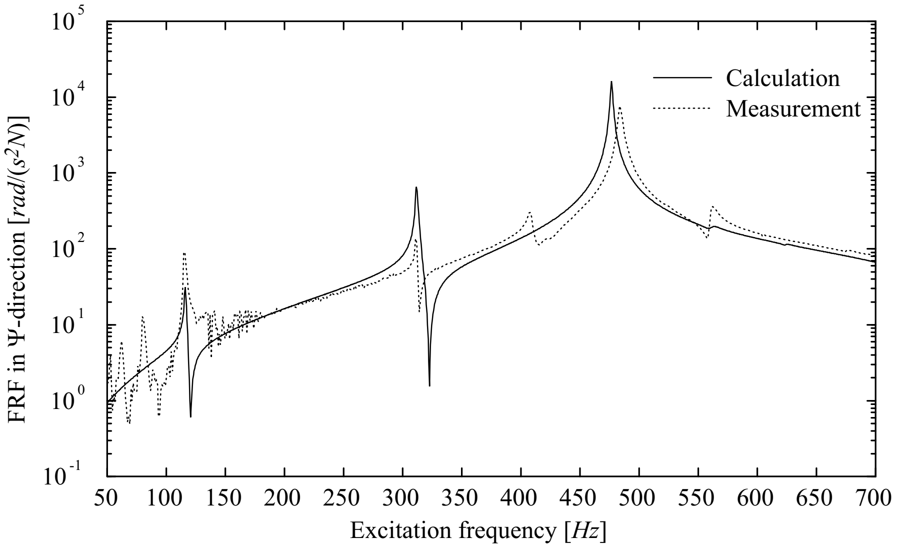

Fig. 5.3-10 Torsional vibration for $F_N=780$ [N]

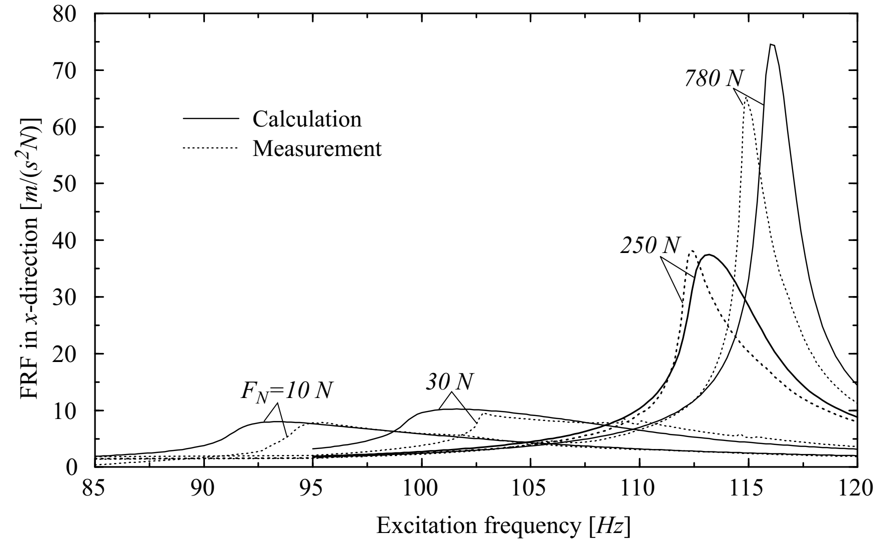

Fig. 5.3-11 Bending vibration for selected values of F_N

5.4 Spin Pit Tests of Bladed Disc Assemblies

In the following, two spin pit tests of bladed disc assemblies are used to verify the developed calculation method to calculate the vibration of multibody systems with friction contacts. On the one hand, a real bladed disc assembly coupled by shrouds at ABB, Baden, Szwitzerland, see (Szwedowicz et al. 2003), and on the other hand a bladed disc assembly coupled by friction dampers at the Institute of Dynamics and Vibration, Leibnitz University Hannover, Germany, see (Götting et al. 2004 and Götting 2005) are used.

In a first step, the normal and tangential contact stiffness between the shrouds have to be determined as described in Chapter 3.1. The magnitudes of the normal and tangential contact stiffnesses can be identified by computing the nodal diameter diagram of the shrouded turbine blades using the FEM and the developed calculation method, see **Fig. 5.4-1**, see (Szwedowicz et al. 2003). The contact stiffnesses can be tuned for the nodal diagram number of interest. If the calculation is tuned for the normal and tangential contact stiffness considering only one nodal diameter number almost all nodal diameters show a good agreement with the FE calculations.

In this analyzed example, the normal stiffness is twice the tangential stiffness. In Fig. 5.4-1, the white symbols represent the eigenfrequencies calculated by the FE model, the triangles refer to the spin pit measurements and the contour plot is the result from the developed calculation method.

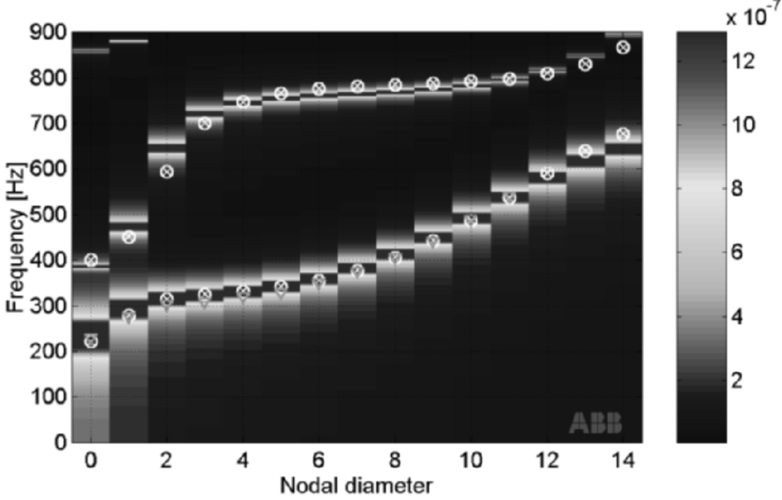

Fig 5.4-1 Nodal diameter diagram

In the following, two different experimental resonance peaks of the shrouded blade are simulated in the spin pit conditions. All measurements were transient spin pit measurements performed with a low rundown speed. In this measurement, transient effects can be neglected. The minimal and maximal magnitudes of the damping ratio and excitation load of the air jet, which were evaluated from other resonance peaks, have been used in the simulations. The considered resonance peaks are measured for two different rotational speeds of the turbine.

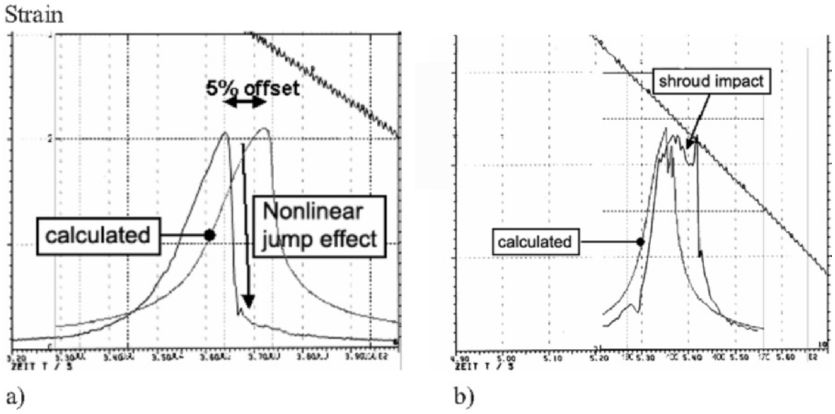

Fig 5.4-2 Spin pit tests and comparison to the calculation for different rotational speeds **a)** *57.1 rps* and **b)** *49.0 rps*

The first comparison has been carried out for a resonance response curves measured at a rotational speed of *57.1 rps*, see **Fig. 5.4-2a**. Furthermore, for a rotational speed of *49.0 rps* a resonance response curve, which involves elastic impacts between the shrouds, has been measured in **Fig. 5.4-2b**. In both cases, the simulations show a good agreement with the experimental results.

Additionally the test stand at the Institute of Dynamics and Vibration, Leibnitz University Hannover, see **Fig. 5.4-3**, is used to verify the developed calculation method. The vibration amplitudes of the rotating bladed disc are measured by strain gauges, which are mounted above the damper platforms of the blades. The assembly consists of *30* blades, which can be coupled by different friction dampers. The excitation force is applied at the tip of the blade by three exciters with constant magnetic field. Hence, the engine order equals three and multiples. Due to manufacturing tolerances and material deviations there is already mistuning in the original system. Therefore, the natural frequencies of each blade can be changed individually by different additional masses at the tip of the blades.

In (Götting 2005) the influence of the damper mass is investigated for cylindrical friction dampers (Z), cottage roof dampers (C) and asymmetric dampers (A). The comparison of simulations and experiments shows a good agreement for all three friction damper designs. One result is shown in **Fig. 5.4-4a**, where cottage roof dampers have been used. The coupled system is investigated with regard to the first bending mode of the blades, where the damper mass has been varied with: C1=25.9 g, C2=41.8 g and C3=117.0 g. The measured strain amplitudes correspond qualitative and quantitative to the calculated results. The resonances frequencies as well as the maximum strain amplitudes can be predicted relative good.

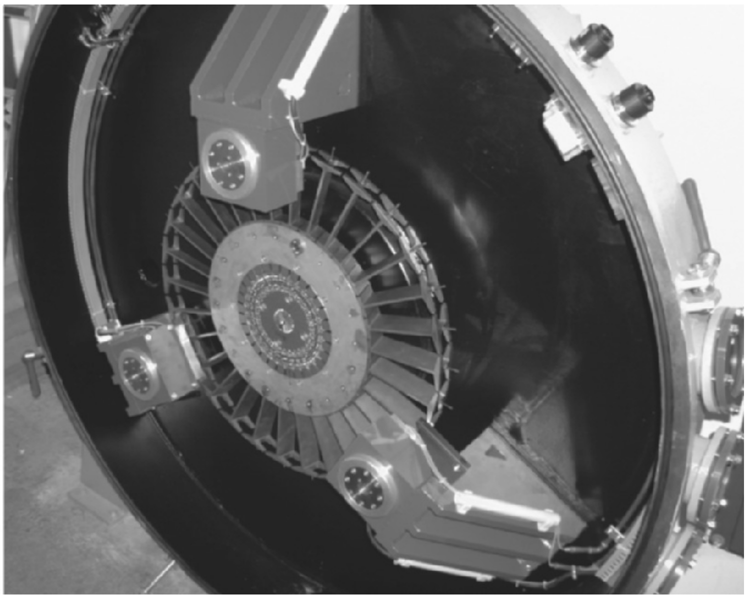

Fig. 5.4-3 Spin pit test stand with friction dampers

The comparison with respect to the above-mentioned three dampers Z, C and A with regard to the measurement and calculation is presented in **Fig. 5.4-4b**. Varying the damper mass the comparison of calculated and measured maximum strain amplitudes is very good. Hence, the developed calculation method has been verified for different contacts within the rotating field. Furthermore, this method can be used to investigate other contacts and other couplings between the blades. The corresponding numerical investigations are presented in the next chapter.

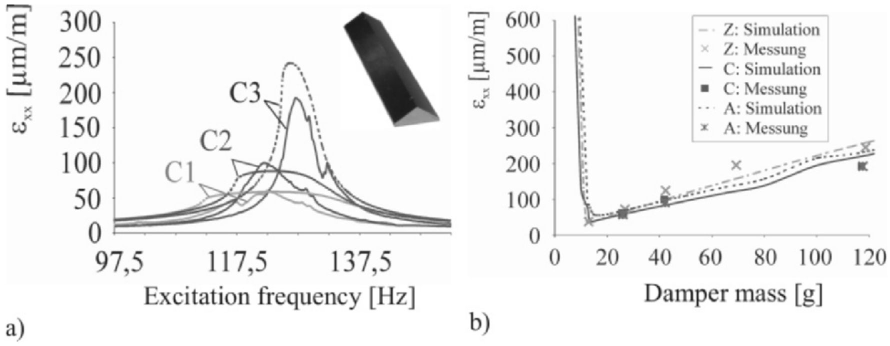

Fig 5.4-4 Comparison of measurements and calculations of a bladed disc coupled by cottage roof dampers **a)** varying the excitation frequency and damper mass **b)** maximum strain amplitude versus the damper mass for different damper designs

5.5 Optimization of Tuned Bladed Disc Assemblies with Friction Contacts

The bladed disc assembly with *24* blades (from the experiments, see Chapter 5.3) which are coupled by means of the first arrangement of the shrouds, is investigated, see also (Sextro 2000). In praxis, the amplitudes of the excitation forces of the system are approximated in a common way, using the stationary gas force and introducing the stimulus, which describes the percentage of the dynamical force amplitudes relative to the stationary gas force. Furthermore, it is assumed, that the excitation forces are monofrequent, while the excitation angular frequency is a multiple of the angular velocity of the rotor described by the engine order.

Before analyzing the global behavior of the bladed disc with shrouds the minimum number of modes has to be determined, which have to be used at least with respect to a relative small error. This minimum number can be estimated by the coupled system, since here all modes of the uncoupled blade are involved to simulate the coupled system. In **Fig. 5.5-1** the frequency response functions of the coupled system with a normal force of $F_N=780$ [N] are calculated varying the number of modes. The relative error between the FRFs with $m=15$ modes and $m=20$ modes is relatively small. Hence, twenty modes are used in the following analysis.

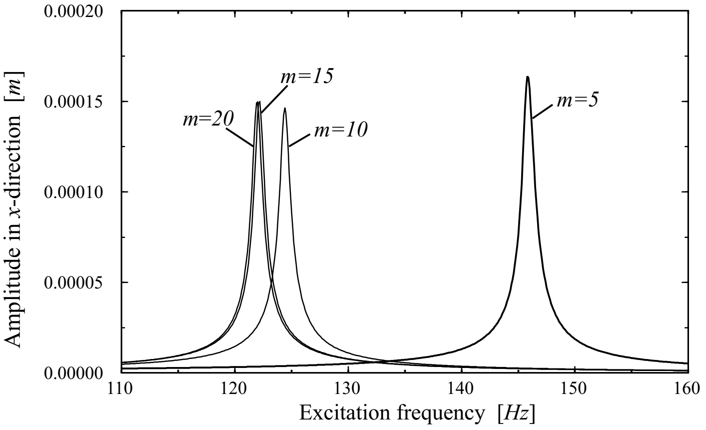

Fig. 5.5-1 Variation of the maximal number of modes

In **Fig. 5.5-2**, the resonance frequency is calculated for all possible engine orders. The normal contact force is again $F_N=780$ [N]. Here, for high engine orders the resonance frequencies decrease slightly. This effect is due to the coupling of the shroud by nonlinear contact stiffnesses.

In **Fig. 5.5-3**, the response as a function of the excitation frequency is shown for different normal contact forces. The engine order is two. Again, with decreasing normal contact force the resonance frequency decreases as well, because the tangential and the normal contact stiffnesses decrease. The reduction of amplitudes is quite impressive. Further theoretical investigation gave an optimal normal force of *3.5* [*N*], where the amplitudes are minimal.

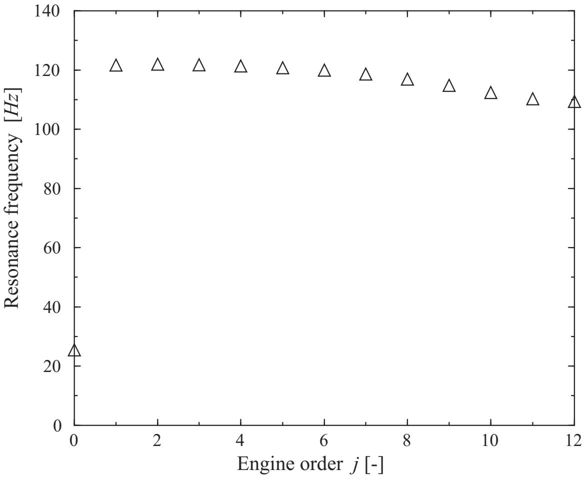

Fig. 5.5-2 Resonance frequency versus engine order

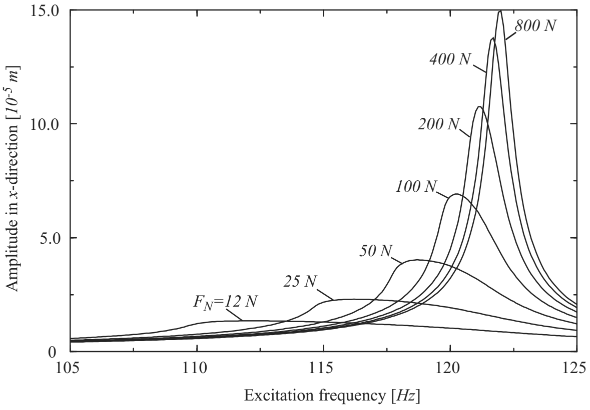

Fig. 5.5-3 Amplitude in x-direction versus excitation frequency

For optimization of the bladed disc assembly the maximum alternating stresses, which occur in the blade foot, are calculated for all possible engine orders, varying the normal contact force, see **Fig. 5.5-4** and **Fig. 5.5-5**. The friction contacts separate for small normal contact forces, which lead to an increase in alternating stresses, especially for high engine orders, see Fig. 5.5-5. To make sure that the maximum alternating stresses are minimal and no separation takes place, the normal contact force has to be adjusted to $F_N=100$ [*N*], see Fig. 5.5-4. For an engine order of $j=12$ the optimal normal force is slightly higher than $F_N=100$ [*N*]. To be able to evaluate these maximum alternating stresses with respect to the endurance limit, the axial stresses due to the centrifugal forces have to be calculated as well.

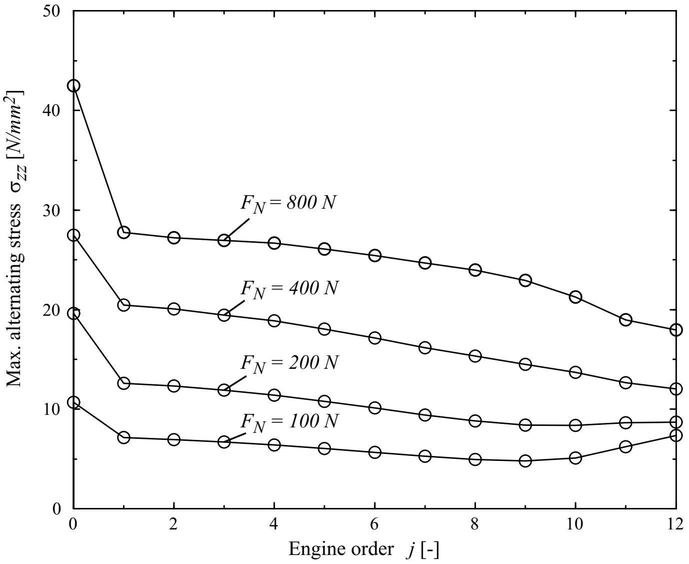

Fig. 5.5-4 Alternating stress versus engine order for selected F_N

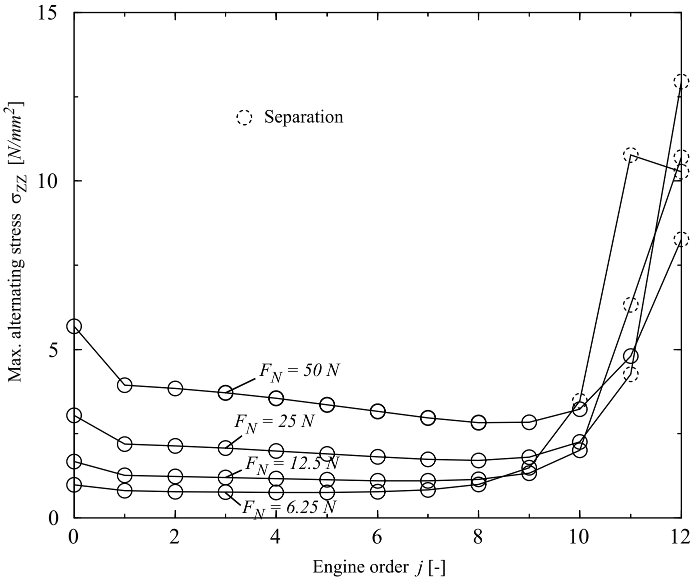

Fig. 5.5-5 Alternating stress versus engine order for selected F_N

Coupling by Damping Elements

An alternative coupling of the blades is given by so called damping elements as shown in **Fig. 5.5-6a**, which are placed within a hole at the tip of the blade. The pressure distribution can be calculated by the Hertzian theory. Note that here the curvature of the contact area has to be modelled additionally. The investigated system has 24 blades. The engine order is two and the excitation forces act in the *z*-direction. In **Fig. 5.5-6b** the bending vibration in the *z*-direction is shown. Again the system response is typical when varying the normal force. Using this coupling torsional vibration are initiated because of the eccentric coupling at the blade tip, see **Fig. 5.5-6c**. The local minimum with respect to the bending and torsional vibration occurs approximately at the same normal force.

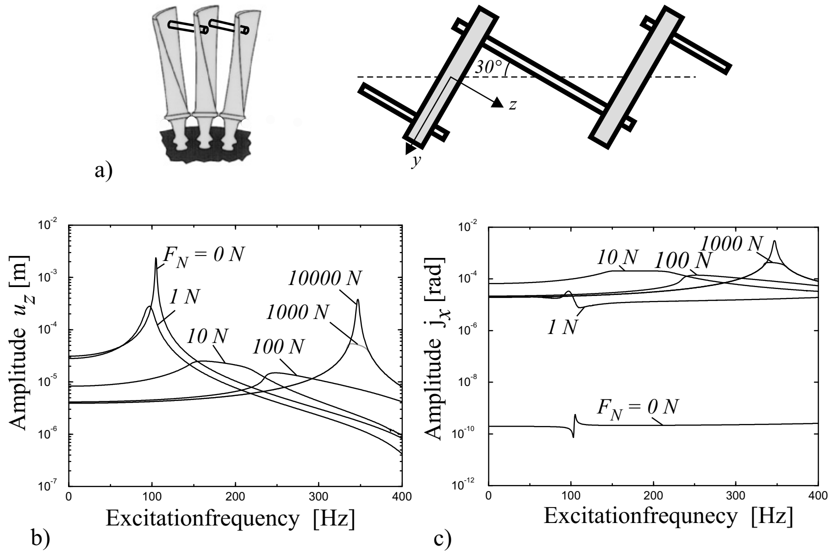

a)

b)

c)

Fig. 5.5-6 a) System description of the damping element, side and top view **b)** Calculated bending vibration and **c)** torsional vibration

In **Fig. 5.5-7a** the vibration amplitude versus the excitation frequency under variation of the engine order is shown, while the normal force with $F_N=100\ N$ is held constant. The resonance frequencies increase with an increasing engine order. The construction is optimal for an engine order of three. In **Fig. 5.5-7b** the resonance frequencies are depicted versus the engine order. By increasing the normal force the coupling between the blades is increase and hence the resonance frequencies increase as well.

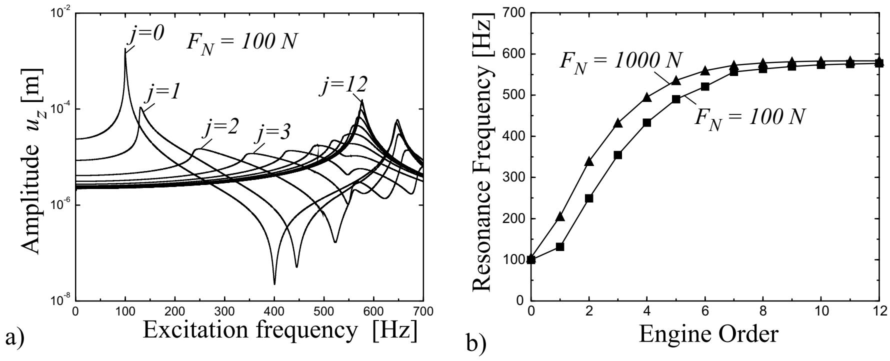

Fig. 5.5-7 a) Variation of the engine order **b)** Resonance frequencies vs engine order

Coupling by Damping Wires

Due to the elasticity of damping wires the calculation of the coupling is great because the damping wire is coupled by several blades, see (Sextro and Popp 2003). Furthermore a high number of modes including the rigid body modes of the damping wire must be used. In **Fig. 5.5-8a** the investigated system is depicted, where seven blades have been coupled by the damping wire. Again the curvature of the borehole is modelled with a radius of 6 mm. The investigated system has 28 blades, while seven blades are coupled in the circumferential direction by the damping wire. In **Fig. 5.5-8b** the system response versus the excitation frequency is shown. Again, one is able to calculate an optimal normal contact force for the first resonance frequency.

Multicoupling

To increase damping for example additionally friction damper can be used. In **Fig. 5.5-9a** on the basis of shroud coupling with a normal force of $F_N=800$ N the normal force for the friction damper is varied. The amplitudes can be reduced by two decades, see **Fig. 5.5-9b**. In case of spatial motion of blades it is in principle difficult to optimize the system with respect to the amplitudes. A better possibility is to calculate the equivalent stress, see **Fig. 5.5-9c**. Note that the amplitude of the equivalent stress corresponds to the monofrequent amplitude of the stress.

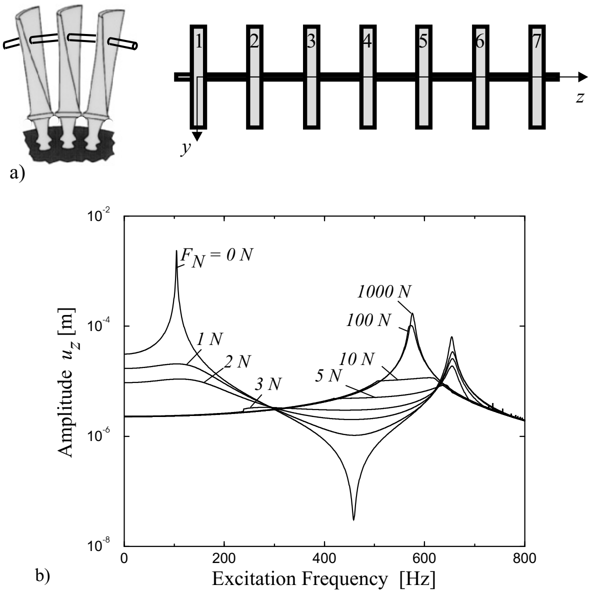

Fig. 5.5-8 Calculation of damping wires **a)** system description **b)** calculated vibration amplitudes

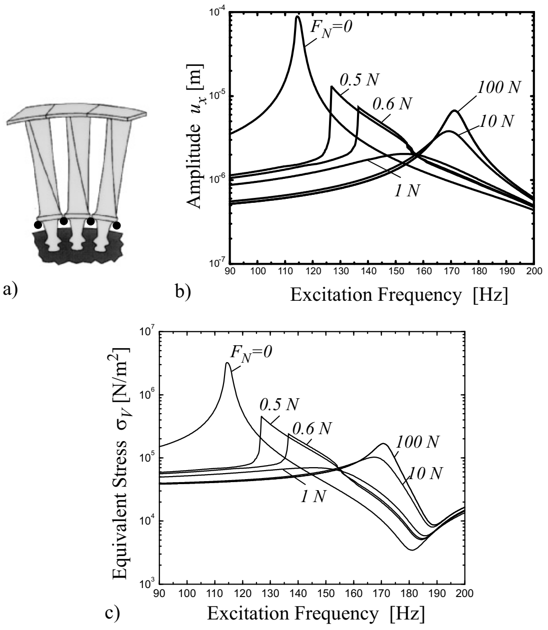

Fig. 5.5-9 a) Investigated system **b)** vibration amplitude vs excitation frequency **c)** equivalent stress vs excitation frequency

5.6 Vibration of Detuned Bladed Disc Assemblies with Friction Contacts

Friction damping of elastic multibody systems, where a large number of degrees of freedom are involved, are described and analyzed for example in (Sextro 1997a, 1997b, 1998a, 1998b; Panning et al. 2000; Krzyzynski et al. 2000; Sextro et al. 2001, Sextro et al. 2002; Panning et al. 2003a and 2003b; Götting et al. 2004). With respect to these references, detuned bladed disc assemblies with friction contacts, where the eigenfrequencies of the blades do vary, have been investigated. This leads to a large numerical and nonlinear dynamic problem, because the complete bladed disc with up to one hundred blades has to be modeled and solved including the friction contact problem.

For statistical varying eigenfrequencies, Monte Carlo simulations are often used to investigate the system response to monofrequent excitation forces. For this case an approximated method has been developed, see (Sextro et al. 2001), to speed up the calculation of the average and variance of vibration amplitudes and the corresponding distribution. This solution procedure is very efficient with respect to the computation time.

Because of large computation time of Monte-Carlo simulations, an approximate method is developed to calculate the system response. In the following, this approximate method will be derived assuming small standard deviations of the eigenfrequencies of the blades. Expanding the vibration amplitude in a Taylor series with respect to a parameter p yields

$$w(p) \approx w(p_{\mathrm{m}}) + \left[\frac{\partial w(p)}{\partial p}\right]_{p=p_{\mathrm{m}}} (p - p_{\mathrm{m}}) \tag{5.6-1}$$

where

$$\frac{\partial w(p)}{\partial p} = \frac{1}{w(p)} \boldsymbol{w}^{\mathrm{T}}(p) \frac{\partial \boldsymbol{w}(p)}{\partial p} . \tag{5.6-2}$$

Differentiating the system equation given by Eq.(5.1-10) yields

$$\frac{\partial \boldsymbol{q}(p)}{\partial p} = - \boldsymbol{A}^{-1}(p) \frac{\partial \boldsymbol{A}(p)}{\partial p} \boldsymbol{q}(p) . \tag{5.6-3}$$

Then the sensitivity S is given by

$$\begin{aligned} S(p_{\mathrm{m}}) &= \left[\frac{\partial w(p)}{\partial p}\right]_{p=p_{\mathrm{m}}} = \\ &- \frac{1}{w(p_{\mathrm{m}})} \boldsymbol{w}^{\mathrm{T}}(p_{\mathrm{m}}) \boldsymbol{T} \boldsymbol{A}^{-1}(p_{\mathrm{m}}) \left[\frac{\partial \boldsymbol{A}(p)}{\partial p}\right]_{p=p_{\mathrm{m}}} \boldsymbol{q}(p_{\mathrm{m}}) . \end{aligned} \tag{5.6-4}$$

The mean value p_{m} and the standard deviation σ_{p} of the parameter p are given by

$$E[p] = p_{\mathrm{m}} \tag{5.6-5}$$

and

$$E[(p - p_{\mathrm{m}})^2] = \sigma_{\mathrm{p}}^2 \tag{5.6-6}$$

respectively. If the standard deviation of the parameter p is small, then it can be shown that the mean value of the mistuned system response is equal to the response of the tuned system

$$E[w(p)] = w(p_{\mathrm{m}}) = w_m\,. \tag{5.6-7}$$

The standard deviation σ_w of the system response w can be calculated using the sensitivity S by

$$\sigma_w^2 = S^2(p_{\mathrm{m}})\,\sigma_{\mathrm{p}}^2\,. \tag{5.6-8}$$

In case of the mistuned bladed disk, all sensitivities due to the eigenfrequencies of each blade have to be calculated. It is assumed that the variations of the eigenfrequencies are random. Therefore the cross correlation of the eigenfrequencies can be neglected. Hence, the resultant standard deviation of the system response is given by

$$\sigma_w^2 = \sum_{j=1}^{n_{\mathrm{M}}} \sum_{i=1}^{n_{\mathrm{S}}} S^2(\omega_{0\mathrm{i,jm}})\,\sigma_{\omega_{0\mathrm{i,j}}}^2\,. \tag{5.6-9}$$

To be able to calculate the envelopes of a mistuned system, the distribution of the amplitudes has to be known. Extensive comparisons with Monte Carlo simulations leaded to the statement that the assumption of a Weibull-distribution is valid from very weak to very strong coupling. The Weibull probability distribution is given by

$$P_{\mathrm{p}}(w^*) = 1 - e^{-(\ln 2) w^{*k}} \tag{5.6-10}$$

with the dimensionless amplitude

$$w^* = \frac{w}{w_0}\,. \tag{5.6-11}$$

Both, the exponent k and the parameter w_0 are unknown and are calculated in the following by means of the mean value w_{m} and the standard deviation σ_w. The corresponding probability density function is given by differentiating Eq.(5.6-10) to obtain

$$p_{\mathrm{p}}(w^*) = k\,(\ln 2)\,w^{*k-1}\,e^{-(\ln 2) w^{*k}}\,. \tag{5.6-12}$$

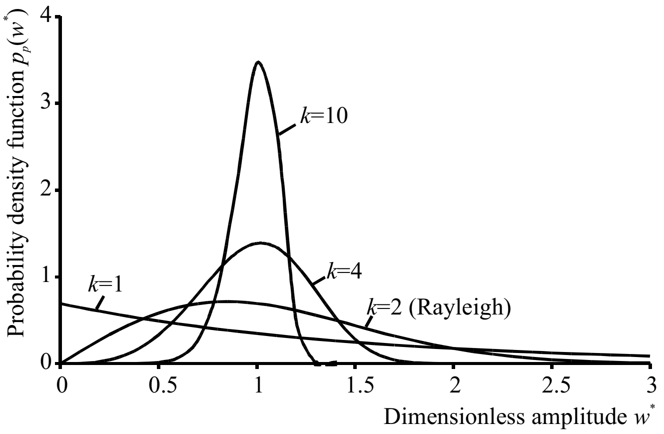

Fig. 5.6-1 Probability density function for the distribution of amplitudes

Fig. 5.6-1 shows the Weibull probability density function for the distribution of amplitudes plotted against the dimensionless amplitude w^* for different values of the exponent *k*. For the special exponent $k = 2$ the Weibull distribution is equivalent to the Rayleigh distribution. The *n*-th moment of the distribution can be calculated by

$$E[w^{*n}] = (\ln 2)^{-\frac{n}{k}}\,\Gamma\left(1+\tfrac{n}{k}\right). \qquad (5.6\text{-}13)$$

The standard deviation follows from

$$\sigma^2_{w^*} = E[w^{*2}] - E[w^*]^2. \qquad (5.6\text{-}14)$$

Inserting Eq.(5.6-13) with n=1 for the first moment and n=2 for the second moment in Eq.(5.6-14) and solving for the parameter w_0 gives

$$w_0 = \frac{(\ln 2)^{\frac{1}{k}}}{\sqrt{\Gamma\left(1+\frac{2}{k}\right) - \Gamma^2\left(1+\frac{1}{k}\right)}}\,\sigma_W. \qquad (5.6\text{-}15)$$

Using Eq. (5.6-13) with n=1 for the mean value and inserting Eq.(5.6-15) results in

$$w_\mathrm{m} = \frac{\Gamma\left(1+\frac{1}{k}\right)}{\sqrt{\Gamma\left(1+\frac{2}{k}\right) - \Gamma^2\left(1+\frac{1}{k}\right)}}\,\sigma_W. \qquad (5.6\text{-}16)$$

Rearranging Eq.(5.6-16) gives a formula to determine the exponent *k* of the Weibull-distribution,

$$1 + s^2 - \frac{\Gamma\left(1+\frac{2}{k}\right)}{\Gamma^2\left(1+\frac{1}{k}\right)} = 0\ , \qquad (5.6\text{-}17)$$

knowing the measure of sensitivity or strength of localization defined by the ratio of the standard deviation to the mean value of the vibration amplitudes

$$s = \frac{\sigma_W}{w_\mathrm{m}}. \qquad (5.6\text{-}18)$$

For example, if this measure *s* is equal to one, the exponent *k* is also equal to one, see **Fig. 5.6-2**. For the Rayleigh distribution with k=2 the measure is s=0.523. There are two possibilities to calculate the exponent *k*. On the one hand, the strength of localization can be calculated from the mistuned response of the system and on the other hand by the approximate method. This numerical comparison is carried out in the following.

The developed approximate analysis of detuned systems can be done with respect to the amplitude variations as shown above as well as for the strain and stress variations. Hence, if measured strain amplitudes are available from strain gauge tests, then it is possible to calculate the mean value and the standard deviation and the exponent *k* of the Weibull-distribution using Eq.(5.6-17). From here, it is possible to estimate the distribution of the strain amplitudes and to evaluate the mistuning effect.

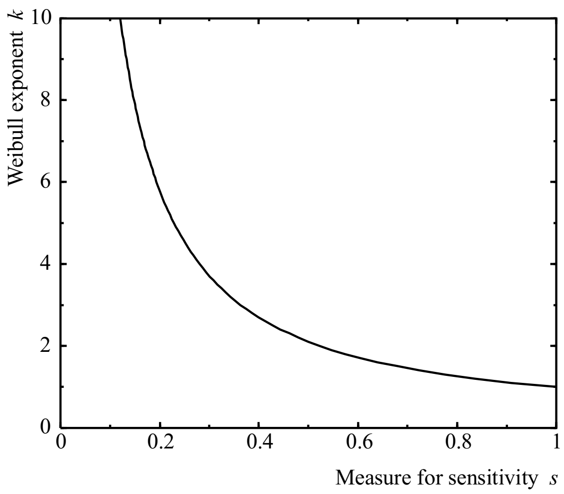

Fig. 5.6-2 Weibull exponent k versus measure for sensitivity s

For example, a bladed disk with friction dampers is mistuned by the eigenfrequencies of the blades. The standard deviation of the eigenfrequencies is 0.325% for each of the first ten modes (n_M=10) and the mean value for the first bending resonance is f_m = 100.2 Hz. The blades are distributed around the disk with the eigenfrequencies of the first mode. The mass of the friction elements corresponds to the optimal mass m_R=23.0 g of the tuned system.

The amplitudes in z-direction of the blades of the mistuned system are shown in **Fig. 5.6-3**. The side peaks correspond to the resonance frequencies of the tuned system for different engine orders. Because of the large computation time of the simulation for one arrangement of the blades around the disk, the approximate method is used to calculate the mean value w_m and the standard deviation σ_w of the amplitudes. By means of this method, the upper and lower envelope w_u and w_l of the amplitudes can be calculated as well. With a probability of 95% the amplitudes are within these envelopes. Calculating the mean value and the standard deviation of the mistuned system response, the exponent k can be calculated as well, using Eq.(5.6-17). In **Fig. 5.6-4** the exponent k is illustrated for the simulated system response and for the approximation. The agreement of both methods is good.

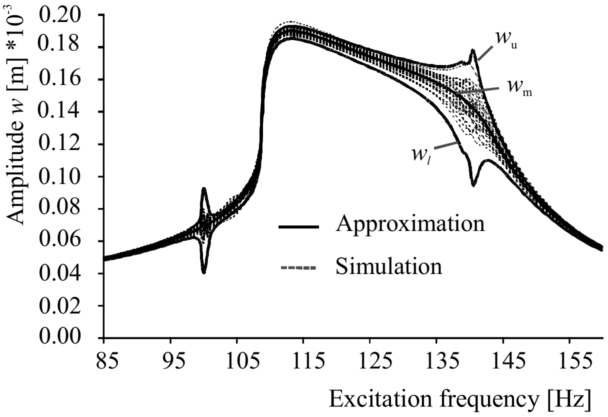

Fig. 5.6-3 Response of the mistuned bladed disk ($\sigma_f / f_m = 0.325$ %)

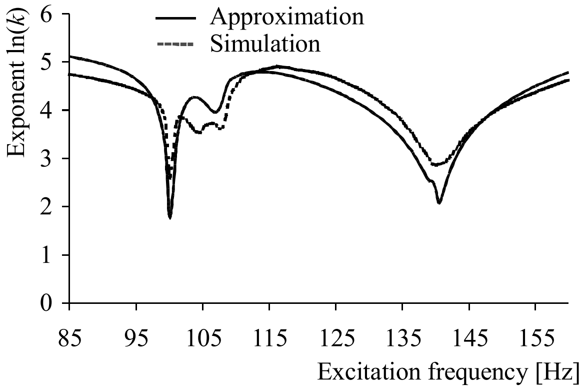

Fig. 5.6-4 Comparison of the calculated exponents ($\sigma_f / f_m = 0.325$ %)

If the related standard deviation of the eigenfrequencies for each mode is increased from 0.325 % up to 1.374 %, see **Fig. 5.6-5**, then the amplitudes increase as well. The exponent k of the approximate method reaches nearly the limiting value of $k = 1$ ($\ln k = 0$), see **Fig. 5.6-6**. Here the probability, that blades vibrate with large amplitude and localization occurs, is very high. Hence, the measure for localization or the exponent k of the Weibull-distribution can be used to find regions where localization occurs with a high probability. A big advantage is that the approximate method holds for all arrangements of mistuned blades distributed around the disk.

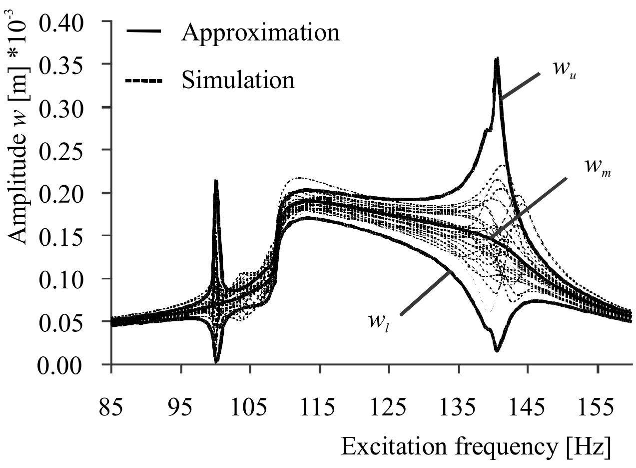

Fig. 5.6-5 Response of the mistuned bladed disk ($\sigma_f / f_m = 1.374$ %)

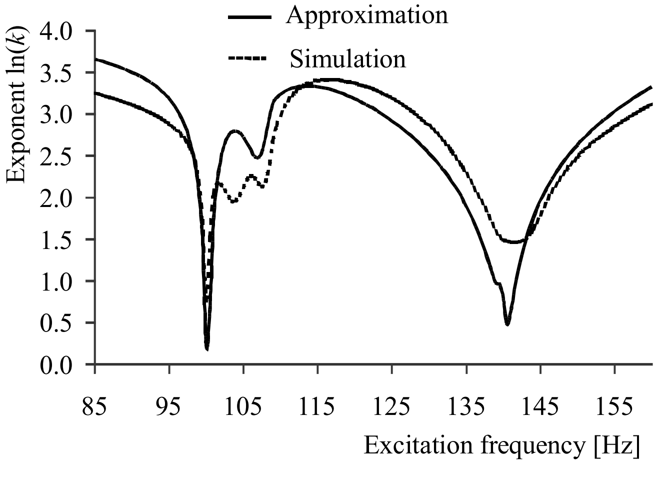

Fig. 5.6-6 Comparison of the calculated exponents ($\sigma_f / f_m = 1.374$ %)

5.7 Elastic Multibody Systems with Extended Friction Contacts

Mechanical systems like the housing of combustion engines, gearboxes and machine tools usually consist of coupled elastic multibody systems, see (Genzo 2005). The coupling in most cases is carried out through extended contact interfaces by means of bolted fastenings. In most cases, the contact interfaces can be considered as dry and extended friction contacts. To verify the developed method a reduced systems is investigated numerical and experimental. The system consists of a freely supported system based on two half pipes coupled in two extended friction contacts through bolt fastenings, see **Fig. 5.7-1**.

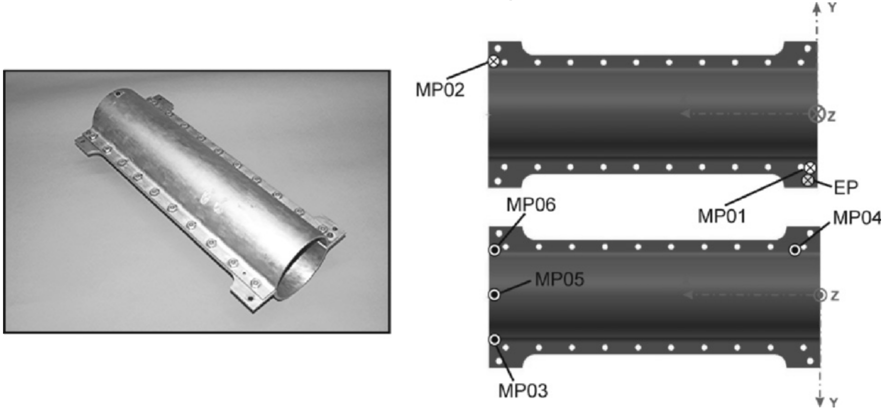

Fig. 5.7-1 Two half pipes coupled by two extended friction contacts

The numerical model consists of local contact models as described in Chapter 5.2, which are applied to each fastening. The corresponding measured and calculated frequency response functions are presented in **Fig. 5.7-2**. The measured first bending resonance agrees very good with the corresponding calculated one. The torsional resonance agrees relative good due to the amplitude. The disagreement with regard to the resonance frequency can be explained by different tangential contact stiffness which has been identified due to the first bending resonance. The coupled bending-torsional resonance is relative good with regard to the comparison while the amplitude of the calculation is underestimated. Here, the difficulty lies in modelling the bolted fastenings, where conditions with no relative motion have to be realized.

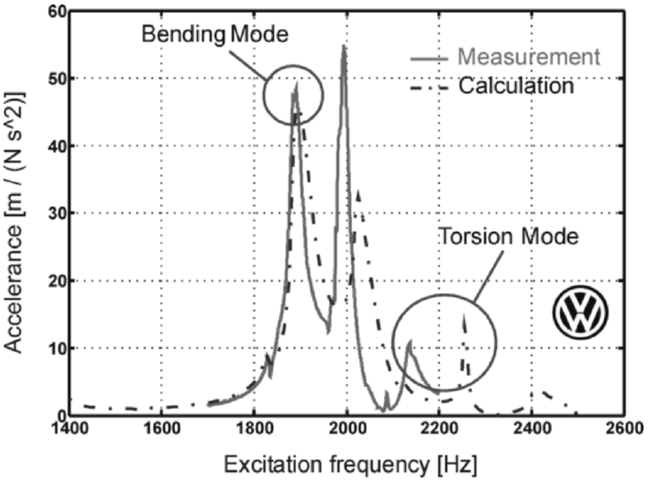

Fig. 5.7-2 Comparison of measurement and calculation

6 Rolling Contact

6.1 Motivation

Railway wheels are getting unround due to wear, see (Knothe 1998; Müller 1998; Küsel and Brommundt 1999; Popp and Schiehlen 2003, Knothe 2003). The wear is distributed like sine waves around the wheel, see **Fig. 6.1-1** and **Fig. 6.1-2**. The unroundness of wheels leads to an increase of noise development, a reduced safety, an increase of the normal loads, which can lead to damage of the wheels, and an increase in cost of maintenance. In case of the Gotthard train the unround wheels are caused by the non-uniform radial elasticity, while in case of the ICE train the problem is unsolved. Hence, there is a need for optimization tools to avoid these problems. Since wear is a long time phenomenon, there is also a need for fast algorithms to calculate the dynamical behavior of wheel-track-systems including the calculation of wear.

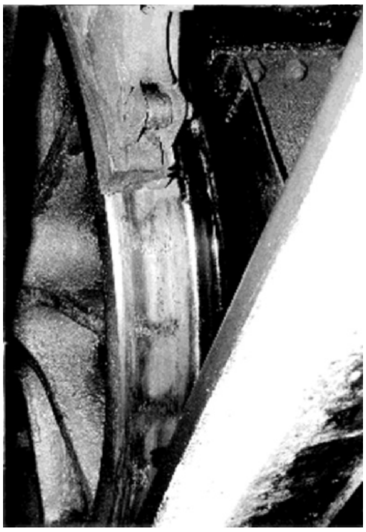

Fig. 6.1-1 Unround wheel of the Gotthard train (Vohla 1996)

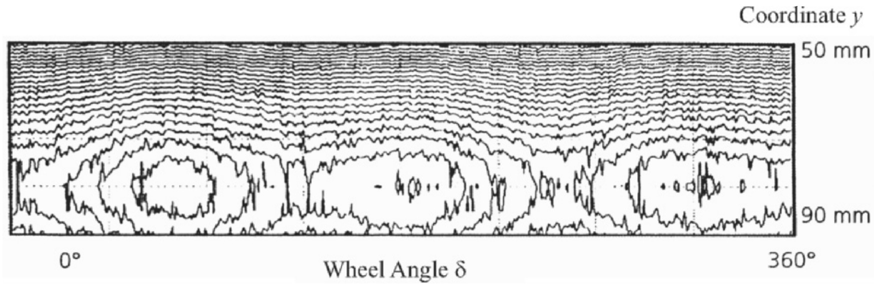

Fig. 6.1-2 Wear profile of an ICE wheel (Moyrs 1998)

To calculate the contact forces for a rolling wheel, Kalker developed the program system CONTACT, see (Kalker 1967, 1990). The theory is based on the Hertzian assumption, that the contact area is very small compared to the sizes of the contacting bodies. Due to the half space assumption, this calculation leads to enormous computation time. To overcome this problem, an alternative program system FASTSIM was developed by Kalker as well. Further contact models are described in (Garg and Dukkipati 1984) and (Ostermeyer 1989). If the half space assumption does not hold, the Finite Element Method can be used to solve the rolling contact problem efficiently, see (Nackenhorst 2000). In (Gutzeit et al. 2006) the calculated longitudinal instationary contact forces of a tire-road contact agree very well to the corresponding experimental results. However, for the dynamical wear problem, the Finite Element Method is limited, because of the large numerical problem within the time domain. The program system FASTSIM neglects the temperature distribution, wear calculation and the influence of the temperature onto other parameters such as the friction coefficient. Due to these physical effects, the developed point contact model can give answers and this will be investigated in the following. Here, the influence of the third body like the lubricant and the worn material is neglected.

6.2 Normal Contact Kinematics

In a first step, the penetration of the wheel and rail in the absence of deformations has to be calculated. In **Fig. 6.2-1**, the reference A-coordinate-system is shown, to describe the position of the contact area, the forces and moments. This coordinate system moves with the average velocity V of both wheels in the x-direction.

The origin 0 of the A-coordinate-system corresponds to the position of first contact, whereby the x- and y-axis are tangential to the wheel and rail surfaces with respect to the origin 0, see **Fig. 6.2-2**. The surfaces of the wheel and rail are described within the W- and T-coordinate-systems, respectively. In the reference state, the coordinate systems and the points $R0$, $S0$ and 0 coincide. The surface position in space can be described by three translations and three rotations with respect to reference points *R0* and *S0* of the surfaces of the wheel and rail, respectively.

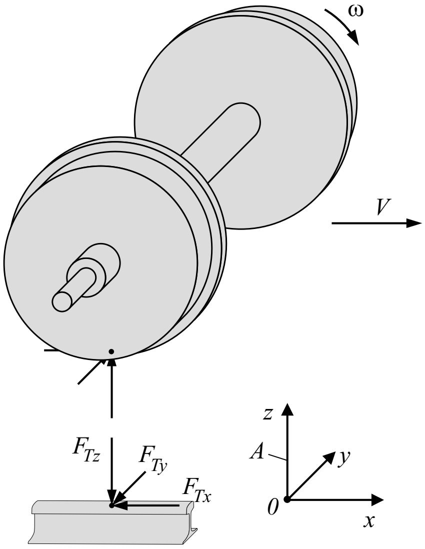

Fig. 6.2-1 Wheel set and rail

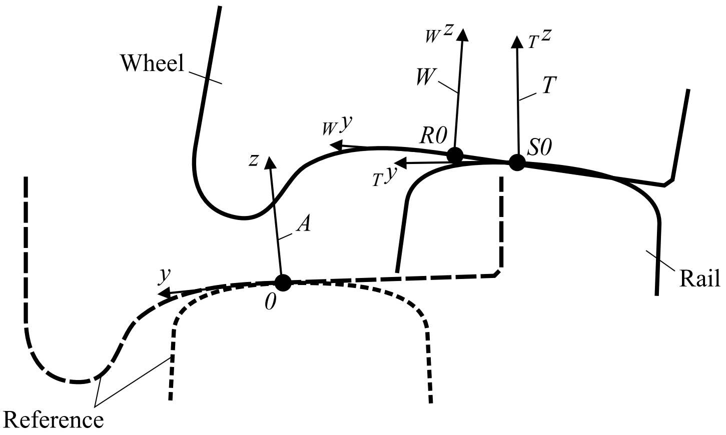

Fig. 6.2-2 Coordinate systems

The spatial position of the rail surface close to the contact is described by

$$ {}_A\boldsymbol{r}_S = {}_A\boldsymbol{u}_{S0} + {}^{AT}\boldsymbol{A}\ {}_T\boldsymbol{r}_S \,, \qquad (6.2\text{-}1)$$

with the relative displacement vector ${}_A\boldsymbol{u}_{S0}$ of the rail reference point *S0*, the coordinates of a point *S* on the rail surface within the *T*-coordinate-system and the transformation matrix ${}^{AT}\boldsymbol{A}$. Assuming small relative angles with respect to the point *S0*

$$\left|\varphi_{S,x,y,z}\right| << 1 \tag{6.2-2}$$

gives corresponding to Eq.(6.2-1)

$$ {}_A\begin{bmatrix} x \\ y \\ z \end{bmatrix}_S = {}_A\begin{bmatrix} u_x \\ u_y \\ u_z \end{bmatrix}_{S0} + \begin{bmatrix} 1 & -\varphi_z & \varphi_y \\ \varphi_z & 1 & -\varphi_x \\ -\varphi_y & \varphi_x & 1 \end{bmatrix}_S {}_T\begin{bmatrix} x \\ y \\ z \end{bmatrix}_S \tag{6.2-3}$$

or using the dimensionless form

$${}_A x_S^* = u_{S0x}^* + {}_T x_S^* - \varphi_{Sz}\ {}_T y_S^* + \varphi_{Sy}\ {}_T z_S^* \tag{6.2-4}$$

$${}_A y_S^* = u_{S0y}^* + {}_T y_S^* + \varphi_{Sz}\ {}_T x_S^* - \varphi_{Sx}\ {}_T z_S^* \tag{6.2-5}$$

$${}_A z_S^* = u_{S0z}^* + {}_T z_S^* - \varphi_{Sy}\ {}_T x_S^* + \varphi_{Sx}\ {}_T y_S^* \tag{6.2-6}$$

with

$$(\ )^* = \frac{(\ )}{a_0}, \tag{6.2-7}$$

where a_0 denotes the unit length or scaling factor. In general, this unit length can be arbitrarily chosen. But to reduce possible numerical problems, this value should be of the same order as the contact size. For example, following Kalkers theory, see (Kalker 1990), this unit length is defined by $a_0 = \sqrt{ab}$, where a and b correspond to the half axes of the contact ellipse calculated by the Hertzian theory.

Since the *T*-coordinate-system is tangential to the rail surface at the reference point *S0* the surface position in the *z*-direction

$$\left|{}_T z_S^*\right| << 1 \tag{6.2-8}$$

is assumed to be small. Then the position of the point *S* lying on the track surface within the *T*-coordinate-system can be calculated

$$\begin{bmatrix} 1 & -\varphi_{Sz} \\ \varphi_{Sz} & 1 \end{bmatrix} \begin{bmatrix} {}_T x_S^* \\ {}_T y_S^* \end{bmatrix} = \begin{bmatrix} {}_A x_S^* - u_{S0x}^* \\ {}_A y_S^* - u_{S0y}^* \end{bmatrix}, \tag{6.2-9}$$

which gives

$${}_T x_S^* = {}_A x_S^* - u_{S0x}^* + \varphi_{Sz}({}_A y_S^* - u_{S0y}^*)\,, \tag{6.2-10}$$

$${}_T y_S^* = {}_A y_S^* - u_{S0y}^* - \varphi_{Sz}({}_A x_S^* - u_{S0x}^*)\,. \tag{6.2-11}$$

Since the *T*-coordinate-system is tangential to the rail surface, the surface of the rail can be described by a polynomial equation of second and higher order terms. Using the mean curvatures R_{S0x} and R_{S0y} with respect to the reference point *S0* of the rail in the *x*- and *y*-direction respectively, the surface can be described by

$$\begin{aligned} {}_T z_S = & -\frac{{}_T x_S^2}{2R_{S0x}}\left(1 + f_{Sx}({}_T x_S)\right) - \frac{{}_T y_S^2}{2R_{S0y}}\left(1 + f_{Sy}({}_T y_S)\right) - \\ & {}_T z_{SW}({}_T x_S, {}_T y_S), \end{aligned} \tag{6.2-12}$$

where ${}_T z_{SW}$ denotes the wear of the rail depending on the coordinates within the *T*-coordinate system. Using the dimensionless notation the surface can be described by

$$\begin{aligned}{}_T z_S^* = &-R_{S0x}^*\ {}_T x_S^{*2}\left(1+f_{Sx}({}_T x_S^*)\right)-R_{S0y}^*\ {}_T y_S^{*2}\left(1+f_{Sy}({}_T y_S^*)\right)-\\ &{}_T z_{SW}^*({}_T x_S^*,{}_T y_S^*)\end{aligned} \tag{6.2-13}$$

with the normalized mean curvatures

$$R_{S0x}^* = \frac{a_0}{2R_{S0x}}, \quad R_{S0y}^* = \frac{a_0}{2R_{S0y}}. \tag{6.2-14}$$

The higher order terms are defined by

$$\begin{aligned} f_{Sx}({}_T x_S^*) &= \sum_i f_{Sxi}\ {}_T x_S^{*i}, \quad \left|f_{Sx}({}_T x_S^*)\right| << 1,\\ f_{Sy}({}_T y_S^*) &= \sum_j f_{Syj}\ {}_T y_S^{*j}, \quad \left|f_{Sy}({}_T y_S^*)\right| << 1, \end{aligned} \tag{6.2-15}$$

which are assumed to be relatively small compared to one. Corresponding to the Eq.(6.2-10) and Eq.(6.2-11) for the rail, the position of the point *R* of the wheel within the *W*-coordinate-system is given by

$${}_W x_R^* = {}_A x_R^* - u_{R0x}^* + \varphi_{Rz}({}_A y_R^* - u_{R0y}^*), \tag{6.2-16}$$

$${}_W y_R^* = {}_A y_R^* - u_{R0y}^* - \varphi_{Rz}({}_A x_R^* - u_{R0x}^*). \tag{6.2-17}$$

Corresponding to Eq.(6.2-6) the position of a point *R* in the *z*-direction of the wheel is calculated by

$${}_A z_R^* = u_{R0z}^* + {}_W z_R^* - \varphi_{Ry}\ {}_W x_R^* + \varphi_{Rx}\ {}_W y_R^* \tag{6.2-18}$$

and corresponding to Eq.(6.2-13), Eq.(6.2-14) and Eq.(6.2-15)

$$\begin{aligned}{}_W z_R^* = &R_{R0x}^*\ {}_W x_R^{*2}\left(1+f_{Rx}({}_W x_R^*)\right)+R_{R0y}^*\ {}_W y_R^{*2}\left(1+f_{Ry}({}_W y_R^*)\right)+\\ &{}_W z_{RW}^*({}_W x_R^*,{}_W y_R^*)\end{aligned} \tag{6.2-19}$$

with

$$R_{R0x}^* = \frac{a_0}{2R_{R0x}}, \quad R_{R0y}^* = \frac{a_0}{2R_{R0y}}, \tag{6.2-20}$$

and

$$\begin{aligned} f_{Rx}({}_W x_R^*) &= \sum_i f_{Rxi}\ {}_W x_R^{*i}, \quad \left|f_{Rx}({}_W x_R^*)\right| << 1,\\ f_{Ry}({}_W y_R^*) &= \sum_j f_{Ryj}\ {}_W y_R^{*j}, \quad \left|f_{Ry}({}_W y_R^*)\right| << 1, \end{aligned} \tag{6.2-21}$$

where ${}_W z_{RW}$ denotes the wear of the wheel depending on the coordinates of the *W*-coordinate system. Using Eq.(6.2-6) and Eq.(6.2-18), the penetration of the solids in the absence of deformations is given by

$$\begin{aligned} u_z^* &= {}_A z_S^* - {}_A z_R^*\\ &= \Delta u_{0z}^* + {}_T z_S^* - {}_W z_R^* - \varphi_{Sy}\ {}_T x_S^* + \varphi_{Ry}\ {}_W x_R^* + \varphi_{Sx}\ {}_T y_S^* - \varphi_{Rx}\ {}_W y_R^* \end{aligned} \tag{6.2-22}$$

with

$$\Delta u_{0z}^* = u_{S0z}^* - u_{R0z}^*. \tag{6.2-23}$$

If the surfaces can be described by second order terms, while holding Eq.(6.2-15) and Eq.(6.2-21), then for the normal contact problem the Hertzian theory can be applied. An improvement of this procedure is described in Chapter 6.4, where average curvatures are calculated within the overlapping region.

6.3 Tangential Contact Kinematics

To be able to calculate the tangential contact forces, the contact region has to be described and the kinematics has to be analyzed. In **Fig. 6.3-1**, a discretized contact area is shown. The corresponding increments are Δx and Δy, while the A-coordinate system moves with the constant velocity V in the x-direction. Due to the direction of velocity V the boundary of the contact area is divided into the so called leading edge where particle are running into the contact and the trailing edge where the particles are running out of the contact region. The corresponding discretization error is discussed in (Kalker 1990). For example, at least *20x20* area elements should be modeled to give a relatively correct answer with respect to a circular contact region.

Within each discretized contact area, the developed point contact model is used to calculate the corresponding three contact forces. Here it is assumed that the damping coefficient β is identical to zero and the inertia effects are neglected ($\Delta m_D=0$), see Chapter 3.7. For calculating the tangential forces, the tangential contact kinematics has to be derived. From Fig. 6.3-1 the displacement of the point M is given by

$$\begin{aligned} x_M &= x_P + u_x, \\ y_M &= y_P + u_y. \end{aligned} \tag{6.3-1}$$

Differentiating with respect to time and assuming a stationary rolling process gives

$$\begin{aligned} v_{Mx} &= v_{Px} + \frac{\partial u_x}{\partial x} V + \underbrace{\frac{\partial u_x}{\partial t}}_{=0}, \\ v_{My} &= v_{Py} + \frac{\partial u_y}{\partial x} V + \underbrace{\frac{\partial u_y}{\partial t}}_{=0} \end{aligned} \tag{6.3-2}$$

with the velocity of the reference coordinate system

$$V = \frac{dx}{dt}, \tag{6.3-3}$$

where it is assumed that the velocity in the x-direction is dominant. Rearranging Eq.(6.3-2) gives the slippage of the point P in the x- and y-direction

$$\begin{aligned} s_{Px} &= s_{Mx} - u'_x, \\ s_{Py} &= s_{My} - u'_y \end{aligned} \tag{6.3-4}$$

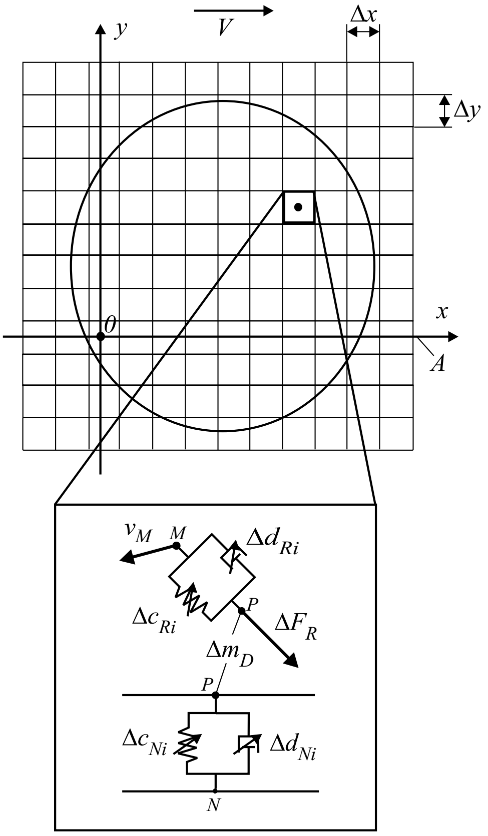

Fig. 6.3-1 Discretized contact area with point contact model

with

$$s_{Px,y} = \frac{v_{Px,y}}{V},$$
$$s_{Mx,y} = \frac{v_{Mx,y}}{V}. \tag{6.3-5}$$

The velocity of the point M is given by

$$\boldsymbol{v}_M = \boldsymbol{v}_0 + \tilde{\boldsymbol{\omega}}\boldsymbol{r}_M \tag{6.3-6}$$

with the velocity $\boldsymbol{v}_0$ of the reference point 0, the angular velocity $\boldsymbol{\omega}$ and the position vector $\boldsymbol{r}_M$ of the point M. Then, the velocity components of the point M in the x- and y-direction are given by

$$v_{Mx} = v_{0x} - \omega_z y_M,$$
$$v_{My} = v_{0y} + \omega_z x_M \tag{6.3-7}$$

or in dimensionless form

$$s_{Mx} = s_{0x} - \psi y^*, \\ s_{My} = s_{0y} + \psi x^* \tag{6.3-8}$$

with the so called creep ratios s_{0x} and s_{0y}

$$s_{0x,y} = \frac{v_{0x,y}}{V}, \tag{6.3-9}$$

the spin parameter

$$\psi = \frac{\omega_z a_0}{V} \tag{6.3-10}$$

and the normalized coordinates of the point M

$$x^* = \frac{x_M}{a_0}, \quad y^* = \frac{y_M}{a_0}. \tag{6.3-11}$$

The components of the relative velocity vector are defined by

$$v_{0x,y} = v_{R0x,y} - v_{S0x,y} \tag{6.3-12}$$

and the relative angular velocity by

$$\omega_z = \omega_z^{(R0)} - \omega_z^{(S0)}. \tag{6.3-13}$$

The z-component of the relative velocity vector is not used, since the viscous damping is neglected. If the contact point P sticks, the slippage in the x- and y-direction is identical to zero,

$$s_{Px} = 0 \quad \wedge \quad s_{Py} = 0. \tag{6.3-14}$$

Inserting this restriction in Eq.(6.3-4) gives

$$u'_x = \frac{\partial u_x^*}{\partial x^*} = s_{Mx}, \\ u'_y = \frac{\partial u_y^*}{\partial x^*} = s_{My}. \tag{6.3-15}$$

Inserting Eq.(6.3-8) in Eq.(6.3-15) and integrating with respect to x^* gives

$$u_x^* = s_{0x} x^* - \psi x^* y^* + h_x, \\ u_y^* = s_{0y} x^* + \tfrac{1}{2}\psi x^{*2} + h_y, \tag{6.3-16}$$

where both integration constants h_x and h_y are independent on x^*. Since the relative displacement at the leading edge is zero

$$u_x^*(x^* = x_A^*, y^*) = 0, \\ u_y^*(x^* = x_A^*, y^*) = 0, \tag{6.3-17}$$

both integration constants can be determined from Eq.(6.3-16) with

$$h_x = -(s_{0x} - \psi y^*) x_A^*, \\ h_y = -(s_{0y} + \tfrac{1}{2}\psi x_A^*) x_A^*, \tag{6.3-18}$$

Inserting Eq.(6.3-18) in Eq.(6.3-16) leads to the relative displacements in the x- and y-direction

$$\begin{aligned} u_x^* &= -(s_{0x} - \psi y^*)(x_A^* - x^*), \\ u_y^* &= -\left(s_{0y} + \tfrac{1}{2}\psi(x_A^* + x^*)\right)(x_A^* - x^*). \end{aligned} \qquad (6.3\text{-}19)$$

Within the contact region these relative displacements are limited due to the maximum friction force, which will be investigated in the Chapter 6.5.

6.4 Contact Stiffnesses

If the half space assumption does not hold, the three contact stiffnesses due to the rolling contact can be found by the Finite Element Method, see for example (Nackenhorst 2000). Fixing the wheel in the center, see Figure 6.2-1, and applying a load with respect to the reference point of the wheel gives the corresponding point contact stiffness. This can be done for all three directions for the wheel as well as for the rail to give three resultant contact stiffnesses. This procedure is straight forward, if the elasticity of the wheel and rail is reduced to springs.

An alternative modeling of the deformations is to describe the wheel by modes, and to apply the Hertzian and Kalkers theory to the contact region to describe the quasi-static deformations. Then, the contact stiffnesses in normal and tangential direction can be derived by the theory of Hertz and Kalker. In general,, the real surface curvatures of a worn wheel are not constant within the overlapping region, see Fig. 6.1-2. Since both theories require constant curvatures of the contact surfaces, average curvatures are calculated to be able to apply these theories. The average curvatures are calculated using the surface description of the rail and the wheel defined in Eq.(6.2-13) and Eq.(6.2-19), respectively. For example, differentiating Eq.(6.2-19) twice with respect to the x_R-coordinate gives

$$\frac{\partial^2 z_R^*}{\partial x_R^{*2}} = 2R_{R0x}^*(1 + f_{Rx}) + 4R_{R0x}^* x_R^* \frac{\partial f_{Rx}}{\partial x_R^*} + R_{R0x}^* x_R^{*2} \frac{\partial^2 f_{Rx}}{\partial x_R^{*2}} + \frac{\partial^2 z_{RW}^*}{\partial x_R^{*2}} \qquad (6.4\text{-}1)$$

with Eq.(6.2-21) and the approximation of the curvature of the worn depth calculated by discrete values of the wheel in x-direction

$$\left.\frac{\partial^2 z_{RW}^*}{\partial x_R^{*2}}\right|_{x_R^* = x_{Ri}^*} \approx \frac{z_{RWi+1}^* - 2z_{Ri}^* + z_{RWi-1}^*}{\Delta x^{*2}}, \qquad (6.4\text{-}2)$$

see (Johnson 1989). Then, the average curvature of the wheel in x-direction is given by

$$A_R^* = \frac{1}{n_x n_y} \sum_{i=1}^{n_x n_y} \left.\frac{\partial^2 z_R^*}{\partial x_R^{*2}}\right|_{x_R^* = x_{Ri}^*}. \qquad (6.4\text{-}3)$$

Corresponding to Eq.(6.4-1) up to Eq.(6.4-3) the average curvatures B_R in the y-direction of the wheel and furthermore the average curvatures A_S and B_S of the rail in x- and y-direction, respectively, can be calculated. For the application of the Hertzian theory the relationship of the principle curvature needs to be known and can be calculated by

$$\frac{A}{B} = \frac{A^*}{B^*} = \frac{A_R^* - A_S^*}{B_R^* - B_S^*}\,. \qquad (6.4\text{-}4)$$

Neglecting higher order terms with respect to the coordinates of the contact surfaces defined in Eq.(6.2-15) and Eq.(6.2-21)

$$\frac{x_S}{R_{S0x}} << 1, \quad \frac{y_S}{R_{S0y}} << 1, \quad \frac{x_R}{R_{R0x}} << 1, \quad \frac{y_R}{R_{R0y}} << 1 \qquad (6.4\text{-}5)$$

and assuming that the curvatures with respect to the worn material are very small compared to the mean curvatures, then the principle relative curvatures A and B in the x- and y-direction, respectively, are given by the mean curvatures with

$$A = \frac{1}{R_{R0x}} + \frac{1}{R_{S0x}}\,, \qquad (6.4\text{-}6)$$

$$B = \frac{1}{R_{R0y}} + \frac{1}{R_{S0y}}\,. \qquad (6.4\text{-}7)$$

Hence, the relationship of the principle curvatures is given by

$$\frac{A}{B} = \frac{R_{R0x}^* + R_{S0x}^*}{R_{R0y}^* + R_{S0y}^*} \qquad (6.4\text{-}8)$$

with the dimensionless mean curvatures defined in Eq.(6.2-14) and Eq.(6.2-20).

To be able to calculate the normal and tangential contact stiffnesses, the so called ellipticity g of the contact area has to be calculated from the Hertzian theory, see (Hill 1993), with

$$g^2 = \frac{A}{B}\frac{\boldsymbol{B}(e)}{\boldsymbol{D}(e)}, \quad \frac{A}{B} \le 1 \qquad (6.4\text{-}9)$$

with the principle relative curvatures A and B as defined above. The relation of the halfaxes of the contact ellipse defines the ellipticity

$$g = \frac{b}{a}, \quad b \le a\,, \qquad (6.4\text{-}10)$$

and the integrals,

$$\boldsymbol{D}(e) = \frac{1}{e^2}\big(\boldsymbol{K}(e) - \boldsymbol{E}(e)\big), \qquad (6.4\text{-}11)$$

$$\boldsymbol{B}(e) = \boldsymbol{K}(e) - \boldsymbol{D}(e)\,, \qquad (6.4\text{-}12)$$

calculated from the complete elliptic integrals of the first and second kind with

$$e^2 = 1 - g^2\,. \qquad (6.4\text{-}13)$$

For the derivation of the formulas, it is assumed that the half axes b in the y-direction is smaller than the half axes a in the x-direction of the contact ellipse. For the case if $b>a$, the radius of curvatures and the half axes a and b have only to be exchanged. The complete elliptic integrals of the first and second kind, respectively, are given by

$$\boldsymbol{E}(e) = \int_0^{\frac{\pi}{2}} \sqrt{1 - e^2 \sin^2 \phi}\; d\phi \tag{6.4-14}$$

and

$$\boldsymbol{K}(e) = \int_0^{\frac{\pi}{2}} \frac{d\phi}{\sqrt{1 - e^2 \sin^2 \phi}}\,. \tag{6.4-15}$$

Since Eq.(6.4-9) has to be solved iteratively, a first good guess is given by

$$g = \left(\frac{A}{B}\right)^{\frac{2}{3}}, \tag{6.4-16}$$

see (Greenwood 1985). The results of the iteration are summarized in a table. Then, the half axes of the contact ellipse are calculated by

$$\begin{aligned} a^2 &= \frac{\Delta u_{0z}}{A}\frac{\boldsymbol{D}(e)}{\boldsymbol{K}(e)}, \\ b^2 &= \frac{\Delta u_{0z}}{B}\frac{\boldsymbol{B}(e)}{\boldsymbol{K}(e)}. \end{aligned} \tag{6.4-17}$$

With respect to the main coordinate system of the ellipse, the penetration is given by Eq.(6.2-22), with

$$u_z^* = \Delta u_{0z}^* \left(1 - \frac{R_{0x}^*}{\Delta u_{0z}^*} x^{*2} - \frac{R_{0y}^*}{\Delta u_{0z}^*} y^{*2} \right) \tag{6.4-18}$$

with the normalized curvatures

$$\begin{aligned} R_{0x}^* &= R_{S0x}^* + R_{R0x}^*, \\ R_{0y}^* &= R_{S0y}^* + R_{R0y}^*, \end{aligned} \tag{6.4-19}$$

defined in Eq.(6.2-14) and Eq.(6.2-20). The half axes of the contact ellipse are found by

$$\begin{aligned} &u_z^*(x^* = a^*, y^* = 0) = 0, \\ &u_z^*(x^* = 0, y^* = b^*) = 0, \end{aligned} \tag{6.4-20}$$

which gives

$$\begin{aligned} a^{*2} &= \frac{\Delta u_{0z}^*}{R_{0x}^*}, \\ b^{*2} &= \frac{\Delta u_{0z}^*}{R_{0y}^*}. \end{aligned} \tag{6.4-21}$$

To satisfy Eq.(6.4-17) from the Hertzian theory, with respect to Eq.(6.4-21), the curvatures are exchanged by using the following formulas

$$R_{0x}^* = A^* \frac{\boldsymbol{K}(e)}{\boldsymbol{D}(e)}, \tag{6.4-22}$$

and

$$R_{0y}^* = B^* \frac{\boldsymbol{K}(e)}{\boldsymbol{B}(e)}, \quad b \le a\ . \tag{6.4-23}$$

For translations the normal contact force in the *z*-direction is given by the Hertzian theory, see (Hill 1993),

$$\begin{aligned} F_N &= \frac{\pi E a}{3(1-\nu^2)\boldsymbol{K}(e)} \Delta u_{0z}, \quad for \quad b \le a \\ F_N &= \frac{\pi E b}{3(1-\nu^2)\boldsymbol{K}(e)} \Delta u_{0z}, \quad for \quad b > a \end{aligned} \tag{6.4-24}$$

and the tangential forces in the *x*- and *y*-direction are given by Kalkers theory, see (Kalker 1990), with

$$\begin{aligned} F_{Fx} &= C_{11} G ab s_{0x}, \\ F_{Fy} &= C_{22} G ab s_{0y}. \end{aligned} \tag{6.4-25}$$

The linear coefficients C_{11} and C_{22} are dependent on the ellipticity, see (Kalker 1990) and can be approximated by polynomials, see (Fingberg 1990). With respect to the wheel-rail contact in the region where the ellipticity is between $g=0.1$ and $g=10.0$ and Poisson's ratio is assumed to be $\nu=0.3$ the corresponding polynomial are given by

$$\begin{aligned} C_{11} &= 3.442 + 0.8980(a/b) + 0.01205(a/b)^2 - 0.00169(a/b)^3, \\ C_{22} &= 2.386 + 1.3578(a/b) - 0.02538(a/b)^2. \end{aligned} \tag{6.4-26}$$

To satisfy Eq.(6.4-24) and Eq.(6.4-25), these three contact forces are used to determine the three contact stiffnesses one in normal and two in tangential direction.

With respect to the main coordinate system of the ellipse, the normal penetration due to the normal displacement of the center points is given from Eq.(6.4-18) by

$$u_z^* = \frac{\Delta u_{0z}^*}{a^{*2}}(x_A^* - x^*)(x^* - x_E^*) = \frac{\Delta u_{0z}^*}{a^{*2}}(x_A^{*2} - x^{*2})\ , \tag{6.4-27}$$

where the start position x_A at the leading edge and end position x_E at the trailing edge are given by

$$x_A^* = a^* \sqrt{1 - \frac{y^{*2}}{b^{*2}}}, \quad x_E^* = -x_A^*\ . \tag{6.4-28}$$

Assuming the elastic foundation model, which corresponds to a constant distribution of contact stiffnesses, the pressure distribution is given by

$$p_N = \frac{2F_N}{\pi a^3 b}(x_A^2 - x^2) \approx \frac{\Delta F_N}{\Delta A} = \frac{\Delta c_{N0} u_z}{\Delta x \Delta y}\ . \tag{6.4-29}$$

Inserting Eq.(6.4-27) and Eq.(6.4-24) for the Hertzian normal contact force and solving for the discrete normal stiffness gives

$$\Delta c_{N0} = c_{N0} \Delta c_{N0}^{*} \tag{6.4-30}$$

with

$$\begin{aligned} c_{N0} &= \frac{\pi E a_0}{3(1-\nu^2)\boldsymbol{K}(e)} \frac{a_0}{b}, \quad for \quad b \le a, \\ c_{N0} &= \frac{\pi E a_0}{3(1-\nu^2)\boldsymbol{K}(e)} \frac{a_0}{a}, \quad for \quad b > a \end{aligned} \tag{6.4-31}$$

and the constant contact stiffness distribution in the normal direction

$$\Delta c_{N0}^{*} = \frac{2}{\pi} \Delta x^{*} \Delta y^{*} . \tag{6.4-32}$$

The tangential traction in the *x*- and *y*-direction is assumed to be proportional to the displacement, hence,

$$\tau_{x,y} = \frac{3F_{Fx,y}}{8a^2 b}(x_A - x) \approx \frac{\Delta F_{Fx,y}}{\Delta A} = \frac{\Delta c_{R0x,y} u_{x,y}}{\Delta x \Delta y} . \tag{6.4-33}$$

Inserting Eq.(6.3-19) with zero spin to describe the tangential displacement and Eq.(6.4-25) in Eq.(6.4-33) and solving for the discrete tangential contact stiffness gives

$$\Delta c_{R0x,y} = c_{R0x,y} \Delta c_{R0x,y}^{*} \tag{6.4-34}$$

with

$$c_{R0x} = C_{11} G \frac{a_0^2}{a}, \quad c_{R0y} = C_{22} G \frac{a_0^2}{a} \tag{6.4-35}$$

and the constant distribution of contact stiffnesses in the tangential direction

$$\Delta c_{R0x}^{*} = \Delta c_{R0y}^{*} = \frac{3}{8} \Delta x^{*} \Delta y^{*} . \tag{6.4-36}$$

Now, we can summarize the results to give the normalized tangential stiffness used in the next Chapter

$$c_{R0x,y}^{*} = \frac{c_{R0x,y}}{\mu_0 c_{N0}} = \frac{3C_{11,22}(1-\nu)\boldsymbol{K}(e)}{2\pi\mu_0} \frac{b}{a}, \quad b \le a \tag{6.4-37}$$

and

$$c_{R0x,y}^{*} = \frac{3C_{11,22}(1-\nu)\boldsymbol{K}(e)}{2\pi\mu_0}, \quad b > a . \tag{6.4-38}$$

Up to here, we assumed a constant distribution of contact stiffnesses. In the following, we will distribute the contact stiffnesses, so that the elliptical pressure distribution of Hertz is modeled exactly. The Hertzian pressure distribution is given by

$$p_N = \frac{3F_N}{2\pi a^2 b} \sqrt{x_A^2 - x^2} \approx \frac{\Delta c_{N0} u_z}{\Delta x \Delta y} . \tag{6.4-39}$$

Again, inserting Eq.(6.4-24) and Eq.(6.4-27) gives

$$c_{N0} = \frac{\pi E a_0}{3(1-\nu^2)\boldsymbol{K}(e)}\frac{a}{b}, \quad for \quad b \le a, \qquad\qquad (6.4\text{-}40)$$
$$c_{N0} = \frac{\pi E a_0}{3(1-\nu^2)\boldsymbol{K}(e)}, \quad for \quad b > a$$

and

$$\Delta c^*_{N0} = \frac{3}{2\pi}\frac{\Delta x^* \Delta y^*}{\sqrt{x_A^{*2} - x^{*2}}}. \qquad\qquad (6.4\text{-}41)$$

The tangential traction is assumed to be, see (Johnson 1989),

$$\tau_{x,y} = \frac{2F_{Fx,y}}{\pi^2 ab}\frac{x_A - x}{\sqrt{x_A^2 - x^2}} \approx \frac{\Delta c_{R0x,y} u_{x,y}}{\Delta x \Delta y}. \qquad\qquad (6.4\text{-}42)$$

Again, inserting Eq.(6.3-19) and Eq.(6.4-25) gives the discrete contact stiffnesses in the x- and y-direction given by Eq.(6.4-34) with

$$c_{R0x} = C_{11} G a_0, \quad c_{R0y} = C_{22} G a_0 \qquad\qquad (6.4\text{-}43)$$

and the non-constant contact stiffness distribution in the tangential direction

$$\Delta c^*_{R0x} = \Delta c^*_{R0y} = \frac{2}{\pi^2}\frac{\Delta x^* \Delta y^*}{\sqrt{x_A^{*2} - x^{*2}}}. \qquad\qquad (6.4\text{-}44)$$

Again, we summarize the results to give the normalized tangential stiffness used for the non-constant distribution of contact stiffnesses in the next Chapter

$$c^*_{R0x,y} = \frac{3C_{11,22}(1-\nu)\boldsymbol{K}(e)}{2\pi\mu_0}\frac{b}{a}, \quad b \le a \qquad\qquad (6.4\text{-}45)$$

and

$$c^*_{R0x,y} = \frac{3C_{11,22}(1-\nu)\boldsymbol{K}(e)}{2\pi\mu_0}, \quad b > a. \qquad\qquad (6.4\text{-}46)$$

Using the non-constant distribution, the global stiffnesses are only dependent on the relationship of the half axes of the ellipse. Now, all three global contact stiffnesses are known, whereby the distribution of discrete contact stiffnesses in the normal direction fulfills exactly the Hertzian normal contact and the distribution in the tangential direction has been approximated. An analytical description of the distribution of tangential contact stiffnesses with respect to Kalkers theory is not possible, since the traction within the rolling contact is calculated numerically. Further investigation on the distribution of contact stiffnesses are investigated in the following Chapter 6.5.

6.5 Generalized Contact Forces

Before calculating the generalized contact forces, the discrete contact forces for each area element have to be calculated. Due to the point contact model described in Chapter 3, the damping influence ($\beta=0$) and the inertia forces are neglected

($\Delta m_D=0$). Then, in case of *sticking* the elastic forces with respect to the point contact model are given corresponding to Eq.(3.7-16)

$$\begin{aligned} \Delta F_{Fx}^* &= c_{R0x}^* \Delta c_{R0x}^* h^* u_x^*, \\ \Delta F_{Fy}^* &= c_{R0y}^* \Delta c_{R0y}^* h^* u_y^*, \\ \Delta F_N^* &= \Delta c_{N0}^* R_Z^* f^* \end{aligned} \tag{6.5-1}$$

with the normalized parameter

$$\Delta F_{Fx,y}^* = \frac{\Delta F_{Fx,y}}{\mu_0 c_{N0} a_0}, \quad \Delta F_N^* = \frac{\Delta F_N}{c_{N0} a_0}, \tag{6.5-2}$$

$$c_{R0x,y}^* = \frac{c_{R0x,y}}{\mu_0 c_{N0}}, \quad \Delta c_{R0x,y}^* = \frac{\Delta c_{R0x,y}}{c_{R0x,y}}, \tag{6.5-3}$$

$$\Delta c_{N0}^* = \frac{\Delta c_{N0}}{c_{N0}} \tag{6.5-4}$$

and the normalized average roughness

$$R_Z^* = \frac{R_Z}{a_0}. \tag{6.5-5}$$

Within the *x,y*-contact plane, the direction of the elastic forces is described by the angle α and can be calculated by

$$\tan\alpha = \frac{\Delta F_{Fy}^*}{\Delta F_{Fx}^*}. \tag{6.5-6}$$

In case of *sliding*, the friction forces act in the opposite direction of the resultant elastic force. The equilibrium with respect to the point P is given by

$$\begin{aligned} \Delta F_{Fx}^* + \Delta F_{Rx}^* &= 0, \\ \Delta F_{Fy}^* + \Delta F_{Ry}^* &= 0, \end{aligned} \tag{6.5-7}$$

with the components of the friction force assuming Coulomb friction

$$\begin{aligned} \Delta F_{Rx}^* &= -\mu^* \Delta F_N^* \cos\alpha, \\ \Delta F_{Ry}^* &= -\mu^* \Delta F_N^* \sin\alpha, \end{aligned} \tag{6.5-8}$$

with the normalized friction coefficient

$$\mu^* = \frac{\mu}{\mu_0}. \tag{6.5-9}$$

The direction of the friction force is opposite to the velocity of the point P, where the direction of the velocity of the point P is defined by

$$\tan\alpha = \frac{\Delta F_{Fy}^*}{\Delta F_{Fx}^*} = \frac{-\Delta F_{Ry}^*}{-\Delta F_{Rx}^*} = \frac{v_{Py}}{v_{Px}} = \frac{s_{Py}}{s_{Px}} \tag{6.5-10}$$

or

$$\cos\alpha = \frac{\dot{x}_P}{v_P} = \frac{v_{Px}}{v_P}, \quad \sin\alpha = \frac{\dot{y}_P}{v_P} = \frac{v_{Py}}{v_P} \tag{6.5-11}$$

with the resultant velocity of the point P

$$v_P = \sqrt{v_{Px}^2 + v_{Py}^2}\ . \tag{6.5-12}$$

Inserting Eq.(6.5-1) and Eq.(6.5-8) in Eq.(6.5-7) gives

$$\begin{aligned} c_{R0x}^* \Delta c_{R0x}^* h^* u_x^* &= \mu^* \Delta F_N^* \cos\alpha, \\ c_{R0y}^* \Delta c_{R0y}^* h^* u_y^* &= \mu^* \Delta F_N^* \sin\alpha \end{aligned} \tag{6.5-13}$$

and differentiating with respect to x^* leads to

$$\begin{aligned} u_x' &= -p_x \alpha' \sin\alpha, \\ u_y' &= p_y \alpha' \cos\alpha \end{aligned} \tag{6.5-14}$$

with the dimensionless parameter

$$p_x = \frac{\mu^* \Delta F_N^*}{c_{R0x}^* \Delta c_{R0x}^* h^*}, \quad p_y = \frac{\mu^* \Delta F_N^*}{c_{R0y}^* \Delta c_{R0y}^* h^*}\ . \tag{6.5-15}$$

Here, the derivations of both parameters p_x and p_y with respect to the coordinate x^* have been neglected, since both parameter do only depend explicit on the normal penetration. Inserting Eq.(6.5-14) in Eq.(6.3-4) gives

$$\begin{aligned} s_{Px} &= s_{Mx} + p_x \alpha' \, sin\,\alpha, \\ s_{Py} &= s_{My} - p_y \alpha' \, cos\,\alpha. \end{aligned} \tag{6.5-16}$$

Furthermore, inserting these equations in Eq.(6.5-10) and rearranging gives the nonlinear differential equation with respect to the angle α

$$\alpha' = \frac{s_{My} \cos\alpha - s_{Mx} \sin\alpha}{p_x \sin^2\alpha + p_y \cos^2\alpha}\ . \tag{6.5-17}$$

Since the contact is discretized, the angle α can be calculated by Euler's method

$$\alpha_i = \alpha_{i-1} - \frac{s_{My} \cos\alpha_{i-1} - s_{Mx} \sin\alpha_{i-1}}{p_x \sin^2\alpha_{i-1} + p_y \cos^2\alpha_{i-1}} \Delta x^* \tag{6.5-18}$$

with the starting condition at the leading edge $x = x_A$ derived from Eq.(6.5-10) by using Eq.(6.5-1), Eq.(6.3-19) and Eq.(6.3-8)

$$\alpha_1 = \arctan\left(\frac{-c_{R0y}^* s_{My}}{-c_{R0x}^* s_{Mx}} \right). \tag{6.5-19}$$

In case of sliding, the contact forces acting onto the wheel are given by

$$\Delta F_{Wx}^* = -\Delta F_{Rx}^*, \quad \Delta F_{Wy}^* = -\Delta F_{Ry}^*, \quad \Delta F_{Wz}^* = \Delta F_N^*\ . \tag{6.5-20}$$

In case of sticking, the contact forces acting onto the wheel are given by

$$\Delta F_{Wx}^* = \Delta F_{Fx}^*, \quad \Delta F_{Wy}^* = \Delta F_{Fy}^*, \quad \Delta F_{Wz}^* = \Delta F_N^*\ . \tag{6.5-21}$$

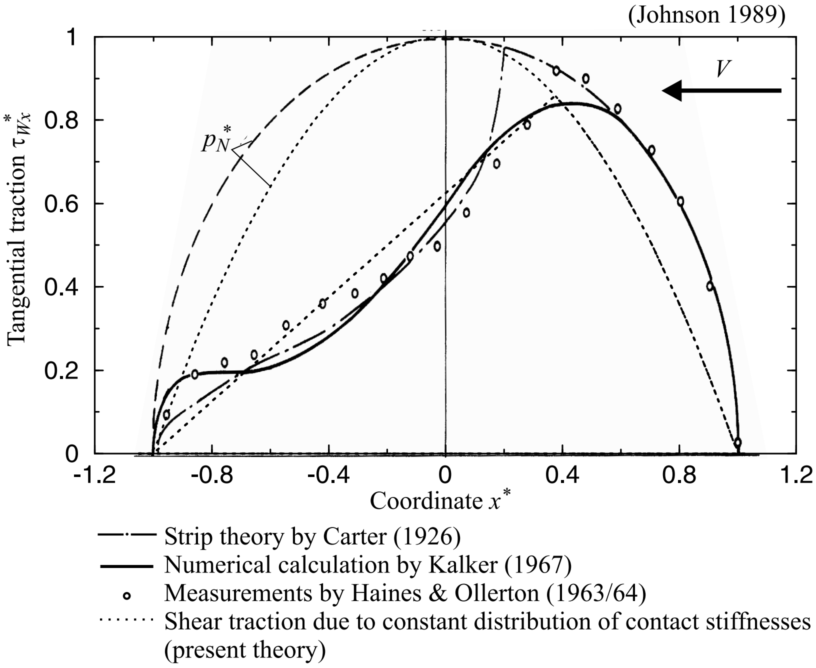
(Johnson 1989)

Fig. 6.5-1 Tangential traction due to different contact models compared with the developed contact model assuming a *constant* distribution of contact stiffnesses

In **Fig. 6.5-1**, the shear traction using different models is shown for the longitudinal force of $F_{Wx}=0.72\mu F_N$. The models are the strip theory developed by Carter, the numerical calculation by Kalker, the measurements by Haines & Ollerton and the shear traction due to the developed point contact model with a constant distribution of contact stiffnesses. The shear traction and the normal pressure distribution is given by

$$\tau_{Wx,y} = \frac{\Delta F_{Wx,y}}{\Delta x \Delta y}, \quad p_N = \frac{\Delta F_{Wz}}{\Delta x \Delta y}, \tag{6.5-22}$$

respectively, or in dimensionless form

$$\tau_{Wx,y}^* = \frac{\tau_{Wx,y}}{\mu_0 p_N(x=0)}, \quad p_N^* = \frac{p_N}{p_N(x=0)}. \tag{6.5-23}$$

Within the stick region, the developed model with constant distributed contact stiffnesses leads to a linear increase in traction. This principle behavior is modeled within the program system FASTSIM of Kalker as well. Therefore, the results are the same, but now the physical interpretation is given. Using the non-constant distribution of contact stiffnesses derived from the Hertzian theory, the limiting value of shear traction is given by the friction coefficient multiplied by the Hertzian or elliptical pressure distribution, see **Fig. 6.5-2**. Here, the non-constant distribution gives a better approximation of the reality, compared to the usage of constant distributed contact stiffnesses, because the measurements show a slightly curved functional behavior within the sticking region as well.

(Johnson 1989)

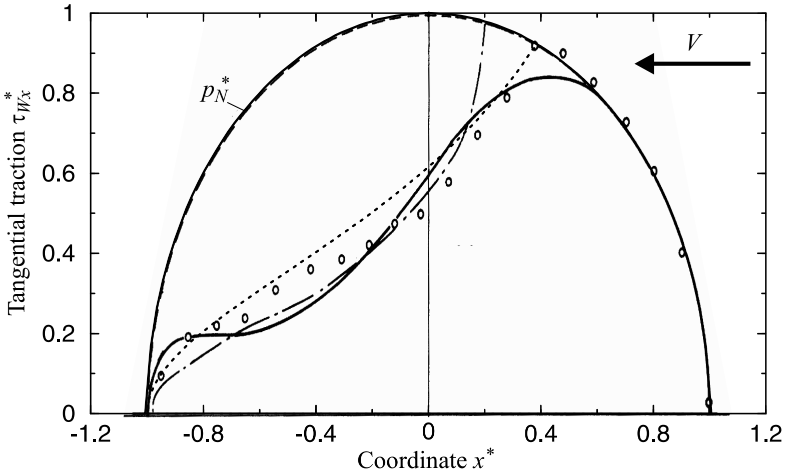

—·— Strip theory by Carter (1926)

—— Numerical calculation by Kalker (1967)

o Measurements by Haines & Ollerton (1963/64)

······ Shear traction due to non-constant distribution of contact stiffnesses (present theory)

Fig. 6.5-2 Tangential traction due to different contact models compared with the developed contact model assuming a *non-constant* distribution of contact stiffnesses

The resultant contact forces will influence the dynamics of the wheel and rail. These forces acting onto the wheel are calculated by the summation of each discrete force

$$\Delta \boldsymbol{F}_W = \begin{bmatrix} \Delta F_{Wx} & \Delta F_{Wy} & \Delta F_{Wz} \end{bmatrix}^T \tag{6.5-24}$$

at the position

$$\boldsymbol{r}_M = \begin{bmatrix} x & y & 0 \end{bmatrix}^T . \tag{6.5-25}$$

In the following, the small rotations of the coordinate systems are neglected. Hence, the corresponding moment with respect to the reference *0* point is determined by

$$\Delta \boldsymbol{M}_W^{(0)} = \tilde{\boldsymbol{r}}_M \Delta \boldsymbol{F}_W . \tag{6.5-26}$$

The dimensionless contact forces are calculated by the summation

$$\boldsymbol{F}_W^* = \sum_{i=1}^{n_x n_y} \Delta \boldsymbol{F}_W^* \tag{6.5-27}$$

and the dimensionless contact moments with respect to the point *0* by

$$\boldsymbol{M}_W^{(0)*} = \sum_{i=1}^{n_x n_y} \tilde{\boldsymbol{r}}_M^* \Delta \boldsymbol{F}_W^* = \sum_{i=1}^{n_x n_y} \begin{bmatrix} y^* \Delta F_{Wz}^* \\ -x^* \Delta F_{Wz}^* \\ x^* \Delta F_{Wy}^* - y^* \Delta F_{Wx}^* \end{bmatrix}, \tag{6.5-28}$$

with

$$F_{Wx,y}^* = \frac{F_{Wx,y}}{\mu_0 c_{N0} a_0}, \quad F_{Wz}^* = \frac{F_{Wz}}{c_{N0} a_0}, \tag{6.5-29}$$

$$M_{Wx,y}^{(0)*} = \frac{M_{Wx,y}^{(0)}}{c_{N0} a_0^2}, \quad M_{Wz}^{(0)*} = \frac{M_{Wz}^{(0)}}{\mu_0 c_{N0} a_0^2}. \tag{6.5-30}$$

Another possibility to normalize Eq.(6.5-27) and Eq.(6.5-28) is to relate each generalized force with respect to the normalized normal contact force in Eq.(6.5-27), which gives

$$F_{Wx,y}^{**} = \frac{F_{Wx,y}^*}{F_{Wz}^*} = \frac{F_{Wx,y}}{\mu_0 F_{Wz}}, \quad F_{Wz}^{**} = 1, \tag{6.5-31}$$

$$M_{Wx,y}^{(0)**} = \frac{M_{Wx,y}^{(0)*}}{F_{Wz}^*} = \frac{M_{Wx,y}^{(0)}}{F_{Wz} a_0}, \quad M_{Wz}^{(0)**} = \frac{M_{Wz}^{(0)*}}{F_{Wz}^*} = \frac{M_{Wz}^{(0)}}{\mu_0 F_{Wz} a_0}. \tag{6.5-32}$$

The resulting moment with respect to the reference point *R0* of the wheel, see Fig. 6.2-2, is calculated by

$$\boldsymbol{M}_W^{(R0)*} = \boldsymbol{M}_W^{(0)*} - \tilde{\boldsymbol{u}}_{R0}^* \boldsymbol{F}_W^* \tag{6.5-33}$$

with the displacement vector

$$\boldsymbol{u}_{R0}^* = \begin{bmatrix} u_{R0x}^* & u_{R0y}^* & 0 \end{bmatrix}^T, \tag{6.5-34}$$

assuming that the displacement in z-direction is very small and, hence, can be neglected. Similar to Eq.(6.5-33), the moment with respect to the reference point *S0* of the rail is given by

$$\boldsymbol{M}_W^{(S0)*} = \boldsymbol{M}_W^{(0)*} - \tilde{\boldsymbol{u}}_{S0}^* \boldsymbol{F}_W^* \tag{6.5-35}$$

with

$$\boldsymbol{u}_{S0}^* = \begin{bmatrix} u_{S0x}^* & u_{S0y}^* & 0 \end{bmatrix}^T. \tag{6.5-36}$$

The generalized forces acting onto the rail are given by Newton's third law "*actio=reactio*"

$$\boldsymbol{F}_T^* = -\boldsymbol{F}_W^*, \quad \boldsymbol{M}_T^{(S0)*} = -\boldsymbol{M}_W^{(S0)*}. \tag{6.5-37}$$

6.6 Validation of the Rolling Contact Model

For a comparison of the calculation with respect to the developed rolling contact model and the results of Kalkers model, the slippage coefficient has to be transformed. The dimensionless formulas for the slippage defined in (Kalker 1990), are given by

$$s_{0x}^{*}=-\xi'=\frac{C_{11}Gab}{3\mu_0F_N}\xi=\frac{c_{R0x}^{*}a^{*j}b^{*}}{3F_N^{*}}s_{0x},\quad s_{0x}=\xi\,, \tag{6.6-1}$$

$$s_{0y}^{*}=-\eta'=\frac{C_{22}Gab}{3\mu_0F_N}\eta=\frac{c_{R0y}^{*}a^{*j}b^{*}}{3F_N^{*}}s_{0y},\quad s_{0y}=\eta \tag{6.6-2}$$

and the dimensionless spin parameter

$$\psi^{*}=-\phi'=\frac{C_{23}Gab}{\mu_0F_N}\phi c=\frac{C_{23}}{C_{22}}\frac{c_{R0y}^{*}a^{*j}b^{*}}{F_N^{*}}\psi,\quad \psi=\phi c \tag{6.6-3}$$

with the unit length of

$$c=a_0=\sqrt{ab} \tag{6.6-4}$$

and the dimensionless halfaxes of the contact ellipse

$$a^{*}=\frac{a}{a_0},\quad b^{*}=\frac{b}{a_0}\,. \tag{6.6-5}$$

For the application of the constant distribution of contact stiffnesses the exponent j is given by $j=2$ and for the non-constant distribution of contact stiffnesses the exponent is given by $j=1$.

In **Fig. 6.6-1**, a theoretical comparison of different calculation methods of the normalized resultant tangential force

$$\left|F_W^{**}\right|=\sqrt{F_{Wx}^{**2}+F_{Wy}^{**2}} \tag{6.6-6}$$

versus the total slippage defined by

$$\left|s_0^{*}\right|=\sqrt{s_{0x}^{*2}+s_{0y}^{*2}} \tag{6.6-7}$$

varying the axial ratio (*a/b*) is shown. It appears that the results of FASTSIM are very good in agreement with the numerical results of the program CONTACT for all Poisson's ratios and axial ratios. Within the stick zone the traction is linear distributed with respect to the use of constant distribution of contact stiffnesses, here, the results are very close to the results of Kalker. The very small differences between both curves are due to the numeric. Here, the assumption for a non-constant distribution of contact stiffnesses does not fit so well. This is surprising, since in this case the normal pressure distribution is identical to the Hertzian distribution.

In **Fig. 6.6-2**, a comparison of measurement with calculations of the resultant tangential contact force versus the total slippage is shown for different axial ratios. Up to now, there exits only the numerical solution of the theoretical description of the rolling contact by Kalker, see (Kalker 1967), which leads to an enormous computation time. In (Vermeulen and Johnson 1964; Shen et al. 1994) approximated calculation methods are presented to overcome this difficulty. The results of Shen-Hedrik-Elkins leads to a better approximation, than the results of Vermeulen and Johnson compared to the measurements. Assuming a constant distribution of contact stiffnesses leads to a solution, which is very close to the solution of Shen-Hedrik-Elkins.. The non-constant distribution of contact stiffnesses leads to a small underestimation of the measured tangential contact forces, but is very close to the measurements.

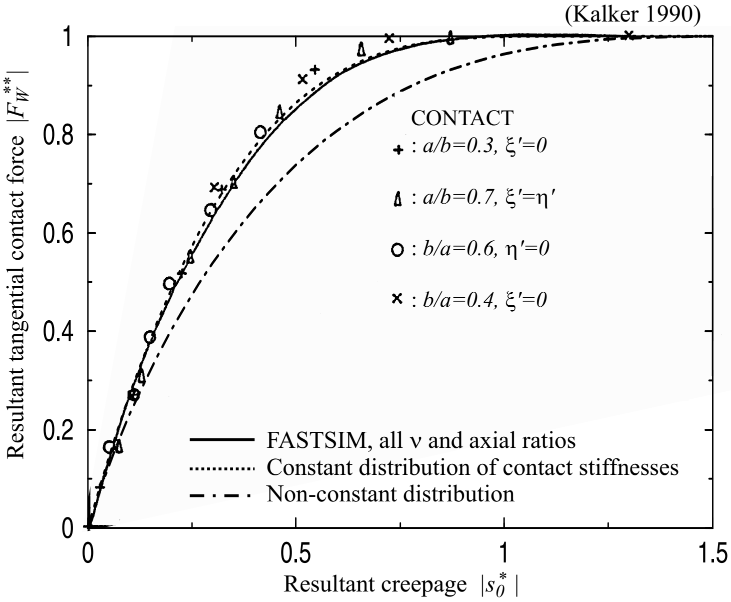
(Kalker 1990)

Fig. 6.6-1 Comparison of calculated resultant tangential contact forces versus resultant slippage

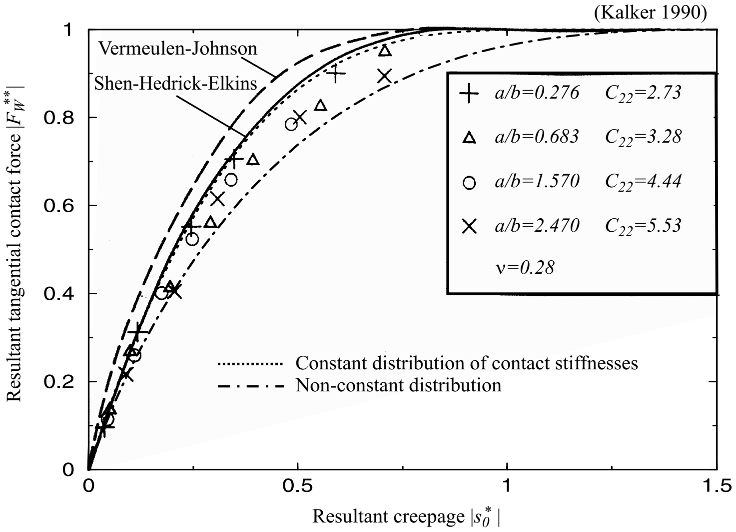
(Kalker 1990)

Fig. 6.6-2 Comparison of measurements and calculations of the tangential contact forces

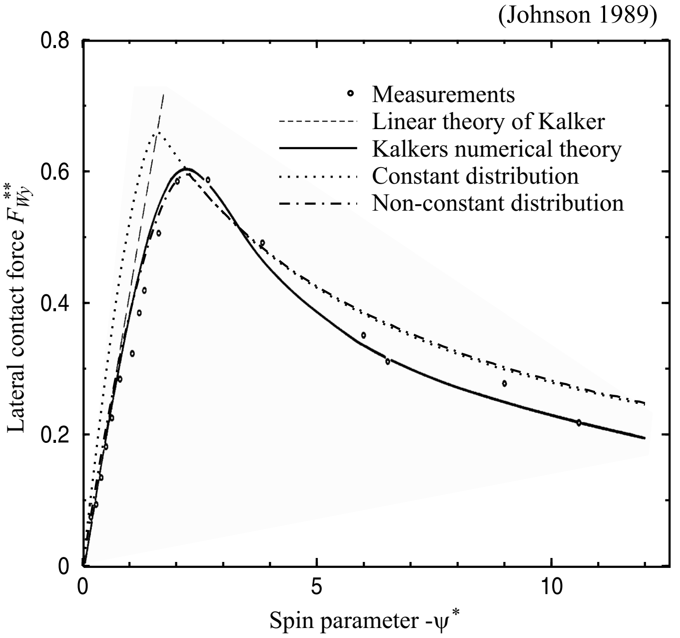

Fig. 6.6-3 Comparison of measurements and calculations of lateral contact forces versus spin

In **Fig. 6.6-3**, measurements and calculations using different models are investigated due to the lateral force versus the spin parameter. The parameters for this investigation are

$$\nu = 0.25, \quad \frac{b}{a} = 1, \quad \frac{C_{23}}{C_{22}} = 0.4, \quad c_{R0x}^{*} = 2.3175, \quad c_{R0y}^{*} = 2.0644 \,.$$

Kalkers numerical method gives the best results with respect to the measurements. Using a constant distribution of contact stiffnesses is not so good, because the maximum tangential force and the slippage coefficient are overestimated. Using the non-constant distribution of contact stiffnesses, the results do fit quite close to the measured data and the numerical results of Kalker.

In **Fig. 6.6-4**, the normal force-displacement relationship for different distribution of contact stiffnesses is shown. The relationship between normal force and normal displacement using a constant distribution of contact stiffnesses leads to a parabolic relationship between force and displacement. The parameter of the non-constant distribution of contact stiffnesses can be adjusted to fulfill the Hertzian theory exactly and can be seen as a further advantage in the use of the non-constant distribution.

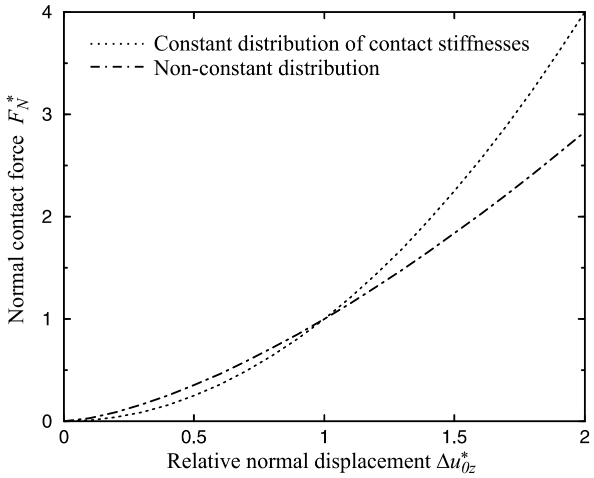

Fig. 6.6-4 Normal force-displacement relationship due to different stiffness distributions

The resultant roughness of both surfaces decreases the contact forces, because the contact area is reduced, which leads to a reduction of contact stiffnesses and therefore to a reduction of contact forces. This physical effect has been investigated theoretically and is shown in **Fig. 6.6-5**, where the resultant tangential forces are decreasing with respect to the dimensionless roughness $R_Z{}^*$ defined in Eq.(6.5-5) and using the non-constant contact stiffness distribution.

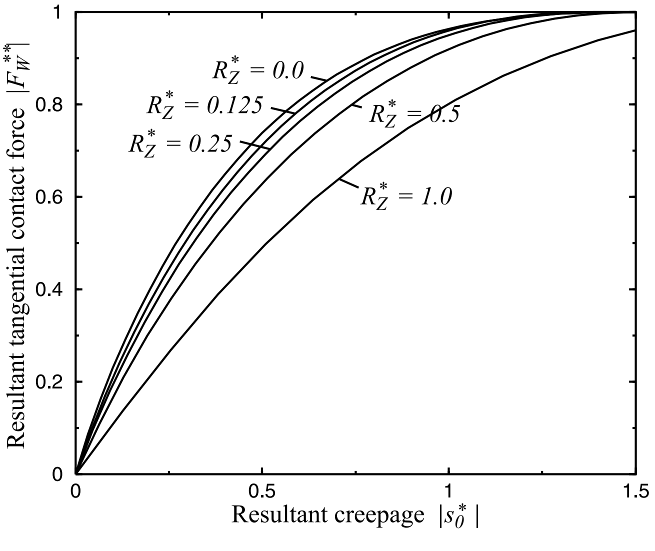

Fig. 6.6-5 Influence of roughness onto the resultant tangential forces

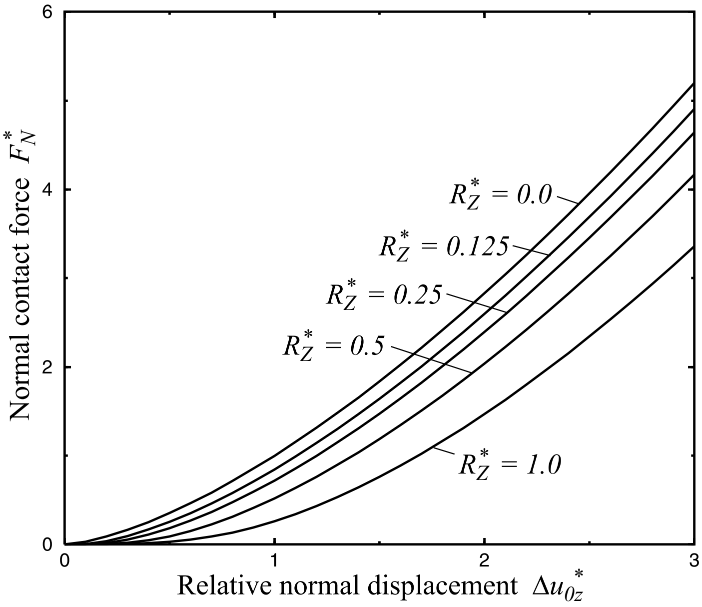

Fig. 6.6-6 Influence of roughness onto the normal contact force

Additionally, the influence of roughness in the normal direction is investigated and is shown in **Fig. 6.6-6**. In contrast to Chapter 3.3, where a rough flat surface has been modeled and experimental verified in Chapter 3.5, here a rough curved surface is modeled and investigated. Again, the normal contact forces decrease due to roughness and can be explained in the same way as described above.

6.7 Contact Temperature Distribution

Since the contact parameters can be dependent on the temperature *T*, the temperature distribution within the contact area has to be calculated. For example, as investigated in Chapter 3.6 the friction coefficient can be dependent on the temperature. For the analysis of the temperature distribution, the average distributed heat source q_H needs to be known. This is given by the frictional power

$$\Delta P_R = \Delta F_R v_P = \mu \Delta F_N v_P \tag{6.7-1}$$

related to the contact area ΔA, with

$$q_H = \frac{\Delta P_R}{\Delta A} \, . \tag{6.7-2}$$

Inserting Eq.(6.7-1) in Eq.(6.7-2) and using dimensionless notations gives

$$q_H^* = \mu^* p_N^* s_P \tag{6.7-3}$$

with the normalized friction coefficient μ^*, the normalized normal pressure p_N^*, the resultant slip s_P

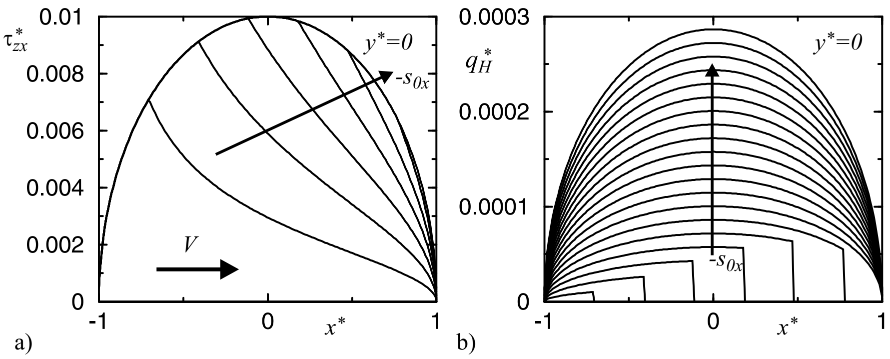

Fig. 6.7-1 **a**) Shear traction and **b**) distributed heat source within the contact interface

$$\mu^* = \frac{\mu}{\mu_0}, \quad p_N^* = \frac{p_N a_0}{c_{N0}} \quad s_P = \frac{v_P}{V} \tag{6.7-4}$$

and the normalized heat source $q_H^{\;*}$

$$q_H^* = \frac{q_H a_0}{\mu_0 c_{N0} V}. \tag{6.7-5}$$

In **Fig. 6.7-1a** and **b**, numerical results of the shear traction and the distributed heat source are presented, varying the longitudinal slippage coefficient $s_{0x}=0.0$ (-0.003)-0.06. In regions, where adhesion takes place, the corresponding distributed heat source is identical to zero because the relative velocity v_P is identical to zero. In the region, where sliding takes place the distributed frictional power shows an elliptical distribution, since the friction coefficient and the relative velocity are constant and the normal pressure distribution is elliptical due to the Hertzian normal pressure distribution.

In (Knothe and Liebelt 1990) the three-dimensional heat transfer problem is reduced to a two dimensional problem for a strip in x-direction and is approximated by the heat transfer equation

$$V\frac{\partial T}{\partial x} = \kappa\frac{\partial^2 T}{\partial z^2}, \tag{6.7-7}$$

with the thermal diffusivity defined by

$$\kappa_R = \frac{\lambda_R}{\rho_R c_R}, \tag{6.7-8}$$

where λ_R denotes the conductivity, ρ_R the density and c_R the specific heat capacity of the wheel. Eq.(6.7-7) holds, if the speed parameter L or the so called Peclet number is larger than $L=5$, see also (Johnson 1989). The boundary conditions are given by

$$-\lambda_R \left.\frac{\partial T}{\partial z}\right|_{z=0} = \alpha_R q_H(x), \quad for \quad z=0, \tag{6.7-9}$$

and

$$T=0, \quad for \quad z\rightarrow\infty, \tag{6.7-10}$$

where α_R denotes the heat partitioning factor. The general solution of Eq.(6.7-7) for an arbitrary heat source is derived in (Knothe and Liebelt 1990; Ertz 2003) and is given by

$$T(x,z) = \frac{\alpha_R}{\lambda_R}\sqrt{\frac{\kappa_R}{\pi V}}\int_0^x G(z,(x,u))\, q_H(u)\, du \tag{6.7-11}$$

with the Green's function

$$G(z,(x,u)) = \frac{1}{\sqrt{x-u}} e^{\left(-\frac{V}{\kappa_R}\frac{z^2}{4(x-u)}\right)} . \tag{6.7-12}$$

In a first step for the solution of the heat transfer equation the heat-partitioning factor α_R needs to be calculated. The temperature of the wheel and the rail have to be the same in the contact region with $z=0$. Furthermore from Eq.(6.7-12) for the wheel and the corresponding equation with respect to the rail, the heat partitioning factors can be calculated with

$$\frac{\alpha_R}{\lambda_R}\sqrt{\frac{\kappa_R}{V}} = \frac{\alpha_S}{\lambda_S}\sqrt{\frac{\kappa_S}{V_S}} , \tag{6.7-13}$$

where the index S is related to the rail. With the requirement

$$\alpha_R + \alpha_S = 1 \tag{6.7-14}$$

and inserting Eq.(6.7-13) in Eq.(6.7-14) and solving for the heat partitioning factor of the wheel gives

$$\alpha_R = \frac{\sqrt{\lambda_R c_R \rho_R V}}{\sqrt{\lambda_R c_R \rho_R V} + \sqrt{\lambda_S c_S \rho_S V_S}} . \tag{6.7-15}$$

For example, if the velocity V_S of the contact with respect to the rail is zero, than from Eq.(6.7-15) it follows, that the heat partitioning factor is $\alpha_R=1$ and therefore in this case the heat flows into the wheel. In the following, the conductivity, the density and the specific heat capacity of the wheel and rail are assumed identical. Furthermore, the slippage are relatively small and hence the velocity of the wheel is approximately equal to the velocity of the contact with respect to the rail, then the heat partitioning factor is given by $\alpha_R=1/2$.

Assuming a constant heat flow rate q_H, the temperature distribution calculated by Eq.(6.7-11) can be solved analytically and is given by

$$T(x) = \frac{2}{\sqrt{\pi}}\sqrt{\frac{\kappa_R}{V}}\frac{\alpha_R q_H}{\lambda_R}\sqrt{x} , \tag{6.7-16}$$

see (Johnson 1989) and (Knothe and Liebelt 1990), where the reference temperature is identical to zero at the position $x=0$. With the normalized temperature

$$T^* = \frac{\lambda_R T}{\alpha_R \mu_0 c_{N0}}\sqrt{\frac{a_0}{2\kappa_R V}} \tag{6.7-17}$$

Eq.(6.7-16) can be rewritten by

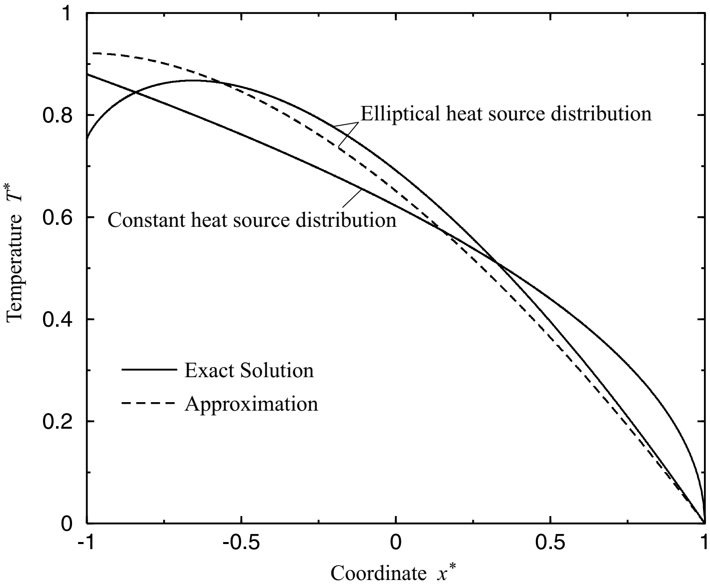

Fig. 6.7-2 Temperature distributions for different pressure distributions

$$T^* = \sqrt{\frac{2}{\pi} q_H^*} \sqrt{x^*} \, . \tag{6.7-18}$$

Squaring Eq.(6.7-18) and noting that due to the discretization of the contact region the step size is defined by

$$x_i^* = x_{i-1}^* + \Delta x^* \, . \tag{6.7-19}$$

Then the temperature distribution can be calculated by

$$T_i^{*2} = T_{i-1}^{*2} + \frac{2}{\pi} q_H^{*2} \Delta x^* \, . \tag{6.7-20}$$

In **Fig. 6.7-2** the temperature distribution is shown for a constant heat source distribution. Within the contact region Eq.(6.7-20) can be used to recalculate the exact solution numerically. Using these solution method for a non-constant heat source distribution defined by

$$q_H^* = \mu_{i-1}^* p_{Ni-1}^* s_{Pi-1} \, , \tag{6.7-21}$$

an approximation can be calculated, which does not lead to an increase in computation time compared to the procedure described in (Knothe and Liebelt 1995).

In Fig. 6.7-2 the temperature distribution for an elliptical heat source distribution is calculated by the exact calculation procedure defined in Eq.(6.7-11) and the described approximated procedure defined in Eq.(6.7-20). The maximum temperature of the approximated method occurs at the trailing edge and is overestimated by approximately *6%* compared to the exact solution. The advantage of the approximated method is that within a reasonable error the calculation of the temperature distribution leads not to an increase in computation time.

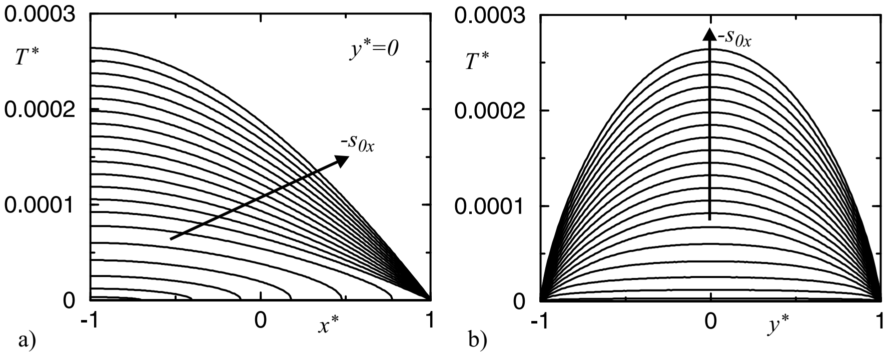

Fig. 6.7-3 Temperature distributions **a**) in x-direction and **b**) at the trailing edge

In **Fig. 6.7-3a**, the temperature distribution within the contact area is shown, which is calculated from the distributed heat source shown in Fig. 6.7-1b, assuming in a first step, that the friction coefficient is independent on the temperature. The starting temperature at the leading edge is assumed to be $T_1^*=0$. Within the contact area, the temperature is identical to zero, where the distributed frictional power is identical to zero. Due to sliding and dry friction, the temperature increases up to the trailing edge, where the maximum temperature occurs. The corresponding temperature at the trailing edge is shown in **Fig. 6.7-3b**, which is approximately parabolic for large slippage values.

The friction coefficient can be dependent on the local temperature. In Chapter 3.6 it has been assumed, that the friction coefficient is linearly dependent on the temperature with

$$\mu_{i-1}^* = \mu^*(T_{i-1}^*) = 1 - \gamma_\mu T_{i-1}^*, \tag{6.7-22}$$

where the slope is defined by

$$\gamma_\mu = \frac{\alpha_R \mu_0 c_{N0}}{\lambda_R \Delta T_E} \sqrt{\frac{2\kappa_R V}{a_0}}, \tag{6.7-23}$$

to explain the decreasing characteristic of the friction coefficient with respect to the relative velocity. In **Fig. 6.7-4**, this influence onto the shear traction is shown using the same contact parameter used for Fig. 6.7-1. Comparing this functional behavior with the traction shown in Fig. 6.7-1a, one can observe, that the traction due to friction is decreasing in the region, where sliding takes place. Integrating the shear traction with respect to the contact area gives a decreasing characteristic for the longitudinal force versus the longitudinal slippage as shown in **Fig. 6.7-5** for different slopes defined in Eq.(6.7-22). This physical phenomenon has been observed already in experiments, cited in (Garg and Dukkipati 1984) for the lateral force and in (Holland and Rick 1997) for the longitudinal force.

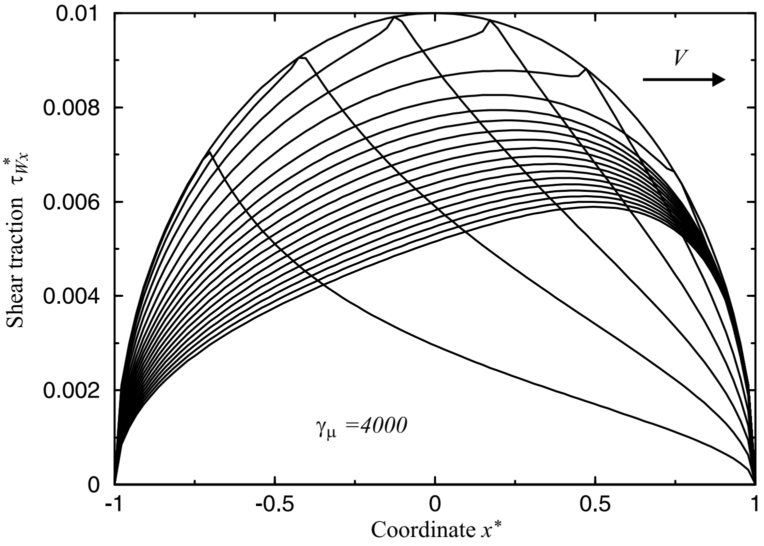

Fig. 6.7-4 Tangential traction due to a decreasing friction factor

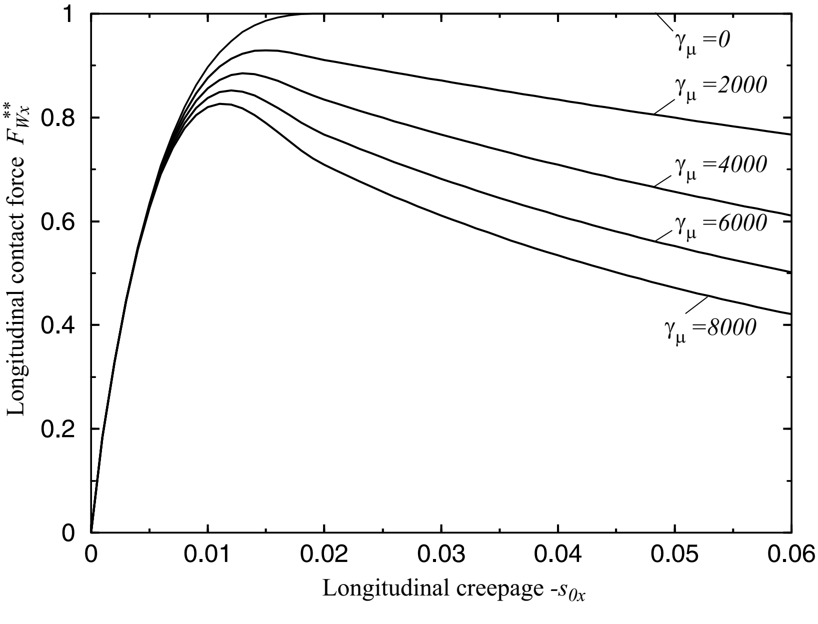

Fig. 6.7-5 Longitudinal contact force with a decreasing characteristic

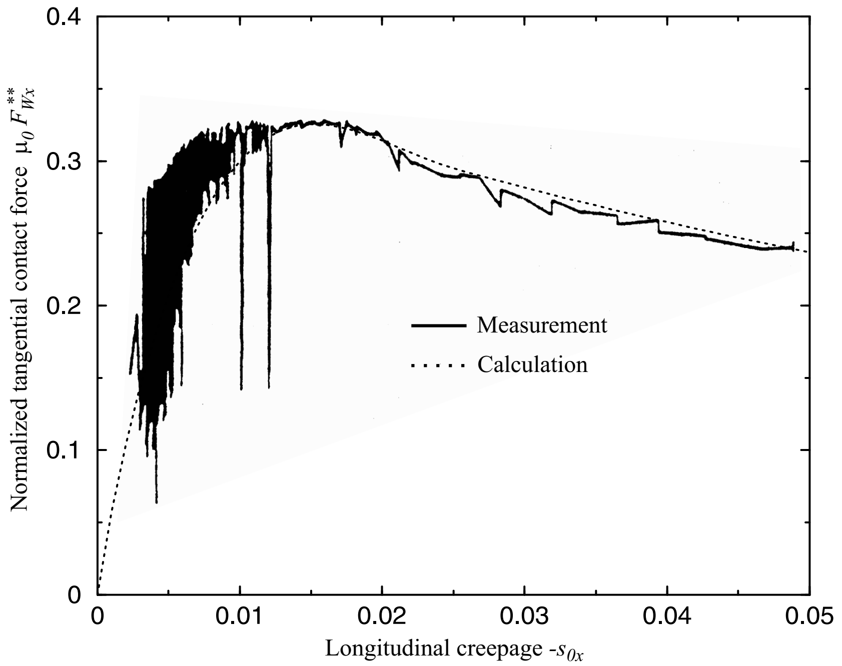

Fig. 6.7-6 Qualitative comparison of measured (Holland and Rick 1997) and calculated longitudinal forces

A qualitative comparison is done with respect to the measurements cited in (Holland and Rick 1997), because the experimental data is not available. In **Fig. 6.7-6**, the measurement and the calculation with the following data for a circular contact area with a friction factor at zero temperature of $\mu_0=0.38$ and a slope of $\gamma_\mu=1400$. The qualitative comparison shows a quite good agreement.

6.8 Wear Calculation

In the following, an algorithm is developed to calculate the wear of the wheel and rail. A common way to approximate the wear is to assume that the volume wear rate is proportional to the frictional power, see also Chapter 3.9,

$$\dot{W} = I_R P_R , \qquad (6.8\text{-}1)$$

with the constant I_R, see (Fleischer 1973) and (Strömberg 1996). Experimental identified data for the proportionality factor I_R are cited in (Krause and Poll 1986). Assuming a stationary process, the volume wear rate can be calculated by

$$\dot{W} = \frac{dW}{dt} = \frac{dW}{dx}\frac{dx}{dt} = \frac{dW}{dx}V = V\,dy\,dz \approx V\,\Delta y\,\Delta z , \qquad (6.8\text{-}2)$$

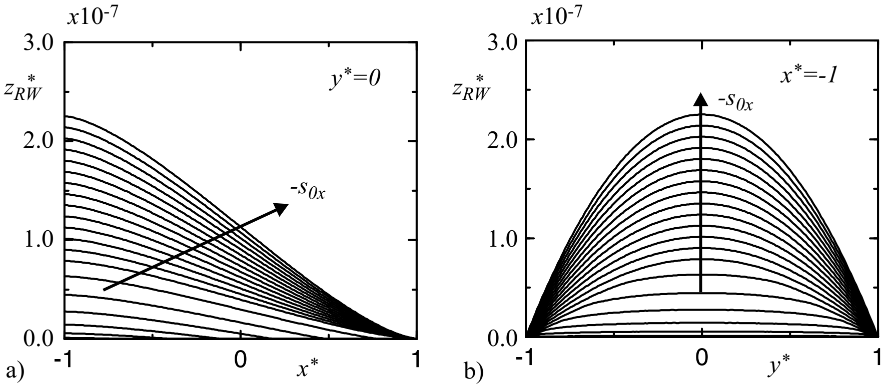

Fig. 6.8-1 **a**) Wear depth versus coordinate $x^*, y^*=0$ and **b**) wear depth versus coordinate $y^*, x^*=-1$

where W denotes the wear volume with respect to the wheel. Solving Eq.(6.8-2) for the wear depth Δz and inserting Eq.(6.8-1), Eq.(6.7-1) and Eq.(6.7-2) gives

$$\Delta z = \frac{I_R}{V} q_H \Delta x\,. \qquad (6.8\text{-}3)$$

and in dimensionless form with Eq.(6.4-5)

$$\Delta z^* = I_R^* q_H^* \Delta x^* \qquad (6.8\text{-}4)$$

with

$$\Delta z^* = \frac{\Delta z}{a_0}, \quad I_R^* = \frac{\mu_0 c_{N0} I_R}{a_0}\,. \qquad (6.8\text{-}5)$$

Then, the resultant wear depth for one strip is given by the summation

$$z_{RW}^* = \sum_{i=1}^{n_x} \Delta z_i^* = I_R^* \Delta x^* \sum_{i=1}^{n_x} q_{Hi}^* \qquad (6.8\text{-}6)$$

assuming that the proportionality factor I_R from Eq.(6.8-1) and the discretization length Δx of the contact area are constant.

Fig. 6.8-1a shows the development of wear depth within the contact region varying the longitudinal slippage $s_{0x}=0.0(-0.003)-0.06$. In principle, the wear depth behaves qualitatively in the same way like the temperature. In **Fig. 6.8-1b**, the resultant wear depth for one run-over is shown varying the longitudinal slippage.

Since the misalignments of the wheel and rail do vary with time, the distribution of wear varies with time, which contributes to the unroundness of the wheel. In **Fig. 6.8-2**, the variation of the normal displacement with

$$\Delta u_{0z}^* = 0.02 + 0.03 \sin\delta$$

is investigated due to the resultant wear and the temperature at the trailing edge within the reference coordinate system. Full separation is included within the calculation method. The angle δ stands for the position of the wheel. The wear due to a harmonic lateral motion of the wheel is shown in **Fig. 6.8-3**. The wear is shown within the *A*-coordinate system and has to be transferred to the wheel *W*-coordinate system, using Eq.(6.2-16) and Eq.(6.2-17) to be able to describe the change of the wheel geometry.

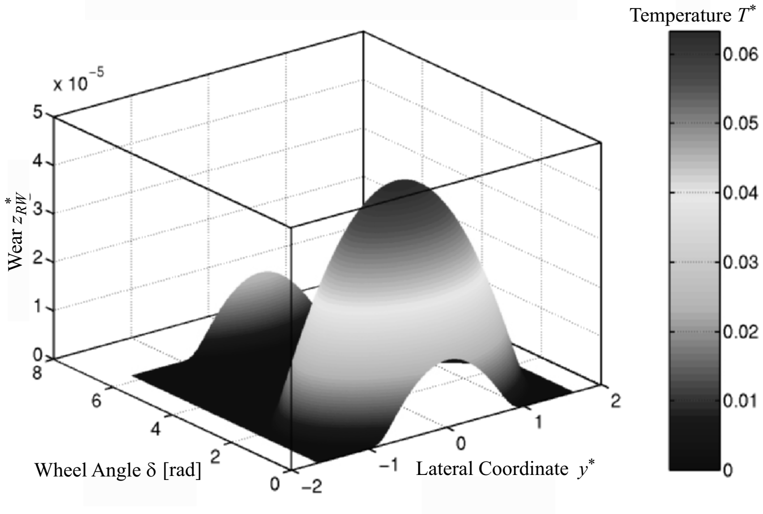

Fig. 6.8-2 Temperature and wear calculation for harmonic normal displacements

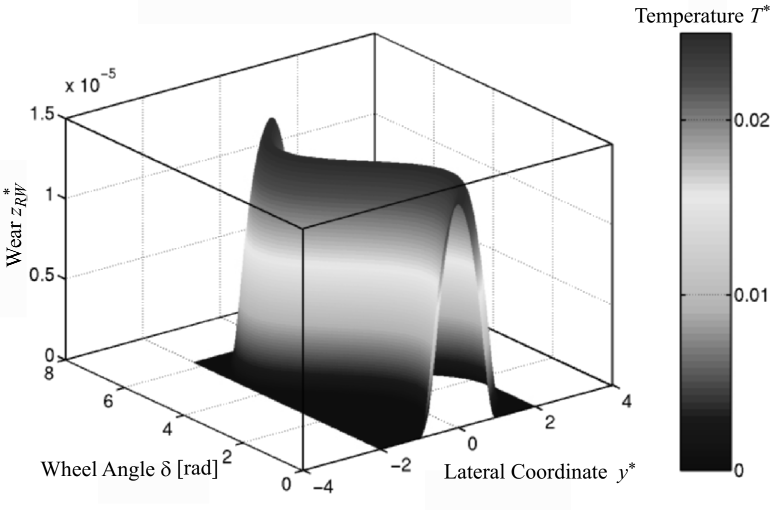

Fig. 6.8-3 Temperature and wear calculation for harmonic varying lateral displacements

This resultant wear depth of the wheel has to be calculated continuously to be able to analyze the change of the wheel surfaces and to analyze the unroundness of the wheel. The stored wear data of the surface is used to modify the profile of the wheel to get the actual profile, see **Fig. 6.8-4**. In analogy, this holds for the rail as well. This completes the full calculation of the wheel-rail-system dynamics including the wear calculation.

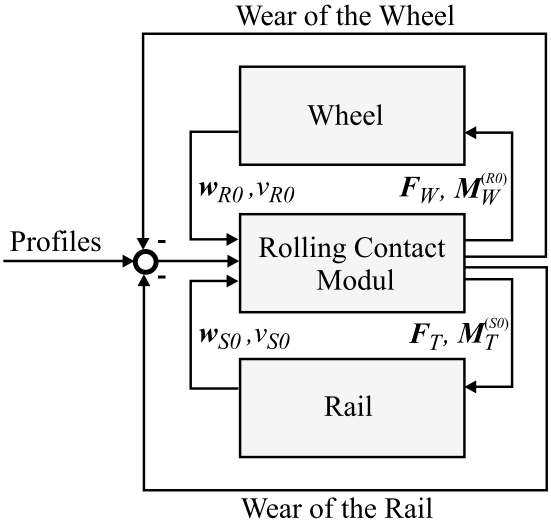

Fig. 6.8-4 Procedure to calculate wear

6.9 Wear of Railway Wheels

To be able to calculate the wear distribution of railway wheels the relative kinematics between wheel and rail must be known. Here the model described in (Kaiser 2005) is used to describe the dynamics. The elasticity of the wheel and the rail are included by the modal description. This model of the vehicle corresponds to an ICE-wagon. The dynamic behavior is calculated beforehand, so that the relative kinematics between wheel and rail is given. Now the wear model described before can be applied to the railway wheels.

One result of this procedure is shown in **Fig. 6-9-1**. The basis of this calculation is one unround wheel with three maxima. The calculation of the contact forces as described above has been used to verify the procedure. The wear of the wheel shows again three maxima, because here the normal forces increases and therefore the frictional power and hence the wear increases. However, there exists a slightly shift between the maxima on the unround wheel and the maxima corresponding to the wear distribution. Furthermore, three additional maxima occur with respect to an increase of lateral slippage. The question, why the wheels are getting unround, can not be explained at this stage, but with this calculation procedure as specially with the developed wear module this question can be analyzed.

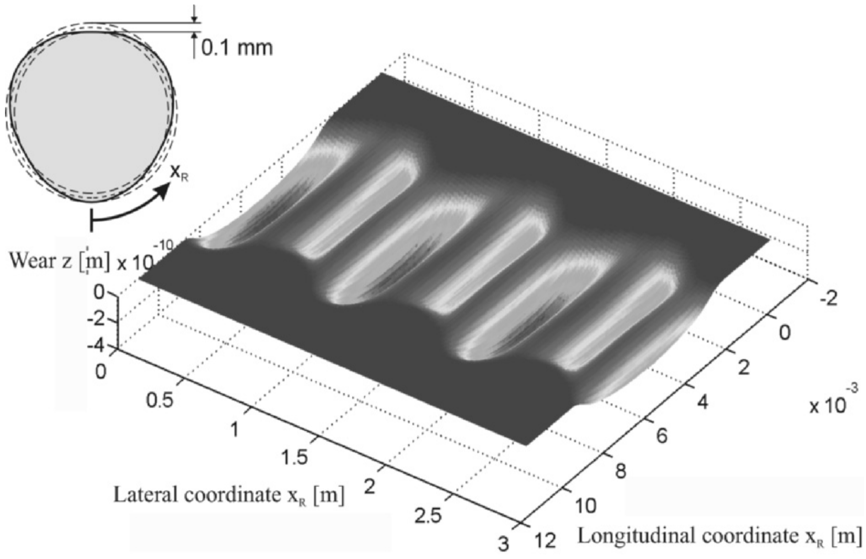

Fig. 6.9-1 Wear of an unround railway wheel

6.10 Instationary Rolling Contact Tyre-Road

The main function of a tire is the transmission of forces between the car and the road. To achieve high acceleration a high friction coefficient is essential. The friction coefficient of rubber material depends on a variety of parameters like relative velocity, normal pressure, contact temperature, surface roughness, wetting and material parameters, see also (Hirschberg et al. 2002). The friction on a dry road is mainly based on hysteresis and adhesion effects as described in Chapter 3.6.

Fast changes of the relative velocity and the normal force occur especially during ABS-braking. Therefore, the time dependent behavior of the tangential forces during these transient changes is of interest. This behavior can not be described by the steady friction characteristic. In **Fig. 6.10-1**, the procedure to calculate instationary rolling systems is depicted. This method can be transferred to any rolling system like the wheel-rail rolling contact. A detailed description of the method is given in (Gutzeit et al. 2006). Here, an overview is given of the calculation procedure.

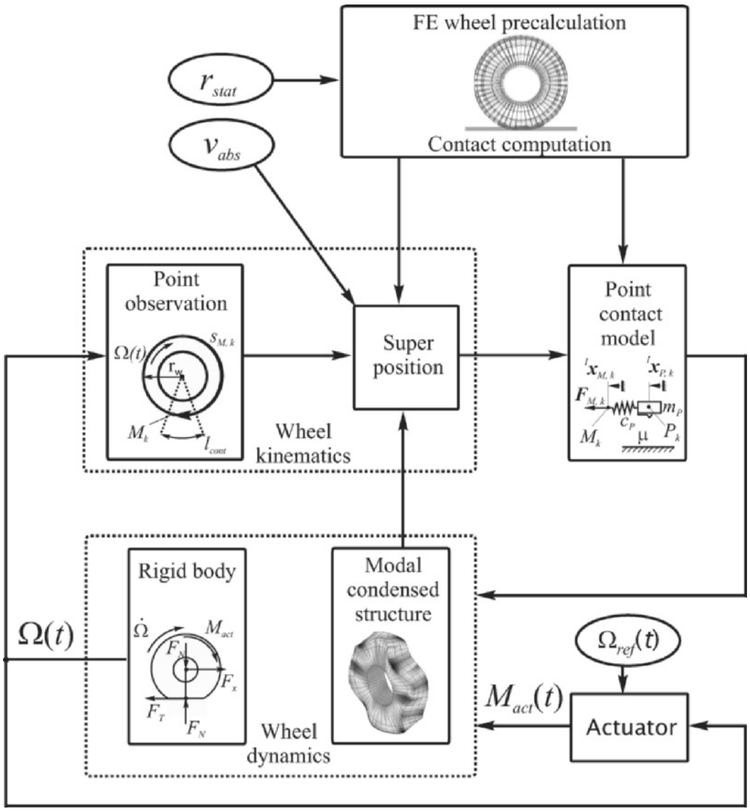

Fig. 6.10-1 Procedure to calculate instationary rolling systems

The deformation of a still-standing wheel under normal load is calculated by FEM, where the contact nodes are free within the contact area. The node of the wheel center is displaced against the ground by r_{stat}. The contact computation can be carried out using the penalty method. Due to the nonlinear behavior of the system, a Newton-Raphson procedure is applied for the calculation of the large static displacements. Then, the static displacements of the all nodes and the static contact pressure distribution are available.

In the simulation, the structure dynamics of the wheels is approximated by a modal approach. The contact behavior is described by using a simplified point contact model. The contact patch is discretized and the local tangential forces for passing material points are obtained. Thus, the shear stress distribution acts on the wheel in addition to the actuation moment M_{act}, which is generated by the actuator realizing the given reference angular velocity $\Omega_{ref(t)}$. The wheel dynamics consist of the rigid body dynamics and the dynamics of the modal condensed structure. With the modal condensed structure, the comparatively small dynamic displacements are computed. Here, gyroscopic effects are neglected due to relative small angular velocities.

In the point contact model, only those material points currently passing the contact patch are observed. The displacements of the material points within the contact plane are gained by superposing of the rigid body motion, the static displacements and the dynamic displacements based on the modal approach. Due to the low time constants, only the first mode was used for the approximation of the structure dynamics. For the calculation of the shear stress distribution, twenty contact elements were used, arranged in a row in the center of the contact zone.

The rolling friction is experimentally tested with an autonomous friction robot using small rubber wheel, see **Fig. 6.10-2**. The robot controls the relative velocity and the normal force and can realizes fast parameter changes of both. Therefore, it is possible to investigate instationary rolling friction contacts. Jumps of the relative velocity and the normal force are studied.

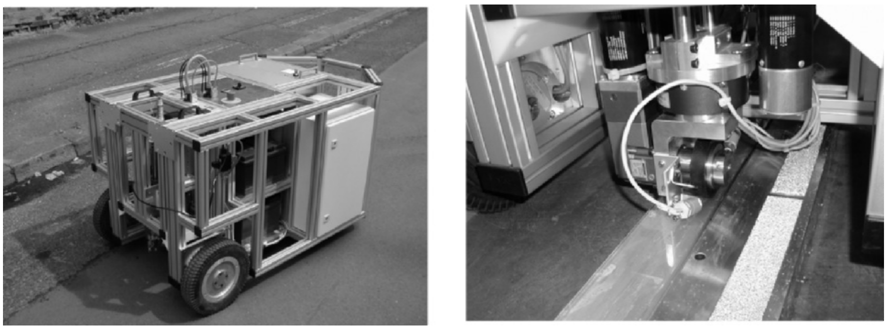

Fig. 6.10-2 Measurement system of rolling contact forces

In a first step, all experiments were accomplished at constant normal force $F_N=40$ N on the wheel and constant reference velocity $v_{abs}=40$ mm/s of the wheel center. **Fig. 6.10-3** shows the comparison between simulations and experiments for steady slippage. The reason for the relative small difference is probably the lack of an appropriate local sliding friction characteristic. The qualitative progression of the simulated characteristically fits relatively well to the experimental results.

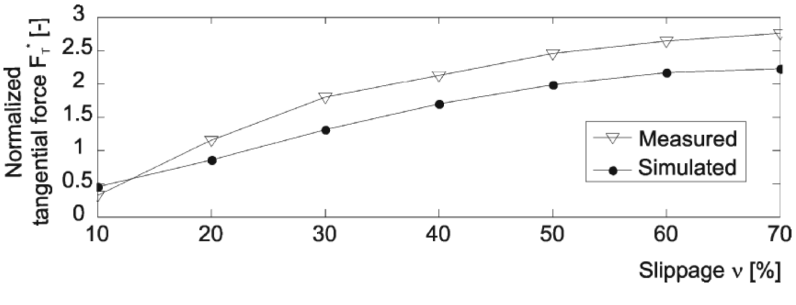

Fig. 6.10-3 Normalized tangential forces for stationary rolling

In the following, jump excitations of the slippage were chosen to investigate the dynamical behavior of the system. For such a slippage jump the normalized tangential force is shown in **Fig. 6.10-4**. To obtain a reference magnitude for the model verification, an exponential characteristic is fitted to both experimental and numerical data. The time constant of this exponential approximation represents the delay of the dynamic contact behavior.

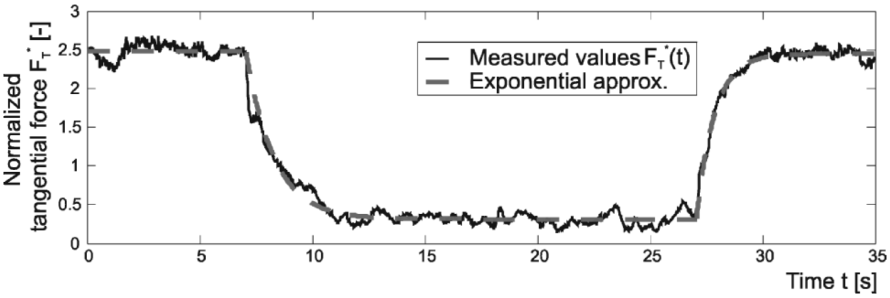

Fig. 6.10-4 Identification of time constants

The comparison of simulations and experiments for instationary excitations by slipping jumps is shown in **Fig. 6.10-5**. The time constant is plotted versus the values of the target slippage. For up-jumps, the results of the model fit well to the experimental data. For down-jumps, the simulation results differ stronger from the experimental data. A more detailed description of the local friction characteristic as presented in Chapter 3.6 will improve these calculations. Nevertheless, the comparison between simulation and measurement is relative good.

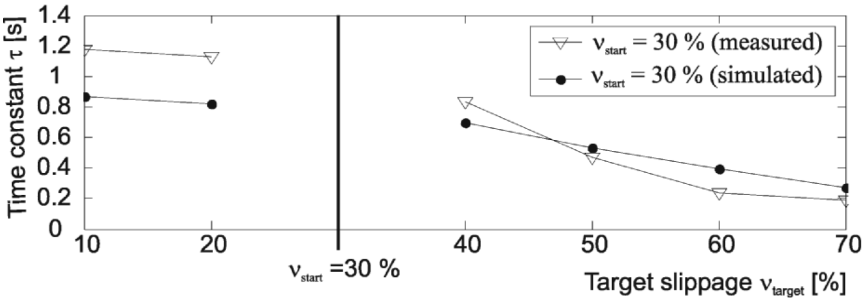

Fig. 6.10-5 Time constant of the longitudinal forces

7 Conclusions

An alternative calculation procedure is developed to handle dynamical contact problems with friction. Most of the technical systems with friction contacts can be reduced to linear elastic bodies contacting each other, where the contact behavior is modeled nonlinear. The modal description of the spatial vibrating elastic bodies leads to a reduction of the degrees of freedom of the system and hence to a reduction of the numerical problem. Due to the non-linearity of the contact behavior and the spatial motion, the generally expanded contact area is discretized. For each discretized contact area, the developed point contact model is used to describe the normal and tangential contact forces. The main assumption with respect to the point contact model is that the point contacts are only coupled by the contact kinematics. The connection of the modal description of the elastic bodies and the point contact model leads to an efficient modeling of dynamical problems with friction.

The point contact model includes the main parameters like the contact stiffnesses in normal and tangential direction. A mesoscopic contact model for rough surfaces is developed with an extension to a hyperbolic contact law for relative large deformations. The measured cumulative height distribution is used to describe the rough surface. Due to the roughness of the contact surfaces, the normal contact force and the tangential contact stiffness are nonlinearly dependent on the relative normal displacements. Both nonlinear effects are verified by experiments. Commonly used contact laws for modeling roughness are recalculated. The decreasing characteristic of the friction coefficient with respect to the relative velocity is investigated experimentally and is explained theoretically by the dependency of the friction coefficient on the temperature.

Parameter studies are carried out with respect to the developed point contact model, which includes all the features described above. Limits of application of the point contact model are related to yielding and to the first eigenfrequency of the layer. The hysteretic behavior is investigated with respect to normal and tangential displacements. Anisotropy with respect to the contact stiffnesses is modeled and the possibility of separation of the contact is included in the contact model and is analyzed. Microslip effects due to roughness lead to a smooth increase of the tangential force relative to the displacement, whereby the temperature effect leads to a decreasing characteristic with respect to the tangential forces.

Friction leads always to a time dependent system, which is shown theoretically by calculating the wear with respect to rough surfaces. The shape of the contact surfaces changes because of wear and therefore the pressure distribution changes as well as the normal force-displacement relationship and the tangential contact stiffnesses.

The developed procedure to model contacts is applied to real contact problems. Experimental investigations are used to verify the numerical results. The investigated problems include the application of the generalized point contact model, the solution methods, the comparison of the measurements with the calculations and parameter studies.

In a first step, the method is applied to two oscillators with a harmonic excitation. On the one hand, an oscillator with elastic contacts is used to check the normal contact modeling. Using higher modes lead to an improvement of the calculation compared to the measurements. Measured multi-periodic and chaotic motions are recalculated. For verifying the tangential contact model, the experimental data of a self-sustained friction oscillator is used. Within the experiments it is observed, that higher periodic motions occur and it is shown that the waviness is one reason for this effect. The comparison of measurements and calculations show a good agreement with respect to both oscillators.

Dry friction is a main factor of self-sustained oscillations in dynamic systems. The mathematical modelling of dry friction forces result in strong nonlinear equations of motion. The bifurcation behaviour of a deterministic system has been investigated by bifurcation theory. The stability of stationary solutions has been analyzed by the eigenvalues of the Jacobian. Period doublings and Hopf-bifurcations as well as turning points could be determined with the program package BIFPACK. Phase plane plots of periodic and chaotic motions have been shown for a better understanding of the bifurcation diagrams. Both, unstable branches and stable coexisting solutions have been calculated. Several jumping effects, which are typical for nonlinear systems, have been found.

Efficient solution methods for calculating the spatial forced vibration of elastic structures with friction contacts including microslip effects due to roughness are developed and applied to bladed disk assemblies with shrouds. The Harmonic Balance Method is used to linearize the normal and tangential contact forces. This leads to a complex stiffness matrix, where the components are nonlinearly dependent on the relative displacements of the contact surfaces. An experimental setup with three elastic structures and two macroscopic non-Hertzian contacts is used to verify the numerical results. The measurements of the spatial motion for bending as well as torsional vibration of the elastic structures show a good agreement with the corresponding calculations. Parameter studies of a bladed disk assembly with shrouds are performed with respect to the alternating stresses in the blade foot to optimize the spatial dynamic behavior with respect to an increased lifetime.

An approximate method is presented to calculate the envelopes of the frequency response functions for statistically varying natural frequencies of the blades. This method is based on a sensitivity analysis and the Weibull-distribution of the vibration amplitudes. From here, a measure for the strength of localization for mistuned cyclic systems is derived. Regions, where localization can occur with a high probability, can be calculated by this method. The mean value and the standard deviation of the vibration amplitudes are calculated. The comparison between the approximate method and the Monte-Carlo simulations shows a good agreement. Therefore, applying this method leads to remarkable reduction of computation time and gives a quick insight into the system behavior. The approximate method can also be applied to systems, which include the elasticity of the disk and/or the coupling by shrouds or other friction devices.

Furthermore, the general friction contact model is applied to the rolling contact problem. The point contact model allows a fast calculation of the generalized contact forces for a spatial motion of the wheel and rail. Therefore, the developed rolling contact model can be used for the determination of the long time behavior of wheel-track-systems. The comparison of measurements and calculations of the contact forces show a good agreement. Since the temperature distribution affects the contact parameters like the friction coefficient, a fast algorithm for calculating the temperature distributions within the contact region for steady rolling is developed. Including the temperature effect, which decreases the friction coefficient leads to a decreasing friction characteristic with respect to the slippage, which is verified by a measurement. Based on a hypothesis the wear of railway wheels was calculated. With the developed calculation procedure, one is able to analyze why the railway wheels are getting unround.

An efficient model for unsteady rolling contact is presented. The model is experimentally validated by measurements of an autonomous vehicle. For the excitation with slippage jumps, an exponential saturation behavior is approximated to both, experimental data and simulation results. The characteristic time constant of the system response is used to verify the model. For increasing target values of the slippage, the time constant decreases. The time constant characteristics are reproduced quiet well by the model.

Due to the developed multi-scaling technique, it is possible to model friction contacts on the micro up to the macro-scale in an efficient way. It could be shown that with the modal reduction and the multi-scaling technique an efficient method has been developed to be able to analyze the dynamics of large elastic multibody systems with friction contacts.

References

Achenbach M, Frank E (2001) Tribologie und Schmierungstechnik 4, pp 43–47

Achenbach M, Herdy M (2003) Kautschuk Gummi Kunststoffe 1-2/2003 pp 24–31

Allgaier R, Gaul L, Keiper W, Willner K (1999) Mode lock-in and friction modelling. In: Gaul and Brebbia: Computational Methods in Contact Mechanics IV, WIT Press, Southampton, Boston, pp 99–108

Antes H, Panagiotopoulos PD (1992) The Boundary Integral Approach to Static and Dynamic Contact Problems - Equality and Inequality Methods. ISNM 108: International Series of Numerical Mathematics, Vol 108, Birkhäuser Verlag, Basel

Aliabadi MH, Brebbia CA (1993) Contact Mechanics: Computational Techniques. International Conference on Contact Mechanics, Computational Mechanics Publications, Southampton, UK

Aliabadi MH (1995) Contact Mechanics II: Computational Techniques. Second International Conference on Computational Methods in Contact Mechanics, Computational Mechanics Publications, Southampton, UK

Aliabadi MH (1997) Contact Mechanics III: Computational Techniques. Third International Conference on Contact Mechanics, Computational Mechanics Publications, Southampton, UK

Amontons M (1699) Über den Widerstand in Maschinen*. Memoires de l' Academie Royale des Sciences*, pp 203–222

Anand A, Soom A (1984) Roughness-Induced Transient Loading at a Sliding Contact During Start-Up. *J of Tribology*, Vol 106, pp 49–53

Archard JF (1953) Contact and Rubbing of Flat Surfaces. *J of Applied Physics*, Vol 24, No 8, pp 981–988

Bathe KJ (1990) Finite-Elemente-Methoden. Berlin: Springer

Bental RH, Johnson KL (1968) An elastic strip in plane rolling contact. *Int J Mech Sci*, Pergamon Press, Vol 10, pp 637–663

Bhushan B (1996) Contact mechanics of rough surfaces in tribology: Single asperity contact. *Appl Mech Rev*, Vol 49, No 5

Blohm W (1991) Untersuchung des nichtlinearen Übertragungsverhaltens von Strukturen mit lokalen Fügestellen. Fortschr. Ber. VDI-Reihe 11, Nr. 164, Düsseldorf: VDI-Verlag

Bohlen St (1987) Zur Berechnung und Messung mechanischer Schwingungen in Strukturen mit nichtlinearem Fügestellenverhalten. VDI-Reihe 11, Nr 91, Düsseldorf: VDI-Verlag

Bowden FP, Tabor D (1956) Friction and Lubrication. John Wiley, New York

Braun J (1996) Einfluß von Preßverbänden auf die Dynamik von Antriebssträngen. Fortschr-Ber VDI-Reihe 11, Nr 231, Düsseldorf: VDI-Verlag

Bremer H, Pfeiffer F (1992) Elastische Mehrkörpersysteme. BG Teubner, Stuttgart

Brendel H (1990) Zur Schwingungsdämpfung von Fugenverbindungen. Hieronymus Buchreproduktion GmbH, München

Brogliato B (1999) Non-smooth mechanics: models, dynamic and control. Springer-Verlag, London, Berlin, Heidelberg

Brommundt E (1997) A simple mechanism for the polygonalization of railway wheels by wear. Mechanics Research Communications. New York: Pergamon Press Vol 24 No 4

Carter FW (1926) On the Action of a Locomotive Driving Wheel. *Proc Royal Society*, A112, pp 151–157

Cattaneo C (1938) Sul Contatto di Due Corpi Elastici: Distribuzione Locale degli Sforzi. *Rend Accad naz Lincei* 27 No 6, pp 342–348, 434–436, 474–478

Coulomb CA (1785) Die Theorie einfacher Schwingungen. *Memoires de mathematique et de physique de l'Academie des Sciences*, 10, pp 161–331

Den Hartog (1985) Mechanical Vibrations. Dover Publications, Inc, New York

Deresiewicz H (1957) Oblique Contact of Nonspherical Elastic Bodies. *J of Applied Mechanics*, 24, pp 623–624

Dieterman HA (1990) Yielding in the Contact Zone of Bodies Interacting by Dry Friction. *Wear*, 137, pp 129–142

Dragos RP (2000) Optimierung des Systemverhaltens von Schienenfahrzeugen. Forschungszentrum für Multidisziplinäre Analysen und Angewandte Strukturoptimierung, Institut für Mechanik und Regelungstechnik, Univ.-Prof. Dr.-Ing. H.A. Eschenauer

Du S, Zagrodzki P, Barber JR, Hulbert GM (1997) Finite Element Analysis of Frictionally Excited Thermoelastic Instability, *J of Thermal Stresses* 20, pp 185–201

Eberhard P (2000) Kontaktuntersuchungen durch hybride Mehrkörpersystem / Finite Elemente Simulationen. Shaker Verlag, Aachen

Ertz M (2003) Temperaturspannungen und Materialbeanspruchung. VDI-Fortschrittsbericht Nr. 549, Reihe 12, Kap. 5

Ewins D (1986) Modal Testing: Theory and Practice. Research Studies Press, John Wiley & Sons Inc, New York

Feeny BF, Moon FC (1993) Bifurcation Sequences of a Coulomb Friction Oscillator. *Nonlinear Dynamics*, 4, pp 25–37

Feeny BF, Guran A, Hinrichs N, Popp K (1998) Historical review on dry friction and stick-slip phenomena. *Applied Mechanics Review*, Vol 51, No 5

Feigenbaum MJ (1980) Universal Behaviour in Nonlinear Systems. In: *Los Alamos Sci. 1*, pp 4–27

Fidlin A (2005) Nonlinear Oscillations in Mechanical Engineering. Springer Verlag

Fingberg U (1990) Ein Modell für das Kurvenquietschen von Schienenfahrzeugen. Fortschr.-Ber. VDI-Reihe 11, Nr. 140, Düsseldorf: VDI-Verlag

Fleischer G (1973) Energetische Methode der Bestimmung des Verschleißes*. Schmierungstechnik* 4, 9, pp 269–274

Gasch R, Knothe K (1987) Strukturdynamik, Band 1: Diskrete Systeme. Springer Verlag, New York, Berlin, Heidelberg

Gasch R, Knothe K (1989) Strukturdynamik, Band 2: Kontinua und ihre Diskretisierung. Springer Verlag, New York, Berlin, Heidelberg

Garg VK, Dukkipati RV (1984) Dynamics of Railway Vehicle Systems. Academic Press Canada

Gaul L (1983) Wave Transmission and Energy Dissipation at Structural and Machine Joints. *J of Vibration, Acoustics, Stress and Reliability in Design*, Vol 105, pp 489–496

Gaul L, Nackenhorst U, Willner K, Lenz J (1994) Nonlinear vibration damping of structures with bolted joints. *Proc of the 12th IMAC*, Honolulu, Hawaii, Vol 1, pp 875–881

Gaul L, Brebbia CA (1999) Computational Methods in Contact Mechanics IV, WIT Press, Southampton, Boston

Gaul L, Nitsche R (2001) Dynamics of Structures with Joint Connections. In Structural Dynamics @ 2000, Part 2: Current States and Future Directions. Editors: DJ Ewins, DJ Inman, Research Studies Press Limited (RSP)

Gaul L (2004) Simulation des dynamischen Verhaltens von Rohrleitungssystemen der Verfahrenstechnik. Teilprojekt B.4, Sonderforschungsbereich 412, Ergebnisbericht 2002-03-04, Universität Stuttgart, pp 179–202

Genzo A, Sextro W, Popp K (2005) Analysis of the Forced Vibration of Two Bolted Half-Pipes with Extended Friction Contacts. Proc. of Applied Mathematics and Mechanics (PAMM), Vol 5

Glocker Ch (1995) Dynamik von Starrkörpersystemen mit Reibung und Stößen. Fortschr.-Ber. VDI-Reihe 18 Nr. 182, Düsseldorf: VDI-Verlag

Goodman LE, Brown CB (1962) Energy Dissipation in Contact Friction: Constant Normal and Cyclic Tangential Loading. *J of Applied Mechanics*, 102(2), pp 17–22

Götting F, Sextro W, Panning L, Popp K (2004) Systematic Mistuning of Bladed Disk Assemblies with Friction Contacts. Proc. of ASME Turbo Expo, ASME-Paper GT 2004-53310, Wien, Österreich, pp 1–11

Götting F (2005) Analyse des Schwingungsverhaltens von verstimmten Beschaufelungen mit Reibelementen. Fortschr.-Ber. VDI-Reihe 11, Nr. 327, Düsseldorf: VDI-Verlag

Graeff-Weinberg K, Berger H (1996) Verbesserte FE-Diskretisierung bei Kontaktaufgaben. *Technische Mechanik*, Band 16, Heft 3, pp 257–270

Greenwood JA, Williamson JBP (1966) Contact of Nominally Flat Surfaces. *Proc of the Royal Society*, London, Vol 295, p 300

Greenwood JA, Tripp JH (1967a) The Elastic Contact of Rough Spheres. *J of Applied Mechanics*, 34, pp 153–159

Greenwood JA (1967b) The Area of Contact Between Rough Surfaces and Flats. *J Lubrication Technology*, pp 81–91

Greenwood JA, Tripp JH (1971) The contact of two nominally flat rough surfaces. *Proc Instn Mech Engrs,* Vol 185 48/71, pp 625–633

Greenwood JA (1984) A unified theory of surface roughness. *Proc Royal Soc Lond* A 393, pp 133–157

Greenwood JA (1985) Formulas for Moderately Elliptical Hertzian Contacts. *J Tribology*, Vol 107, pp 501–504

Greenwood JA (1992a) Contact of Rough Surfaces. In: Fundamentals of Friction: Macroscopic and Microscopic Processes, eds IL Singer, HM Pollock, Kluwer Academic Publishers. Printed in the Netherlands, pp 37–56

Greenwood JA (1992b) Problems with Surface Roughness. In: Fundamentals of Friction: Macroscopic and Microscopic Processes, eds IL Singer, HM Pollock, Kluwer Academic Publishers. Printed in the Netherlands, pp 57–76

Gutzeit F, Sextro W, Kröger M. (2006) Unsteady Rolling Contact of Rubber Wheels. In: Lecture Notes in Applied and Computational Mechanics, Vol 27, Eds.: Wriggers P and Nackenhorst U, Springer, Berlin, Heidelberg

Hagedorn P (1984) Nichtlineare Schwingungen. Wiesbaden: Akademische Verlagsgesellschaft

Haines DJ, Ollerton E (1963) Contact stress distribution on elliptical contact surfaces subjected to radial and tangential forces. *Proc of the Institution of Mechanical Engineers*, Vol 177, No 4, pp 95–114

Hertz H (1882) Über die Berührung fester elastischer Körper. *J für die reine und angewandte Mathematik*, Crelle, Vol 92, pp 156–171

Hess DP, Soom A (1991a) Normal Vibrations and Friction Under Harmonic Loads: Part I - Hertzian Contacts. *J of Tribology*, Vol 113, pp 80–86

Hess DP, Soom A (1991b) Normal Vibrations and Friction Under Harmonic Loads: Part II - Rough Planar Contacts. *J of Tribology*, Vol 113, pp 87–92

Hess DP, Soom A (1992) Normal and Angular Motions at Rough Planar Contacts During Sliding With Friction. *J of Tribology*, Vol 114, pp 567–578

Hess DP, Wagh NJ (1995) Evaluating Surface Roughness From Contact Vibrations. *J of Tribology*, Vol 117, pp 60–64

Hill DA, Nowell D, Sackfield A (1993) Mechanics of Elastic Contacts. Butterworth – Heinemann Ltd, Oxford

Hinrichs N (1997a) Reibungsschwingungen mit Selbst- und Fremderrgung: Experiment, Modellierung und Berechnung. Fortschr.-Ber. VDI-Reihe 11, Nr. 240, Düsseldorf: VDI-Verlag

Hinrichs N, Oestreich M, Popp K (1997b) Dynamics of Oscillators with Impact and Friction. *J Chaos, Solitons & Fractals*, Vol 8, No 8, Pergamon Press, pp 535–558

Hinrichs N, Oestreich M, Popp K (1998) On the Modelling of Friction Oscillators. *J of Sound and Vibration*, 216(3), pp 435–459

Hirschberg W, Rill G, Weinfurter H (2002) User-Appropriate Tyre-Modelling for Vehicle Dynamics in Standard and Limit Situations. Vehicle System Dynamics, Vol 38, No 2, pp 103–125

Hoffmann N (2006) Transient Growth and Stick-Slip in Sliding Friction. *J of Appl Mech* 73, 642

Holland J, Rick F (1997) Einfluß der Kontakttemperatur auf den Kraftschlußbeiwert. *Tribologie und Schmierungstechnik* 44, Jahrgang 2

Hunt KH, Crossley FRE (1975) Coefficient of restitution interpreted as damping in vibroimpact. *J Appl Mech*, Vol 16, pp 440–445

Hurty WC (1960) Vibrations of Structural Systems by Component Mode Synthesis. *J of the Engineering Mechanics Division* 86, EM 4, pp 51–69

Hurty WC (1965) Dynamic Analysis of Structural Systems Using Component Modes. *AIAA J,* Vol 3, No 4, pp 678–685

Ibrahim RA (1994) Friction Induced Vibration, Chatter, Squeal and Chaos. Part I: Mechanics of Friction. Part II: Dynamics and Modelling. *Applied Mechanics Reviews*, Vol 47, No 7, pp 227–254

Iooss G, Joseph P (1980) Elementary Stability and Bifurcation Theory. New York: Springer-Verlag

Jacobson BO (1991) Rheology and Elastohydrodynamic Lubrication. *Tribology Series*, 19, Elsevier, Amsterdam

Jäger J (1996) Stepwise Loading of Half-Spaces in Elliptical Contact. *ASME J of Applied Mechanics*, Vol 63, pp 766–773

Jäger J (1998) A New Principle in Contact Mechanics. *J of Tribology*, Vol 120, pp 677–684

Jäger J (1999) Equal Layers in Contact with Friction. In: Gaul and Brebbia: Computational Methods in Contact Mechanics IV, WIT Press, Southampton, Boston, pp 99–108

Johnson KL (1989) Contact Mechanics. Cambridge, New York, Melbourne, Cambridge University Press

Kaiser I and Popp K (2005) Interaction of elastic wheelsets and elastic rails: modeling and simulation. J. of Vehicle System Dynamics

Kalker JJ (1967) On the rolling contact of two elastic bodies in the presence of dry friction. Doctoral Dissertation, Technical University Delft (Nda. Drukkerig Bedrigf NV - Leiden)

Kalker JJ (1990) Three-dimensional Elastic Bodies in Rolling Contact. Solid Mechanics and Its Application. Vol 2, Kluwer Academic Publishers, Dordrecht, Boston, London

Kammerer H (1998) Nichtglatte Dynamik eines fremderregten elastischen Balkens mit Reibglied. Institut für Mechanik, Universität Fridericiana Karlsruhe (TH), Bericht-Nr. M98/1, Herausgeber: Prof. Dr.-Ing. K. Schweizerhof, Prof. Dr.-Ing. P. Vielsack

Kikuchi N, Oden JT (1988) Contact Problems in Elasticity - A Study of Variational Inequalities and Finite Element Methods. Philadelphia: SIAM, (Studies in Applied Mathematics)

Klamt K (1990) Zur optimalen Schwingungsdämpfung durch trockene Reibung in lokalen und ausgedehnten Fügestellen. Fortschr.-Ber. VDI-Reihe 11, Nr. 134, Düsseldorf: VDI-Verlag

Klarbring A (1985) Contact Problems in Linear Elasticity, Friction Laws and Mathematical Programming Applications. Linköping Studies in Science and Technology, Dissertations, No 133, VTT-Grafiska, Vimmerby, Sweden

Knothe K, Liebelt S (1995) Determination of temperatures for sliding contact with applications for wheel-rail systems. *Wear* 189, pp 91–99

Knothe K (1999) Gleisdynamik und Wechselwirkung zwischen Fahrzeug und Fahrweg. *ZAMM* 79, pp 723–737

Knothe K, Stichel S (2003) Schienenfahrzeugdynamik. Springer Verlag

Kragelski IV, Dobychin MN, Kombalov VS (1982) Friction and Wear - Calculation Methods. (Translated from the Russian by N Standen), Pergamon Press

Krause H, Poll G (1980) Mechanik der Festkörperreibung. VDI-Verlag, Düsseldorf

Krause H, Poll G (1986) Wear of Wheel-Rail Surfaces. *Wear*, 113, pp 103–122

Kreuzer E (1987) Numerische Untersuchung nichtlinearer dynamischer Systeme. Berlin: Springer-Verlag

Krzyzynski T, Popp K, Sextro W (2000) On Some Regularities in the Dynamic Response of Cyclic Periodic Structures. *J of Chaos, Solitons & Fractals*, Vol 11, No 10, pp 1597–1609

Küsel M, Brommundt E (1999) Entwicklung von Unrundheiten gummigefederter Eisenbahnräder. *ZAMM* 79, pp 299–300

Leven RW, Koch BP, Pompe B (1982) Chaos in dissipativen Systemen. Berlin : Akademischer Verlag

Lindner M, Sextro W, Popp K (2004) Hysteretic Friction of a Sliding Rubber Element. Proc. of Applied Mathematics and Mechanics (PAMM), Vol 4

Ludema KC (1996) Friction wear lubrication - A textbook in tribology, CRC Press, Boca Raton, New York

Magnus K (1976) Schwingungen. 3rd Edition, Stuttgart: Teubner

Magnus K, Popp K (1997) Schwingungen. Teubner Studienbücher Mechanik, 5. Auflage, Stuttgart

Martins JAC, Barbarin S, Raous M, Pinto da Csta A (1999) Dynamic stability of finite dimensional linearly elastic systems with unilateral and Coulomb friction. *Computer Methods in Applied Mechanics Engineering* 177, pp 289–328

Menq C-H, Bielak J, Griffin H (1986a) The Influence of Microslip on Vibratory Response. Part I: A New Microslip Model. *J of Sound and Vibration*, 107(2), pp 279–293

Menq C-H, Griffin H, Bielak J (1986b) The Influence of Microslip on Vibratory Response. Part II: A Comparison with Experimental Results. *J of Sound and Vibration*, 107(2), pp 295–307

Meywerk M (1999) Polygonalization of railway wheels. *Archive of Applied Mechanics* 69, pp 105–120

Miyamoto M (1973) Effect of Dry Friction in Link Suspension on Forces Vibration of Two-Axle Car. In: Quarterly Reports Vol. 14 No. 2, pp 99–103

Mindlin RD (1949) Compliance of Elastic Bodies in Contact. *J of Applied Mechanics* 16, pp 259–268

Mindlin RD, Mason WP, Osmer JF, Deresiewicz H (1952) Effects of an Oscillating Tangential Force on the Contact Surfaces of Elastic Spheres. ASME: 1st US National Congress of Applied Mechanics (Chicago, Ill. 1951), New York: ASME, pp 203–208

Moldenhauer P, Lindner M, Kröger M, Popp K (2005) Modelling of hysteresis and adhesion friction of rubber in time domain. In: Austrell P E, Kari L (eds) Constitutive models for rubber IV, pp 515–520. Balkema, Rotterdam

Moon FC (1987) Chaotic Vibrations. New York: John Wiley & Sons

Moore AJ (1975) Principles and Applications of Tribology. Pergamon Press, Oxford, New York, Toronto

Moyrs GB (1998) Zur Entstehung und Verstärkung von Unrundheiten an Eisenbahnrädern bei hohen Geschwindigkeiten. Dissertation, Universität Karlsruhe (TH)

Müller PC, Schiehlen WO (1977) Lineare Schwingungen. Wiesbadeb: Akademische Verlagsgesellschaft

Musiol F (1994) Erklärung der Vorgänge in der Kontaktzone von trockenlaufenden Reibpaarungen über gesetzmäßig auftretende Phänomene im Reibprozeß. Dissertation von F. Musiol, Technische Universität Berlin

Müller St (1998) Linearized Wheel-Rail Dynamics-Stability and Corrugation. Fortschr.-Ber. VDI-Reihe 12, Nr. 369, Düsseldorf: VDI-Verlag

NAG (1986) The NAG Fortran Workstation Library Handbook. Published by the Numerical Algorithms Group (NAG)

Nackenhorst U (2000) Rollkontaktdynamik - Numerische Analyse der Dynamik rollender Körper mit der Finite Elemente Methode. Bericht aus dem Institut für Mechanik, Universität der Bundeswehr Hamburg, Heft November 2000

Natke HG (1992) Einführung in Theorie und Praxis der Zeitreihen- und Modalanalyse: Identifikation schwingungsfähiger elastomechanischer Systeme. Braunschweig: Vieweg

Newmark NM (1959) A method of computation for structural dynamics. *J of the Engineering Mechanics Division* 85, pp 67–94

Oden JT, Martins JAC (1985) Models and Computational Methods for Dynamic Friction Phenomena. *Computer Meth Appl Mech Engng*, Vol 52, pp 527–634

Oestreich M, Hinrichs N, Popp K (1996) Bifurcation and stability analysis for a non-smooth friction oscillator. *Archive of Applied Mechanics* 66, pp 301–314

Oestreich M (1998) Untersuchung von Schwingern mit nichtglatten Kennlinien. Fortschr.-Ber. VDI-Reihe 11, Nr. 258, Düsseldorf: VDI-Verlag

Ogden RW (1984) Non-Linear Elastic Deformations. Ellis Horwood and John Wiley, Chichester

Ostermeyer GP (1989) Das auf einer nachgiebigen Schiene rollende Rad - Ein Beitrag zur Modellierungs- und Untersuchungsmethodik. Schmidt Buchbinderei & Druckerei, Braunschweig

Ostermeyer GP (2000) Friction Models with Discrete Layers. *ZAMM* 80, pp 61–64

Ostermeyer GP (2003) On the Dynamics of the Friction Coefficient. WEAR 254, pp 852–858

Ostermeyer GP, Müller M (2006) Dynamic Interaction of Friction and Surface Topography in Brake Systems. Tribology International, 39, pp 370-380

Ottl D (1981) Schwingungen mechanischer Systeme mit Strukturdämpfung. Number 603, VDI-Fortschritt-Berichte, Düsseldorf

Panagiotopoulos PD (1993) Hemivariational Inequalities: Applications in Mechanics and Engineering. Berlin: Springer-Verlag

Panning L, Sextro W, Popp K (2000) Optimization of Interblade Friction Damper. *Proc of the International Gas Turbine & Aeroengine Congress & Exhibition*, ASME-Paper 2000-GT-541, Munich, Germany

Panning L, Sextro W, Popp K (2001) Vibrational Behaviour of Turbine Blade Assemblies with Friction Dampers. Zeitschrift für angewandte Mathematik und Mechanik (ZAMM), 81, pp 207–208

Panning L, Sextro W, Popp K (2002) Optimization of the Contact Geometry between Turbine Blades and Underplatform Dampers with respect to Friction Damping. Proc. of ASME Turbo Expo, ASME-Paper GT-2002-30429, Amsterdam, Niederlande

Panning L, Sextro W, Popp K (2003a) Design of Friction Dampers for Mistuned Bladed Disks. Proc. of Applied Mathematics and Mechanics (PAMM), Vol 3

Panning L, Sextro W, Popp K (2003b) Spatial Dynamics of Tuned and Mistuned Bladed Disks with Cylindrical and Wedge-Shaped Friction Dampers. Int. Journal of Rotating Machinery, 9(3), pp 219–228

Panning L, Popp K, Sextro W, Götting F, Kayser A, Wolter I (2004) Asymmetrical Underplatform Dampers in Gas Turbine Bladings: Theory and Application. Proc. of ASME TURBO Expo, ASME-Paper GT 2004-53316, Wien, Österreich, pp 1–12

Persson BNJ (1997) Sliding friction. Physical principles and applications. Springer, Berlin, Heidelberg

Petrov EP (2004) A Method for Use of Cyclic Symmetry Properties in Analysis of Nonlinear Multiharmonic Vibrations of Bladed Disks. Journal of Turbomachinery, ASME, Vol 126, pp 175–183

Pfeiffer F, Glocker Ch (1996) Multibody Dynamics with Unilateral Contacts. Wiley Series in Nonlinear Science, John Wiley & Sons, Inc, New York

Pfeiffer F, Glocker Ch (1999) Unilateral Multibody Contacts. *Proc of the IUTAM Symposium*, Munich, Germany, Kluwer Academic Publishers, Dordrecht, Netherlands

Popp K, Schiehlen W (1986) Fahrzeugdynamik. B.G. Teubner, Stuttgart

Popp K, Stelter P (1989) Nonlinear Oscillations of Structures Induced by Dry Friction. In: Proceedings of IUTAM Symposium on nonlinear dynamics in engineering systems, Stuttgart

Popp K (1994) Nichtlineare Schwingungen mechanischer Strukturen mit Füge- oder Kontakt-stellen. *ZAMM* 74, pp 147–165

Popp K, Hinrichs N, Oestreich M (1995a) Dynamical behaviour of a friction oscillator with simultaneous self and external excitation. *Sadhana*, Vol 20, Parts 2–4, pp 627–654

Popp K, Hinrichs N, Oestreich M (1995b) Numerische Untersuchung von Stick-Slip-Bewegungen mit Hilfe geglätter Reibkennlinien. *ZAMM* 75, pp 63–64

Popp K, Hinrichs N, Oestreich M (1996) Analysis of a self excited friction oscillator with external excitation. In: Guran, A, Pfeiffer, F, Popp, K: Dynamics of Friction and Damping. World Scientific Publishing, Singapure

Popp K (1998) Non-smooth mechanical systems - an overview. *Forschung im Ingenieurwesen* 64, Springer-Verlag, pp 223–239

Popp K, Panning L, Sextro W (2003) Vibration Damping by Friction Forces - Theory and Applications -. Journal of Vibration and Control, Vol 9, pp 419–448

Popp K, Schiehlen W (Eds.) (2003) System Dynamics and Long-Term Behaviour of Railway Vehicles, Track and Subgrade. Lecture Notes in Applied Mechanics, Vol 6, Springer

Popp K (2005) Modelling and control of friction induced vibrations. Mathematical and Computer Modeling of Dynamical Systems 11, 345

Reddy JN (1993) An Introduction to the Finite Element Method. Second Edition, McGraw-Hill, Inc, New York

Ripke B (1995) Hochfrequente Gleismodellierung und Simulation der Fahrzeug-Gleis-Dynamik unter Verwendung einer nichtlinearen Kontaktmechanik. VDI-Fortschritt-Bericht, Reihe 12, Nr. 249, VDI-Verlag, Düsseldorf

Sanliturk KY, Ewins DJ (1996) Modelling Two-dimensional Friction Contact and Its Application Using Harmonic Balance Method. *J of Sound and Vibration*, 193(2)

Schütte O, Heimann B (1998) Contact Models of External Cylindrical Grinding. *Machine Dynamics Problems* Vol 20, pp 245–262

Schiehlen W (1986) Technische Dynamik. B.G. Teubner, Stuttgart

Schiehlen W (1990) Multibody Systems Handbook. New York, Springer-Verlag

Schwertassek R, Wallrapp O (1999) Dynamik flexibler Mehrkörpersysteme. Methoden der Mechanik zum rechnergestützten Entwurf und zur Analyse mechatronischer Systeme. Friedr. Vieweg & Sohn Verlagsgesellschaft mbH, Braunschweig/Wiesbaden

Seireg AA (1998) Friction and Lubrication in Mechanical Design. Marce Dekker, Inc, New York, Basel, Hong Kong

Sextro W, Popp K (1996) Dynamical Behaviour of a Bladed Disk with Friction Dampers. The 2nd European Nonlinear Oscillation Conference, *Proc of EUROMECH*, Vol 1, Prag

Sextro W (1997a) Schwingungsverhalten von Schaufelkränzen mit Reibelementen bei Frequenzverstimmung. Fortschr.-Ber. VDI-Reihe 11, Nr. 245, Düsseldorf: VDI-Verlag

Sextro W, Popp K, Wolter (1997b) Improved Reliability of Bladed Disks due to Friction Dampers. *Proc of the International Gas Turbine & Aeroengine Congress & Exhibition*, ASME-Paper 97-GT-189, Orlando, Florida, USA

Sextro W, Popp K, Wolter I (1998a) Three-dimensional Vibration of Bladed Disk Assemblies with Friction Dampers. The 7th International Symposium on Transport Phenomena and Dynamics of Rotating Machinery, *Proc of ISROMAC-7*, Vol B, Honolulu, Hawaii, pp 621–630

Sextro W, Popp K, Wolter I (1998b) Vibrational Behaviour of Tuned and Detuned Bladed Disks with Friction Dampers. International Congress on Combustion Engines, *Proc of the 22nd CIMAC*, Vol 1, Kopenhagen, Dänemark, pp 257–270

Sextro W (1999a) Experimental Verification of a Non-Hertzian Contact Model. In: Gaul and Brebbia: Computational Methods in Contact Mechanics IV, WIT Press, Southampton, Boston, pp 181–190

Sextro W (1999b) Forced Vibration of Elastic Structures with Friction Contacts, *Proc of ASME-DETC 1999*, No DETC99/VIB-8180, Las Vegas, Nevada

Sextro W, Popp K (1999c) Ein ebenes Reibkontaktmodell zur Berechnung von Schaufelschwingungen mit Reibelementen. *ZAMM* 79, pp 311–312

Sextro W (2000) The Calculation of the Forced Response of Shrouded Blades with Friction Contacts and Its Experimental Verification. *Proc of the International Gas Turbine & Aeroengine Congress & Exhibition*, ASME-Paper 2000-GT-540, Munich, Germany

Sextro W, Popp K, Krzyzynski (2001) Localization in Nonlinear Mistuned Systems with Cyclic Symmetry. *Journal of Nonlinear Dynamic*, Vol. 25, Special Issue on Nonlinear Modes and Localization in Dynamical Systems, pp 207–220

Sextro W, Popp K (2003) Optimierung des Schwingungsverhaltens elastischer Strukturen mit Reibfugen am Beispiel von Turbomaschinenschaufeln. FVV-Abschlussbericht, Heft 753

Sextro W, Panning L, Götting F, Popp K (2002) Fast Calculation of the Statistics of the Forced Response of Mistuned Bladed Disk Assemblies with Friction Contacts. Proc. of ASME Turbo Expo, ASME-Paper GT-2002-30427, Amsterdam, Niederlande

Sextro W, Moldenhauer P, Wangenheim M, Lindner M, Kröger M (2006) Contact Behaviour of a Sliding Rubber Element. In: Lecture Notes in Applied and Computational Mechanics, Vol. 27, Eds: Wriggers P. and Nackenhorst U, Springer, Berlin, Heidelberg

Seydel R (1988) From Equilibrium to Chaos; Practical Bifurcation and Stability Analysis. Amsterdam: Elsevier

Seydel R (1988) BIFPACK - A Program Package for Continuation, Bifurcation and Stability Analysis. Mathematische Institute der Julius-Maximilians-Universität Würzburg, Version 2.3

Shabana A (2005) Dynamics of Multibody Systems. Third Edition, Cambridge University Press

Shaw SW (1986) On the Dynamic Response of a System with Dry Friction. *J of Sound and Vibration*, 108(2), pp 305–325

Shen ZY, Hedrick JK, Elkins JA (1984) A Comparison of Alternative Creep-Force Models for Rail Vehicle Dynamic Analysis. In: The Dynamics of Vehicles, Ed. JK Hedrick, *Proc of the 8th IAVSD Symposium*, MIT, Cambridge, MA Swets and Zeltinger, Lisse, the Netherlands, pp 591–605

SIMULINK (1999) Dynamic System Simulation for MATLAB. The Math Works, Inc, Handbook

Singer IL, Pollock HM (1992) Fundamentals of Friction: Macroscopie and Microscopie Processes. NATO ASI Series E, Vol 220, Kluver, Dortrecht

Soom A, Chen J-W (1986) Simulation of Random Surface Roughness-Induced Contact Vibrations at Hertzian Contacts During Steady Sliding. *J of Tribology*, Vol 108, pp 123–127

Stelter P (1990) Nichtlineare Schwingungen reibungserregter Strukturen, Fortschr.-Ber. VDI-Reihe 11, Nr. 137, Düsseldorf: VDI-Verlag

Stelter P, Sextro W (1991) Bifurcations in Dynamic Systems with Dry Friction. *International Series of Numerical Mathematics*, Vol 97, pp 343–347

Stelter P (1992) Nonlinear Vibrations of Structures Induced by Dry Friction. *Nonlinear Dynamics* 3, pp 329–345

Strömberg N, Johansson L, Klarbring A (1996) Derivation and Analysis of a Generalized Standard Model for Contact, Friction and Wear. *Int J of Solids Structures*, Vol 33, No 13, pp 1817–1836

Szwedowicz J, Sextro W, Visser R, Masserey PA (2003) On Forced Vibration of Shrouded Turbine Blades. Proc. of ASME Turbo Expo, ASME-Paper GT-2003-38808, Atlanta, USA

Thomas TR (Ed) (1982) Rough Surfaces. London: Longman

Treyde T (1995) Modellierung des Kontaktes zwischen den Deckplatten von Turbinenschaufeln. Fortschr.-Ber. VDI-Reihe 11, Nr. 224, Düsseldorf: VDI-Verlag

Troger H, Steindl A (1991) Nonlinear Stability and Bifurcation Theory. Springer Verlag

Vermeulen PJ, Johnson KL (1964) Contact of Nonspherical Elastic Bodies Transmitting Tangential Forces. *J of Applied Mechanics* 31, pp 338–340

Vohla GKW (1996) Werkzeuge zur realitätsnahen Beschreibung der Laufdynamik von Schienenfahrzeugen. Fortschr.-Ber. VDI-Reihe 12, Nr. 270, Düsseldorf: VDI-Verlag

Vu Van T (1990) Zur Behandlung von Stoßkontaktproblemen mit Reibung unter Verwendung der Finiten-Element Methode. Forschungs- und Seminarbericht aus dem Bereich der Mechanik der Universität Hannover, Bericht-Nr. F90/2

Wallaschek J, Hach KH, Stolz U, Mody P (1999) A Survey of the Present State of Friction Modelling in the Analytical and Numerical Investigation of Brake Noise Generation. ASME-DETC 1999, No DETC99/VIB-8357, Las Vegas, Nevada

Wang C-H, Soom A (1983) Interpretation of rubbing noise radiated from a pin-on disk configuration. ASME, 83-WA-NCA-4, pp 1–6

Wang M (1995) Untersuchungen über hochfrequente Kontaktschwingungen zwischen rauhen Oberflächen. Fortschr.-Ber. VDI-Reihe 11, Nr. 217, Düsseldorf: VDI-Verlag

Warnecke HJ, Dutschke W (1984) Fertigungsmeßtechnik - Handbuch für Industrie und Wissenschaft. Berlin, Heidelberg, New York, Springer Verlag

Williams ML, Landel RF, Ferry JD (1955) J Amer Chem Soc 77, pp 3701–3707

Willner K (1995a) Ein statistisches Modell für den Kontakt metallischer Körper. Universität der Bundeswehr Hamburg, Institut für Mechanik, Univ.-Prof. Dr.-Ing. H. Witfeld

Willner K, Gaul L (1995b) A penalty approach for contact description by FEM based on interface physics. Contact Mechanics II Ferrara, Computational Mechanics Publications, Southampton, pp 257–264

Willner K (1997) Elasto-plastic contact of rough surfaces. Contact Mechanics III, Comp. Mech. Publ, Southampton, pp 297–264

Willner K (1999) Thermomechanical coupling in contact problems. Computational Methods in Contact Mechanics IV, WIT Press, Southhampton, Boston, pp 89–98

Willner K (2000) Contact Laws for Rough Surfaces. *ZAMM* 80, pp 73–76

Winkler E (1867) Die Lehre von der Elastizität und Festigkeit. Prag: Dominicus

Wißbrock H (1985) Untersuchungen zur Fugendämpfung zusammengesetzter Bauteile. Fortschr.-Ber. VDI-Reihe 11, Nr. 68, Düsseldorf: VDI-Verlag

Woo KL, Thomas TR (1980) Contact of Rough Surfaces: A Review of Experimental Work. *Wear*, 58, pp 331–340

Wösle M (1997) Dynamik von räumlichen strukturvarianten Starrkörpersystemen. Fortschr.-Ber. VDI-Reihe 18, Nr. 213, Düsseldorf: VDI-Verlag

Wriggers P (1981) Zur Berechnung von Stoß- und Kontaktproblemen mit Hilfe der Finiten Element Methode. Forschungsberichte aus dem Bereich der Mechanik der Universität Hannover, Germany, Nr. F81/1

Wriggers P, Miehe C (1994) Contact constraints within coupled thermomechanical analysis - A finite element model. *Comp Methods Appl Mech Engrg,* 113, pp 301–319

Wriggers P (1995) Finite Element Algorithms for Contact Problems. *Archives of Computational Methods in Engineering*, State of the art reviews, Vol 2, 4, pp 1–49

Wriggers P (1996) Finite Element Methods for Contact Problems with Friction. *Tribology International*, Vol 29, No 8, pp 651–658

Wriggers P, Nackenhorst U (Eds.) (2006) Analysis and Simulation of Contact Problems. Lecture Notes in Applied and Computational Mechanics. Vol 27, Springer Verlag

Yang BD, Chu ML, Menq CH (1998a) Stick-Slip-Separation Analysis and Nonlinear Stiffness and Damping Characterization of Friction Contacts Having Variable Normal Load. *J of Sound and Vibration*, 210(4), pp 461–481

Yang BD, Menq CH (1998b) Characterization of 3D Contact Kinematics and Prediction of Resonant Response of Structures Having 3D Frictional Constraint. *J of Sound and Vibration*, 217(5), pp 909–925

Zavarise G, Schrefler BA, Wriggers P (1992a) Consistent Formulation for Thermomechanical Contact based on Microscopic Interface Laws. *Proc of COMPLAS III*, eds DRJ Owen, E Hinton, EE Onate, Pineridge Press

Zavarise G, Wriggers P, Stein E, Schrefler BA (1992b) Real Contact Mechanisms and Finite Element Formulation - A Coupled Thermomechanical Approach. *Int J Num Meth Engng*, Vol 35, pp 767–786

Zavarise G, Wriggers P, Stein E, Schrefler BA (1992c) A Numerical Model for Thermomechanical Contact based on Microscopic Interface Laws. *Mech Res Comm*, Vol 19, pp 173–182

Zavarise G, Wriggers P (1995) Elastoplastic Contact Problems Solved by the Cross-Constraint Method. *Proc of COMPLAS IV*, eds DRJ Owen, E Hinton, EE Onate, Pineridge Press

Nomenclature

Rare used parameters are defined within the text.

a	Halfaxis of the ellipse [*m*]
a_0	Unit length [*m*]
A	Contact area [m^2]
A_0	Nominal contact area [m^2]
b	Halfaxis of the ellipse [m]
$b_{\eta,\zeta,\xi}$	Harmonic linearized damping coefficient [*N/m*]
b_0	Width of nominal contact area [*m*]
$c_{\eta,\zeta,\xi}$	Harmonic linearized stiffness coefficient [*N/m*]
c_N	Normal contact stiffness [*N/m*]
c_{N0}	Nominal normal contact stiffness [*N/m*]
c_R	Tangential contact stiffness [*N/m*]
c_{R0}	Nominal tangential contact stiffness [*N/m*]
C	Linear Kalker coefficient [-]
D_j	Modal damping of the j^{th} mode [-]
E	Modulus of elasticity [N/m^2]
f	Frequency [Hz]
F	Force [*N*]
F_R	Friction force [*N*]
g	Ellipticity [-]
G	Shear modulus [N/m^2]
h	Height [*m*]
h_0	Height of the nominal contact area [*m*]
i	Complex unit [-]
I_R	Wear constant of the wheel [m^2/N]
j	Engine order [-]
J	Inertia [kgm^2]
k_S	Slope parameter [*s/m*]
K	Contact coefficient [*N/m*]
ℓ	Length of the deformed layer [*m*]
ℓ_0	Length of the undeformed layer [*m*]
L	Peclet number or Speed parameter [-]
m	Mass [*kg*]
m_D	Reduced point mass [*kg*]
M	Moment [*Nm*]
$n_{x,y,z}$	Number of area elements in the *x,y,z*-direction [-]
N	Number of elastic structures [-]
p	Probability density function [-]
p_N	Normal pressure [N/m^2]
$p_{x,y}$	Dimensionless parameter [-]
p_v	Pressure parameter [*s/m*]
P_R	Frictional power [*W*]
q_H	Distributed heat source [W/m^2]
Q	Heat [*J*]
r	Displacement [*m*]
R	Radius of curvature [*m*]
R_Z	Average surface roughness [*m*]
s	Slip coefficient [-]

t	Time [*s*]
T	Temperature [*K*]
T_E	End temperature [*K*]
u, v, w	Relative displacement in x, y, z-direction, respectively [*m*]
u_G	Position of equilibrium [*m*]
u_R	Surface height [*m*]
v_P	Absolute velocity of the point P [*m/s*]
$v_{x,y,z}$	Velocities in x,y,z-direction [*m/s*]
V	Average velocity [*m/s*]
W	Wear volume [m^3]
$W_{x,z}$	Work [*J*]
x, y, z	Coordinates [*m*]
Y	Yielding stress [N/m^2]

Greek Symbols

α	Angle [*rad*]
$\alpha_{R,S}$	Heat partitioning factor of the wheel, rail [-]
β	Damping factor [*s*]
δ	Transformation angle [*rad*]
Δ	Increment
ε	Strain [-]
ϕ	Angle [*rad*]
γ	Slope parameter [*1/K*]
η	Coordinate [*m*]
$\varphi_{x,y,z}$	Relative angle [*rad*]
κ	Thermal diffusivity [m^2/s]
λ	Wave length [*m*]
λ_R	Thermal conductivity of the wheel [$N/(sK)$]
μ	Friction coefficient [-]
ν	Poisson's ratio [-]
ρ	Density [kg/m^3]
σ	Stress [N/m^2]
τ	Shear stress [N/m^2]
τ_S	Shear strength [N/m^2]
ω	Angular frequency [*rad/s*]
ω_0	Angular excitation frequency [*rad/s*]
ω_{0j}	Angular eigenfrequency of the j^{th} mode [*rad/s*]
ξ	Coordinate [*m*]
ψ	Spin parameter [-]
Ψ	Torsional angle [*rad*]
ζ	Coordinate [*m*]

Vectors and Matrices

$\boldsymbol{a}$	Acceleration vector
$\boldsymbol{A}$	Transformation matrix
$\boldsymbol{b}$	Body force vector
$\boldsymbol{B}$	Operator matrix
$\boldsymbol{E}$	Unit matrix
$\boldsymbol{f}_b$	Generalized force vector of body forces
$\boldsymbol{f}_E$	Generalized force vector of excitation
$\boldsymbol{f}_O$	Generalized contact force vector
$\boldsymbol{f}_p$	Generalized force vector of external forces
$\boldsymbol{F}_{T,W}$	Contact force vector
$\boldsymbol{F_C}$	Point contact force vector
$\boldsymbol{F_S}$	Elastic force vector
$\boldsymbol{F_{SD}}$	Damping force vector
$\boldsymbol{G}$	Transformation matrix
$\boldsymbol{H}$	Matrix of elasticity
$\boldsymbol{K}$	Stiffness matrix
$\boldsymbol{M}_{T,W}$	Contact moment vector
$\boldsymbol{N}$	Matrix of Ansatzfunctions
$\boldsymbol{q}$	Vector of modal coordinates
$\boldsymbol{r}$	Vector of displacement
$\boldsymbol{S}$	System matrix
$\boldsymbol{T}$	Modal matrix
$\boldsymbol{u}$	Vector of generalized relative displacements
$\boldsymbol{w}$	Generalized displacement vector
$\boldsymbol{x}$	Vector of coordinates

Indices

$[\,\hat{}\,]$	Complex
$[\ ]^i$	Imaginary part
$[\ ]^r$	Real part
$[\ ]^T$	Transposed of [ ]
$[\ ]^*$	Dimensionless
$[\ ]_E$	Related to points of excitation
$[\ ]_i$	Related to the i^{th} blade
$[\ ]_{L,R}$	Left, right
$[\ ]_M$	Related to the point M
$[\ ]_{N,T}$	Normal, tangential
$[\ ]_O$	Related to the point O
$[\ ]_P$	Related to the point P
$[\ ]_{R,S}$	Related to the wheel, rail
$[\ ]_{x,y,z}$	In x,y,z-direction
$[\ ]_0$	Related to the point 0
$[\ ]_{1,2}$	Related to the body $1,2$

Index